



Article

Passive Sampling of Gaseous Elemental Mercury Based on a Composite TiO₂NP/AuNP Layer

Antonella Macagnano ^{1,2,*}, Paolo Papa ¹, Joshua Avossa ¹, Viviana Perri ¹, Marcello Marelli ³,
Francesca Sprovieri ⁴, Emiliano Zampetti ¹, Fabrizio De Cesare ^{1,2}, Andrea Bearzotti ¹ and
Nicola Pirrone ⁴

¹ Institute of Atmospheric Pollution Research—National Research Council (IIA-CNR), Research Area of Rome 1, Via Salaria km 29,300, 00016 Monterotondo, Italy; p.papa@iia.cnr.it (P.P.); joshua.avossa@iia.cnr.it (J.A.); v.perri@iia.cnr.it (V.P.); e.zampetti@iia.cnr.it (E.Z.); decesare@unitus.it (F.D.C.); a.bearzotti@iia.cnr.it (A.B.)

² Department of Innovation in Biological Systems, Food and Forestry University of Tuscia (DIBAF), Via S. Camillo de Lellis, 00100 Viterbo, Italy

³ Institute of Molecular Science and Technologies—National Research Council (ISTM-CNR), Via G. Fantoli 16/15, 20138 Milano, Italy; m.marelli@istm.cnr.it

⁴ Institute of Atmospheric Pollution Research—National Research Council (IIA-CNR), Division of Rende, c/o UNICAL-Polifunzionale, 87036 Arcavacata di Rende (CS), Italy; sprovieri@iia.cnr.it (F.S.); pirrone@iia.cnr.it (N.P.)

* Correspondence: antonella.macagnano@cnr.it or a.macagnano@iia.cnr.it; Tel.: +39 06 90672395-2401

Received: 6 September 2018; Accepted: 5 October 2018; Published: 7 October 2018



Abstract: Passive sampling systems (PASs) are a low cost strategy to quantify Hg levels in air over both different environmental locations and time periods of few hours to weeks/months. For this reason, novel nanostructured materials have been designed and developed. They consist of an adsorbent layer made of titania nanoparticles (TiO₂NPs, ≤25 nm diameter) finely decorated with gold nanoparticles. The TiO₂NPs functionalization occurred for the photocatalytic properties of titania-anatase when UV-irradiated in an aqueous solution containing H₂AuCl₄. The resulting nanostructured suspension was deposited by drop-casting on a thin quartz slices, dried and then incorporated into a common axial sampler to be investigated as a potential PAS device. The morphological characteristics of the sample were studied by High-Resolution Transmission Electron Microscopy, Atomic Force Microscopy, and Optical Microscopy. UV-Vis spectra showed a blue shift of the membrane when exposed to Hg⁰ vapors. The adsorbed mercury was thermally desorbed for a few minutes, and then quantified by a mercury vapor analyzer. Such a sampling system reported an efficiency of adsorption that was equal to ≈95%. Temperature and relative humidity only mildly affected the membrane performances. These structures seem to be promising candidates for mercury samplers, due to both the strong affinity of gold with Hg, and the wide adsorbing surface.

Keywords: TiO₂NPs; AuNPs; photocatalysis; mercury vapors adsorbing layer; PAS device

1. Introduction

A thin film is commonly thought of as a layer with a thickness ranging from fractions of one nanometer to several micrometers; however, it is difficult to draw a border line between thick and thin films on the basis of their thickness, overall when the film is a nanocomposite or hybrid structure [1,2]. When a layer is designed to selectively adsorb gas or VOCs (volatile organic compounds), it has to be both chemically (to favor more specific interaction forces between adsorbent and adsorbate) and physically (to increase the number of the adsorbing sites, e.g., by acting on roughness and porosity) treated. The surface layer in contact with the environment is the main responsibility of the adsorbing process, and the relationship between the gas phase concentration and the adsorbed phase

concentration at a constant temperature is reported as an adsorption isotherm, whereas the shape depicts the affinity relationships between the adsorbate and the adsorbent [3]. Therefore, most of the chemical sensors and samplers for monitoring mercury in the atmosphere have been designed with these features taken into account. Mercury is a toxic pollutant, and it is considered by WHO (World Health Organization) as one of the top 10 chemicals of major public health concern [4]. It is continuously traveling through water, soil, and atmosphere, in various forms, to different parts of the world, and it is commonly emitted from both natural sources, as volcanoes, wildfire, and soil, and human activities, as fossil fuel burning, waste incineration, power plants, and artisanal mining [5,6]. There is a huge and quickly growing body of scientific literature on the distribution of mercury in several ecosystems: atmosphere is the principal transport pathway of Hg emissions, whereas soil and water play a significant role in the reallocation of Hg in several ecosystems [7]. Mercury in the atmosphere can be carried as gaseous elemental mercury (GEM) and gaseous oxidized mercury (GOM), which together are named as total gaseous mercury (TGM, $C_{\text{mean}}: \approx 1.4 \pm 0.15 \text{ ng m}^{-3}$) and particle-bound mercury (PBM). Among them, GEM holds the most long atmospheric residence time (≈ 1 year) due to the relatively high vapor pressure and inertness to atmospheric oxidation [5,8]; conversely, GOM and PBM have much shorter atmospheric stays, being put down closer to their source locations [9,10]. Adsorbents based on sulfur-treated carbons, alumina, and zeolites, have been among the most commonly investigated materials that are able to capture mercury from the environment [11]. More recently, ZnS nanoparticles (NPs) have been developed and variously implemented as alternatives to remove Hg^0 from polluted environments [12]. The strong affinity between heavy metals (e.g., mercury) and noble metals, such as gold and silver, has been also investigated in literature as a suitable strategy to capture and reveal such a pollutant in air. Therefore, a series of filters, and detecting systems exploiting such features, have been designed to remove and detect, respectively, these pollutants within the environment. Specifically, when a removal process is required, as well as the detection of a very low concentration, cartridge-like structures with a high surface-volume ratio are preferred [13,14], and large amounts of volumes containing the pollutant are fluxed throughout the cartridge/filter, entrapping it inside. Conversely, when real-time detection or diffusion processes are investigated, thin film structures are commonly preferred. Both sensors and adsorbing devices based on metal thin films, and more recently, porous or nanostructured, have been reported in literature [15–17]. Nanostructured thin film layers, made with nanoparticles, are preferentially assembled in ordered structures, conforming to the surface with precise control over chemical and physical properties, in reproducible scaffolding. Some examples of deposition techniques that are commonly used include the electrodeposition of metal oxide and metal nanoparticles [18], the deposition of nanoparticle monolayers via the Langmuir Blodgett technique [19], sol-gel chemistry-based deposition of nanoparticles [20], layer-by-layer dip coating [21], in situ synthesis of nanoparticles using polymeric thin films as templates [22,23] self-assembling [24], and electrospray [25]. Further, depending on the functionalization or charges on the nanoparticle (NP) shells, ordered thin layer or 3D structures can also be designed by drop-casting, which is one of the simplest and cheapest deposition techniques [26,27], even if it is rarely able to assemble homogeneous layers, especially on large surfaces, mainly due to differences in evaporation rates through the substrate, or concentration fluctuations that can lead to variations in internal structure and film thickness. When the substrate is a porous matrix, the dropped nanocomponents, depending on their affinity to the surface, can penetrate and decorate the pores' surfaces, thus assuming a peculiar 3D-structure that is more or less conformal to the substrate scaffold. Such a porous layer, comprising interconnected void volumes and high surface-area-to-volume ratio, facilitates gas and VOC diffusion through its bulk, as well as gas/VOC adsorption onto its binding sites.

In the present study, highly pure quartz (SiO_2) microfibrinous filters have been used as suitable substrates decorated with a nanocomposite material by dropping, capable of adsorbing, and then quantifying vapors of mercury from the atmosphere, as a promising thin structure for passive air sampler (PAS). The latter are generally designed to be cheap, simple to operate, and to work without electricity. For mercury analysis, the most basic requirement is that a PAS is able to sorb a sufficient

amount of mercury for accurate and precise quantification. The peculiarity of the passive samplers relies on unassisted molecular diffusion of gaseous agents (i.e., volatile vapors of elemental mercury) through a diffusive surface onto an adsorbent material. Unlike active (pumped) sampling, passive samplers require no electricity (expensive pumps), have no moving parts, and are simple to use (no pump operation or calibration). After sampling, the adsorbed mercury should be desorbed off the adsorbent by solvent (chemical procedure) or thermal desorption (physical procedure). Passive samplers have to be commonly compact, portable, unobtrusive, and inexpensive. They are able to give information on the average pollution levels over time periods of a few hours, to weeks/months. They do not require supervision, and can be used in hazardous environments. Passive samplers have been designed, using a variety of synthetic materials (like sulfur-impregnated carbon (SIC), chlorine-impregnated carbon (CIC), bromine-impregnated carbon (BIC), gold-coated sorbents (GCS), etc.) and housings for Hg collection [28,29]. Activated carbon is suggested to be the most suitable sorbent material for PASs, since it is low cost and provides a large surface area [30]. On the other hand, the amalgamation between Au and Hg is also considered as an effective alternative strategy to design mercury samplers, even if it is not very popular since more expensive [28]. However, a large variety of materials based on nanotechnology have already been applied for this purpose, even if the state of art in those nanomaterial-based passive samplers is still in the early stages [31–37]. Sampling rate and adsorption capacity are the two key factors to evaluate the performance of a passive sampler. The PAS sampling rate depends on the shape of the sampler, and it is affected by meteorological factors [38–40]; meanwhile, the adsorption capacity depends on the affinity between the adsorbate and adsorbent, as well as the adsorbing layer structure (i.e., specific surface area, pore size distribution and number of binding site), and it is affected by temperature and potential chemical interferents in the air. All of these samplers work on the basis of diffusion. Most commercially available passive/diffusive samplers are planar or axial in shape [31]. Commonly, the adsorbing matrix is disk-shaped structured, with different thicknesses and porosities. Alternatively, they can have a radial shape, consisting of a columnar sorbent surrounded by a cylindrical diffusive barrier, with the purpose of increasing the sampling rate by maximizing the surface area across which diffusion occurs (Radiello® [41]). Other passive samplers for mercury vapor collection on the basis of diffusion have been constructed using a variety of synthetic materials (i.e., gold and silver surfaces, and sulfate-impregnated carbon) and housings [31,39,42].

In this work, an alternative approach adopted in the place of conventional ones has been described, designing onto a SiO₂ micro-fibrous filter, a coating (partially penetrated inside the filter) made of an aggregation of densely packed nanoparticles of TiO₂ finely decorated with smaller nanoparticles of gold AuNPs. Such a layer was achieved by exploiting the capability of TiO₂ (anatase) to photoreduce aqueous HgAuCl₄ into elemental gold when irradiated with UV-light [43]. Furthermore, when a polymer (e.g., polyvinylpyrrolidone, PVP) was added to the HgAuCl₄ aqueous solution, globose gold nanoparticles could be grown onto the metal oxide particles, obtaining a nanocomposite material with promising properties in adsorbing mercury from the atmosphere. These novel nanocomposite structures have here been considered as being very attractive adsorbing layers for passive sampling, due to both the strong affinity between mercury and gold, wide adsorbing surface due to the nanosize of the materials (expected high efficiency and lifetime), the robustness of the materials and the chance to use them for many times, thus avoiding the spread of waste materials into the environment.

2. Materials and Methods

All chemicals were acquired from Sigma Aldrich (Milan, Italy), and used without further purification: polyvinylpyrrolidone (PVP, $M_n = 1,300,000$ g/mol), titanium (IV) oxide (anatase, ≤ 25 nm diameter, Sigma Aldrich, Milan, Italy) and gold (III) chloride hydrate (HgAuCl₄, 99.999%). Ultrapure water ($5.5 \cdot 10^{-8}$ S cm⁻¹) was produced by MilliQ-EMD Millipore. Quartz slice filters (Whatman™, Little Chalfont, UK) were 400 μ m thick, and 2 cm wide with ≈ 2 μ m pore size and ≤ 3 μ m fiber diameter.

Titanium (IV) oxide (anatase) were suspended in an aqueous solution of PVP/ HAuCl_4 for preliminary investigations (600 mg TiO_2 / 60 mL PVP_{aq} / 0.03 mg HAuCl_4). Such a suspension was UV-irradiated for 1 hr (365 nm, Helios Italquartz, Italy), thus changing the color from yellow to blue-violet, and subsequently centrifuged and rinsed with water at least three times to remove PVP excess (Thermo Scientific SL16R 230V, Langensfeld, Germany; T : 4 °C; t : 15 min ($\times 3$); RCF: 5000 g). The resulting precipitated was vortexed, diluted with a few cc of ultrapure water, and deposited on the quartz slices by drop casting using a customized mask of Teflon® (d : 11.25 mm, ≈ 10 mg), then heated to 80 °C, and finally to 450 °C under a clean air flow, in order to remove both possible traces of polymer and mercury absorbed during preparation.

The nanostructured layers were analyzed by UV-Vis spectrophotometry (Spectrophotometer UV-2600, Shimadzu, integrating sphere ISR-2600Plus, Duisburg, Germany) before and after gold nano-functionalization, and by AFM (Nanosurf Flex-AFM, Liestal, Switzerland), which captured the layer surface images in tapping mode using 190Al-G tips, 190 kHz, 48 N/m.

Powder samples for transmission electron microscopy (TEM) measurements were gently grounded in an agate mortar, dispersed in isopropyl alcohol, sonicated for 10 minutes, and dropped onto a holey-carbon coated copper TEM grid. TEM and scanning transmission electron microscopy (STEM) analysis were performed by a ZEISS Libra 200FE microscope (Oberkochen, Germany) after complete solvent evaporation overnight in air. The size distribution were manually calculated counting more than 400 NPs by iTEM software (Olympus SIS, Muenster, Germany).

Optical micrographs were provided by Zeiss Axiophot Stereomicroscope equipped with a color videocamera (Axio Cam MRC, Wexford, Ireland) using a computer assisted image analysis system (AxioVision, Wexford, Ireland). The side-view of the quartz slice coated with AuNPs/ TiO_2 NPs film was provided by a Portable USB Digital Microscope $1\times$ – $5000\times$ Magnification Mini Microscope Camera ($1\times$ – $5000\times$, Bangweier, Guangdong, China) by placing the sample between a microscope slide and a base support: the remaining floating sample was 45° tilted and displayed in the same picture.

A prototype of thermal desorption system was also planned in CNR-IIA and developed (Spaziani Rolando, Italy) in order to be connected to the most commons analytical systems of mercury. The prototype was manufactured in quartz and housed in a heater system (De Marco Forneria, Italy) to allow the fast desorption of the Hg^0 adsorbed on the thin layer of the nanostructured material, flowing pure (Air 5.0, Praxair-Rivoira, Italy) throughout the desorption chamber.

Mercury Vapor Analyzer Tekran 2537A (Tekran Instruments C., Toronto, ON Canada) was used to quantify the mercury desorbed from the nanocomposite film. The exposure of the adsorbing layers to injected volumes (μL) of mercury vapors (Tekran 2505, Mercury Calibration Unit) were carried out within customized sealed Duran glass samplers (V : 8.5 mL) to study the efficiency of the membrane. Conversely, the AuNPs- TiO_2 NPs adsorbing discs were placed into customized glass samplers with diffusive caps (nylon membrane) for sampling rate calculation, and deployed with concentrations of mercury in relative humidity (%RH)- and temperature (T)-controlled measuring rooms. Such measuring rooms were monitored by the mercury vapor analyzer and a humidity-temperature transmitter (Relative Humidity and Temperature Probe HMP230, Vaisala Corporation, Helsinki, Finland).

3. Results and Discussion

Exploiting the photocatalytic properties of TiO_2 , gold nanoparticles were selectively grown under UV light irradiation on titania nanoparticles through the photoreduction of HAuCl_4 in the presence of an organic capping reagent (PVP). The light yellow-colored aqueous suspension of TiO_2 NPs containing HAuCl_4 and PVP when exposed to UV-light irradiation for 1 hr under magnetic stirring assumed a blue-purple color, due to the formation of gold nanoparticles (Figure 1). Subsequently to the centrifugation and then the resuspension of the pellet by ultrapure water, known amounts of the heterogeneous mixture, under stirring, were picked up and deposited onto several substrates to be

characterized. Before each morphological and physical-chemical measurements, the samples were heated at 450 °C per 1 hr to eliminate the PVP traces and the potential mercury adsorbed.

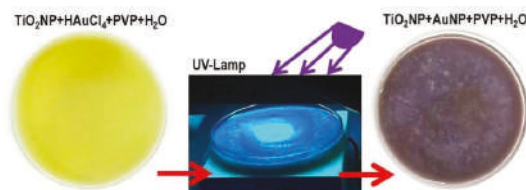


Figure 1. Functionalization of TiO₂ nanoparticles by UV-irradiation in a 0.1 M PVP (polyvinylpyrrolidone) aqueous suspension.

Due to the inhomogeneity of the film, all the spectra here depicted were carried out only over a selected area of the Au/TiO₂NPs film coating a flat substrate (SiO₂ wafer). The sample reported a reflectance minimum (about 15%) at 550 nm wavelength, thus confirming the growth of metal gold on the TiO₂ nanoparticles, and another stronger signal, with an onset at 380 nm, related to the charge transfer from the valence band to the conduction band of the titania nanoparticles [44]. The UV-Vis diffuse reflectance spectrum is depicted in Figure 2. The broad band (550 nm) was attributable to the characteristic localized surface plasmon resonance (LSPR) band of AuNPs, ranging between 500 and 600 nm [45,46]. This visible band was presumed to arise from the combined oscillations of the valence electrons confined in a cage of nanometer dimensions [47]: the position and shape of the surface plasmon band is affected by many parameters, including the dielectric constant of the medium, the particle size and shape and the coulomb charge of the nanoparticle. When AuNPs are joined to metal oxides, such as TiO₂, the material appears to be purple-brown colored, due to the characteristic surface plasmon band of gold.

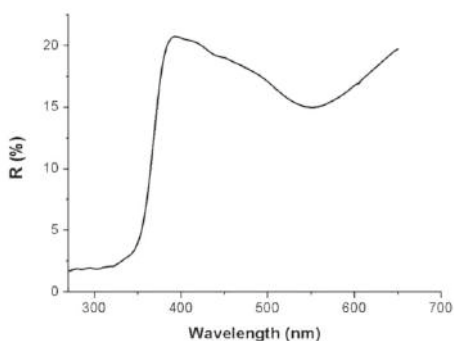


Figure 2. UV-Vis diffuse reflectance spectrum of AuNPs/TiO₂ layer in 270–670 nm wavelength range.

However, the minimum value of the reflectance band could be blue- or red-shifted, depending on the value of the average size of particles (i.e., the peak absorbance wavelength increases with particle diameter), as their aggregation (which is enhanced by a red-shift in the spectrum, as well as the broadening of adsorption peaks, and a decrease in peak intensities), functionalization, and inter-particles distance [48]. In literature, it was observed that the surface plasmon oscillation of gold nanoparticles in a suspension red shifted from ~520 to 530 nm as the particle diameter increased from 5 to 40 nm [49].

Both AuNP shape and size should be mainly related to the PVP concentration (the capping agent) and UV-light intensity, respectively [43,50] over the photocatalytic process. Specifically, the average particle size decreases as the intensity of the light increases. This effect of light intensity on the

gold particle size could be very general, and it could be used to tune the average particle size to the optimum value when preparing Au/TiO₂ using this route. Additionally, both the size and the number (or density) of the nanoparticles can increase directly with the duration of irradiation.

The gold nanoparticle size distribution of the sample (Figure 3b) was centered around the mean value of 32.6 nm (70% of NPs ranging between 5 to 40 nm). A STEM micrograph (Figure 3a) showed a good particle dispersion onto the support (Figure 3b), whereas the HRTEM (High-Resolution Transmission Electron Microscopy) ones (Figure 3c,d) revealed well-shaped and highly crystalline gold nanoparticles that were in intimate contact with the anatase crystalline support (AuNPs appear slightly darker with respect to the anatase support). Interestingly, the gold NPs shared similar sizes with the support grains, assembling together into homogeneous aggregates.

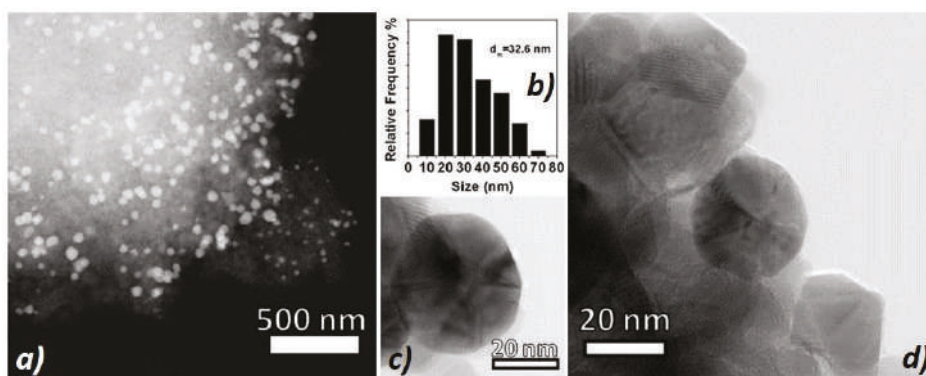


Figure 3. (a) A representative STEM micrograph of an Au/TiO₂ anatase sample at low magnification—AuNPs (gold nanoparticles) appear brighter over the greyish support; (b) AuNPs size distribution and representative HRTEM (High-Resolution Transmission Electron Microscopy) micrographs of (c) a gold NP and (d) a AuNP/TiO₂NPs cluster where a AuNP appears rounder and slightly darker than anatase ones.

Exploiting the properties of gold nanostructures due to the mercury adsorption, miniaturized sensing devices were demonstrated to be able to detect picograms of mercury in the air, like gold-microcantilevers [16] by changing their resonant frequency in real time. Au-TiO₂NPs deposited onto gold electrodes have been investigated as electrochemical sensors to detect Hg (II) in water [51]. Nanocomposite sensors made of titania nanofibers decorated with gold nanoparticles showed a limit of detection of 6 pptv (parts per trillion by volume) and 2 pptv, respectively, depending on the strategy of sampling [52]. Furthermore, devices based on resistivity changes in very thin gold films are also commercially available (Jerome[®] J405 mercury vapor analyzer) with a 0.01 $\mu\text{g m}^{-3}$ resolution and a $750 \pm 50 \text{ cc min}^{-1}$ flow rate [53]. In the case of passive samplers, gold nanostructures have been used, for instance, by deploying very thin gold electrodes (50 nm) to Hg⁰ for 100 min, and then measuring the changes in resistance (Limit of Detection, LOD: 1 $\mu\text{g/m}^3$): in this case, the analysis was provided by the same device [54]. Mercury also induces changes in the optical properties of gold films [55]. Exploiting this feature, in literature, porous glass discs were coated with AuNPs, showing a linear range within 0.1–15 ng Hg⁰ and a LOD of 0.4 ng [56]: the exposure to Hg⁰ caused a color change from red to violet-purple.

Here, the AuNP-TiO₂NP layer was exposed to a known concentration of elemental mercury vapors (14 mg/m^3) at increasing time (room temperature, 35% RH).

The diffuse reflectance spectra (Figure 4A) depicted an apparent wavelength blue shift of ≈ 2.7 nm after 15 min of exposure, up to ≈ 4.6 nm, and ≈ 6.6 nm after 60 and 120 min, respectively, according to a non-linear curve (Figure 4B), suggesting a quicker process initially and slower afterwards, also reported in literature [57]. A possible explanation has been provided by Mie theory [58]: since mercury

is expected to be adsorbed strongly onto gold surface and Au is more electronegative than Hg (2.5 and 2.0, respectively) [59], mercury may be able to donate the electron density to gold NPs [60] causing the surface plasmon mode to blue-shift [58]. The related changes (0.1%) in reflectance, which seem to increase with dependence on the exposure time (up to 60 min), may be due to the change of the refractive index for mercury entrapment inside the nanocomposite layer [49].

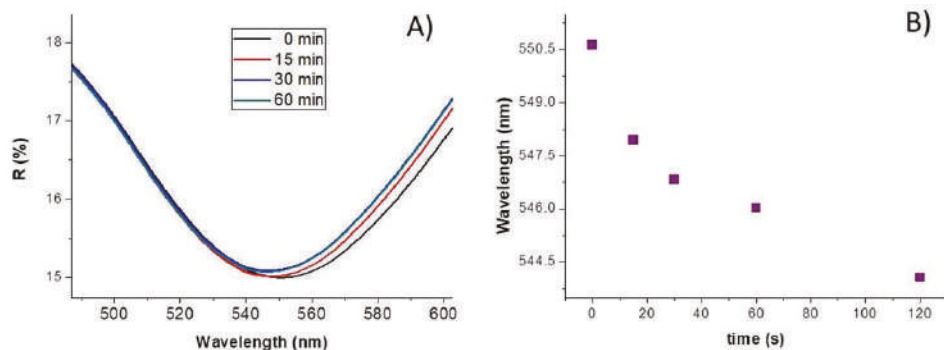


Figure 4. Comparison of UV-Vis diffuse reflectance spectra of AuNPs/TiO₂ layer in a 450–650 nm wavelength range at different exposure times to Hg⁰ vapor pressure at 20 °C and 35%RH (A); a curve plot depicting the wavelength values of the AuNPs/TiO₂ layer at increasing exposure time to Hg⁰ (B).

Similarly, a coating dispersed on a fibrous quartz surface of about 0.99×10^2 mm² was achieved by slowly dropping hundreds microliters of the aqueous suspension through a suitable mask, defining the area to be covered, and allowing water in excess to flow away through the disk filter. After deposition, the layer looked quite compact and it conformed to the quartz disc surface (Figure 5). The coating penetrated inside the quartz filter for about 25% of its thick layer, confirmed by the color change of cross filter section in Figure 5, right. Optical micrographs show that the composite film was conformal to the microfibrous surface of the supporting scaffold (Figure 5, inset), keeping its roughness characterized by valleys and overhangs.

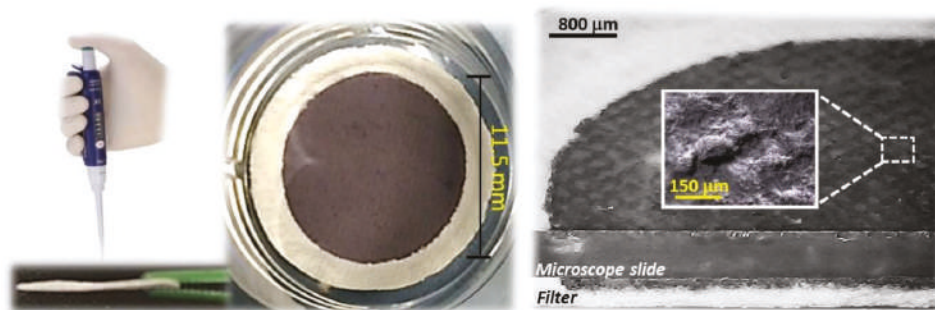


Figure 5. (Left) Drop deposition of TiO₂/AuNPs aqueous suspension; top view (middle) and side view (right) of the resulting disc. The inset depicts an optical magnification of the film surface.

Such a layer, since partially withheld by quartz microfibers, was stable and easy to be handled without suffering apparent damages or detachment. Figure 6 presents Atomic Force Microscope (AFM) surface topography images of the functionalized quartz filters. The coating surface showed a rough material provided of different sized grains (Ra: 5.4 ± 1.4 nm, average roughness) with ridges and valleys conforming to the fibrous substrate (Figure 6a). At higher magnification (Figure 6b,c), grains

(Ra: 140 ± 85 nm) appeared densely packed with a series of void spaces (darker areas), due to their uneven boundaries.

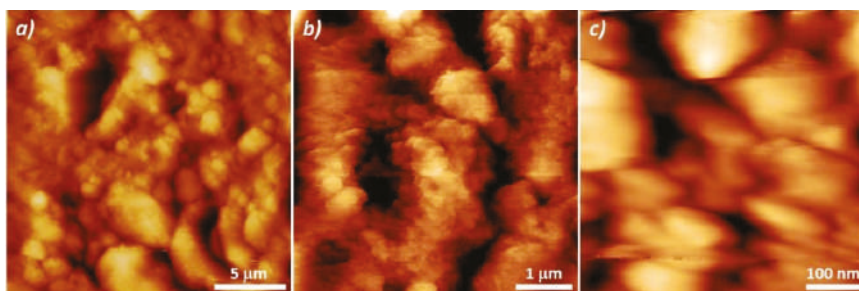


Figure 6. Atomic Force Microscope topography images of the quartz filter surface coated with a TiO_2/AuNP layer, at different magnifications.

In order to calibrate the adsorbing membrane to mercury vapors, the adsorbing disc was placed on the bottom of a suitable sealed glass chamber that was 2.5 cm height, and with a volume of 8.5 mL, where increasing amounts of Hg^0 vapors (μL) were injected by a gas-tight syringe at $\sim 20^\circ\text{C}$ (under dry air). The injected volumes were selected to lower the experimental error as much as possible. Further, each amount was first theoretically estimated and then experimentally measured by injection into the analytical instrument. Finally, the disc was subjected to thermal desorption under an air flow that collected the desorbed mercury and delivered it to the mercury analyzer. In Figure 7, the adsorbed mass of Hg^0 versus the exposure time is reported. It was noted that 15 min of film exposure appeared to be sufficient to adsorb 90% of the injected mass. However, all of the estimated injected mass values were not completely adsorbed, even after an hour, probably due to the partial nonspecific sorption of mercury to the glass container.

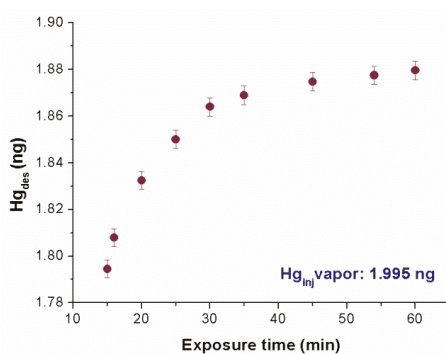


Figure 7. Adsorption curve of a known amount of injected Hg^0 vapors (C: 0.235 ng/mL) versus exposure times ranging between 15 and 60 min.

Therefore, to investigate the effects of humidity and temperature, further measurements of adsorption at different Hg^0 vapor concentrations were carried out by exposing the same membrane to the pollutant just for 15 min. The relative humidity changes were controlled and generated by a mass flow controller flowing dry air, and increasing the concentrations of the water vapors throughout the measuring chamber. Temperature values were provided by dipping the measuring chamber into a thermal bath. In order to obtain the membrane performances at -20°C , the measuring chamber was put into a fridge at -20°C . After exposure to Hg^0 by injection (15 min) the sample was resumed and desorbed for quantification. Experimental results reported a slight increase of the adsorbed mass when

the relative humidity increased up to 70% RH (relative humidity) within the measurement chamber. Specifically, when 645 pg of Hg vapor were injected into the differently humidified measuring chamber, the nanostructured material was slightly affected by the water molecules, improving entrapment by an additional amount of 0.4 ± 0.01 pg of the analyte per %RH unit (Figure 8, right).

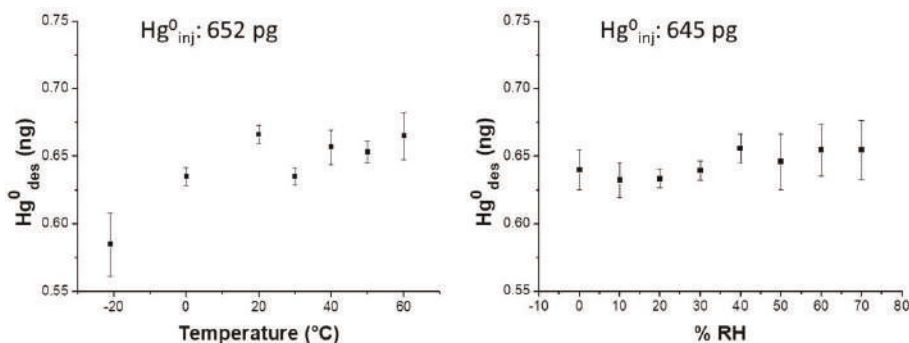


Figure 8. Plots depicting the desorbed mercury from a AuNP/TiO₂NP film upon exposure, within a sealed glass vessel that is similar to the passive sampler (PAS) container, to: (left) a known mass of Hg⁰ vapor (about 652 ± 0.01 pg) when temperature of the sampler changed (ranging between -20 and 60 °C; dry air); (right) a known mass of Hg⁰ vapor (about 645 ± 0.01 pg) when the %RH in the sampler changed (ranging between 5% and 70% relative humidity; room temperature). Each point in both the graphs is the resulting mean value from 5-times repeated-measures (error bars depict standard deviations).

Notably, when %RH was ranging between 50–70%, the desorbed values oscillated between 0.632 ng and 0.656 ng, i.e. they increased the values spread, and then the error. Similarly, temperature also slightly affected the analyte adsorption onto the PAS membrane, since the curve slope increased by 0.62 pg per Celsius degree over a thermal range of -20 – 60 °C when approximately 645 pg Hg⁰ mass was injected (Figure 8, left).

Injected mercury vapor mass values were compared to the amount of Hg⁰ that was actually adsorbed onto the exposed layer, in order to value its efficiency. Such a parameter was measured by adding a few microliters containing increasing masses of Hg⁰ vapor into the measuring chamber at room temperature and in dry air. Five replicate measurements were provided for each injection. Upon a 15 min-deployment time, the adsorbing disc was thermally desorbed, and the collected vapors were delivered to the analytical instrument and then measured. The linear relationships between the mass injected and the mass adsorbed until 10 ng were depicted in the plot of Figure 9, suggesting a high absorbance of the nanostructured material. The affinity between mercury and the nanostructured material was confirmed also by the slope value of the linear fitting ($S: 0.950 \pm 0.005$, $R^2: 0.998$) calculated on 15 min of sampling per each step. The mercury adsorbed mass when the disc was exposed to saturated mercury vapors for 18 h ($T: 20$ °C) was estimated to be more than 15 µg, confirming that such a thin layer was a very highly sorbent device for mercury.

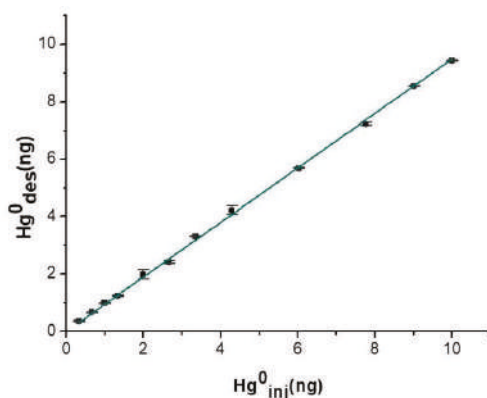


Figure 9. Adsorption curve of mercury vapors (measured as PAS-desorbed mercury) at increasing injected amounts of mercury vapors (ng).

Samples were completely restored after dozens of cycles of measurements, confirming the potential to use the same sample for many exposures. The functioning of the diffusive samplers is based on the movement of the contaminant molecules across a concentration gradient. In the collecting device (the case of a passive sampler, Figure 10) the contaminants diffuse from an area of higher concentration towards an area of lower concentration. According to the first Fick's Law, the rate at which the chemicals diffuse is represented by the following formula:

$$Q = D \left(\frac{A}{L} \right) C t, \quad (1)$$

where Q is the amount of the sample collected (ng), D is the diffusion coefficient (cm^2/min), A is the cross-sectional area of the diffusion path (cm^2), L is the diffusive path length (cm), C is the airborne concentration (mg/m^3) and t is the sampling time (min). Each contaminant has its own diffusion coefficient that is determined by its unique chemical and physical properties. The A/L parameter is determined by the sampler's geometry; the product of $D (A/L)$ is the theoretical sampling rate of a diffusive sampler for a specific compound (e.g., elementary mercury).

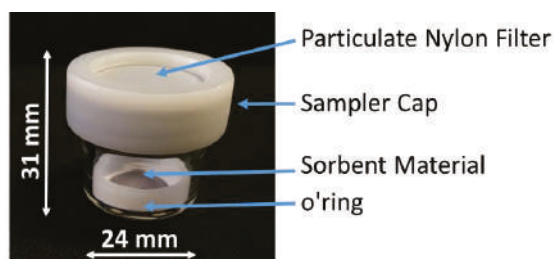


Figure 10. Prototype of mercury passive sampler comprising a diffusive membrane (particulate filter), the fibrous disc coated with AuNP/TiO₂NP (sorbent material), and a borosilicate vessel allowing the axial diffusion of Hg⁰ from the cap to the bottom. The O-ring stops the disk on the tube bottom.

In order to experimentally evaluate the sampling rate (SR) of the proposed passive sampler, a useful method is given by the use of the empirical equation (2) [28]:

$$SR = Q/(Ct) \quad (2)$$

where Q is the amount of the adsorbed mercury (ng), C is the exposition concentration (ng m^{-3}), and t is the deployed time (days) of the sample, named as PS. In our case, several measurements have been performed, exposing three passive samplers (PS1, PS2, PS3) at three different vapor mercury concentrations for 3, 7, and 15 days of sampling time. All of the measurements were performed in three measuring chambers, where three different ambient vapor mercury concentrations, of 1.2, 3.5, and 4.5 ng m^{-3} , were kept constant. As previously mentioned, the PAS device here described works exploiting the unassisted axial diffusion process of the mercury vapor through the diffusive membrane, along the glass vessel (diffusion path), up to the adsorbing film placed on the vessel bottom. This PAS comprises a see-through borosilicate vessel, a cap made of a nylon membrane for gas diffusion and particulate stopping, a locking ring to keep the adsorbing membrane to the vessel bottom, and finally the adsorbing membrane (the violet discs in Figures 10 and 11). The PAS fabrication was easy and quite reproducible, since all of the membranes that were decorated by a given volume of the suspension, reported the same weight ($10.00 \pm 0.25 \text{ mg}$), obviously with the uncertainty (2.5%) generated by the deposition technique and by the irregularity of the hosting substrate. The resulting nanostructures looked very stable, since they were partially entrapped inside the filter and did not appear to be decolored or scratched, even after 1 year of measurements. The pictures in Figure 11 shows a batch of the fibrous quartz discs decorated with the AuNP-TiO₂NP layers, and their placement into the device in order to be characterized as potential PAS for mercury. Each adsorbing disc was mercury thermally desorbed before (to have a clean substrate) and after (to measure the concentration in air) each exposure, and the desorbed vapors were delivered to the analytical instrument. Commonly, 10 min of heating was sufficient to both restore the adsorbing disc, and to measure the amount of Hg⁰ that was adsorbed throughout the deployment time. For each measure, quartz discs were heated under clean and dry air flow until the Tekran Analyzer displayed values of Hg⁰ that were close to zero.

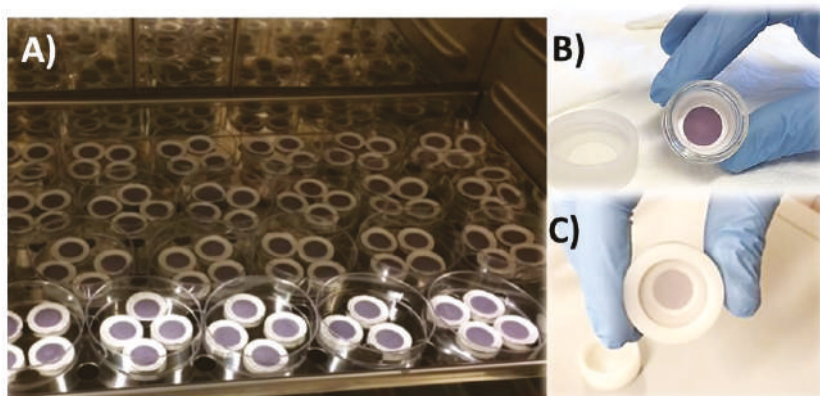


Figure 11. A fabrication step of the PAS devices: many of AuNPs-TiO₂/quartz discs drop-deposited and placed in an oven to facilitate the solvent evaporation (A); the placement of the adsorbing disc on the borosilicate vessel bottom (B); the PAS device with the particulate filter mounted (C).

After each exposure, using Equation (2), the sampling rate (SR) of each passive was calculated, and the relative results were reported in Table 1.

Table 1. Passive devices sampling rate values.

Sampler	⁽¹⁾ Hg ⁰ Vapor Concentration (ng/m ³)	Hg ⁰ Adsorbed Mass (ng)	Exposure Time (days)	Sampling Rate (m ³ /days)
PS1	3.5	0.140	3	0.013
PS2	3.5	0.143	3	0.014
PS3	3.5	0.144	3	0.014
PS1	1.2	0.124	7	0.015
PS2	1.2	0.124	7	0.015
PS3	1.2	0.116	7	0.014
PS1	3.5	0.357	7	0.015
PS2	3.5	0.355	7	0.014
PS3	3.5	0.359	7	0.015
PS1	4.5	0.463	7	0.015
PS2	4.5	0.471	7	0.015
PS3	4.5	0.452	7	0.014
PS1	1.2	0.279	15	0.016
PS2	1.2	0.272	15	0.015
PS3	1.2	0.269	15	0.015
PS1	3.5	0.727	15	0.014
PS2	3.5	0.736	15	0.014
PS3	3.5	0.720	15	0.014
PS1	4.5	0.978	15	0.014
PS2	4.5	0.962	15	0.014
PS3	4.5	0.951	15	0.014

¹ measured by TEKRAN 2537A unit, the temperature was 24 °C (with a fluctuation of 1 °C), and the RH% was 40% (with a fluctuation of 2%) over the whole experiment.

The mean value of sampling rate was estimated to be 0.014 ± 0.0007 (m³/day). Figure 12 depicts the SR values related to the exposure to increasing concentrations of mercury vapors. The reported error bars are referred to the standard deviation (*SD*) of uncertainty, showing a low dispersion of the overall values at increasing concentrations. In literature, generally depending on the range of environmental mercury concentration to be monitored, several PASs have been designed with different SRs [28], ranging from 0.00031 m³/day based on gold-coated silica placed in an axial tube without diffusive membrane [61], to 0.13 m³/day based on sulfur-impregnated activated carbon (axial tube, no diffusive membrane) [38,42], and to 6.6 m³/day based on gold-coated quartz fiber filters [62]. Furthermore, since SRs are commonly affected by environmental conditions (strong wind, pressure, proximity to the coast or to desert and sandy areas, rain), protective shells have also been used, improving the reliability of the measurements (SR: 0.121 ± 0.005 m³/day) [63]. Physically, SR quantifies the volume of air that is effectively stripped of the pollutant per unit of time. As previously described, it depends on the diffusion coefficient of the compound in air, but also on other parameters as the diffusive path length of the PAS device: by changing parameters as the length or the quality of the diffusive barriers, SR can be modulated. Thus, higher SR values are commonly preferred when very low-polluted environments may be measured with a certain accuracy and for a short time (e.g., wearable devices that are commonly suitable for 1 or 2 deployment days). Conversely, PASs with lower SR values are desired for longer times of monitoring (up to one year) to ensure the presence of free adsorbing sites on the membrane. On the other hand, SR values that are too low could be responsible for a low resolution of the PAS devices when exposed in poorly polluted sites, making them unattractive as accurate measurement tools, since, accordingly, highly sensitive analytical techniques are required.

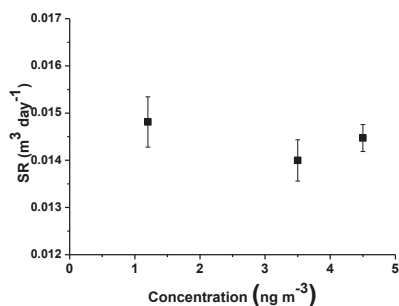


Figure 12. Estimated sampling rate vs concentration (ranging from 1.2 to 4.5 ng m⁻³).

A comparison between the estimated concentrations, calculated using the experimental sampling rate (SR) and the measured values by the vapor mercury analyzer, has been reported in Figure 13.

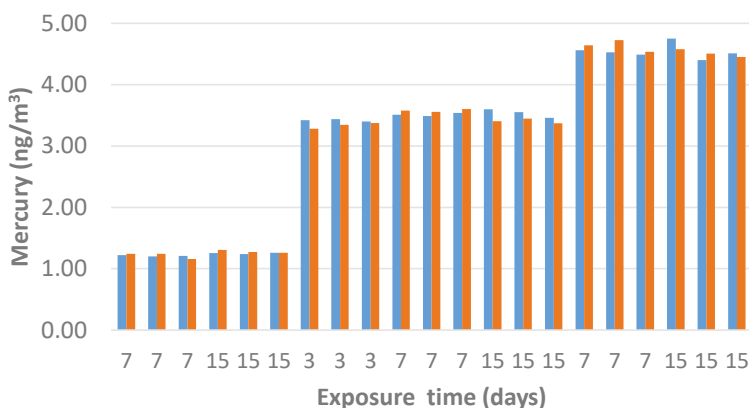


Figure 13. Comparison between the PAS estimated concentration using the experimental sampling rate (red bar) and the measured values by the vapor mercury analyzer (blue bar).

The resulting PAS values were similar to those that were reported by the analytical device over exposure times ranging between three and 15 days and to different concentrations of Hg⁰ vapors, ranging between 1.2 and 4.6 ng/m³. Specifically, when the mercury analyzer measured average concentration values of 1.23, 3.49, and 4.59 ng/m³, PAS values were reported to be 1.25, 3.44, and 4.57 ng/m³, respectively, with an average deviation of ~1.2%.

4. Conclusions

Since thin film structures are preferred for the development of passive samplers, a nanostructured mercury vapor-adsorbing layer made of TiO₂NPs and photo-decorated with AuNPs was designed and assembled by drop-casting onto a microporous filter of SiO₂. The decorated disc looked quite compact and it conformed to the SiO₂ microfibrinous surface, keeping its roughness made of valleys and overhangs, and penetrating inside the quartz filter for less than a quarter of its thickness. Such a resulting layer was stable and easy to be handled without suffering apparent damage or detachment.

The gold nanoparticles, grown on TiO₂NPs, shared similar size with the support grains, assembling together into homogeneous aggregates. However if the AuNP shapes were regular (spherical, highly crystalline), their size distribution became heterogeneous, ranging between 5 and 40 nm.

Exploiting both the high surface/volume ratio and the strong affinity between gold and mercury, the membranes, investigated as potential passive samplers for gaseous elemental mercury, showed a high absorbency (up to 15 µg), together with a 95% efficiency of absorption, with only slight effects due to temperature (+0.1% per Celsius degree, in a thermal range between −20 and 60 °C) and relative humidity (+0.06% per %RH unit, between a dry and a 70% humid environment).

Samples could be restored after dozens of cycles of measurements by thermal desorption, confirming their potential to use the same sample for many exposures.

When the adsorbing discs were placed inside axial passive samplers, a sampling rate of 0.014 m³/day was estimated when they were tested in controlled environments. Their features were compared to those of the analytical measuring instrument, reporting an average deviation of ~1.2%. Such a value suggested the chance to be applied for both short and longer monitoring campaigns. Therefore, due to their ease of preparation, their high sensitivity to gaseous elemental mercury due to the strong affinity between mercury and gold, high efficiency and a long lifetime, the AuNP/TiO₂NP-based devices are expected to be promising candidates for passive sampling strategies.

On the other hand, further studies are needed to evaluate the effect of thickness on the efficiency and adhesiveness of the quartz support. Similarly, the AuNP size and shape, as well as its density will be investigated too, in order to assess their effects onto the sensitivity and compactness of the aggregated hybrid nanoparticles inside the film. Finally, further investigations are in progress in environments that are polluted with potential interferents, such as chlorides and sulfides, and in extreme environmental conditions, in order to be considered for monitoring campaigns over the globe.

Author Contributions: Conceptualization and Design, A.M.; Methodology, A.M, E.Z., A.B., F.D.C, F.S., J.A., V.P. and N.P.; Validation, P.P., E.Z. and V.P.; Material Characterization, M.M., A.M., F.D.C. and J.A.; Experimental Investigation, P.P., M.M., V.P. and J.A.; Resources, A.M., F.S., N.P.; Project administration, N.P.; Data Curation, E.Z., P.P., F.D.C., A.B. and A.M.; Writing—Original Draft Preparation, A.M.; Writing—Review & Editing, All the Authors; Supervision, A.M., N.P.

Funding: This research was funded by UNEP-GEF Project named “Development of a Plan for Global Monitoring of Human Exposure to and Environmental Concentrations of Mercury”, grant number 4E59 of the Global Environment Facility (GEF) to UNEP, and with the co-finance of WHO Europe, CNR-IIA and UNEP.

Acknowledgments: Authors gratefully thank Capoecera A. and Esposito G. for their technical support in providing Hg⁰ vapor measurements and assembling PAS devices, respectively.

Conflicts of Interest: The authors declare that the research was conducted in the absence of any commercial or financial relationships that could be construed as a potential conflict of interest.

References

- Ohring, M. *Material Science of Thin Film*, 2nd ed.; Academic Press: Cambridge, MA, USA, 2001; ISBN 9780125249751.
- Macagnano, A. New Applications of Nanoheterogeneous Systems. In *Nanostructured Polymer Blends*; Thomas, S., Shanks, R., Chandrasekharakurup, S., Eds.; Elsevier Science: Exeter, UK, 2013; pp. 449–493. ISBN 9781455731596.
- Huang, H.; Haghghat, F.; Blondeau, P. Volatile organic compound (VOC) adsorption on material: Influence of gas phase concentration, relative humidity and VOC type. *Indoor Air* **2006**, *16*, 236–247. [[CrossRef](#)] [[PubMed](#)]
- Mercury and Health. Available online: <http://www.who.int/news-room/fact-sheets/detail/mercury-and-health> (accessed on 4 September 2018).
- Pirrone, N.; Cinnirella, S.; Feng, X.; Finkelman, R.B.; Friedli, H.R.; Leaner, J.; Mason, R.; Mukherjee, A.B.; Stracher, G.B.; Streets, D.G.; et al. Global mercury emissions to the atmosphere from anthropogenic and natural sources. *Atmos. Chem. Phys.* **2010**, *10*, 5951–5964. [[CrossRef](#)]
- Pacyna, E.G.; Pacyna, J.M.; Sundseth, K.; Munthe, J.; Kindbom, K.; Wilson, S.; Steenhuisen, F.; Maxson, P. Global emission of mercury to the atmosphere from anthropogenic sources in 2005 and projections to 2020. *Atmos. Environ.* **2010**, *44*, 2487–2499. [[CrossRef](#)]

7. Kim, M.K.; Zoh, K.D. Fate and transport of mercury in environmental media and human exposure. *J. Prev. Med. Public Heal.* **2012**, *45*, 335–343. [[CrossRef](#)] [[PubMed](#)]
8. Skov, H.; Christensen, J.H.; Goodsite, M.E.; Heidam, N.Z.; Jensen, B.; Wählin, P.; Geernaert, G. Fate of elemental mercury in the arctic during atmospheric mercury depletion episodes and the load of atmospheric mercury to the arctic. *Environ. Sci. Technol.* **2004**, *38*, 2373–2382. [[CrossRef](#)] [[PubMed](#)]
9. Pirrone, N.; Mason, R. *Mercury Fate and Transport in the Global Atmosphere: Emissions, Measurements and Models*, 1st ed.; Springer Science+Business Media: New York, NY, USA, 2009; ISBN 978-0-387-93958-2.
10. United Nations Environment Programme (UNEP). *Global Mercury Assessment 2013: Sources, Emissions, Releases and Environmental Transport*; United Nations: New York, NY, USA, 2015; ISBN 978-9211587272.
11. Otani, Y.; Emi, H.; Kanaoka, C.; Uchijima, I.; Nishino, H. Removal of mercury vapor from air with sulfur-impregnated adsorbents. *Environ. Sci. Technol.* **1986**, *22*, 708–711. [[CrossRef](#)]
12. Li, H.; Feng, S.; Qu, W.; Yang, J.; Liu, S.; Liu, Y. Adsorption and oxidation of elemental mercury on chlorinated ZnS surface. *Energy Fuels* **2018**, *32*, 7745–7751. [[CrossRef](#)]
13. Macagnano, A.; Zampetti, E.; Bearzotti, A.; De Cesare, F. Electrospinning for Air Pollution Control. In *Electrospinning for Advanced Energy and Environmental Applications*; Cavaliere, S., Ed.; CRC Press: Boca Raton, FL, USA, 2017; ISBN 9781138749085.
14. Alagappan, P.N.; Heimann, J.; Morrow, L.; Andreoli, E.; Barron, A.R. Easily regenerated readily deployable adsorbent for heavy metal removal from contaminated water. *Sci. Rep.* **2017**, *7*, 6682. [[CrossRef](#)] [[PubMed](#)]
15. Mcnerney, J.J.; Buseck, P.R.; Hanson, R.C. Mercury detection by means of thin gold films. *Science* **1972**, *178*, 611–612. [[CrossRef](#)] [[PubMed](#)]
16. Thundat, T.; Wachter, E.A.; Sharp, S.L.; Warmack, R.J. Detection of mercury vapor using resonating microcantilevers. *Appl. Phys. Lett.* **1995**, *66*, 1695–1697. [[CrossRef](#)]
17. Rex, M.; Hernandez, F.E.; Campiglia, A.D. Pushing the limits of mercury sensors with gold nanorods. *Anal. Chem.* **2006**, *78*, 445–451. [[CrossRef](#)] [[PubMed](#)]
18. Zhao, L.Y.; Eldridge, K.R.; Sukhija, K.; Jalili, H.; Heinig, N.F.; Leung, K.T. Electrodeposition of iron core-shell nanoparticles on a H-terminated Si(100) surface. *Appl. Phys. Lett.* **2006**, *88*, 033111. [[CrossRef](#)]
19. Paul, S.; Pearson, C.; Molloy, A.; Cousins, M.A.; Green, M.; Kolliopoulou, S.; Dimitrakis, P.; Normand, P.; Tsoukalas, D.; Petty, M.C. Langmuir-Blodgett film deposition of metallic nanoparticles and their application to electronic memory structures. *Nano Lett.* **2003**, *3*, 533–536. [[CrossRef](#)]
20. Fan, H.; Wright, A.; Gabaldon, J.; Rodriguez, A.; Brinker, C.J.; Jiang, Y.B. Three-dimensionally ordered gold nanocrystal/silica superlattice thin films synthesized via sol-gel self-assembly. *Adv. Funct. Mater.* **2006**, *16*, 891–895. [[CrossRef](#)]
21. Lee, D.; Rubner, M.F.; Cohen, R.E. All-nanoparticle thin-film coatings. *Nano Lett.* **2006**, *6*, 2305–2312. [[CrossRef](#)] [[PubMed](#)]
22. Boontongkong, Y.; Cohen, R.E. Cavitated block copolymer micellar thin films: Lateral arrays of open nanoreactors. *Macromolecules* **2002**, *35*, 3647–3652. [[CrossRef](#)]
23. Segalman, R.A. Patterning with block copolymer thin films. *Mater. Sci. Eng. R Rep.* **2005**, *48*, 191–226. [[CrossRef](#)]
24. Kinge, S.; Crego-Calama, M.; Reinhoudt, D.N. Self-assembling nanoparticles at surfaces and interfaces. *ChemPhysChem* **2008**, *9*, 20–42. [[CrossRef](#)] [[PubMed](#)]
25. Suh, J.; Han, B.; Okuyama, K.; Choi, M. Highly charging of nanoparticles through electrospray of nanoparticle suspension. *J. Colloid Interface Sci.* **2005**, *287*, 135–140. [[CrossRef](#)] [[PubMed](#)]
26. Fontana, L.; Fratoddi, I.; Venditti, I.; Ksenzov, D.; Russo, M.V.; Grigorian, S. Structural studies on drop-cast film based on functionalized gold nanoparticles network: The effect of thermal treatment. *Appl. Surf. Sci.* **2016**, *369*, 115–119. [[CrossRef](#)]
27. Bearzotti, A.; Papa, P.; Macagnano, A.; Zampetti, E.; Venditti, I.; Fioravanti, R.; Fontana, L.; Matassa, R.; Familiari, G.; Fratoddi, I. Environmental Hg vapours adsorption and detection by using functionalized gold nanoparticles network. *J. Environ. Chem. Eng.* **2018**, *6*, 4706–4713. [[CrossRef](#)]
28. McLagan, D.S.; Mazur, M.E.E.; Mitchell, C.P.J.; Wania, F. Passive air sampling of gaseous elemental mercury: a critical review. *Atmos. Chem. Phys.* **2016**, *16*, 3061–3076. [[CrossRef](#)]
29. McLagan, D.S.; Mitchell, C.P.J.; Steffen, A.; Hung, H.; Shin, C.; Stuppel, G.W.; Olson, M.L.; Luke, W.T.; Kelley, P.; Howard, D.; et al. Global evaluation and calibration of a passive air sampler for gaseous mercury. *Atmos. Chem. Phys.* **2018**, *18*, 5905–5919. [[CrossRef](#)]

30. Lee, S.H.; Rhim, Y.J.; Cho, S.P.; Baek, J.I. Carbon-based novel sorbent for removing gas-phase mercury. *Fuel* **2006**, *85*, 219–226. [[CrossRef](#)]
31. Huang, J.; Lyman, S.N.; Hartman, J.S.; Gustin, M.S. A review of passive sampling systems for ambient air mercury measurements. *Environ. Sci. Process. Impacts* **2014**, *16*, 374–392. [[CrossRef](#)] [[PubMed](#)]
32. James, J.Z.; Lucas, D.; Koshland, C.P. Gold nanoparticle films as sensitive and reusable elemental mercury sensors. *Environ. Sci. Technol.* **2012**, *46*, 9557–9562. [[CrossRef](#)] [[PubMed](#)]
33. Sedghi, R.; Heidari, B.; Behbahani, M. Synthesis, characterization and application of poly(acrylamide-co-methylenbisacrylamide) nanocomposite as a colorimetric chemosensor for visual detection of trace levels of Hg and Pb ions. *J. Hazard. Mater.* **2015**, *285*, 109–116. [[CrossRef](#)] [[PubMed](#)]
34. Zhang, Y.; Zeng, G.M.; Tang, L.; Li, Y.P.; Chen, Z.M.; Huang, G.H. Quantitative detection of trace mercury in environmental media using a three-dimensional electrochemical sensor with an anionic intercalator. *RSC Adv.* **2014**, *4*, 18485–18492. [[CrossRef](#)]
35. Kang, T.; Yoo, S.M.; Kang, M.; Lee, H.; Kim, H.; Lee, S.Y.; Kim, B. Single-step multiplex detection of toxic metal ions by Au nanowires-on-chip sensor using reporter elimination. *Lab Chip* **2012**, *12*, 3077–3081. [[CrossRef](#)] [[PubMed](#)]
36. Botasini, S.; Heijo, G.; Méndez, E. Toward decentralized analysis of mercury (II) in real samples. A critical review on nanotechnology-based methodologies. *Anal. Chim. Acta* **2013**, *800*, 1–11. [[CrossRef](#)] [[PubMed](#)]
37. Santos, E.B.; Ferlin, S.; Fostier, A.H.; Mazali, I.O. Using gold nanoparticles as passive sampler for indoor monitoring of gaseous elemental mercury. *J. Braz. Chem. Soc.* **2017**, *28*, 1274–1280. [[CrossRef](#)]
38. Guo, H.; Lin, H.; Zhang, W.; Deng, C.; Wang, H.; Zhang, Q.; Shen, Y.; Wang, X. Influence of meteorological factors on the atmospheric mercury measurement by a novel passive sampler. *Atmos. Environ.* **2014**, *97*, 310–315. [[CrossRef](#)]
39. Gustin, M.S.; Lyman, S.N.; Kilner, P.; Prestbo, E. Development of a passive sampler for gaseous mercury. *Atmos. Environ.* **2011**, *45*, 5805–5812. [[CrossRef](#)]
40. Tuduri, L.; Harner, T.; Hung, H. Polyurethane foam (PUF) disks passive air samplers: Wind effect on sampling rates. *Environ. Pollut.* **2006**, *144*, 377–383. [[CrossRef](#)] [[PubMed](#)]
41. Król, S.; Zabiegała, B.; Namieśnik, J. Monitoring VOCs in atmospheric air II. Sample collection and preparation. *TrAC-Trends Anal. Chem.* **2010**, *29*, 1101–1112. [[CrossRef](#)]
42. Zhang, W.; Tong, Y.; Hu, D.; Ou, L.; Wang, X. Characterization of atmospheric mercury concentrations along an urban-rural gradient using a newly developed passive sampler. *Atmos. Environ.* **2012**, *47*, 26–32. [[CrossRef](#)]
43. Li, D.; McCann, J.T.; Gratt, M.; Xia, Y. Photocatalytic deposition of gold nanoparticles on electrospun nanofibers of titania. *Chem. Phys. Lett.* **2004**, *394*, 387–391. [[CrossRef](#)]
44. Rahulan, K.M.; Ganesan, S.; Aruna, P. Synthesis and optical limiting studies of Au-doped TiO₂ nanoparticles. *Adv. Nat. Sci. Nanosci. Nanotechnol.* **2011**, *2*. [[CrossRef](#)]
45. Jain, P.K.; Lee, K.S.; El-Sayed, I.H.; El-Sayed, M.A. Calculated absorption and scattering properties of gold nanoparticles of different size, shape, and composition: Applications in biological imaging and biomedicine. *J. Phys. Chem. B* **2006**, *110*, 7238–7248. [[CrossRef](#)] [[PubMed](#)]
46. Njoki, P.N.; Lim, I.-S.; Mott, D.; Park, H.-Y.; Khan, B.; Mishra, S.; Sujakumar, R.; Luo, J.; Zhong, C.-J. Size correlation of optical and spectroscopic properties for gold nanoparticles. *J. Phys. Chem. C* **2007**, *111*, 14664–14669. [[CrossRef](#)]
47. Primo, A.; Corma, A.; García, H. Titania supported gold nanoparticles as photocatalyst. *Phys. Chem. Chem. Phys.* **2011**, *13*, 886–910. [[CrossRef](#)] [[PubMed](#)]
48. Amendola, V.; Meneghetti, M.; Amendola, V.; Meneghetti, M. Size evaluation of gold nanoparticles by UV-VIS spectroscopy size evaluation of gold nanoparticles by UV-VIS spectroscopy. *J. Phys. Chem. C* **2009**, *113*, 4277–4285. [[CrossRef](#)]
49. Morris, T.; Copeland, H.; McLinden, E.; Wilson, S.; Szulcowski, G. The effects of mercury adsorption on the optical response of size-selected gold and silver nanoparticles. *Langmuir* **2002**, *18*, 7261–7264. [[CrossRef](#)]
50. McGilvray, K.L.; Decan, M.R.; Wang, D.; Scaiano, J.C. Facile photochemical synthesis of unprotected aqueous gold nanoparticles. *J. Am. Chem. Soc.* **2006**, *128*, 15980–15981. [[CrossRef](#)] [[PubMed](#)]
51. Zhou, L.; Xiong, W.; Liu, S. Preparation of a gold electrode modified with Au–TiO₂ nanoparticles as an electrochemical sensor for the detection of mercury(II) ions. *J. Mater. Sci.* **2015**, *50*, 769–776. [[CrossRef](#)]

52. Macagnano, A.; Perri, V.; Zampetti, E.; Ferretti, A.M.; Sprovieri, F.; Pirrone, N.; Bearzotti, A.; Esposito, G.; De Cesare, F. Elemental mercury vapor chemoresistors employing TiO₂ nanofibers photocatalytically decorated with Au-nanoparticles. *Sens. Actuators B Chem.* **2017**, *247*, 957–967. [[CrossRef](#)]
53. Gold Film Mercury Vapor Analyzer. Available online: <https://www.azic.com/jerome/j405/> (accessed on 4 September 2018).
54. Mattoli, V.; Mazzolai, B.; Raffa, V.; Mondini, A.; Dario, P. Design of a new real-time dosimeter to monitor personal exposure to elemental gaseous mercury. *Sens. Actuators B Chem.* **2007**, *123*, 158–167. [[CrossRef](#)]
55. Morris, T.; Kloepper, K.; Wilson, S.; Szulczewski, G. A spectroscopic study of mercury vapor adsorption on gold nanoparticle films. *J. Colloid Interface Sci.* **2002**, *254*, 49–55. [[CrossRef](#)] [[PubMed](#)]
56. De Barros Santos, E.; Moher, P.; Ferlin, S.; Fostier, A.H.; Mazali, I.O.; Telmer, K.; Brolo, A.G. Proof of concept for a passive sampler for monitoring of gaseous elemental mercury in artisanal gold mining. *Sci. Rep.* **2017**, *7*, 16513. [[CrossRef](#)] [[PubMed](#)]
57. Ravindranath, R.; Periasamy, A.P.; Roy, P.; Chen, Y.W.; Chang, H.T. Smart app-based on-field colorimetric quantification of mercury via analyte-induced enhancement of the photocatalytic activity of TiO₂-Au nanospheres. *Anal. Bioanal. Chem.* **2018**, *410*, 4555–4564. [[CrossRef](#)] [[PubMed](#)]
58. Henglein, A. Physicochemical properties of small metal particles in solution: “Microelectrode” reactions, chemisorption, composite metal particles, and the atom-to-metal transition. *J. Phys. Chem.* **1993**, *97*, 5457–5471. [[CrossRef](#)]
59. Pauling, L. *Nature of the Chemical Bond and the Structure of Molecules and Crystals: An Introduction to Modern Structural Chemistry*, 3rd ed.; Cornell University Press: New York, NY, USA, 1960; ISBN 9780801403330.
60. Bajpai, R.P.; Kita, H.; Azuma, K. Adsorption of water on Au and mercury on Au, Ag, Mo and Re: Measurements of the changes in work function. *Jpn. J. Appl. Phys.* **1976**, *15*, 2083–2086. [[CrossRef](#)]
61. Brown, R.J.C.; Burdon, M.K.; Brown, A.S.; Kim, K.H. Assessment of pumped mercury vapour adsorption tubes as passive samplers using a micro-exposure chamber. *J. Environ. Monit.* **2012**, *14*, 2456–2463. [[CrossRef](#)] [[PubMed](#)]
62. Huang, J.; Choi, H.-D.; Landis, M.S.; Holsen, T.M. An application of passive samplers to understand atmospheric mercury concentration and dry deposition spatial distributions. *J. Environ. Monit.* **2012**, *14*, 2976. [[CrossRef](#)] [[PubMed](#)]
63. McLagan, D.S.; Mitchell, C.P.J.; Huang, H.; Lei, Y.D.; Cole, A.S.; Steffen, A.; Hung, H.; Wania, F. A High-Precision Passive Air Sampler for Gaseous Mercury. *Environ. Sci. Technol. Lett.* **2016**, *3*, 24–29. [[CrossRef](#)]



© 2018 by the authors. Licensee MDPI, Basel, Switzerland. This article is an open access article distributed under the terms and conditions of the Creative Commons Attribution (CC BY) license (<http://creativecommons.org/licenses/by/4.0/>).



Article

Strongly Iridescent Hybrid Photonic Sensors Based on Self-Assembled Nanoparticles for Hazardous Solvent Detection

Ayaka Sato, Yuya Ikeda, Koichi Yamaguchi and Varun Vohra *

Department of Engineering Science, the University of Electro-communications, 1-5-1 Chofugaoka, Chofu, Tokyo 182-8585, Japan; s1413079@edu.cc.uec.ac.jp (A.S.); b1366569@crystal.ee.uec.ac.jp (Y.I.); kyama@ee.uec.ac.jp (K.Y.)

* Correspondence: varun.vohra@uec.ac.jp; Tel.: +81-42-443-5359

Received: 15 February 2018; Accepted: 14 March 2018; Published: 16 March 2018

Abstract: Facile detection and the identification of hazardous organic solvents are essential for ensuring global safety and avoiding harm to the environment caused by industrial wastes. Here, we present a simple method for the fabrication of silver-coated monodisperse polystyrene nanoparticle photonic structures that are embedded into a polydimethylsiloxane (PDMS) matrix. These hybrid materials exhibit a strong green iridescence with a reflectance peak at 550 nm that originates from the close-packed arrangement of the nanoparticles. This reflectance peak measured under Wulff-Bragg conditions displays a 20 to 50 nm red shift when the photonic sensors are exposed to five commonly employed and highly hazardous organic solvents. These red-shifts correlate well with PDMS swelling ratios using the various solvents, which suggests that the observable color variations result from an increase in the photonic crystal lattice parameter with a similar mechanism to the color modulation of the chameleon skin. Dynamic reflectance measurements enable the possibility of clearly identifying each of the tested solvents. Furthermore, as small amounts of hazardous solvents such as tetrahydrofuran can be detected even when mixed with water, the nanostructured solvent sensors we introduce here could have a major impact on global safety measures as innovative photonic technology for easily visualizing and identifying the presence of contaminants in water.

Keywords: hazardous organic solvents; photonic nanostructures; self-assembly; polymer nanoparticles; biomimetic solvent sensors; iridescence

1. Introduction

Organic solvents are widely used in multiple industries and for daily chores. For instance, they are employed for industrial printing, coatings, adhesives, painting or cleaning, and in numerous types of advanced technological research and production such as the organic electronics field [1–4]. A large number of these organic solvents are considered as hazardous and can lead to either environmental or health issues [1–8]. Chlorinated solvents such as chloroform (CF) or chlorobenzene (CB), as well as heterocyclic ethers such as tetrahydrofuran (THF), can damage numerous organs including liver, kidneys, and the central nervous system. Although strict rules on hazardous solvent waste disposal are in place in developed countries, this may not be the case on a global scale. Consequently, developing simple and low-cost technologies to visually detect the presence of contaminants (hazardous organic solvents and their vapors) in air or in water is of major importance for reducing the risks that result from organic solvent usage.

Photonic crystals found in nature have well-defined nano- or micro-structures [9–15] and have inspired strategies for the development of biomimetic sensing technologies based on structural coloration [13–17]. In particular, some animals provide perfect examples of visible color-tunable

photonic materials [10–12]. The panther chameleons (*Furcifer Pardalis*) can, for instance, change their skin color by modifying the lattice parameters of their iridophores between the excited and the relaxed states [10]. Various methods for fabricating bio-inspired materials with similar structural coloration properties have been explored over the past two decades, which are either based on lithographic techniques (e.g., electron-beam lithography, imprint lithography, holographic lithography, or two-photon lithography) [18–21] or on self-assembled materials [22–24]. Although lithographic techniques can generate well-defined architectures, colloidal self-assembly has been drawing increasing interest in the field, as it provides a low-cost alternative to fabricating materials with structural coloration properties. This was first achieved with silicon-based monodisperse spherical particles with submicrometer diameters [25,26], but these hard particles were quickly replaced with soft polymer nanoparticles, as they can be produced at a lower cost and their properties can be easily adapted through simple chemistry (e.g., to generate core-shell structures with different refractive indices) [16,23,27].

Several studies have demonstrated that polymer nanoparticles as fused films or embedded in elastomer matrices can be applied to water or organic solvent sensors fabrication [16,27,28]. Similarly to the chameleon's camouflage properties, the color variation observed from these films can be correlated with changes in the lattice parameters of the photonic crystals and/or changes in refractive indices upon diffusion of the organic molecules inside the matrix. The spectral changes are generally described by the Bragg diffraction equation that is derived from Bragg and Snell's laws (Equation (1)), which relates the maximum peak wavelength (λ) with the incident angle (θ) and the effective refractive index (n_{eff}):

$$m\lambda = 2d_{111}\sqrt{n_{\text{eff}}^2 - \sin^2\theta} \quad (1)$$

in which d_{111} corresponds to the distance between adjacent nanoparticle centers in the (111) plane and m is the order of diffraction. d_{111} and n_{eff} can be calculated following Equations (2) and (3).

$$d_{111} = \sqrt{2/3}D_{\text{particle}} \quad (2)$$

$$n_{\text{eff}}^2 = \sqrt{0.74 n_{\text{particle}}^2 + 0.26 n_{\text{fill}}^2} \quad (3)$$

in which D_{particle} and n_{particle} correspond to the diameter and refractive index of the nanoparticle, respectively, and n_{fill} is the refractive index of the filling matrix. One of the most commonly used matrices for this application is a cross-linked silicon-based elastomer, polydimethylsiloxane (PDMS). Depositing uniform three dimensional nanoparticle structures on hydrophobic substrates has been one of the challenges to produce strongly iridescent materials. This was successfully achieved by using techniques such as dip-coating [16,29] or Langmuir-Blodgett deposition [30,31]. However, the commonly employed thin film deposition technique—spin-coating—is usually avoided, as it has a tendency to create non-uniform films due to the fast drying kinetics resulting from the quick rotation of the substrate [24]. Uniform nanoparticle photonic crystals from aqueous dispersions could be deposited on PDMS substrates by solving the wetting issue through a time-consuming chemical surface functionalization of the substrate [32].

Here, we introduce an innovative hybrid material based on spin-coated monodisperse polystyrene (PS) nanoparticles coated with a thin metallic layer and embedded in a PDMS matrix. By increasing the wettability of PDMS using a surface plasma treatment, we could form spin-coated, crack-free, close-packed, three-dimensional photonic structures on PDMS which, once coated with silver (Ag), exhibit strong iridescent colors. After depositing a second layer of PDMS on top of the Ag-coated photonic crystals, we produce a mechanically resistant material that can repeatedly be used as photonic chemical sensor for numerous organic solvents. Unlike previous studies on photonic sensors fabricated using self-assembled PS nanoparticles [16,28,33], we demonstrate that this approach is not limited to water and alcohols but can be applied to the detection and identification of hazardous solvents such as CF, CB, and THF, which can contaminate water and represent a real danger to human health and the

environment. Using a set of five test organic solvents, we observe the dynamic reflectance peak shifts that result from variations in d_{111} as a result of the PDMS swelling. Furthermore, we verified that the prepared materials can be employed to detect small amounts of hazardous solvents mixed in water and, consequently, our study opens the path to low-cost photonic sensors for water contamination detection.

2. Materials and Methods

A schematic representation of the fabrication procedure for the PDMS-based photonic sensors is presented in Figure 1. $2.5 \times 2.5 \text{ cm}^2$ PDMS substrates (Dow Corning, Sylgard[®] 184, Midland, MI, USA) were fabricated by pouring a 10:1 mixture of the base and curing agent after intense mixing of the two components and depositing it in a square-shaped container before curing it at $80 \text{ }^\circ\text{C}$ for 2 h. The PDMS thickness (1.5 mm) was controlled by the deposited volume of uncured mixture. After the curing step, the PDMS substrates were exposed to oxygen plasma for 30 min using a pressure of 500 mTorr and a light intensity of 10 W at 10 MHz. The contact angle between the 600 nm diameter PS nanoparticle aqueous dispersion (Thermo Fisher 5060A, Waltham, MA, USA, size uniformity $\leq 3\%$, $n_{\text{particle}} = 1.59$ at 589 nm), and the PDMS substrates was accurately measured using a plug-in for the ImageJ 1.47v software, which follows a computational method that is described elsewhere [34]. The monodisperse PS nanoparticle dispersion diluted to 5 wt % was spin-coated on top of the modified surface PDMS substrates at 600 rpm for 1 min.

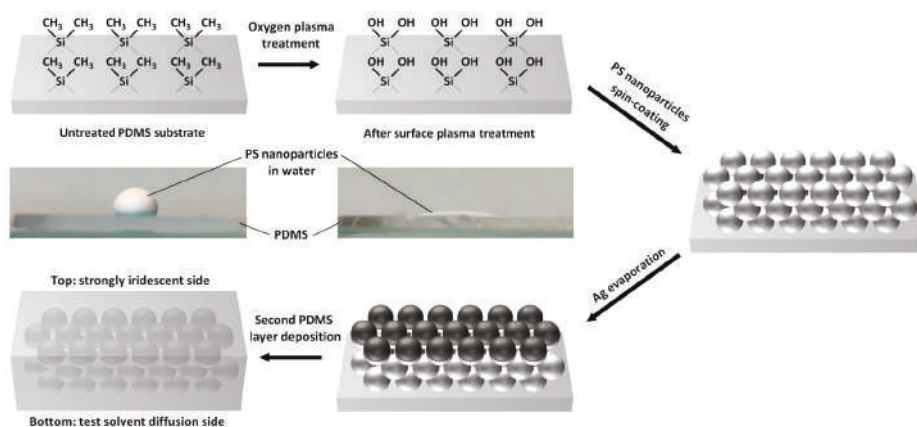


Figure 1. Schematic description of the multistep fabrication process for strongly iridescent hybrid photonic materials. The photographs correspond to PS nanoparticle aqueous dispersions deposited on PDMS substrates before and after oxygen plasma treatment.

The PS-coated PDMS substrates used for metallization were placed in an evaporation chamber until a vacuum level of 10^{-6} Torr was reached and then an 70 nm-thick Ag layer was deposited on the substrates at an evaporation rate of $0.3 \text{ nm}\cdot\text{s}^{-1}$. The Ag-coated substrates employed for PDMS embedded photonic sensor fabrication were then once again placed in a square-shaped box and covered with the same volume of PDMS mixture that was cured in the same conditions as the substrate fabrication step. The resulting photonic sensors have a thickness of approximately 3 mm, which ensures that no buckling will occur when they are exposed to the organic solvents.

SEM images of the metallized PS nanoparticles that are deposited on PDMS substrates were collected using a Field Emission SEM (Hitachi, SU3500, Tokyo, Japan) at 10 kV and with magnifications of $5000\times$ and $10,000\times$. The reflectance measurements were carried out by placing the samples on a horizontal stage with an incident light oriented 52.3° with respect to the vertical axis (Figure 2a). The light collected at an angle of 18.3° with respect to the vertical axis was analyzed using a

BlueWave-VIS Spectrometer (StellarNet, Inc., Tampa, FL, USA) from 450 to 750 nm. These angles correspond to the Wulf-Bragg conditions ($\theta = 17^\circ$) for the close-packed nanoparticles in the (111) plane. The reflectance spectra were collected using a standard halogen lamp (StellarNet, Inc., Tampa, FL, USA, SL1 Tungsten Halogen Light Source) and normalized using the reflection spectra of Ag-covered glass substrates. All measurements were performed in the experimental room's atmospheric conditions with temperatures of 25 °C and a relative humidity of 55%.

The PDMS swelling ratios were calculated by immersing the hybrid photonic materials (3 mm-thick, area of $2.5 \times 2.5 \text{ cm}^2$) into the various test solvents. The difference in weight before and after immersion for 1 h at room temperature and the molecular weight of the molecules was employed to calculate the amount of solvent that diffused into the hybrid material. Testing of the photonic materials as hazardous organic solvent sensors was performed using the same geometry as described above, and reflectance spectra were measured at regular time intervals after dropping 100 μL of each test solvent on the hybrid material surface (test solvent diffusion side in Figure 1). The sensitivity measurements were performed by gradually increasing the amount of THF placed on the photonic sensor surface. Similarly, 5 μL of THF were mixed into 95 μL of water, and the solvent mixture was deposited on top of the PDMS-based material to observe the changes in reflectance peak.

3. Results and Discussion

3.1. Strongly Iridescent Hybrid Photonic Films

After spin-coating the PS nanoparticles on a PDMS substrate, a 70 nm-thick Ag layer is deposited on top of these films, which are then covered with a second PDMS layer to ensure that the photonic structure is not damaged by repeated solvent diffusion. As demonstrated by the photographs in Figure 1, surface plasma treatment of the PDMS substrate is an essential step for ensuring that PS nanoparticles can be deposited from aqueous dispersions onto these high surface energy elastomeric substrates. Surface plasma treatment is a well-known technique that is often applied to improving the wetting properties of aqueous solutions onto hydrophobic layers such as poly(3,4-ethylenedioxythiophene) polystyrene sulfonate or PDMS [16,35,36].

The oxygen plasma treatment performed on PDMS modifies the functional groups present at its surface. In fact, the surface of pristine PDMS substrates is mainly composed of methyl groups. During plasma treatment, oxidation of these methyl groups takes place, which results in the formation of silanols that enable wetting from aqueous solutions and dispersions [37]. In the case of the PS nanoparticles dispersion we employed for our photonic material fabrication, average contact angles with the PDMS substrate of 107.5° and 24.9° were obtained before and after plasma treatment, respectively (Figure 1). This major change in contact angle and surface wetting properties enabled the spin-coating of wet layers of PS nanoparticle aqueous suspensions on PDMS substrates. Although the nanoparticles are dispersed in water, PS is intrinsically hydrophobic. The interactions between PS nanoparticles and the hydrophobic substrate (PDMS) are consequently likely to form uniform close-packed colloid photonic crystals. The scanning electron microscope (SEM) images in Figure 2b clearly demonstrate that a honeycomb close-packed arrangement of the PS nanoparticles on plasma-treated PDMS was successfully achieved. The photonic materials exhibits crack-free iridescence over areas as large as 5 cm^2 , confirming that, unlike previous attempts to fabricate PDMS-PS nanoparticle composites based on drop-casting, uniform arrangements were obtained [28]. Furthermore, coating the nanoparticles with a thin Ag layer considerably increased the reflectance of the PDMS-PS nanoparticle composites with values approximately 2.4 times higher than materials based on bare PS nanoparticles embedded in the silicon elastomer matrix (Figure 2c).

The face-centered cubic arrangements exhibit a (111) diffraction plane that is oriented at an angle of 35.3° with respect to the sample (Figure 2b). Consequently, for θ values, we consider the angle with respect to the [111] normal direction rather than the direction that is normal to the sample plane. To facilitate the visual detection of hazardous solvent traces, we selected the geometry in which θ has a

value of 17° , as it results in a green structural coloration with a reflectance peak maximum around 550 nm (Figure 2c). Similarly to previous studies on photonic opal structures, we could observe a small spatial distribution of the diffraction peak, which may be a consequence of multiple diffractions from different Bragg planes that interact with each other (Figure 2d) [38]. This may also explain why the observed reflectance peak at 550 nm in Bragg conditions does not perfectly match the results from calculations using Equation (1), which predict a reflectance peak around 497 nm. The presence of packing defects (Figure 2b) and the dispersity in nanoparticle dimensions may also contribute to the observed differences between theoretical and experimental data. As the material present on the sample dropping side of these strongly iridescent multilayer films is PDMS, they may be employed to detect the presence of hazardous organic solvents, which can diffuse inside the silicon elastomer matrix [39].

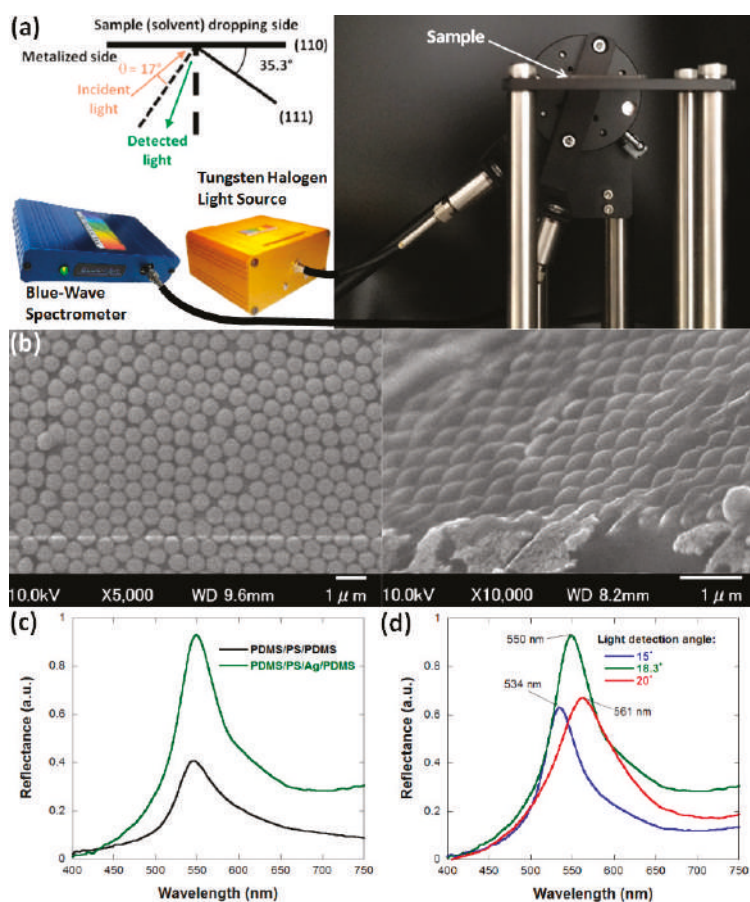


Figure 2. (a) Schematic representation and experimental set-up for the reflectance measurements; (b) top-view SEM image of the surface (left) and tilted-view SEM image of the cross-section (right) of Ag-coated PS nanoparticles deposited on plasma-treated PDMS; (c) reflectance spectrum of bare and Ag-coated PS nanoparticles embedded in PDMS for the third order of Bragg diffraction from the (111) plane observed at 17° with respect to the [111] direction; and (d) spatial and spectral distribution of the reflectance peak with incident light oriented 53.3° with respect to the vertical axis.

3.2. Hazardous Solvent Detection in Biomimetic Photonic Sensors

To test the hybrid photonic materials we developed for hazardous organic solvent sensing applications, we selected five test solvents with various PDMS swelling ratios (Table 1). In addition to CF, CB, and THF, we used dichloromethane (DCM) and dimethoxyethane (DME), which are suspected of causing cancer or may damage fertility and unborn children.

Table 1. Summarized data on tested solvent and observed reflectance peak shift when 100 μ L of solvent are deposited on the hybrid sensor.

Solvent	THF	DME	CF	CB	DCM
Refractive index (n_{solvent})	1.40	1.38	1.45	1.52	1.42
PDMS swelling ratio (mmol/g of PDMS)	17.8	11.6	17.7	7.7	7.9
Reflectance peak (nm)	601	592	597	569	575

The five tested solvents exhibit dynamic shifts of the reflectance peak that were initially observed at 550 nm. Taking into account Equations (1) and (3), the measured red shifts (Figure 3) of the reflectance peak either originate from an increase in the distance between neighboring centers in the (111) plane or larger n_{eff} values. The refractive indices of the test solvents (n_{solvent}) are summarized in Table 1. Interestingly, although THF and PDMS are relatively similar from an optical point-of-view, with n_{THF} and n_{PDMS} having values of 1.40 and 1.41, respectively, a 50 nm red shift of the reflectance peak can be observed, which suggests that the key parameter for the response from the photonic sensor is the PDMS swelling ratio. In fact, CF, which has a refractive index of 1.45 but almost the same swelling ratio as THF, yields similar values of reflectance peak shift.

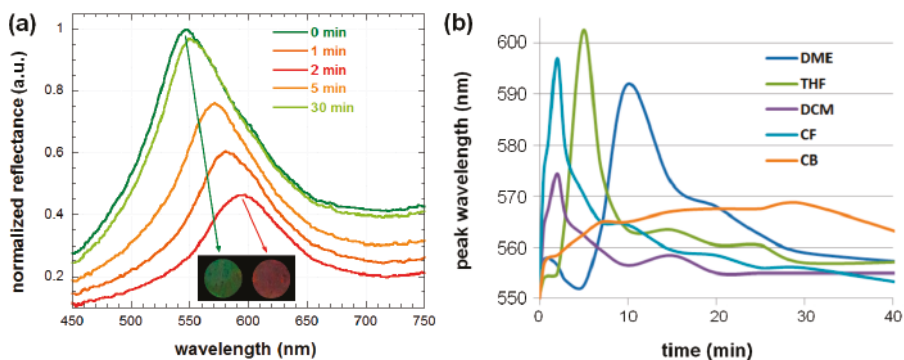


Figure 3. (a) Time-resolved reflectance spectra of 100 μ L CF dropped from the non-metal side onto the hybrid photonic sensor; (b) time-dependent evolution of the reflectance peak wavelength of various solvents dropped on the hybrid photonic sensor. The inset in (a) corresponds to the observed sample with an area of 5 cm^2 before deposition of CF and 2 min after the deposition.

Using the solvent with a high swelling ratio (CF), we verified that the changes in reflected color from green to red (597 nm) can be visually recognized within a few minutes (inset of Figure 3a). In fact, the five test solvents can be categorized in three classes of swelling ratios with values close to 18 (CF and THF), 12 (DME), and 8 (DCM and CB) mmol/g of PDMS, respectively. These three classes of solvents yield shifts of approximately 50 nm, 40 nm, and 20 nm, respectively. Consequently, it is safe to assume that the working mechanism of these biomimetic photonic sensors is very similar to the color-tuning properties of the chameleon skin and principally relies on a deformation of the photonic crystal lattice upon swelling of PDMS by the solvents (increase in d_{111}) [10]. Note that the standard deviation for 10 measurements using the same solvent is less than 1 nm, which implies

that even small differences in reflectance peak wavelength (e.g., 601 and 597 nm for THF and CF, respectively) can be employed to identify the nature of the solvent that diffuses into the photonic sensor. Nonetheless, to ensure that each solvent can be precisely identified, we used a dynamic approach based on the solvent diffusion rate into the PDMS matrix. As displayed in Figure 3b, CF and DCM reach their maximum reflectance shifts within 2 min, whereas THF, DME, and CB take longer times of approximately 5, 10, and 30 min, respectively.

The time-dependent measurements not only allow for a better recognition of the solvents but also provide important information for understanding the differences observed in reflectance shifts from solvents with similar PDMS swelling ratios. For instance, CF and THF have PDMS swelling ratios of 17.7 and 17.8 mmol/g, respectively. Nonetheless, as CF has a higher refractive index compared to THF, a larger red shift is expected. Repeated measurements confirm that the reflectance measured from the sensors in the presence of THF is red-shifted by approximately 5 nm as compared to the results from CF. Our hypothesis for this contradictive result is that the solvent diffusion kinetics, which determine the amount of solvent present in the vicinity of the PS nanoparticles at a given time, will affect the increase in d_{111} as represented in Figure 4.

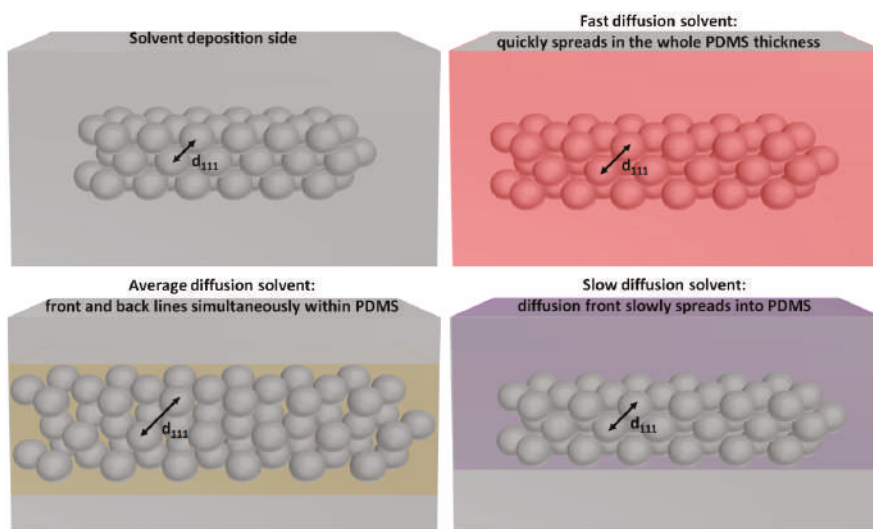


Figure 4. Schematic representation of the increased distance between adjacent PS nanoparticles embedded in the PDMS matrix when solvents with fast, average, and slow diffusion speeds are deposited on the surface of the photonic sensors.

As the reflectance peak shifts back to the initial position (550 nm) after a certain time, we neglected the effect of PS solubility on the various test solvents and considered that the solvents preferentially diffuse into PDMS. When CF is deposited on top of the photonic sensor, it quickly diffuses inside PDMS, which results in an almost homogenous distribution of the solvent molecules inside the whole elastomeric matrix thickness (approximately 3 mm). On the other hand, in the case of THF, the diffusion is slower and, consequently, the solvent swollen area gradually moves in the vertical direction within PDMS. The schematic representations in Figure 4 are exaggerated for clarity of presentation. In the case of fast diffusing solvents (e.g., CF), a smaller amount of solvent molecules remain in the direct proximity of the PS nanoparticles at the time when the maximum reflectance peak shift is recorded. This also explains why a smaller shift is observed for CF with respect to THF, which has slower diffusion kinetics even though the two solvents have similar swelling ratios (measured by immersing the photonic sensors into the various solvents). A slower diffusion rate consequently seems to be

beneficial for precise measurement of the maximum peak shift due to swelling of the PDMS matrix. Nonetheless, if the diffusion of the solvent inside PDMS is too slow, the distance between the diffusion front and back will increase, which will also result in less solvent molecules in the vicinity of the PS nanoparticles at a given time. Consequently, a larger red-shift can be observed when comparing DCM to CB despite the fact that they have similar swelling ratios. The hypothesis of time-dependent swelling of PDMS suggests that the reflectance shifts should also depend on the volume of solvent that is in contact with the sensor.

We verified the detection threshold (sensitivity) of the photonic sensors we developed here by varying the amounts of solvents used as test samples (Table 2). All the reflectance wavelengths in Table 2 correspond to the maximum shift observed during each test. The time at which these maximum shifts were observed varies depending on the test solvent. Additionally, considering the experimental error on the reflectance peak measurements, we can suppose that the minimum volume of solvent that can be detected by the photonic sensor is 5 μL (shifts larger than 5 nm). To verify whether this detection threshold can be applied to, for example, THF mixed in water, we prepared a low concentration (5 vol %) mixture of THF in water. The mixed solvent was deposited on the photonic sensors, which resulted in a reflectance peak wavelength of 569 nm collected 5 min after deposition. As this value is very close to the one measured for 5 μL of THF deposited on the sensor, we can speculate that all the THF molecules mixed in water diffuse from the mixed solvent into the PDMS based photonic sensors. These sensors consequently have a great potential as innovative technology for precisely and rapidly detecting the presence of hazardous, solvent-contaminated water.

Table 2. Photonic sensor reflectance peak wavelength with respect to deposited amount of solvent.

Solvent Amount (μL)	0	2	5	10	20	50	100	
Reflectance Peak (nm)	THF	550	552	567	574	599	601	
	DME	550	555	562	571	578	591	592
	CF	550	551	558	569	589	599	597
	CB	550	552	557	567	571	570	569
	DCM	550	554	561	569	574	574	575

4. Conclusions

In summary, we have successfully fabricated strongly iridescent hybrid photonic sensors based on self-assembled spin-coated PS nanoparticles on plasma-treated PDMS substrates. The addition of the reflective Ag layer resulted in strong structural coloration properties that can be easily observed by naked eye. The formation of close-packed structures was confirmed by SEM measurements, and we employed the green Bragg reflection peak ($\lambda = 550$ nm) to probe the diffusion of hazardous organic solvents into the photonic sensor.

Using a set of five organic solvents, we verified that these multilayer nanostructured materials can be used for the detection and identification of hazardous water contaminants. Direct visualization of the changes in reflectance peak wavelengths for a given amount of solvent can be highly beneficial for rapid analysis of the water purity with respect to these organic solvents, which can be harmful to the human health and the environment. After closely studying the behavior of the various solvents and correlating the observed reflectance peak shifts with the parameters present in the Bragg diffraction equation, we concluded that, similarly to the chameleon skin, the changes in visible color of the sensors strongly depend on the PDMS swelling by the test solvent. As each solvent has a different diffusion rate into PDMS, reliable contaminant identification can be achieved by analyzing the data in terms of time-dependent reflectance peak shift.

Lastly, we verified that hazardous solvent amounts as low as 5 μL can be detected using the hybrid photonic sensors, even when they are tested as low concentration contaminants in water. This opens the path for facile and rapid recognition of a variety of hazardous solvents that can either affect some organs such as the liver or the lungs but also result in infertility or increase the probability

of harm to unborn children. As this technology can be easily employed as simple water purity test in developing countries in which sometimes no strict rules on industrial solvent disposal exist, the sensors we produced for our study could find major applications in global safety measure implementation.

Acknowledgments: The authors would like to acknowledge the University of Electro-Communications for providing financial support through the Research Support for Young Faculty Members Program. The authors would also like to express their gratitude to Prof. Takashi Hirano for kindly accepting to share his solvents for the purpose of this research.

Author Contributions: V.V. and K.Y. conceived and designed the experiments; A.S. and Y.I. performed the experiments and analyzed the data; V.V. wrote the paper.

Conflicts of Interest: The authors declare no conflict of interest.

References

- Kristensen, P.; Irgens, L.M.; Kjersti Daltveit, A.; Andersen, A. Perinatal Outcome among Children of Men Exposed to Lead and Organic Solvents in the Printing Industry. *Am. J. Epidemiol.* **1993**, *137*, 134–144. [[CrossRef](#)] [[PubMed](#)]
- Olson, B.A. Effects of organic solvents on behavioral performance of workers in the paint industry. *Neurobehav. Toxicol. Teratol.* **1982**, *4*, 703–708.
- Agnesi, R.; Valentini, F.; Mastrangelo, G. Risk of spontaneous abortion and maternal exposure to organic solvents in the shoe industry. *Int. Arch. Occup. Environ. Health* **1997**, *69*, 311–316. [[CrossRef](#)] [[PubMed](#)]
- Vohra, V.; Mróz, W.; Inaba, S.; Porzio, W.; Giovannella, U.; Galeotti, F. Low-Cost and Green Fabrication of Polymer Electronic Devices by Push-Coating of the Polymer Active Layers. *ACS Appl. Mater. Interfaces* **2017**, *9*, 25434–25444. [[CrossRef](#)] [[PubMed](#)]
- Hardell, L.; Eriksson, M.; Lenner, P.; Lundgren, E. Malignant lymphoma and exposure to chemicals, especially organic solvents, chlorophenols and phenoxy acids case-control study. *Br. J. Cancer* **1981**, *43*, 169–176. [[CrossRef](#)] [[PubMed](#)]
- Sallmén, M.; Lindbohm, M.-L.; Kyyrönen, P.; Nykyri, E.; Anttila, A.; Taskinen, H.; Hemminki, K. Reduced fertility among women exposed to organic solvents. *Am. J. Ind. Med.* **1995**, *27*, 699–713. [[CrossRef](#)] [[PubMed](#)]
- Sherman, J.; Chin, B.; Huijbers, P.D.; Garcia-Valls, R.; Hatton, T.A. Solvent replacement for green processing. *Environ. Health Perspect.* **1998**, *106*, 253–271. [[CrossRef](#)] [[PubMed](#)]
- Prat, D.; Hayler, J.; Wells, A. A survey of solvent selection guides. *Green Chem.* **2014**, *16*, 4546–4551. [[CrossRef](#)]
- Sun, J.; Bhushan, B.; Tong, J. Structural coloration in nature. *RSC Adv.* **2013**, *3*, 14862–14889. [[CrossRef](#)]
- Teyssier, J.; Saenko, S.V.; van der Marel, D.; Milinkovitch, M.C. Photonic crystals cause active colour change in chameleons. *Nat. Commun.* **2015**, *6*, 6368. [[CrossRef](#)] [[PubMed](#)]
- Máthger, L.M.; Land, M.F.; Siebeck, U.E.; Marshall, N.J. Rapid colour changes in multilayer reflecting stripes in the paradise whiptail, *Pentapodus paradiseus*. *J. Exp. Biol.* **2003**, *206*, 3607–3613. [[CrossRef](#)] [[PubMed](#)]
- Yoshioka, S.; Matsuhana, B.; Tanaka, S.; Inouye, Y.; Oshima, N.; Kinoshita, S. Mechanism of variable structural colour in the neon tetra: Quantitative evaluation of the Venetian blind model. *J. R. Soc. Interface* **2011**, *8*, 56–66. [[CrossRef](#)] [[PubMed](#)]
- Fenzl, C.; Hirsch, T.; Wolfbeis, O.S. Photonic Crystals for Chemical Sensing and Biosensing. *Angew. Chem. Int. Ed.* **2014**, *53*, 3318–3335. [[CrossRef](#)] [[PubMed](#)]
- Yi, W.; Xiong, D.B.; Zhang, D. Biomimetic and Bioinspired Photonic Structures. *Nano Adv.* **2016**, *1*, 62–70. [[CrossRef](#)]
- Li, Q.; Zeng, Q.; Shi, L.; Zhang, X.; Zhang, K.-Q. Bio-inspired Sensors Based on Photonic Structures of Morpho Butterfly Wings: A Review. *J. Mater. Chem. C* **2016**, *4*, 1752–1763. [[CrossRef](#)]
- Kuo, W.-K.; Weng, H.-P.; Hsu, J.-J.; Yu, H.H. A bioinspired color-changing polystyrene microarray as a rapid qualitative sensor for methanol and ethanol. *Mater. Chem. Phys.* **2016**, *173*, 285–290. [[CrossRef](#)]
- Burgess, B.; Loncar, M.; Aizenberg, J. Structural colour in colourimetric sensors and indicators. *J. Mater. Chem. C* **2013**, *1*, 6075–6086. [[CrossRef](#)]
- Zhang, S.; Chen, Y. Nanofabrication and coloration study of artificial Morpho butterfly wings with aligned lamellae layers. *Sci. Rep.* **2015**, *5*, 16637. [[CrossRef](#)] [[PubMed](#)]
- Wu, C.-S.; Lin, C.-F.; Lin, H.-Y.; Lee, C.-L.; Chen, C.-D. Polymer-based photonic crystals fabricated with single-step electron-beam lithography. *Adv. Mater.* **2007**, *19*, 3052–3056. [[CrossRef](#)]

20. Aryal, M.; Ko, D.-H.; Tumbleston, J.R.; Gadisa, A.; Samulski, E.T.; Lopez, R. Large area nanofabrication of butterfly wing's three dimensional ultrastructures. *J. Vac. Sci. Technol. B* **2012**, *30*, 061802. [[CrossRef](#)]
21. Siddique, R.H.; Hüinig, R.; Faisal, A.; Lemmer, U.; Hölscher, H. Fabrication of hierarchical photonic nanostructures inspired by Morpho butterflies utilizing laser interference lithography. *Opt. Mater. Express* **2015**, *5*, 996–1005. [[CrossRef](#)]
22. Vohra, V.; Galeotti, F.; Giovannella, U.; Anzai, T.; Kozma, E.; Botta, C. Investigating phase separation and structural coloration of self-assembled ternary polymer thin films. *Appl. Phys. Lett.* **2016**, *109*, 103702. [[CrossRef](#)]
23. Zulian, L.; Emilietri, E.; Scavia, G.; Botta, C.; Colombo, M.; Destri, S. Structural Iridescent Tuned Colors from Self-Assembled Polymer Opal Surfaces. *ACS Appl. Mater. Interfaces* **2012**, *4*, 6071–6079. [[CrossRef](#)] [[PubMed](#)]
24. Zheng, H.; Ravaine, S. Bottom-Up Assembly and Applications of Photonic Materials. *Crystals* **2016**, *6*, 54. [[CrossRef](#)]
25. Míguez, H.; López, C.; Meseguer, F.; Blanco, A.; Vázquez, L.; Mayoral, R.; Ocaña, M.; Fornés, V.; Mifsud, A. Photonic crystal properties of packed submicrometric SiO₂ spheres. *Appl. Phys. Lett.* **1997**, *71*, 1148–1150. [[CrossRef](#)]
26. Blanco, A.; Chomski, E.; Grabtchak, S.; Ibisate, M.; John, S.; Leonard, S.W.; Lopez, C.; Meseguer, F.; Míguez, H.; Mondia, J.P.; et al. Large-scale synthesis of a silicon photonic crystal with a complete three-dimensional bandgap near 1.5 micrometres. *Nature* **2000**, *405*, 437–440. [[CrossRef](#)] [[PubMed](#)]
27. Duan, L.; You, B.; Zhou, S.; Wu, L. Self-assembly of polymer colloids and their solvatochromic-responsive properties. *J. Mater. Chem.* **2011**, *21*, 687–692. [[CrossRef](#)]
28. Fenzl, C.; Hirsch, T.; Wolfbeis, O.S. Photonic Crystal Based Sensor for Organic Solvents and for Solvent-Water Mixtures. *Sensors* **2012**, *12*, 16954–16963. [[CrossRef](#)] [[PubMed](#)]
29. Shieh, J.-Y.; Kuo, J.-Y.; Weng, H.-P.; Yu, H.H. Preparation and Evaluation of the Bioinspired PS/PDMS Photochromic Films by the Self-Assembly Dip–Drawing Method. *Langmuir* **2013**, *29*, 667–672. [[CrossRef](#)] [[PubMed](#)]
30. Reculusa, S.; Ravaine, S. Synthesis of Colloidal Crystals of Controllable Thickness through the Langmuir–Blodgett Technique. *Chem. Mater.* **2003**, *15*, 598–605. [[CrossRef](#)]
31. Kuo, W.-K.; Hsu, J.-J.; Nien, C.-K.; Yu, H.H. Moth-Eye-Inspired Biophotonic Surfaces with Antireflective and Hydrophobic Characteristics. *ACS Appl. Mater. Interfaces* **2016**, *8*, 32021–32030. [[CrossRef](#)] [[PubMed](#)]
32. Ko, Y.G.; Shin, D.H.; Lee, G.S.; Choi, U.S. Fabrication of colloidal crystals on hydrophilic/hydrophobic surface by spin-coating. *Colloids Surf. A* **2011**, *385*, 188–194. [[CrossRef](#)]
33. Kuo, W.-K.; Weng, H.-P.; Hsu, J.-J.; Yu, H.H. Photonic Crystal-Based Sensors for Detecting Alcohol Concentration. *Appl. Sci.* **2016**, *6*, 67. [[CrossRef](#)]
34. Stalder, A.F.; Kulik, G.; Sage, D.; Barbieri, L.; Hoffmann, P. A Snake-Based Approach to Accurate Determination of Both Contact Points and Contact Angles. *Colloids Surf. A* **2006**, *286*, 92–103. [[CrossRef](#)]
35. Vohra, V.; Anzai, T.; Inaba, S.; Porzio, W.; Barba, L. Transfer-printing of active layers to achieve high quality interfaces in sequentially deposited multilayer inverted polymer solar cells fabricated in air. *Sci. Technol. Adv. Mater.* **2016**, *17*, 530–540. [[CrossRef](#)] [[PubMed](#)]
36. Zappia, S.; Scavia, G.; Ferretti, A.M.; Giovannella, U.; Vohra, V.; Destri, S. Water-Processable Amphiphilic Low Band Gap Block Copolymer: Fullerene Blend Nanoparticles as Alternative Sustainable Approach for Organic Solar Cells. *Adv. Sustain. Syst.* **2018**, *2*, 1700155. [[CrossRef](#)]
37. Bhattacharya, S.; Datta, A.; Berg, J.M.; Gangopadhyay, S. Studies on surface wettability of poly(dimethyl) siloxane (PDMS) and glass under oxygen-plasma treatment and correlation with bond strength. *J. Microelectromech. Syst.* **2005**, *14*, 590–597. [[CrossRef](#)]
38. Shishkin, I.; Rybin, M.V.; Samusev, K.B.; Golubev, V.G.; Limonov, M.F. Multiple Bragg diffraction in opal-based photonic crystals: Spectral and spatial dispersion. *Phys. Rev. B* **2014**, *89*, 035124. [[CrossRef](#)]
39. Ng Lee, J.; Park, C.; Whitesides, G.M. Solvent Compatibility of Poly(dimethylsiloxane)-Based Microfluidic Devices. *Anal. Chem.* **2003**, *75*, 6544–6554. [[CrossRef](#)]





Article

Protective Properties of a Microstructure Composed of Barrier Nanostructured Organics and SiO_x Layers Deposited on a Polymer Matrix

Radek Prikryl¹, Pavel Otrisal^{2,*}, Vladimír Obsel³, Lubomír Svorc⁴, Radovan Karkalic⁵ and Jan Buk⁶

¹ Institute of Materials Science, Faculty of Chemistry, Brno University of Technology, Purkynova 464/118, 612 00 Brno, Czech Republic; prikryl@fch.vut.cz

² Nuclear, Biological and Chemical Defence Institute of the University of Defence, Sidliste Vita Nejedleho, 68201 Vyškov, Czech Republic

³ DEZA, Hochmanova 1, 628 01 Brno, Czech Republic; vobsel@seznam.cz

⁴ Institute of Analytical Chemistry, Faculty of Chemical and Food Technology, Slovak University of Technology in Bratislava, Radlinskeho 9, 812 37 Bratislava, Slovakia; lubomir.svorc@stuba.sk

⁵ Department of Military Chemical Engineering, Military Academy, GeneralaPavlaJurisicaSturma 33, 11000 Belgrade, Serbia; radovan.karkalic@va.mod.gov.rs

⁶ P A R D A M, Ltd., Zizkova 2494, 413 01 Roudnicenad Labem, Czech Republic; jan.buk@pardam.cz

* Correspondence: pavel.otrisal@unob.cz; Tel.: +420-973-452-335

Received: 25 June 2018; Accepted: 29 August 2018; Published: 31 August 2018



Abstract: The SiO_x barrier nanocoatings have been prepared on selected polymer matrices to increase their resistance against permeation of toxic substances. The aim has been to find out whether the method of vacuum plasma deposition of SiO_x barrier nanocoatings on a polyethylene terephthalate (PET) foil used by Aluminium Company of Canada (ALCAN) company (ALCAN Packaging Kreuzlingen AG (SA/Ltd., Kreuzlingen, Switzerland) within the production of CERAMIS[®] packaging materials with barrier properties can also be used to increase the resistance of foils from other polymers against the permeation of organic solvents and other toxic liquids. The scanning electron microscopy (SEM) microstructure of SiO_x nanocoatings prepared by thermal deposition from SiO in vacuum by the Plasma Assisted Physical Vapour Deposition (PA-PVD) method or vacuum deposition of hexamethyldisiloxane (HMDSO) by the Plasma-enhanced chemical vapour deposition (PECVD) method have been studied. The microstructure and behavior of samples when exposed to a liquid test substance in relation to the barrier properties is described.

Keywords: barrier material; nanocoating of SiO_x; polymeric matrix; plasma deposition; PVD; PA-PVD; PECVD; permeation; CERAMIS[®]; SorpTest

1. Introduction

Multilayer structures generally increase the protective properties of barrier materials [1–4]. The effect of a combination of the location of the barrier layers on the Protection Factor (BF) is shown in Figure 1.

Within the production of packaging materials for sensitive commodities and in chemical protection, this principle has been used for many years [5,6]. Multilayer barrier materials usually have better performance properties than the individual components from which they are made [7,8]. They are mostly cheaper and better processed [9–11]. This principle is also used by Aluminium Company of Canada (ALCAN) company in the production of SiO_x-based CERAMIS[®] [12] packaging materials, which form a barrier layer between polymer foils (usually polyethylene terephthalate

(PET) and polypropylene (PP)) during their lamination [13–16]. The principle of this technology of reactivating steaming the SiO_x barrier layer from the SiO substrate in vacuum is illustrated in Figure S1.

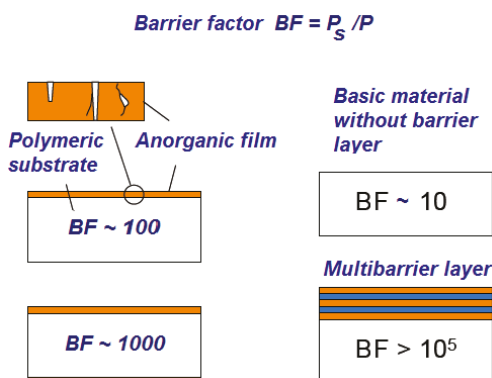


Figure 1. Influence of the barrier nanolayers arrangement on the protective properties of polymeric barrier materials.

In the Aluminium Company of Canada (ALCAN) brochure, this packaging material states that it creates an excellent barrier against gaseous and liquid harmful substances, independent of temperature and humidity. It is transparent for microwaves, suitable for heat sterilization and pasteurization, printable by common printing processes and it allows detection of metals. Due to the patented SiO_x barrier coating technology used by ALCAN was not available, one of the obtained samples was evaluated for protective properties against sulphur mustard (HD) and 1,6-dichlorohexane (DCH). For a CERAMIS[®] CO 20 sample weighing 18.2 g/m² (PET 12 μm, SiO_x 60 nm, PP 20 μm), the protective properties against the permeation of HD and DCH have been found to be greater than 70 h.

Although this material exhibits high resistance to the permeation of selected toxic compounds, it has one major disadvantage from the point of view of its possible utility in anti-gas protection. Its considerable stiffness and imprecision does not allow it to be used for the construction of protective clothing. It was therefore the effort to apply the SiO_x barrier layer to more suitable polymeric matrices.

Vacuum plasma deposition technology of barrier layers within normal temperatures is particularly suitable for the preparation of advanced surfaces with specific properties on flexible polymer and textile substrates [17–20]. A synoptical example of this advanced technology is the advanced novoFlex[®]600 equipment for coating polymeric materials in the footage developed by the Fraunhofer Institute for Organic Electronics, Electron Beam and Plasma Technology FEP (Dresden, Germany).

Another way to prepare SiO_x barrier nanolayers on polymeric or textile materials is a method of plasma deposition from a mixture of siloxane substrates and oxygen. As the suitable substrates hexamethyldisiloxane (HMDSO) and tetraethylorthosilicate (TEOS), which most closely approximate to the structure of SiO_x are considered [21].

The barrier layers could be prepared as flexible based on polymeric materials. One of the materials is Parylene. It is a commercial name for the group of poly-*p*-xylylene polymers. Dimmer of poly-*p*-xylylene is thermally evaporated (sublimated) from a powder within a low pressure of tens of Pascals. Steams of this dimmer joint a pyrolytic chamber. Within the temperature of approximately 680 °C comes to the split of the dimmer joint a pyrolytic chamber. These molecules are reactive and devaporate on the surface of coated materials (in the same way as on walls of the reactive chamber). They polymerize in radical mechanism and form a linear polymeric polymer that is deposited as a very thin barrier layer. This layer is very homogenous and inert. The deposition of parylene was first observed by Szwarc in 1947, and Gorham later described a more efficient, general synthetic way to prepare poly-*p*-xylylene through the vacuum vapour-phase pyrolysis of paracyclophane at has

been used till nowadays [22,23]. This polymerisation is self-initiated and non-terminated, requires no solvent or catalyst, produces no by-products except for the unreacted precursor. The polymer thin film is deposited spontaneously at the room temperature thus no thermal stress is induced in a coated object. Recently, parylene is one of the most well-known chemical vapour deposited (CVD) polymers and number of its applications has grown dramatically over the years.

The excellent resistance of polymeric packaging materials with the SiO_x barrier layer against the permeation of oxygen and humidity has conducted to the conception that the plasma deposition of SiO_x nanolayer and/or parylene film on the suitable polymeric matrix could be used for preparation of even constructive materials for protective garments resistant against toxic liquids and gases. This phenomenon has become a subject of our research. The aim of the study was to test these structures on the various polymers be used to increase the resistance against the permeation of organic solvents and other toxic liquids. The swelling of the polymeric substrate and material of nanostructured films is the main problem of barrier films functionality because of some destructions.

2. Materials and Methods

2.1. Source Materials, Substrates and Polymeric Matrices

SiO powder provided by Merck KGaA (Darmstadt, Germany) was used as source material for Plasma Assisted Physical Vapour Deposition (PA-PVD) process, hexamethyldi-siloxane (HMDSO) CAS 107-46-0 (Sigma-Aldrich, Prague, Czech Republic) was utilized as source materials for PE-CVD method. For PVD process of organics film the 1,3,5-triazine-2,4,6-triamine (melamine), CAS 108-78-1 (Sigma-Aldrich, Prague, Czech Republic) was used. Dimer of chlorinated *p*-xylylene (parylene C) (KunShanZhangShengNaNo Tech Company, Kunshan, China), CAS 28804-46-8 was utilized as source material for CVD method. Bis(2-chloroethyl) sulphide (sulphur mustard, HD) CAS 505-60-2 (Military Technical Institute of Protection, Brno, Czech Republic) and 1,6-Dichlorohexane CAS 218-491-7 (Sigma-Aldrich, Prague, Czech Republic) were used as test chemicals for verification of the quality of new developed barrier materials with nanolayers. Polyvinylidenechlorid (PVDC), CAS 9002-85-1 foil of 20 μm was used for lamination of PEVA foil. Thin films were prepared on polymeric foils from polyethylenevinyl acetate (PEVA), CAS 24937-78-8, foil of 200 μm thickness, polypropylene (PP) foil of 30 μm thickness and polyethylentereftalate (PET) foil of 8 μm thickness. Si wafer WFP 6005 provided by ON Semiconductor (ON Semiconductor Czech Republic, Rožnov pod Radhoštěm, Czech Republic) was used as substrate for thin film characterization by energy-dispersive X-ray spectroscopy—EDX (ON Semiconductor Czech Republic, Ltd., Rožnov pod Radhoštěm, Czech Republic). EDX is a part of Scanning Electron Microscope ZEISS EVO LS 10 (Oberkochen, Germany). This spectroscopy provides elemental information about the composition of the structure of the surface of a sample. Performed in conjunction with SEM. Elements with atomic numbers down to carbon can be viewed with Energy Dispersive Spectroscopy (EDS).

2.2. Apparatuses for the Samples Preparation

The equipment for thermal lamination of plastic films without the use of binders was used as method for special multilayer structure fabrication. The original vacuum apparatus (Faculty of Chemistry, Brno University of Technology) for the preparation of barrier nanocoatings base on SiO_x and melamine on a polymeric matrix by the PVD, PA-PVD and PECVD method was used. The construction is evident from Figure S2.

Plasma surface activation was carried out before each first layer preparation under pressure of 10 Pa and oxygen flow of 10 sccm. The plasma discharge RF power of 13.56 MHz was set to 50 W for 10 min.

PVD process of SiO and Melamine based layers was carried out in following steps. The vacuum system was evacuated to base pressure of 1×10^{-5} Pa, then process started at pressure 1×10^{-4} Pa of source material vapour. Sample thickness varied from 50 to 150 nm controlled by deposition time.

PA-PVD process of SiO_x based films preparation was carried out under process pressure of 3×10^{-2} Pa and oxygen mass flow of 5 sccm. The RF power of 13.56 MHz plasma discharge was 200 W. The sample thickness varied from 50 nm to 150 nm and was controlled by adjusting the deposition time.

PE-CVD process of SiO_x based films deposition from HMDSO vapour was used under following conditions. The process pressure of 8–10 Pa was controlled by pump speed and monomer HMDSO flow, argon mass flow was kept as constant of 2 sccm and oxygen mass flow of 5 sccm. RF power of 13.56 MHz was used in range of 10–100 W, typical Self Bias Voltage was around 100 V. Sample thickness varied from 50–150 nm and was controlled by tuning the deposition time.

For the CVD process of parylene film preparation the original vacuum system developed on Brno University of Technology (Brno, Czech Republic) was used. It works on the principle of Gorham method described above. The conditions used for the process were as follows: pressure of monomer vapour was controlled to 8–10 Pa by temperature of dimer evaporator, the temperature of pyrolytic chamber was kept to 680 °C. The sample thickness was controlled by initial weight of dimer load.

2.3. Measuring Instruments

The high-resolution JEOL-6700F scanning electron microscope (JEOL, Tokyo, Japan) was used for the evaluation of nanocoatings surface microstructure at Institute of Scientific Instruments of the Czech Academy of Sciences, Brno, Czech Republic. This microscope is suitable for observing fine structures, such as multi-layer coatings and nanoparticles produced by nanotechnologies. Thanks to very slow electrons, it is also suitable for observing non-conducting samples.

The original SorpTest device was utilized for the study and quantitative testing of the barrier materials resistance against the permeation of volatile toxic substances, including chemical warfare agents [24]. The SorpTest device is a semiautomatic measuring system using an innovated PVDF permeation cell enabling continual monitoring dynamic and static permeation rate of gases of volatile toxic compound through barrier materials with the employment of the reversible quartz crystal microbalance (QCM) sensor with the polymeric detection layer. With the help of this device it is possible to determine the period during which the limit of the toxic substance penetrates through the barrier material. The rate of permeation of vapours of the tested chemical through the barrier material within its contamination with the liquid phase is monitored. Schema of the SorpTest system is presented Figure S3.

The original equipment developed at the Faculty of Chemistry of the Brno University of Technology was used to determine oxygen transmission rate (OTR) under static conditions. The principle of measurement is similar to principle given in American Society for Testing Material (ASTM) D3985-17. OTR is the steady state rate at which oxygen gas permeates through a film at specified conditions of temperature and relative humidity. Values are expressed in cc/m²/24 h units.

3. Results and Discussion

3.1. Protective Properties

As a carrier material for barrier layers, PEVA has been used as a representative of an easily swellable polymer and PP as a representative of a low swellable polymer. Barrier layers of melamine, parylene, PVDC and SiO_x have been applied to them occasionally combined with each other [25]. The prepared samples have been evaluated from the point of view of protective properties, microstructure and behaviour when exposed to the liquid phase of the test chemical. The PET foil is not suitable as the carrier material; otherwise testing the protective properties would be unbearably long.

Combinations of PEVA material with layers of parylene (by CVD), PVDC (by lamination) and SiO_x (PE-CVD) have been prepared and evaluated. Due to the low protection properties of PEVA foil itself against liquid toxic substances, in our case, sulphur mustard (HD) and 1,6-dichlorohexane (DCH), the protective properties of these materials have been verified within one and both-sides coating with a thin layer of PVDC and SiO_x. For one-sided coating, the PVDC has a breakthrough time value (BT_γ)

of 55 min and 129 min from the site of PEVA. This difference has been caused due to the presence of the directional effect of permeation caused by the different swell ability of both materials. The PEVA foil itself had the RD_Y only 27 min. For both-sided PVDC lamination, BT_Y was found to be 188 min on one side and the second side. For DCH, these values are slightly lower and approximately equal to 51 min on PEVA side and 78 min on both sides covering from both sides (Figure 2).

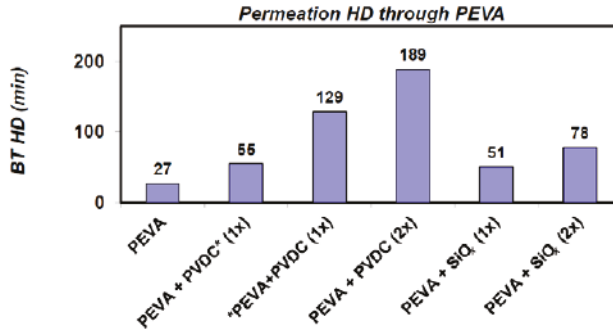


Figure 2. Breakthrough times of modified polyethylene vinyl acetate (PEVA) foil determined by the MikroTest method.

Further combinations of PEVA foil with barrier layers of SiO_x (by PE-CVD or PA-PVD), melamine (by PVD) and PVDC (by lamination) have been prepared [26,27]. These have been subsequently evaluated for resistance against the permeation of DCH. Interestingly, the resulting BT values for DCH in most combinations have been approximately the same and ranged from 23 to 33 min. The exception was only a combination with PVDC, with a single-sided coverage of BT 70 min from the PEVA side and 166 min with double-sided coverage. These results indicate that the exposure to DCH results in the rapid destruction of most barrier layers as a result of swelling of the carrier polymer so that the resulting protective properties of the starting material do not increase too much (Figure 3). The change in microstructure of the barrier layers following the DCH exposure described below also corresponds to these considerations.

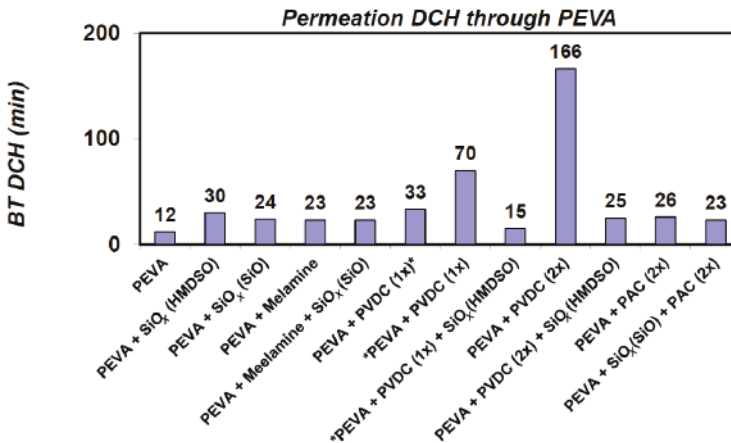


Figure 3. The resistance of the PEVA foil modified with different barrier layers against 1,6-dichlorohexane (DCH).

In order to remove the impact of the swelling on the protective properties of the studied barrier layers, polypropylene has been used as the carrier polymer. The results shown in Figure 4 confirm previous considerations of the negative effect of the swelling of the carrier polymer on the protective properties of the applied barrier nanolayers.

Permeation DCH through structures on PP

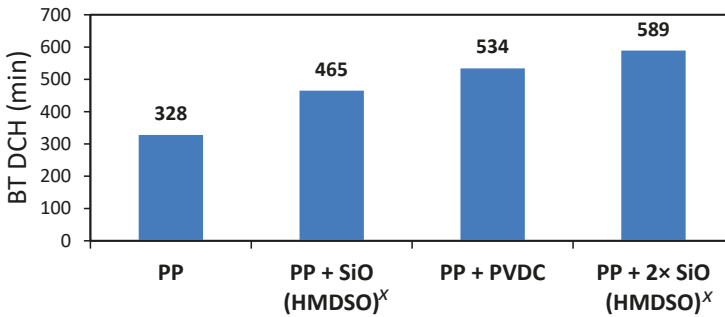


Figure 4. Resistance of the PP foil modified with different barrier layers against DCH permeation.

A similar situation occurs when assessing the protective properties with the help of oxygen permeation (OTR), which also does not come to swelling of the carrier polymer (Figure 5).

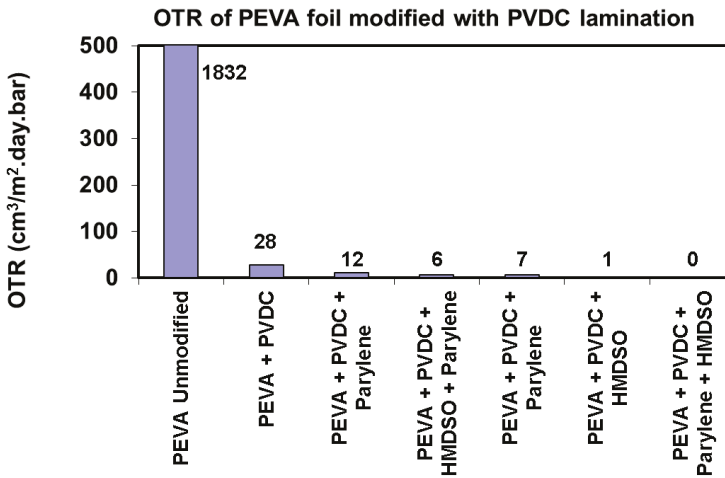


Figure 5. Oxygen permeation values detected for PEVA foil with barrier layers of PVDC, plasma polymerized HMDSO and parylene.

3.2. Microstructure

The analysis is mainly focused on microstructure assessment of inorganic nanocoatings SiO_x, which, when exposed to liquid test chemicals, unlike organic nanocoatings, resulted in significant destruction due to swelling of the polymer matrix. From a large number of SEM micrographs have been selected primarily those that were typical for the studied material and regularly repeated on different

samples. Within large magnification, most researched SiO_x layers were found to have characteristic granular substructures of tens of nanometres dimensions, which are the basic building blocks of these nanocoatings.

It is necessary to realize that within the plasma deposition of nanostructured SiO_x barrier layers is a key parameter their elasticity and ductility, which usually is not more than 3% [27,28]. With gradual deformation of the substrate, the effect of ductility on protective properties can also be evaluated by OTR measurements, as there is no swelling of the carrier polymer which causes cracking and thus deterioration of the protective properties. When exposed to a liquid test chemical, the evaluation of the quality of the barrier layers is strongly dependent on the properties of the carrier substrate [29,30]. If a polymer resistant to swelling is used, the results of the protective properties evaluation are similar to those of the OTR. When using an easily swellable polymer, the cracks and defects in the barrier layer polymer are rapidly contaminated by the liquid test chemical and the subsequent swelling causes further destruction of the barrier layer and thereby deterioration of the protective properties.

However, the thickness of the barrier layer is also a crucial parameter. Basically, all publications dealing with the effect of the SiO_x nanocoating thickness on barrier properties indicate an optimum where OTR values are best. The principle of thickness dependence on OTR is explained by the fact that in the nucleation area the discrete centres are first formed on the polymer substrate. The best OTR values are then achieved when they are interconnected. However, if a uniform nanolayer is rapidly formed in another region, its thickness is preferably increased and the growth of discontinuous centres is slowed down. However, a faster increase of the thickness of the barrier nanolayer at these sites above the optimum value, however, results in microcracks resulting from internal stress in the layer material which getting the OTR value worse.

As a basic comparison layer, a nanostructured SiO_x layer on the silicon substrate has been prepared by PECVD by plasma deposition. It is apparent from Figure 6 and Figure S6 that the prepared nanocoating is homogeneous with a uniform microstructure that does not change even after prolonged exposure to DCH.

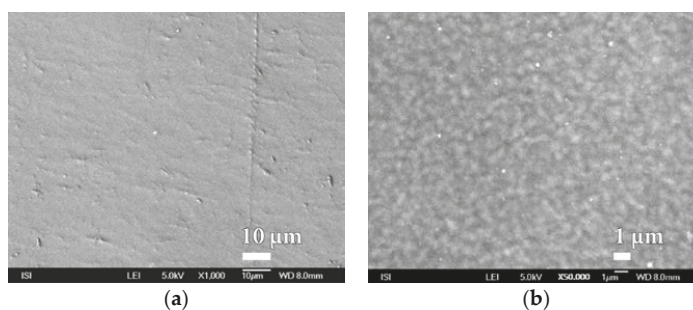


Figure 6. Scanning electron microscopy (SEM) micrographs of the surface of the nanolayer of SiO_x prepared by HMDSO method on the silicon substrate at various magnifications before exposure to DCH (a) 1000 \times and (b) 50,000 \times .

When assessing the quality of the SiO_x nanocoatings, the surface quality of the carrier polymer foil should be taken into account in order to determine if found defects do not copy the underlying material. Figure 7 and Figure S7 shows the typical non-homogeneity of the surface of the PEVA foil to be taken into account when assessing the microstructure of SiO_x nanocoatings.

For this reason, efforts were made to optimize plasma deposition conditions in order to improve the surface homogeneity of the polymer film used. One from the options was to modify the polymer matrix for less swelling. After verifying a number of PEVA surface treatment options, it was finally chosen to laminate it (at 110 °C without the binder) with a thin PVDC foil that showed good adhesion

to the material. Another option was to replace the PEVA foil with a less-swelling PP film with a better surface. The use of PET foil that would be most suitable for plasma barrier coating was problematic because we could not measure too high BT values changes in protective properties in real time after applying different barrier layers. Polymeric matrices thus prepared were subjected to SiO_x barrier nanocoatings with plasma deposition. Prepared samples have been evaluated not only from the point of permeation resistance and for microstructure of barrier nanocoatings surface before and after exposure of the DCH test chemical with high resolution SEM. It is evident from Figure 8 and Figure S8 that the quality of the PVDC surface is significantly better than the original PEVA foil. It has been shown that this material is not porous even at high magnification ($80,000\times$) and therefore it can be advantageously used for the deposition of other barrier layers based on melamine, parylene and mainly SiO_x plasma technology.

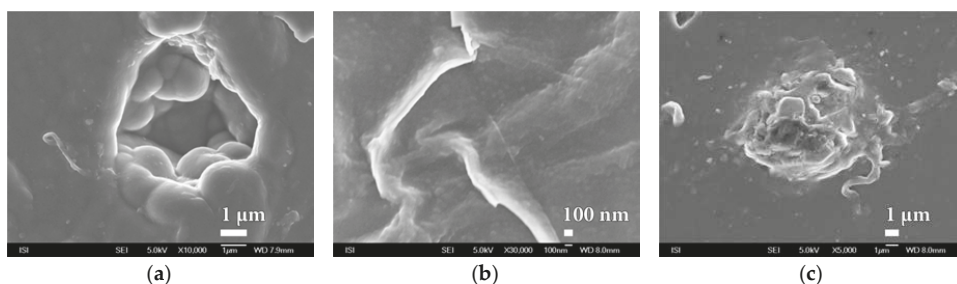


Figure 7. The exhibitions of different inhomogeneity on the surface of the used polymer foil PEVA at various magnifications of (a) $10,000\times$; (b) $30,000\times$; (c) $5,000\times$.

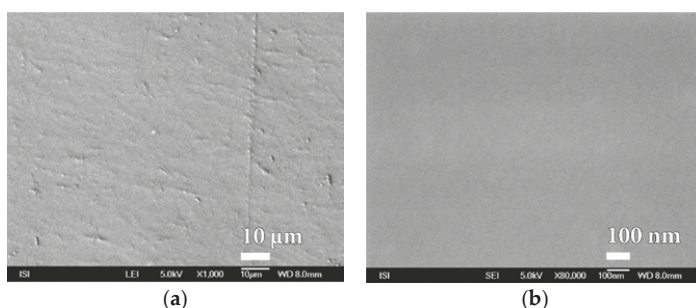


Figure 8. SEM micrographs of PVDC foil surface laminated at $110\text{ }^\circ\text{C}$ to PEVA foil at magnification of (a) $1000\times$ and (b) $80,000\times$.

However, it is interesting to note that even with short-term oxygen plasma treatment, the surface of the PVDC foil is significantly wrinkled, while its homogeneity remains unchanged (Figure 9 and Figure S9).

A homogeneous layer of SiO_x with a well-developed microstructure which is probably very thin is formed with plasma deposition by PVD method on the surface of the PVDC foil (Figure 10 and Figure S10).

Similarly, within plasma deposition with the PVD method, at this time on the surface of PEVA foil, behaves even melamine and parylene C. The characteristic microstructure of the surface of these barrier nanocoatings is shown in Figures 11 and 12. In both cases a compact and fairly homogeneous barrier nanocoating with a well-developed microstructure copying the PEVA foil surface is formed.

A comparison of the microstructures in Figures 10–12 and Figure S10–S12 show that melamine produces a coarser microstructure than SiO_x but thicker than parylene C. Further SiO_x nanocoatings on PEVA film have been prepared by plasma deposition with the HMDSO method. Within this method of preparation, it is possible, in accordance with conditions during exposure, to form a SiO_x nanocoating of the different character than within plasma deposition by PVD method.

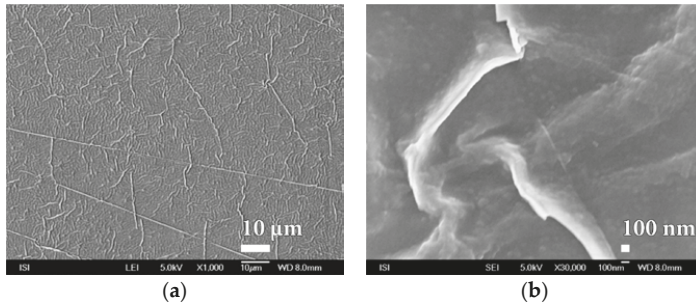


Figure 9. SEM micrographs of PVDC foil surface laminated to PEVA foil after short exposure to oxygen plasma treatment at magnification of (a) 1000× (b) 30,000×.

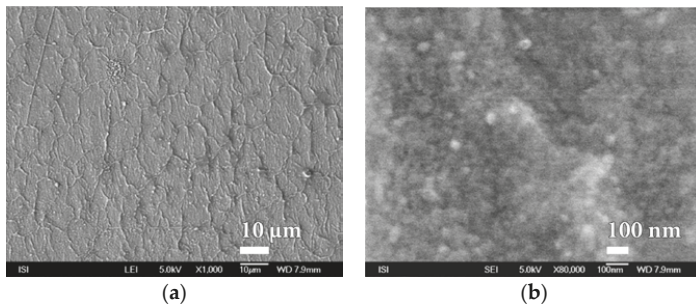


Figure 10. SEM micrographs of the surface SiO_x barrier nanocoating prepared by plasma deposition with the PVD method on PVDC foil laminated on the PEVA foil, at magnification of (a) 1000× and (b) 80,000×.

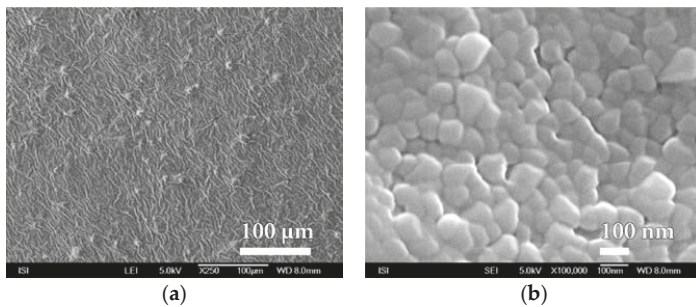


Figure 11. SEM micrographs of melamine nanocoating surface on PEVA SiO_x foil prepared by PVD plasma deposition method at magnification of (a) 250× and (b) 100,000×.

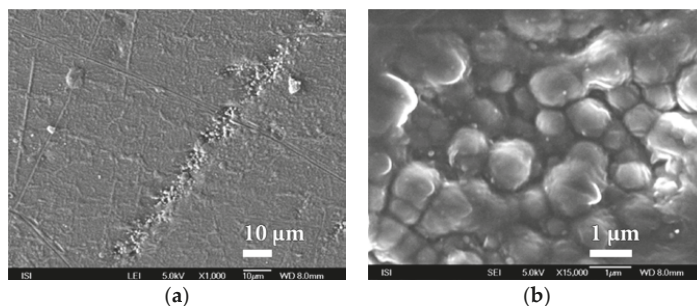


Figure 12. SEM micrographs of parylene nanocoating surfaces on PEVA SiO_x foil prepared by PVD plasma deposition method at magnification of (a) 1000× and (b) 15,000×.

The different appearance of SiO_x nanocoatings prepared under various experimental conditions, documented in Figure 13 and Figure S13, is probably related to the nanocoating thickness and properties of the carrier substrate.

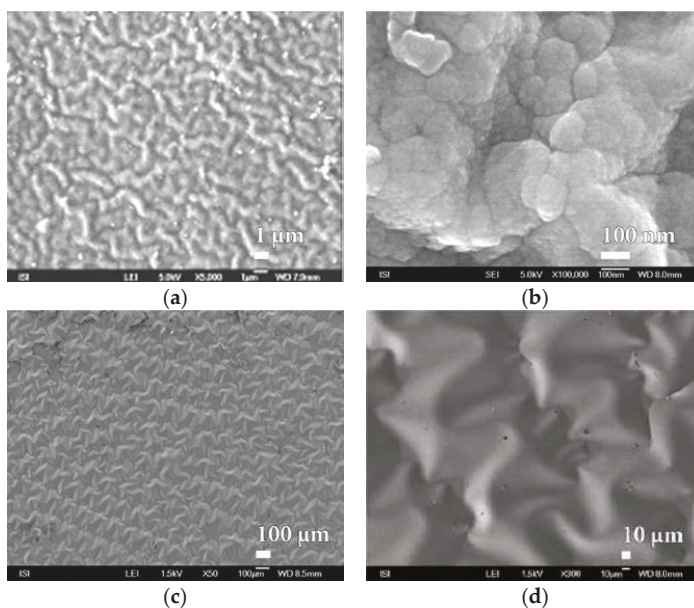


Figure 13. SEM micrographs of SiO_x barrier nanocoating surface prepared by the plasma deposition by HMDSO method on PEVA foil at magnification of (a) 5000× and (b) 100,000× and on PEVA foil stained with aluminium at magnification of (c) 50× and (d) 300×.

This assumption confirms the deposition of SiO_x by the HMDSO method on the silicon wafer surface, documented in Figure 14 and Figure S14.

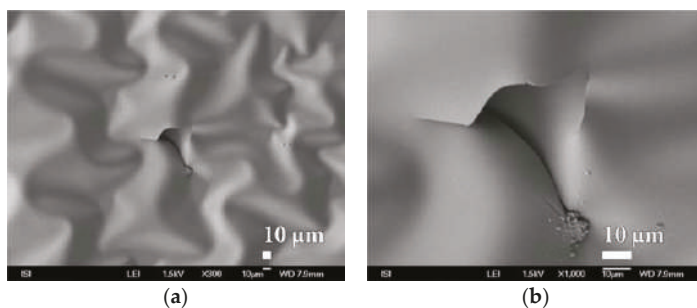


Figure 14. SEM micrographs of surface SiO_x barrier nanocoating prepared by plasma deposition by HMDSO on the silicon wafer at magnification of (a) 300× and (b) 1000×.

The SiO_x nanocoating has been deposited on the surface of the Viton elastomer by the HMDSO method for comparison, documented in Figure 15 and Figure S15. Interestingly, in this case a homogeneous barrier layer has been formed, however with a porous microstructure.

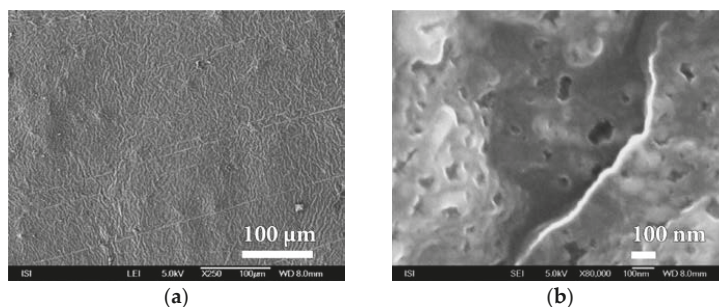


Figure 15. SEM micrographs of surface SiO_x barrier nanocoating prepared by plasma deposition by HMDSO method on the Viton fluorelastomer at magnification of (a) 250× and (b) 80,000×.

The nanocoating SiO_x has been deposited on the surface of both PP and PET foils by the HMDSO method. The formed nanocoating has been both nonporous and homogeneous with a well-developed microstructure copying the surface of the PP foil, as shown in Figure 16.

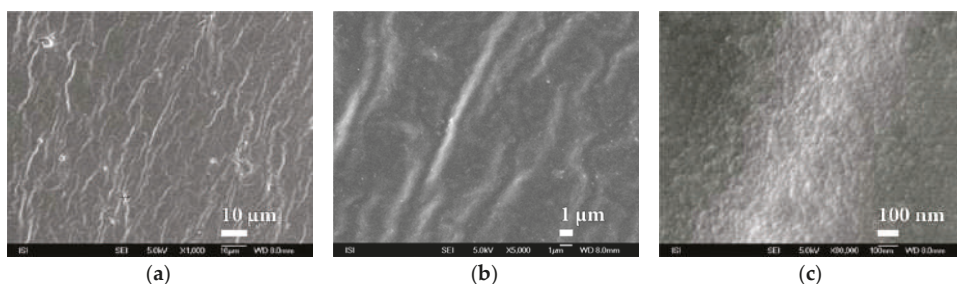


Figure 16. SEM micrographs of SiO_x barrier nanocoating surface prepared by plasma deposition by HMDSO method on the PP foil at magnification of (a) 1000×, (b) 5000× and (c) 80,000×.

If samples of polymeric materials with a SiO_x barrier layer are exposed to liquid DCH, an easily swellable PEVA polymer matrix will dramatically change the appearance of this nanocoating. Liquid DCH permeating through micro cracks or other leaks to the polymeric matrix apparently will not prevent its rapid swelling which causes destruction of the SiO_x nanopowder [30–32]. This effect will not appear at all or only to a small extent in the scope of PP foils or PET foils. It is conformable with the discussion above related to the protective properties of these materials. The destruction of the SiO_x barrier layer due to the polymer matrix embossment can be demonstrated by many of the examples shown in Figure S4. However, visual changes due to the polymer matrix swelling from visual changes due to mechanical damage to the SiO_x barrier layer, as documented in Figure S5, are required.

During the study of SiO_x nanocoatings after destruction, sites with such great damage have been found. It was possible to precisely determine the thickness of deposited barrier layer moving around 100 nm (Figure 17 and Figure S16). It even appears that in some cases the SiO_x nanocoating has a multilayer character of approximately 100 nm (Figure 17a).

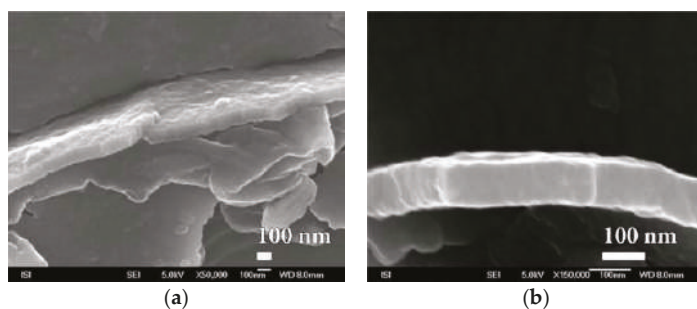


Figure 17. SEM photographs of SiO_x barrier nanocoating fracture prepared by plasma deposition by HMDSO method on PEVA foil at magnification of (a) 50,000 \times and (b) 150,000 \times .

Another interesting finding is the typical spherical substructure characteristic of most studied SiO_x nanocoatings. This substructure, clearly recognizable only with sufficiently large magnification, is also found inside deep material defects and even creates interesting structures on the surface and on the smooth surface of the PEVA foil, as can be seen from Figure 18.

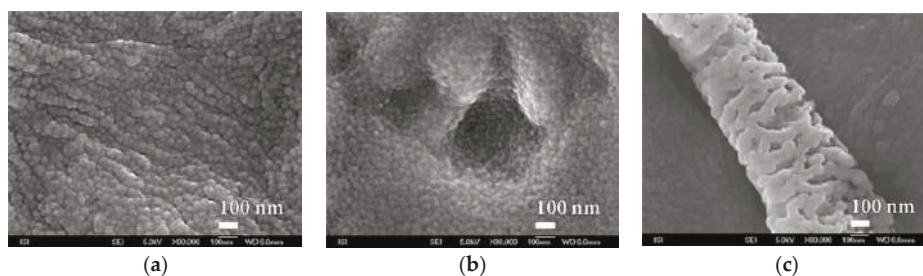


Figure 18. SEM micrographs of SiO_x nanocoating substructure prepared by plasma deposition by HMDSO method on the PEVA foil at magnification of 80,000 \times of three different areas. (a) Typical surface morphology; (b) layer defect and (c) surface abnormality.

4. Conclusions

It has been shown that the plasma deposition in vacuum can form barrier nanopowders from SiO_x and other suitable substrates on the polymer matrix. It is clear from the results that the HMDSO

method, which makes it possible to influence the SiO_x nanocoating thickness and quality better, is more appropriate. Within forming practically applicable barrier materials with nanocoating of SiO_x it is necessary to be respect several essential requirements. The nanocoating SiO_x must be deposited primarily on a low swellable polymeric foil and, due to its brittleness, it must immediately be laminated with another foil due to prevention of its mechanical damaged. This is in a harmony with the production process of ALCAN Company within the production of packaging with barrier properties of CERAMIS[®] technology. The aim of further research in this field should be to improve the fixation of barrier nanocoatings on the polymer matrix and their resistance to mechanical stress. If it is real to prepare reactive coatings or deposition of suitable metallic oxides with catalytic properties it would enable this process to be used for the preparation of nanocoatings and nanomaterials with self-decontaminating or photocatalytic properties during further research.

Supplementary Materials: The following are available online at <http://www.mdpi.com/2079-4991/8/9/679/s1>, Figure S1: The principle of CERAMIS[®] reactive steam technology and examples of SiO_x[®] coated materials, Figure S2: The scheme of the PE-CVD/PA-PVD apparatus for the preparation of SiO_x nanocoatings SiO_x with steaming form powder SiO in vacuum, Figure S3: Diagram and real appearance of the SorpTest device for testing the resistance of barrier materials against the permeation of gaseous and liquid toxic substances, Figure S4: Scanning electron microscopy (SEM) micrographs of examples of visual changes of the SiO_x barrier layer caused by polymer matrix swelling with visible different kinds of cracks, Figure S5: Scanning electron microscopy (SEM) micrographs of examples of visual changes of the SiO_x barrier layer caused by mechanical damage, Figure S6: Scanning electron microscopy (SEM) micrographs of the surface of the nanolayer of SiO_x prepared by HMDSO method on the silicon substrate at various magnifications of 20,000× before exposure to DCH, Figure S7: The exhibitions of different inhomogeneity on the surface of the used polymer foil PEVA at various magnification of (a) 30,000×, (b) 15,000×, (c) 80,000×, Figure S8: SEM micrographs of PVDC foil surface laminated at 110 °C to PEVA foil at magnification of 30,000×, Figure S9: SEM micrographs of PVDC foil surface laminated to PEVA foil after short exposure to oxygen plasma treatment at magnification of 5000, Figure S10: SEM micrographs of the surface SiO_x barrier nanocoating prepared by plasma deposition with the PVD method on PVDC foil laminated on the PEVA foil, at magnification of 5000×, Figure S11: SEM micrographs of melamine nanocoating surface on PEVA SiO_x foil prepared by PVD plasma deposition method at magnification of 30,000×, Figure S12: SEM micrographs of parylenenanocoating surface on PEVA SiO_x foil prepared by PVD plasma deposition method at magnification of 5000×, Figure S13: SEM micrographs of SiO_x barrier nanocoating surface prepared by the plasma deposition by HMDSO method on PEVA foil at magnification of (a) 1000× and on PEVA foil stained with aluminium at magnification (b) 1000×, Figure S14: SEM micrographs of surface SiO_x barrier nanocoating prepared by plasma deposition by HMDSO on the silicon wafer at magnification of 1000×, Figure S15: SEM micrographs of surface SiO_x barrier nanocoating prepared by plasma deposition by HMDSO method on the Viton fluorelastomer at magnification of 5000×, Figure S16: SEM photographs of SiO_x barrier nanocoating fracture prepared by plasma deposition by HMDSO method on PEVA foil at magnification of 100,000×.

Author Contributions: Conceptualization, P.O. and V.O.; Methodology, P.O. and V.O.; Validation, R.P., P.O., V.O. and R.K.; Formal Analysis, R.P., P.O., V.O. and L.S.; Investigation, P.P., V.O., L.S., R.K. and J.B.; Resources, R.P., V.O., R.K. and J.B.; Data Curation, R.P., P.O., V.O. and L.S.; Writing-Original Draft Preparation, P.O. and V.O.; Writing-Review & Editing, P.O. and R.P.; Supervision, P.O. and R.P.; Project Administration, P.O. and V.O.; Funding Acquisition, R.P.

Funding: This work was supported by Czech Ministry of Education, Youth and Sports, Project number LO1211, Material Research Centre at Faculty of Chemistry, Brno University of Technology.

Acknowledgments: We would like to thank all subjects who volunteered in the study.

Conflicts of Interest: The authors declare no conflict of interest.

References

1. Kogelschatz, U.; Eliasson, B.; Egli, W. Dielectric-barrier discharges principle and applications. *J. Phys. Arch.* **1997**, *7*, C4-47–C4-66. [[CrossRef](#)]
2. Otrisal, P.; Florus, S.; Svorc, L.; Barsan, G.; Mosteanu, D. A new colorimetric assay for determination of selected toxic vapours and liquids permeation through barrier materials using the minitest device. *Rev. Plast.* **2017**, *54*, 748–751.
3. Kmochova, A.; Tichy, A.; Zarybnicka, L.; Sinkorova, Z.; Vavrova, J.; Rehacek, V.; Durisova, K.; Kubelkova, K.; Pejchal, J.; Kuca, K. Modulation of ionizing radiation-induced effects by NU7441, KU55933 and VE821 in peripheral blood lymphocytes. *J. Appl. Biomed.* **2016**, *14*, 19–24. [[CrossRef](#)]

4. Krumpolec, R.; Zahoranova, A.; Cernak, M.; Kovacik, D. Chemical and physical evaluation of hydrophobic pp-HMDSO layers deposited by plasma polymerization at atmospheric pressure. *Chem. Listy* **2012**, *106*, 1450–1454.
5. Radovan, K.M.; Negovan, I.D.; Dalibor, J.B.; Smiljana, M.M.; Dejan, I.R.; Marija, M.D.; Branko, K.V. Dynamic adsorption characteristics of thin layered activated charcoal materials used in chemical protective overgarments. *Indian J. Fibre Text. Res.* **2016**, *41*, 402–410.
6. Mosteanu, D.; Barsan, G.; Otrisal, P.; Giurgiu, L.; Oancea, R. Obtaining the volatile oils from wormwood and tarragon plants by a new microwave hydrodistillation method. *Rev. Chim.* **2017**, *68*, 2499–2502.
7. Sun, Y.J.; Fu, Y.B.; Chen, Q.; Zhang, C.M.; Sang, L.J.; Zhang, Y.F. Silicon dioxide coating deposited by PDPs on PET films and influence on oxygen transmission rate. *Chin. Phys. Lett.* **2008**, *25*, 1753–1756.
8. Felts, J.T. Transparent barrier coatings update: Flexible substrates. *J. Plast. Film. Sheeting* **1993**, *9*, 139–158. [[CrossRef](#)]
9. Macák, J.M.; Hromádko, L.; Bulánek, R.; Koudelková, E.; Buk, J.; Tejkl, M. Process for Preparing Submicron Fibers of Amorphous Silica and Submicron Fibers of Amorphous Silica Prepared in Such a Manner. Available online: <https://1url.cz/qtyDc> (accessed on 12 June 2018).
10. Madocks, J.; Marcus, P.; Morse, P. Silicon dioxide coatings on plastic substrates by large area plasma enhanced chemical vapour deposition process. In Proceedings of the 49th Annual Technical Conference, Washington, DC, USA, 22–27 April 2006; pp. 569–573.
11. Hoskova-Mayerova, S.; Maturo, A. Algebraic hyperstructures and social relations. *Italian J. Pure. Appl. Math.* **2018**, *39*, 701–709.
12. Anonymous. CERAMIS® Barrier Films: Transparent SiO_x Barrier Films for Ultimate Product Protection. Available online: <https://1url.cz/Pt734> (accessed on 23 June 2018).
13. Roberts, A.P.; Henry, B.M.; Sutton, A.P.; Grovenor, C.R.M.; Briggs, G.A.D.; Miyamoto, T.; Kano, M.; Tsukahara, Y.; Yanaka, M. Gas permeation in silicon-oxide/polymer (SiO_x/PET) barrier films: Role of the oxide lattice, nano-defects and macro-defects. *J. Membr. Sci.* **2002**, *208*, 75–88. [[CrossRef](#)]
14. Erlat, A.G.; Spontak, R.J.; Clarke, R.P.; Robinson, T.C.; Haaland, P.D.; Tropsha, Y.; Harvey, N.G.; Vogler, E.A. SiO_x gas barrier coatings on polymer substrates: Morphology and gas transport considerations. *J. Phys. Chem. B* **1999**, *103*, 6047–6055. [[CrossRef](#)]
15. Felts, J.; Finson, E.J. Transparent SiO₂ barrier coatings: Conversion and production status. In Proceedings of the 37th Annual Technical Conference Proceedings, Boston, MA, USA, 8–13 May 1994; pp. 139–143.
16. Foest, R.; Schafer, J.; Quade, A.; Ohl, A.; Weltmann, K.D. Miniaturized atmospheric pressure plasma jet (APPJ) for deposition of SiO_x films with different Silicon-organics compounds—A comparative study. In Proceedings of the 35th EPS Conference on Plasma Phys, Hersonissos, Greece, 9–13 June 2008.
17. Gaur, S.; Vergason, G. Plasma polymerization: For industrial production. In Proceedings of the 44th Annual Technical Conference Proceedings, Philadelphia, PA, USA, 21–26 April 2001.
18. Huang, X. Fabrication and Properties of Carbon Fibers. *Materials* **2009**, *1*, 938–947. [[CrossRef](#)]
19. Horova, I.; Kolacek, J.; Vopatova, K. Full bandwidth matrix selectors for gradient kernel density estimate. *Comput. Stat. Data Anal.* **2013**, *57*, 364–376. [[CrossRef](#)]
20. Raynaud, P.; Clergereaux, R.; Segui, Y.; Gherardi, N.; Despax, B. Plasma Nanolayering, Nanoclustering, Nanotexturing: Challenges for Future Processes for Mass Production. Available online: <https://1url.cz/Yt73j> (accessed on 23 June 2018).
21. Starostin, S.A.; Aldea, E.; Vries, H.W.; Creatore, M.; van de Sanden, M.C.M. Application of atmospheric pressure glow discharge (APGD) for deposition of thin silica like films on polymeric webs. In Proceedings of the 28th International Conference on Phenomena in Ionized Gases (ICPIG), Prague, Czech Republic, 15–20 July 2007.
22. Fortin, J.B.; Lu, T.-M. *Chemical Vapor Deposition Polymerization: The Growth and Properties of Parylene Thin Films*; Springer Science & Business Media: New York, NY, USA, 2003. [[CrossRef](#)]
23. Gorham, W.F. A new, general synthetic method for the preparation of linear poly-*p*-xylylenes. *J. Polym. Sci. Part A* **1966**, *4*, 3027–3039. [[CrossRef](#)]
24. Míša, M.; Obšel, V. System for Measuring Permeation of Gases and Vapors Through Barrier Membranes. Available online: <https://1url.cz/Bty4h> (accessed on 11 June 2018).
25. Yasuda, H. *Plasma Polymerization*; 1st Issue; Academic Press: Orlando, FL, USA, 1985.

26. Smith, A.W.; Copeland, N. Clear barrier coatings by plasma CVD for packaging applications. In Proceedings of the 43th Annual Technical Conference Proceedings, Washington, DC, USA, 22–27 April 2006; pp. 636–641.
27. Izu, M.; Dotter, B.; Ovshinsky, S.R. Roll-to-roll microwave PECVD machine for high-barrier film coatings. *J. Photopolym. Sci. Technol.* **1995**, *8*, 195–204. [[CrossRef](#)]
28. Hones, P.; Levy, F.; Randall, N.X. Influence of deposition parameters on mechanical properties of sputter-deposited Cr₂O₃ thin films. *J. Mater. Res.* **1999**, *14*, 3623–3629. [[CrossRef](#)]
29. Jahromi, S.; Moosheimer, S.U. Oxygen barrier coatings based on supramolecular assembly of melamine. *Macromolecules* **2002**, *33*, 7582–7587. [[CrossRef](#)]
30. Howells, D.G.; Henry, B.M.; Leterrier, Y.; Manson, J.A.E.; Madocks, J.; Assender, H.E. Mechanical properties of SiO_x gas barrier coatings on polyester films. *Surf. Coat. Technol.* **2008**, *202*, 3529–3537. [[CrossRef](#)]
31. Ozeki, K.; Nagashima, Y.; Ohgoe, Y.; Hirakuri, K.K.; Mukaibayashi, H.; Masuzawa, T. Gas barrier properties of diamond-like carbon films coated on PTFE. *Appl. Surf. Sci.* **2009**, *25*, 7286–7290. [[CrossRef](#)]
32. Stodola, P. Using metaheuristics on the multi-depot vehicle routing problem with modified optimization criterion. *Algorithms* **2018**, *11*, 74. [[CrossRef](#)]



© 2018 by the authors. Licensee MDPI, Basel, Switzerland. This article is an open access article distributed under the terms and conditions of the Creative Commons Attribution (CC BY) license (<http://creativecommons.org/licenses/by/4.0/>).

Article

Electrospinning of Polystyrene/Polyhydroxybutyrate Nanofibers Doped with Porphyrin and Graphene for Chemiresistor Gas Sensors

Joshua Avossa¹, Roberto Paolesse^{1,2}, Corrado Di Natale^{1,3}, Emiliano Zampetti¹, Giovanni Bertoni⁴, Fabrizio De Cesare^{1,5}, Giuseppe Scarascia-Mugnozza⁵ and Antonella Macagnano^{1,5,*}

- ¹ Institute of Atmospheric Pollution Research–National Research Council (IIA-CNR), Research Area of Rome 1, Via Salaria km 29.300, 00016 Monterotondo, Italy; joshua.avossa@iia.cnr.it (J.A.); paolesse@uniroma2.it (R.P.); dinatale@uniroma2.it (C.D.N.); e.zampetti@iia.cnr.it (E.Z.); decesame@unitus.it (F.D.C.)
 - ² Department of Chemical Science and Technology, University of Tor Vergata, Via della Ricerca Scientifica 00133 Rome, Italy
 - ³ Department of Electronic Engineering, University of Tor Vergata, Via del Politecnico 1, 00133 Rome, Italy
 - ⁴ Institute of Materials for Electronics and Magnetism–National Research Council (IMEM-CNR), Parco Area delle Scienze 37/A, 43124 Parma, Italy; giovanni.bertoni@imem.cnr.it
 - ⁵ Department for Innovation in Biological, Agro-food and Forest Systems (DIBAF), Via S. Camillo de Lellis, 00100 Viterbo, Italy; gscaras@unitus.it
- * Correspondence: antonella.macagnano@cnr.it or a.macagnano@iia.cnr.it; Tel.: +39-069-067-2395-2401

Received: 17 January 2019; Accepted: 12 February 2019; Published: 17 February 2019



Abstract: Structural and functional properties of polymer composites based on carbon nanomaterials are so attractive that they have become a big challenge in chemical sensors investigation. In the present study, a thin nanofibrous layer, comprising two insulating polymers (polystyrene (PS) and polyhydroxybutyrate (PHB)), a known percentage of nanofillers of mesoporous graphitized carbon (MGC) and a free-base tetraphenylporphyrin, was deposited onto an Interdigitated Electrode (IDE) by electrospinning technology. The potentials of the working temperature to drive both the sensitivity and the selectivity of the chemical sensor were studied and described. The effects of the porphyrin combination with the composite graphene–polymer system appeared evident when nanofibrous layers, with and without porphyrin, were compared for their morphology and electrical and sensing parameters. Porphyrin fibers appeared smoother and thinner and were more resistive at lower temperature, but became much more conductive when temperature increased to 60–70 °C. Both adsorption and diffusion of chemicals seemed ruled by porphyrin according its combination inside the composite fiber, since the response rates dramatically increased (toluene and acetic acid). Finally, the opposite effect of the working temperature on the sensitivity of the porphyrin-doped fibers (i.e., increasing) and the porphyrin-free fibers (i.e., decreasing) seemed further confirmation of the key role of such a macromolecule in the VOC (volatile organic compound) adsorption.

Keywords: electrospinning deposition; chemosensor; nanocomposite conductive polymers; polyhydroxybutyrate; polystyrene; H₂TPP; VOCs selectivity; mesoporous graphene

1. Introduction

Chemical sensors are usually conceived as electronic devices comprising a sensing material, in charge of interacting with the target analyte, and a transducer, to transform such an interaction into an electric/optical signal [1]. Among the main drivers for the design of advanced chemical sensors,

the key characteristics include sensitivity, selectivity, and rapid detection of target molecules. Over the last decade, the combination of nanostructured materials with many transducers has boosted the advances in this area, leading to significant enhancements in their sensing performance [2,3]. Consequently, together with a plethora of complex nanostructures, polymer nanocomposites have been designed and investigated as promising candidates for developing advanced materials for sensors. These joint materials benefit from the synergy between filler nanoparticles and polymer chains: they are both on similar length scales and with a very large interfacial surface area when compared to the volume of the material [4]. On the other hand, polymers are one of the most extensively exploited classes of materials due to the great variety of available chemical moieties with their relatively low cost, easy processing, and potential for designing and fabricating recycled and sustainable materials for sensors of the last generation [5]. More specifically, the development of polymeric composites based on carbon nanomaterials, such as carbon nanotubes (CNTs) and graphene (G), has been given a great deal of attention as a path to achieve new sensing materials with new structural (e.g., mechanical stability) and functional properties, likely better performing than pure components. Among the remarkable features of these two carbon allotropes to be used to design a chemical sensor, there are high electrical conductivity and large surface area [6]. Both nanomaterials have the same honeycomb lattice with sp^2 -hybridized carbon atoms, but with a two-dimensional sheet in graphene and its rolling up in one (SWNT, single-wall nanotubes) or more concentric tubes (MWNT, multi-wall nanotubes). Chemiresistors based on carbon-polymer combinations comprise features such as great stability, improvement of lifetime, tunable selectivity, ability to work at room temperature, good reversibility and reproducibility, low power consumption and cost effectiveness [7]. Generally, in these systems, current passes through continuous pathways of the conductive carbon particles between the parallel electrodes of the transducers. The sorption of a chemical vapor can cause softening/swelling of the polymer film, breaking some of the continuous pathways and increasing the resistance of the composite. Therefore, polymers can be designed to be more or less selective to different classes of VOCs, taking into account their solvation parameters according to vapor solubility (linear solvation energy relationships (LSER)) [8]. Obviously, much attention has been paid to properly modifying both polymers (functionalization of polymer chains) and polymer films (layer structure) to be simultaneously more selective to defined VOCs and optimized to host carbon nanofillers [9–11]. Therefore, chemiresistors based on Nafion–CNT [12] and poly(2,5-dimethylaniline)–CNT [13] have revealed intriguing performances in measuring air humidity and acid vapors, respectively. More recently, many nanocomposite polymer–graphene materials have been investigated and used successfully as sensors for industrial chemical reagents, drugs and explosives [14,15], thus highlighting comparable [16], and in some studies even better performances [17], than those of CNT-based sensors. This aspect sounds attractive since graphene is synthesized according to lower cost procedures and it is a material with the highest electrical conductivity known at room temperature (6000 Sc m^{-1}) [18], a huge surface area ($2.63 \times 10^3 \text{ m}^2 \text{ g}^{-1}$) and a complete impermeability to any gases [19]. The efficiency of graphene–polymer composite seems to be related to the molecular-level dispersion of graphene [20] that commonly occurs by using a proper surfactant and/or selecting a polymer matrix that, through π – π stacking or hydrophobic (van der Waals) interactions, preserve the intrinsic electronic properties of graphene and allow a nanofiller homogeneous distribution [21]. Regarding a graphene hosting layer framework, thin and porous films, facilitating gas/VOCs diffusion, are preferred to get fast sensor responses and to avoid layer poisoning (hysteresis effects). A very porous layer with a controlled distribution of the nanofillers can be developed by electrospinning (ES) deposition. This is a technology able to produce advanced multifunctional polymer nanocomposites (2D and 3D micro- or nanofibrous layers) and has been conceived as one of the most promising strategies to design and fabricate highly sensitive nanocomposite films at low cost and with high production rates [22]. The process uses a high voltage to provide sufficient charges in the polymer solution such that a jet is ejected from the tip of a spinneret toward a grounded collector: the solvent evaporates on the path and the

polymer nanofibers can be grown according to various arrangements and different morphologies. Thus, graphene nanoparticles can be added in the polymer solution for electrospinning, and nanofibers can be investigated as potential conductive material for chemical sensors. In a recent study, Avossa et al. [23] used the temperature to modulate the sensitivity of nanocomposite polymer nanofibers (polystyrene, polyhydroxybutyrate, mesoporous graphitized carbon (PS-PHB-MGC)) to gas and VOCs, making the sensor more selective to NO₂ (LOD: 2 ppb, limit of detection) when operated at 80 °C, whereas VOCs adsorption decreases.

A polymer doping agent is an alternative to the functionalization or substitution of polymer matrix for tuning the sensor selectivity. Different porphyrin species have been used to dope organic polymer. For instance, porphyrins combined with poly(2-phenyl-1,4-xylylene) have led to a huge variation in responses depending on the selected analytes (toluene, ethylacetate, ethanol, and propanone) [24]. Porphyrins have excellent sensing properties (their framework, peripheral substituents and the core that could be practically occupied by all metals of the periodic table) that make them an effective object of study and sensor applications of the last thirty years [25]. In the literature, there are several cases of porphyrins subjected to electrospun deposition in combination with electrospinnable polymers, so that their dispersion [26] and arrangement inside fibers as well as their photocatalytic [27] and sensing features [28,29] have been investigated extensively [30]. On the other hand, the best performances seem to be achieved when porphyrin occupies the outer part of the fiber [31] or when polymer fibers are very porous. Electrospun polymer fibers with a ternary composite combination (porphyrin, graphene oxide and nylon) are also manufactured [32] to be investigated towards more advanced applications.

In this paper, we present the design and the creation of a nanofibrous conductive chemical sensor based on a quaternary combination of two insulating polymers (PS and PHB, named as PsB) doped with 5,10,15,20-tetraphenylporphyrin (H₂TPP) and mesoporous graphene nanopowder. Porphyrin, due to its molecular structure, is expected to give a significant contribution to the sensing properties of the polymer composite fibers [23], by coordinating the planar surfaces of MGC and the phenyl rings of PS (effects on fiber morphology and structure) and “capturing” selectively volatile organic compounds (VOCs) (effects on sensor sensitivity and selectivity). The polymers were selected because they are versatile (widely used in many consumer products), eco-compatible, biodegradable (PHB), recyclable (PS) [33,34] and resistant to thermal excursions (thermoplastics). Additionally, they are both soluble in chloroform and insoluble in H₂O, meaning that they could be deposited by a unique electrospun mixture with a single needle, and were expected to be stable to changes in environmental humidity. In this more complex fibrous matrix, a preliminary study on the dependence of the sensor selectivity on the temperature was also carried out and is described below.

2. Materials and Methods

Mesoporous graphitized carbon nanopowder (MGC) (<500 nm; available surface area: 50–100 m²/g; average pore diameter: 137 Å), hexadecyltrimethylammonium bromide (CTAB) (~99%), polystyrene (PS) (M_w = 192,000 g/mol), chloroform (≥99%), toluene (≥99.8%), acetic acid (≥99%), and poly[(R)-3-hydroxybutyric] acid (PHB) (natural origin) were purchased from Sigma-Aldrich (Merck KGaA, Darmstadt, Germany). Ethanol (≥99.8%) was obtained from Fluka (Buchs, Switzerland). All chemicals were used without further purification. A 5,10,15,20-tetraphenylporphyrin (H₂TPP) was prepared following literature protocol [35]. Standardized pure air (5.0) was purchased from Praxair-RIVOIRA (Rome, Italy) and stored in cylinders.

Interdigitated Electrodes (IDEs), provided by Micrux Technologies (Oviedo, Spain), were fabricated on borosilicate substrate (IDE sizes: 10 mm × 6 mm × 0.75 mm; Pt/Ti electrodes, 120 pairs, 10 μm wide × 5 mm long × 150 nm thick, with 10 μm gap) and rinsed with soap and a “base piranha” mixture at 60 °C for ~15 min, (3:1, v/v, ammonia water and hydrogen peroxide water solution) and finally with Milli-Q water (~18 MΩ cm) before any use.

The electrospun dispersion was prepared by first solubilizing 450 mg of PS pellets into 9 mL of chloroform under magnetic stirring. After complete dissolution, 60 mg of PHB were added into the

solution and mixed at 50 °C for 2 h. Then, 150 mg of CTAB and 1 mL of ethanol were poured into the system and mixed overnight at 50 °C under magnetic stirring. Suspensions composed of 1.3 mg of MGC with and without 15 mg of H₂TPP were poured into 2 mL of the PS/PHB/CTAB solution and sonicated for at least 1 h.

The resulting polymer dispersions were loaded into glass syringes (1 cm long stainless steel and blunt tips) and connected to a syringe pump (Model KDS 200, KD Scientific). The fibers depositions were carried out in a home-made (IIA-CNR, Monterotondo, Rome, Italy) and ventilated clean box equipped at ambient condition. The electrospinning apparatus consisted of a high power AC-DC converter, a high voltage oscillator (100 V) driving a high voltage (ranging from 1 to 50 kV), a syringe pump and a rotating conductive pipe with a 45 mm diameter grounded collector. The fibrous layers were fabricated by applying ~6 kV DC voltage between the syringe tip and the collector (8 cm of distance), at a pump feeding rate of 700 $\mu\text{L h}^{-1}$. Deposition time was fixed at 2 min to obtain a thin and adhering coverage of the surface (IDEs and SiO₂ wafers and High Precision Quartz slices). UV-Vis spectrophotometer (UV-2600 Shimadzu, Kyoto, Japan) was used to collect UV spectra of the fibrous layer at the solid state.

Optical micrographs were captured by a Leitz-Wetzlar (Metallux 708082, Wetzlar, Germany) microscope, for the evaluation of the quality coverage of the fibers deposited onto the IDE.

Fibers morphological analyses were carried out by means of micrographs from Scanning Electron Microscopy (SEM) and Transmission Electron Microscopy (TEM). The electrospun nanofibrous fabrics deposited on thin SiO₂ wafers and sputter-coated with gold in a Balzers MED 010 unit were analyzed for SEM by a JEOL JSM 6010LA electron microscope (High Equipment Centre, University of Tuscia, Viterbo, Italy). Scanning transmission electron microscopy (STEM) images were acquired in annular dark field mode (ADF) on a JEOL JEM-2200FS microscope operated at 200 kV and with a spot size of 2 nm (IMEM-CNR, Parma, Italy). The H₂TPP/PS-PHB-MGC fibers were deposited on a lacey carbon coated copper grid, to reduce electrostatic charging of the fibers under the electron beam. Chemical mapping of carbon and oxygen were obtained from energy dispersive X-ray spectroscopy (EDXS) using a Si-Li detector (JEOL JED-2400, Akishima, Tokyo, Japan).

The resulting chemiresistors (IDEs + NFs, where NFs means nanofibers) were sealed in a measurement glass chamber (~100 mL volume) and connected to an electrometer (Keithley 6517, Solon, Ohio, USA) capable of measuring their electrical parameters and sending data to a PC (LabVIEW 2014 Software, National Instruments, Austin, TX, USA). The current, provided under dry and clean air, was recorded by applying potential values from -4.0 to 4.0 V in steps of 0.4 V at different temperatures (25, 40, 50, 60, and 70 °C). Current versus applied voltage values were used to calculate the resistance of the fibrous coated IDE and its correlation to the temperature, as well as a potential hysteresis of the material when it was electrically stressed. All batches of the chemiresistors fabricated on different dates but keeping the identical deposition parameters reported the same electrical features, confirming the reproducibility of the deposition technique.

Dynamic sensor measurements were carried out at different working temperature (T_w : 50, 60, and 70 °C, generated by a micro-heater placed below each sensing area of the IDE) using: (i) 4-channel MKS 247 managing up to four MKS mass flow controllers (MFC), set in the range 0–200 sccm (standard cubic centimeter per minutes); and (ii) Environics S4000 (Environics, Inc., Tolland, CT, USA) flow controller, containing three MFCs supplying three flow rates (up to 500, 250 and 2.5 sccm, respectively), managed by its own software. Pure air was used as the gas carrier and it was blended with increasing concentrations of vapors of water (H₂O), acetic acid (AcAc) and toluene (Tol), respectively, obtained through air bubbling in customized borosilicate bubblers (Rolando Spaziani S.r.l., Nettuno, Rome, Italy). A total gas flow of 300 sccm passed through the measurement chamber, housing the IDEs. Each measurement was carried out after the complete recovery of the starting current (the baseline) under dry and clean air flow. IDE responses were calculated as $\Delta I/I_0$, where ΔI is the current variation and I_0 is the current when the air flowed.

3. Results and Discussion

Electrospinning technology was used to create nanocomposite nanofibrous layers in a single step using a single needle. The depositions were easily carried out onto several substrates, specifically silicon dioxide thin slices (for fibers morphological, chemical and optical characterization) and customized borosilicate IDE transducers (for measuring electrical and sensing features of the thin nanofibrous coating). Each substrate, fixed onto the grounded rotating cylinder facing the needle tip, was able to collect the ejected fibers within the deposition cone (Figure 1). Fibers did not look aligned over the electrode, but arranged to form a porous network placed on the IDE surface. Despite the heterogeneity of the polymer suspensions, the electrospun jet streams occurred without discontinuity, so that fibers were collected for a few minutes.

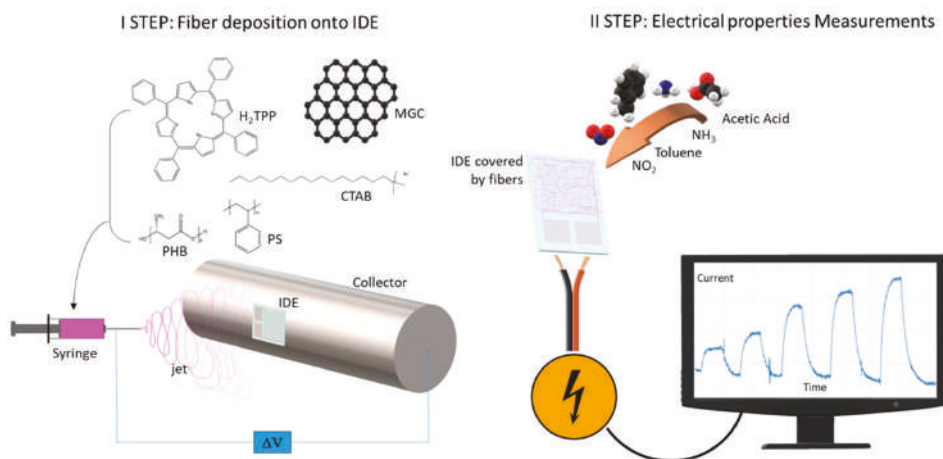


Figure 1. Sketch of electrospinning technique able to coat an IDE (interdigitated electrode) with composite nanofibers (left); and current measurements upon interaction of the chemosensor with gaseous molecules (right).

Shortly, the deposition process was generated by the application of a definite electrical field between the polymer suspension droplet at the metal nozzle and the grounded substrate placed at a distance. Due to the application of the electrical field, the polymer drop first changed shape (from spherical to conical) and then was elongated until the electrostatic forces exceeded the surface tension of the polymer suspension and forced the ejection of the liquid jet. Finally, dry and fine fibers were collected following the jet bending and stretching processes (by forces with opposing effects) [36], solvent evaporation and then splaying. The resulting fabrics appeared soft and cotton candy-like, and resulted easy to peel when electrospun processes were carried out for a longer time. Thus, to improve the fibers adhesion, it was necessary to thoroughly clean all the surfaces (base-piranha solution) and, following the deposition, incubate all the substrate at 60 °C under slight vacuum. The nanocomposite fabrics were pink (Figure 2c), turning to orange when the thickness increased but white/light gray (Figure 2d) if porphyrin-free. Nanocomposite fibers without porphyrin (PsB-MGC) previously investigated [23] appeared extremely rough on the surface and decorated with brighter islands, but fairly uniform in term of shape (cylindrical) and size ($d: 550 \pm 170$ nm) (Figure 2b). The fibers combined with H₂TPP (H₂TPP-PsB-MGC) kept the same circular cross-sectional shape but appeared much smaller in size ($d: 174 \pm 50$ nm) (Figure 2a). A possible reason for this phenomenon could be attributed to the polymer percentage decreasing in the final electrospun mixture [37,38] when porphyrin molecules were added. Furthermore, a higher voltage applied to the porphyrin mixture necessary to engage the electrospun process ($V_{H_2TPP-PsB-MGC} \approx 6$ kV; $V_{PsB-MGC} = 2.9$ kV) could also be

responsible for the fiber diameter reduction when combined to a lower feed rate (i.e., $700 \mu\text{L h}^{-1}$ and $900 \mu\text{L h}^{-1}$ used for H_2TPP -PsB-MGC and PsB-MGC suspensions, respectively) [39,40]. Porphyrin fibers looked smoother and had small spherical/elliptical bumps protruding from the whole the surface of the fibers (Figure 2a, inset). Therefore, the addition of the porphyrin to the composite system seemed to substantially change the morphology of the resulting fibers: in addition to dispersion forces, H_2TPP could interact with PS and graphene by π - π interactions and with PHB by hydrogen bond. However, long, continuous and unbeaded fibers proved an appropriate combination of electrospinning set of parameters.

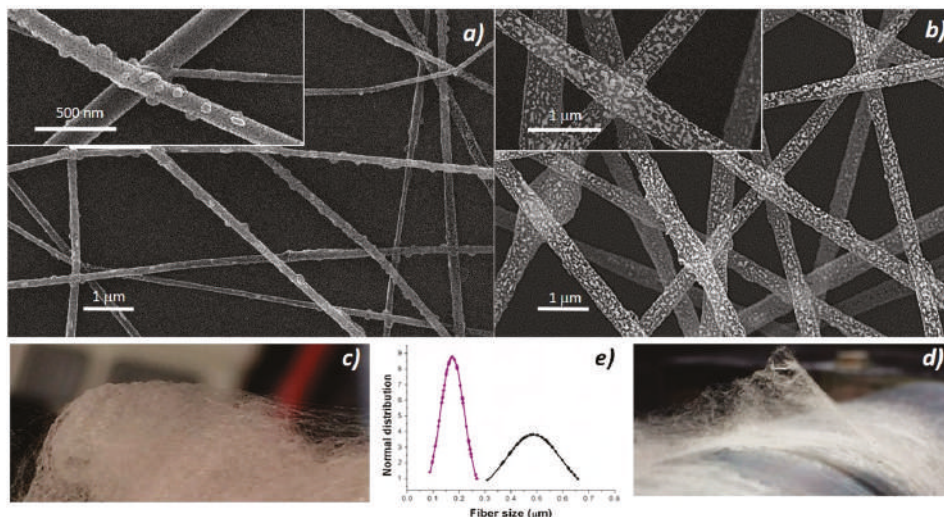


Figure 2. SEM micrographs of H_2TPP -PsB-MGC (a) and PsB-MGC (b) [23] and their respective pictures placed under (c,d). Diameter distribution graph (e) of H_2TPP -PsB-MGC (purple) and PsB-MGC fibers (black) (b).

Figure 3 shows a magnified TEM micrograph focusing on a single H_2TPP -PsB-MGC fiber. The shape is regular but the heterogeneity of the fiber seems to be confirmed by areas with different contrast among the diverse nanoaggregates. For ADF-STEM imaging, the contrast (brightness/darkness) is approximately proportional to the square of the averaged atomic number projected in beam direction z and it depends linearly on the thickness [41] (in particular, the bigger is the atomic number, the brighter is the image). The bright regions inside the polymer/porphyrin fiber could be due to Br^- , counterion to CTA^+ (Cetyltrimethylammonium) in the surfactant. The cationic surfactant was used to decrease the aggregation of MGC particles and improve their solubility/stability in the polymer matrix. Thus, the brightest area (a higher scattering, i.e., higher intensity in the image) distributed along the inner part of the fiber is supposed to be consequently and indirectly related also to graphene dispersion. As concerns the distribution of both polymers (PS and PHB), the electrospun nanofibers were expected to result in a bulk matrix mainly composed of one of the two polymers hosting an approximately inhomogeneous dispersion of the second polymer, as a consequence of the poor polymer-polymer miscibility. According to the literature, when two polymers are soluble in the same solvent but incompatible with each other, they solidify in different domains [42] during fiber formation [43]. In the inset of Figure 3, the EDXS chemical map is shown, as obtained from C-K (blue) and O-K peaks (green). Oxygen looks to be more concentrated at the surface of the fiber, leading us to suppose a higher presence of PHB at the surface (carbonyl, hydroxyl and ether groups). On the other hand, the distribution of the porphyrin can hardly be highlighted by this technique since H_2TPP is also substantially constituted by C atoms with the exception of the four N atoms in the core of the

macrocycle (but having close atomic number); thus, the contrast is too low to recognize the porphyrin. A high affinity between PS and H₂TPP (π - π stacking of the aromatic rings) is reported in literature where the homogeneous dispersion of the porphyrin in the surface and inside PS electrospun fibers is described using fluorescence microscopy (homogeneously red colored fibers) [28]. A weak π - π stacking could also occur between graphene flakes surface and porphyrin molecules [44]. Therefore, porphyrin could be fairly dispersed among PS chains and MGC nanofillers in fiber inner part, and PHB arranged to the outermost part.

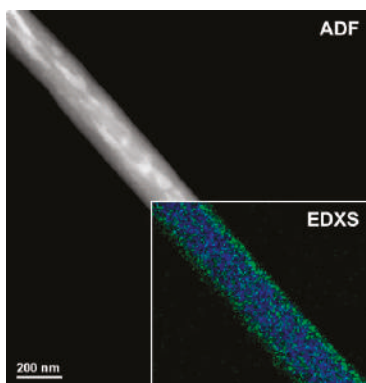


Figure 3. Annular dark field mode-scanning transmission electron microscopy (ADF-STEM) image of a porphyrin-doped fiber. The inset shows the corresponding energy-dispersive X-ray spectroscopy (EDXS) chemical map from carbon (blue) and oxygen (green).

The UV-Vis diffuse reflectance (R%) spectrum of a H₂TPP-PsB-MGC fibrous layer (Figure 4) showed the characteristic features of the H₂TPP chromophore, with the Soret (reflectance minimum about 2.5% at 415 nm) and Q bands well defined (VI: 516 nm, R: 13%; III: 550 nm, R: 19%; II: 591 nm, R: 23%; I: 648 nm, R: 22%). Although the Soret band showed the expected broadening in the solid state, the absence of wavelength shifts seemed to indicate that the porphyrin could be well dispersed in the polymeric matrix. This hypothesis is also supported by the narrow Q bands.

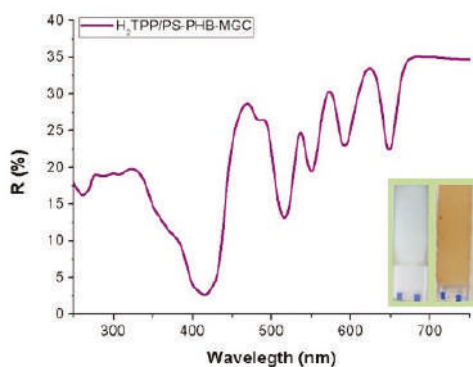


Figure 4. Diffuse reflectance ultraviolet-visible (DR-UV-Vis) spectrum of a H₂TPP/PsB-MGC thick fibrous layer (the orange one in inset). Inset shows also a porphyrin-free fibrous coating (the white-grey one).

The nanocomposite fibrous layer, comprising many interfaces between each component, was expected to be an intriguing system for the development of chemical sensors, due to both the wide adsorption surface and the surface energy potentials involved [45]. Optical microscope pictures (Figure 5b) depicted a Pt-Ti microtransducer coated with 2 min-deposited fibers, which appeared optically transparent and with some small black MGC aggregates spread inside fibers, suggesting that the graphene distribution was not completely homogeneous but enclosed within the polymer wires. Increasing the deposition time, a thicker layer was obtained, but the adhesion resulted inhomogeneous and it was more easily peelable from the transducer. To measure the electrical parameters of the resulting chemiresistor, both at room and increasing temperatures up to 70 °C, each IDE, during the current vs. voltage measurements, was positioned onto a customized micro-heater fabricated on alumina substrate. The supplied voltage ranged between −4 V and +4 V. Current–voltage curves displayed a quasilinear relationship between the current changes and the imposed increasing voltage values. Indeed, both PS and PHB, being thermoplastics, can be heated to their melting point (T_{M_PS} : 240 °C; T_{M_PHB} : 175 °C), cooled, and reheated again without substantial degradation. The experimental melting point of porphyrin is also high enough (T_{M_H2TPP} : ≥ 300 °C [46]) to allow the sensor to work properly in the established range. However, further heating involved an initial increase in current followed by a slow and irreversible increase in resistance, probably due to an irreversible arrangement of MGC inside fibers. For this reason, all experiments were carried out up to 70 °C. To investigate the contribution of the porphyrin to the chemiresistor electrical features, the same amount of graphene was used [23] to produce the fibers with and without porphyrin: indeed, upon the addition of porphyrin, MGC final mass percentage resulted about 1%. However, at room temperature (25 °C), porphyrin chemiresistor was more resistive (about 1.2×10^8 M Ω) than the porphyrin-free one (about 3.4×10^6 M Ω). The current inside fibers is supposed to occur by tunneling of electrons among MGC particles through a small insulating barrier (percolation theory). The electrical properties of such fibrous layers depend on both the quantity and the quality of the “texture” covering the electrodes. Therefore, the resulting measured electrical resistance is related to the individual fiber resistance (due to its dimension and shape), the fiber density (number of fibers per unit of surface area) and the electrode coverage. In porphyrin-fibers, nanofillers appeared distributed within the inner part of fibers, whereas the MGC aggregation inside PsB-MGC was supposed outer, then closer to the IDE metal-electrodes and with a smaller polymer barrier. A reason of this effect could be due to the arrangement of MGC inside fibers due to the porphyrin addition. Furthermore, it is known that conductivity can increase more than one order of magnitude when fiber diameter increases [47]. Porphyrin fibers were estimated to be much thinner than PsB-MGC one. On the other hand, thinner fibers are commonly preferred for sensor applications, since smaller-diameter wires are expected to have a faster response associated with a quicker diffusion of gas molecules through the fiber. Additionally, the collected porphyrin fibrous coatings showed a lower density of the PsB-MGC nanofibers over the electrodes (i.e., layer more porous, Figure 5b), although it increased with the same deposition time. This result could be a further reason to explain a lower conductivity of H₂TPP fibrous chemiresistor. The electrical signals at 25 and 40 °C were noisy, thus the porphyrin chemiresistor did not seem to work properly. Conversely, increasing the electrode working temperature, current increased considerably, especially when temperature value was set at 70 °C. Consequently, the signal to noise ratio increased too, and the baseline looked more stable.

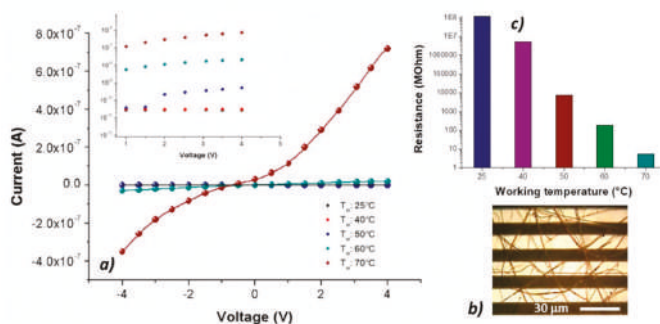


Figure 5. Current vs. voltage diagram at 25, 40, 50, 60 and 70 °C and 25, 40, 50 and 60 °C in the inset (a); optical image of the IDE covered by H₂TPP-PsB-MGC fiber (b); and resistance values diagram at 25, 40, 50, 60 and 70 °C (c).

When the sensor was heated from 25 to 40 °C, the electrical resistance changed by two orders of magnitude (from 10⁸ to 10⁶ MΩ) (Figure 5c and inset). The exponential decreasing of the resistance values to the increasing 10 °C steps has been reported in the semi-logarithm bar-plot of Figure 5c, where resistance changed from $\approx 7 \times 10^3$ to ≈ 5 MΩ, going from 50 to 70 °C. Such a non-linear dependence of conductivity on the heating apparently confirms the prevalence of the tunneling current (depending on the small dielectric barriers (insulating polymer) between the particles [48]) in comparison with the contact one [49,50], which usually should dominate in highly filled composites in contact with each other. The tunnel contribution is described by Equation (1):

$$\rho_T = e \left(\frac{\pi w}{2} \sqrt{\frac{2mV_0}{2\pi}} \right) \quad (1)$$

where ρ_T is the tunnel resistivity, m is the electron rest mass, h is Planck's constant, V_0 is the height of the barrier, and w is its width [51]. Commonly, in a polymer nanocomposite matrix, the gap among nanofillers tends to increase with temperature due to the polymer phase volume expansion (i.e., polymer crystalline phase melting [52]) or the amorphous phase softening [53] during melting, resulting in a resistivity rise of several decades. In the fibrous chemiresistors here described, with and without porphyrin [23], the different results could be explained by the phenyl group rotation in polystyrene (polymer backbone chain reorientation [54]), which could favor strong π - π interactions existing between aromatic organic molecules and the basal plane of MGC. Such a rearrangement could be responsible for the connectivity improvement of the conductive network of the nanofillers, inducing the enhancement of the electrical conductivity [55]. The interfacial force between graphene and PS could be enhanced by surface modification, which reduced the interfacial thermal resistance and dispersed graphene more uniformly [56]. A significant contribution to the MGC rearrangement inside fibers could also be generated by the aromatic planes of H₂TPP facing graphene surfaces. Indeed, comparing both the fibrous layers resistance values, H₂TPP-PsB-MGC became less resistive than PsB-MGC, when the working temperature reached and went over 60 °C (Figure 6), notwithstanding the disadvantaged parameters listed above of the porphyrin layers to be conductive. More specifically, its resistance value reached ≈ 5.7 MΩ versus ≈ 81.6 MΩ of PsB-MGC measured at the same temperature (T_w : 70 °C) in dry and clean air. Furthermore, the steep slope of H₂TPP-PsB-MGC curve (Figure 6) could also be affected by the temperature effects on charge transport among porphyrin that is strongly temperature dependent [57]. It means that at lower temperature H₂TPP could work as barrier while at higher temperature it should promote conduction.

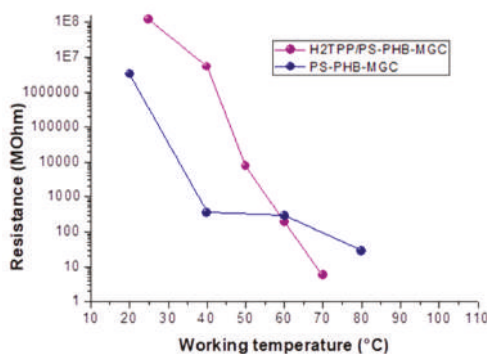


Figure 6. Resistance vs. working temperature for H₂TPP-PsB-MGC (purple) and PsB-MGC (blue) fibers.

Vapor measurements were carried out according to a dynamic mode: the sensor was exposed to a gaseous stream of molecules, the content of which was ruled by blending a stream of pure air with a second stream saturated with the vapor to be analyzed. Thus, the fibrous chemosensor was firstly deployed to increasing percentages of water vapors, ranging 0–50% with increments of 10%, and with working temperature values set at 40, 50 and 60 °C. Both transient responses and response curves are depicted in Figure 7a,b. The current, reported as I/I_0 (I : the current value; I_0 : starting current value under clean air) linearly increased when humidity percentage increased, too. A reason for this positive trend was the presence of the cationic surfactant inside the fibers that facilitated the dispersion of the carbon nanostructures [58]. Another reason could be related to the structure of the nanofillers, having here a mesoporous configuration, capable of easily entrapping water molecules and then interacting by the oxygen atoms making part of the framework of each MGC sheet [23]. When the chemosensor (T_w : 50 °C) was exposed to 50% relative humidity, it became seven times more conductive than the dried one. An inverse relationship occurred when working temperature increased: under 50% RH (relative humidity), the sensor became six (60 °C) and three times (70 °C) more conductive than under dry air, therefore generally the sensor responses to water vapors decreased with temperature. The related sensitivity values, defined as the change of measured signal per analyte concentration unit, i.e., the slope of the sensor responses graph [59] (Figure 7c), showed a decrease of 64% and 78% when the sensor worked, respectively, at 60 and 70 °C. Sensitivity is a key parameter in sensor design, because it represents an index related to the sensor ability to “capture” an analyte. In fact, such a fibrous layer was designed to be scarcely affine to water molecules, having two hydrophobic polymers (PS and PHB) and planar structures of H₂TPP and MGC preferring π - π interactions (despite H-bonds due to MGC structural defects and a cationic surfactant water soluble). Further, they were insoluble in H₂O, meaning that the resulting fibers could be exposed to a wide range of relative humidity percentages without undergoing structural changes. The lowering of the affinity index to vapor due to the heating should be presumably caused by the decrease of the vapor molecules diffusion mainly caused by the backbone polymer chains motion [60,61]. In addition, in agreement with the kinetic theory of matter, the sorbed molecules (H-bonds and Van der Waals forces), gaining kinetic energy when heated, were able to “fly” out of the binding site. Indeed, furnishing the sufficient kinetic energy to desorb the “captured” material is the usual strategy to restore/regenerate an adsorbent [62]. A very similar behavior is reported for PsB-MGC nanosensors [23].

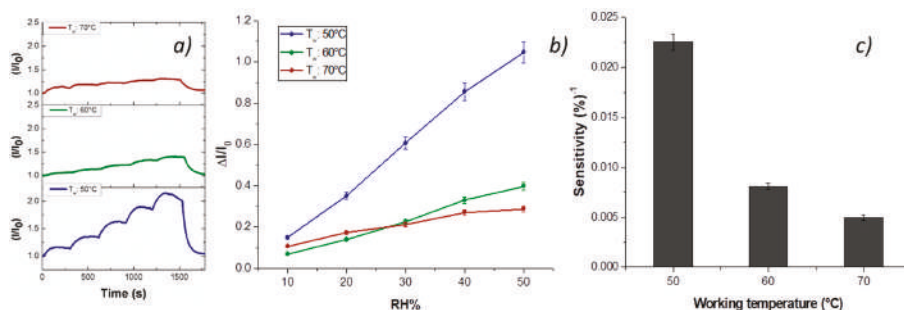


Figure 7. Normalized current (I/I_0) versus time during water vapor measurement (10%, 20%, 30%, 40% and 50% RH) at 70, 60 and 50 °C (a); $\Delta I/I_0$ –RH percentage diagram (response curves) (b); and sensitivity of the H₂TPP-PsB-MGC electrode at the different working temperatures (c).

To investigate a potential role of the porphyrin as a selective sensing agent, the fibrous chemosensor was deployed to toluene and acetic acid vapors, the two chemicals that, among the VOC chemical classes previously tested, reported the lowest and the highest, respectively, affinity to PsB-MGC fibers. Additionally, when working temperature increased, the PsB-MGC sensitivity values decreased greatly, making that sensor suitable to work at room (or close to room) temperature for VOC detection. Furthermore, the interest in testing both the chemicals is reinforced by the fact they have proved to be common organic indoor air pollutants [63] and extremely toxic by inhalation [64,65]. Finally, both acetic acid and toluene, being solvents of PHB and PS, respectively, were expected to be able to easily penetrate inside fibers. However, the analyzed vapors flowed in low concentrations (acetic acid and toluene up to 1000 and 1200 ppm, respectively) to avoid the poisoning of the sensing layers. Such a missing effect (i.e., the poisoning) was supported by no change in the baseline of the transient sensor responses, confirming that no chemical interaction had resulted in a permanent variation of the polymer structure. Thus, known concentrations of toluene vapors were generated and flowed throughout the sensor measuring chamber, and the related electrical changes are depicted in Figure 8. The shape of the transient responses (Figure 8a) pointed out quick responses to toluene at each temperature, ranging between 50 and 70 °C, suggesting a Langmuir-like kinetics and reaching the plateau in a few minutes. However, unexpectedly, the sensor response (current values) increased by heating (Figure 8), reporting the highest sensitivity at 70 °C ($S_{\text{ToI}70}$: 1.76×10^{-3} ppm⁻¹; $S_{\text{ToI}50}$: 9.63×10^{-5} ppm⁻¹). The exposure to acetic acid vapors also induced fast responses, linearly related to increasing concentrations of the sample (Figure 9). At higher temperature, sensitivity to acetic acid increased too ($S_{\text{AcAc}70}$: 14×10^{-3} ppm⁻¹; $S_{\text{AcAc}50}$: 4.4×10^{-4} ppm⁻¹) according to an exponential rate (Figure 9d,e). Further, a better signal/noise ratio was gathered as the temperature increased.

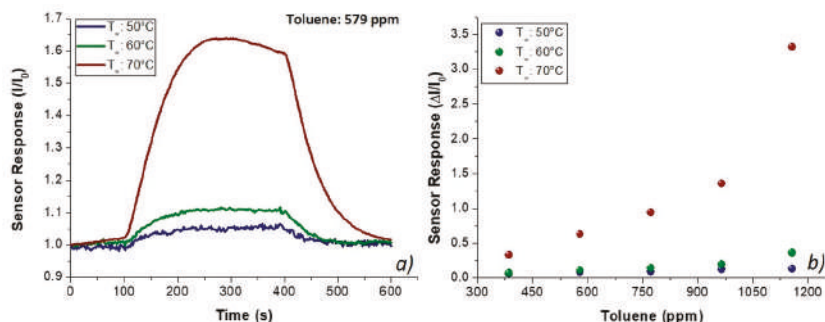


Figure 8. Transient responses (I/I_0 versus time) upon injection of 579 ppm of toluene in dry air (a); and response curves ($\Delta I/I_0$) to different toluene concentrations at increasing temperature values (50, 60 and 70 °C) (b).

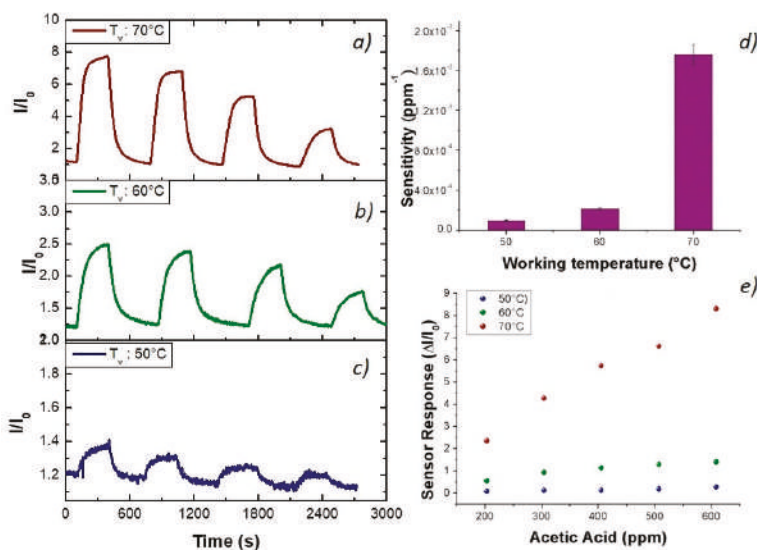


Figure 9. Transient responses (I/I_0 versus time) upon injection of different concentration of acetic acid in dry air at 70 $^\circ\text{C}$ (a); 60 $^\circ\text{C}$ (b); and 50 $^\circ\text{C}$ (c); sensitivity dependence on the working temperature (d); and response curves ($\Delta I/I_0$) to increasing acetic acid concentrations and increasing temperature (e).

Figure 10 depicts, in semi-logarithm scale, a comparison among the sensitivities to the selected chemicals, enhancing the different affinity of the material to each analyte, the same positive trend for the VOCs and the divergent trend (i.e., sensitivity decreasing) for water vapors. Therefore, going from 50 to 70 $^\circ\text{C}$, the sensitivity to water vapors became five times lower; conversely, to acetic acid and toluene, it was about 32 and 18 times greater, respectively. Another significant sensor feature is the limit of detection (LOD) defined as the lowest concentration of the analyte that can be detected by the sensor under given conditions, particularly at a given temperature. Thus, $\text{LOD}_{\text{AcAc}70}$ and $\text{LOD}_{\text{Tol}70}$ (three standard deviations of the blank) were lowered up to ~ 1 and ~ 3 ppm, respectively.

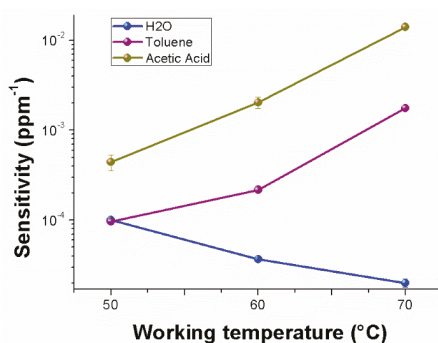


Figure 10. Sensitivity values changes to water vapors, toluene and acid acetic, respectively, depending on the sensor working temperature.

Porphyrim contribution to the sensor features was highlighted by the shape of the normalized response rate, which described the current variation per ppm in time during the exposure to the VOCs flow (Figure 11a). When toluene molecules kept in touch with the fibrous surface within the first 60 s (60 $^\circ\text{C}$), a seven times higher response rate to toluene was measured for H₂TPP-PsB-MGC sensor than PsB-MGC

(specifically from $6.75 \times 10^{-4} \pm 1.95018 \times 10^{-5} \text{ ppm}^{-1} \text{ s}^{-1}$ to $4.90 \times 10^{-3} \pm 6.27 \times 10^{-5} \text{ ppm}^{-1} \text{ s}^{-1}$). This temperature value was chosen because the current values of both sensors were comparable (Figure 11). The kinetic adsorption profile followed a classical Langmuir profile in both sensors but with different magnitude and adsorption rate. Since both sensors were operating at the same temperature and same toluene concentration, the main parameters involved in the sensor response were expected to be related to the number of the available binding sites and the adsorption energy (features defining the affinity between analyte and surface) [66]. Additionally, toluene could efficiently mediate the electron transfer between porphyrin and MGC. On the other hands, this organic compound could provide conformational changes of both macromolecules and hosting polymer chains (PS), thus contributing to the redistribution of the graphene network, which is responsible for the charge flow. When the sensors were exposed to acetic acid, the H₂TPP inside fibers apparently was responsible for the changes in both response magnitude and adsorption curve shape, Langmuir-like and Henry-like to with and without porphyrin sensor, respectively (Figure 11), indicating a higher affinity of porphyrin fibers to the analyte. Both transient response and calibration curves are the results of the ad/absorbing processes that depend on the chemical affinity of the VOCs to the material. The nanofibrous thin film can be considered as a complex and heterogeneous system where MGCs, and their arrangement through the fibers, are responsible for the resulting electrical features. Thus, the analytes have to be able to diffuse through the polymer–porphyrin matrix to be adsorbed onto the mesopores (or structural defects) and/or the planar surfaces of graphene, determining the changes in the charge density. The mesoporous structure could work as nucleation center for entrapping and growing molecules, such as AcAc, with multiple functional groups. Simultaneously, specific hydrogen bond interaction with the four nitrogen atoms, arranged in the core of the macrocycle structure, could occur [67]. Since all VOCs induced a rise in current, the effect on network distribution inside fibers could be considered the dominant one. The active contribution of porphyrin to the VOCs adsorption and to the electrical mechanisms is visualized in Figure 11b,d, whereas the changes of sensitivities in temperature for both sensors enhanced the opposite curve trend: sensitivity decreasing by heating in PsB-MGC sensor and conversely increasing in H₂TPP-PsB-MGC.

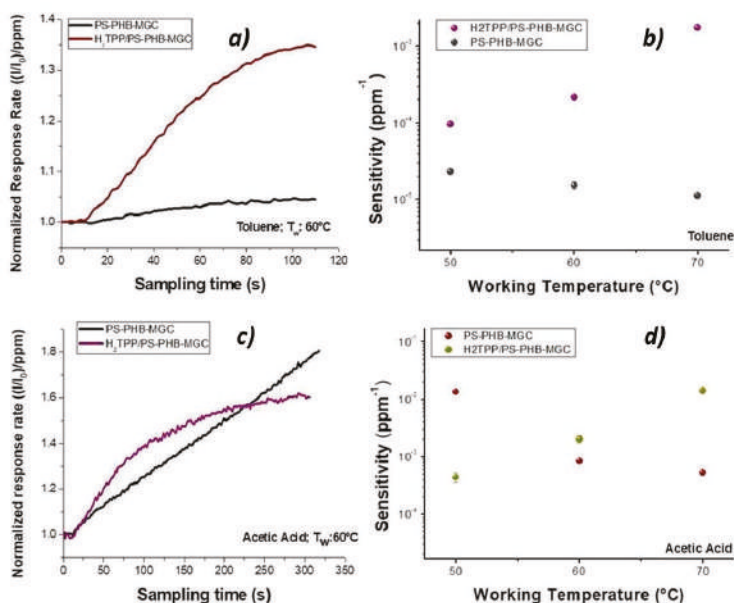


Figure 11. Comparison of the normalized response rate (a,c) and sensitivities (b,d) of H₂TPP-PsB-MGC and PsB-MGC to toluene (a,b) and acetic acid (c,d), respectively.

4. Conclusions

The present study reported the development of a conductive nanofibrous and nanocomposite polymer sensor combined with a free-base tetraphenylporphyrin, having the role of driving the selectivity and sensitivity of the polymer layer. Electrospinning technology allowed, in a single step and for 2 min, the fabrication of a pink-colored and highly porous layer adhering to the surface of the electrode. The sensor was able to work in a stable and reproducible way between 50 and 70 °C without any significant degradation, and revealing non-linear relationships between the conductivity and the temperature. The electrical conductivity increased when temperature increased, presumably due to the improving of the connectivity of the MGC networks. The effects of the porphyrin appeared significantly in the morphology of fibers (which were smoother and thinner than the porphyrin-free fibers) and in the electrical features. In fact, H₂TPP-Ps-MGC resulted more resistive at lower temperature, but became much more conductive than PsB-MGC when the chemiresistor worked at 60–70 °C, due to the rearrangement of MGC through the polymer fiber and presumably favored by the aromatic planes of H₂TPP facing graphene surfaces and phenyl groups of PS. It means that, at a higher temperature, H₂TPP tends to promote the fibrous layer conductivity. Furthermore, porphyrin not only increased the sensor sensitivity to toluene vapor (i.e., adsorption and diffusion favored), which was not revealed by PsB-MGC, but also increased with increasing temperature, differently from what occurred in PsB-MGC, whereas the sensitivity to VOCs decreased with heating. Further studies are needed to understand the whole mechanism of ad/absorption occurring between MGC–polymer–porphyrin and the VOCs/gas as well as the role of each polymer inside the fibers when the working temperature changed. However, this preliminary study suggests that this complex and nanostructured polymer matrix is expected as a challenging tool, where sensitivity and selectivity, now driven by temperature and a free-base porphyrin, would be designed and ruled taking into account a series of new combinations to create polymer composite sensors able to work alone or in array, at low cost, with fast responses, easy to be produced in large-scale and to be applied for multifaceted environments.

Author Contributions: Conceptualization, R.P., C.D.N. and A.M.; Data curation, A.M.; Formal analysis, J.A. and C.D.N.; Investigation, J.A., G.B., F.D.C., G.S.-M. and A.M.; Methodology, J.A., E.Z. and A.M.; Resources, R.P., E.Z., G.B., F.D.C. and G.S.-M.; Supervision, A.M.; Validation, J.A.; Writing—original draft, A.M.; and Writing—review and editing, all authors.

Funding: This research was funded by a 2-Year National Project, BRIC ID.12 2016—National Institute for Insurance against Accidents at Work (INAIL), titled: “Design and development of a sensory system for the measurement of volatile compounds and the identification of job-related microorganisms”.

Acknowledgments: The authors gratefully thank G. Tranfo of National Institute for Insurance against Accidents at Work for her crucial support in the BRIC ID.12 2016 Project and A.R. Taddei of High Equipment Centre, Electron Microscopy Section, University of Tuscia (VT), Italy, for providing SEM micrographs. Finally, the authors thank A. Capocecera for his technical support in developing customized software for laboratory measurements.

Conflicts of Interest: The authors declare no conflict of interest.

References

1. Bhattacharya, S.; Agarwal, A.K.; Chanda, N.; Pandey, A.; Sen, A.K. (Eds.) *Environmental, Chemical and Medical Sensors*; Springer: Singapore, 2018; ISBN 978-981-10-7751-7.
2. Tuantranont, A. Applications of Nanomaterials in Sensors and Diagnostics. In *Nanomaterials for Sensing Applications: Introduction and Perspective*; Springer: Berlin/Heidelberg, Germany, 2013; ISBN 978-3-642-36025-1.
3. Banica, F.G. Nanomaterials applications in chemical sensors. In *Chemical Sensors and Biosensors: Fundamentals and Applications*; John Wiley & Sons Ltd.: Chichester, UK, 2012; p. 135, ISBN 9780470710661.
4. Salvagione, H.J.; Diez-Pascual, A.M.; Lazaro, E.; Vera, S.; Gomez-Fatou, M.A. Chemical sensors based on polymer composites with carbon nanotubes and graphene: the role of the polymer. *J. Mater. Chem. A* **2014**, *2*, 14289–14328. [[CrossRef](#)]
5. Macagnano, A.; Perri, V.; Zampetti, E.; Bearzotti, A.; De Cesare, F. Humidity effects on a novel eco-friendly chemosensor based on electrospun PANi/PHB nanofibres. *Sens. Actuators B Chem.* **2016**, *232*, 16–27. [[CrossRef](#)]

6. Morris, J.E.; Iniewski, K. *Graphene, Carbon Nanotubes and Nanostructures (Techniques and Applications)*; CRC Press: Boca Raton, FL, USA, 2013; ISBN 1466560568.
7. Quercia, L.; Loffredo, F.; Francia, G.D. Influence of filler dispersion on thin film composites sensing properties. *Sens. Actuators B Chem.* **2005**, *109*, 153–158. [[CrossRef](#)]
8. Grate, J.W.; Abraham, M.H.; Wise, B.M. *Design and Information Content of Arrays of Sorption-Based Vapor Sensors Using Solubility Interactions and Linear Solvation Energy Relationships*; Springer: New York, NY, USA, 2009.
9. Feller, J.F.; Castro, M.; Kumar, B. Polymer–carbon nanotube conductive nanocomposites for sensing. In *Polymer–Carbon Nanotube Composites Preparation, Properties and Applications*; McNally, T., Pötschke, P., Eds.; Woodhead Publishing: Cambridge, UK, 2011; pp. 760–803. ISBN 978-1-84569-761-7.
10. Lonergan, M.C.; Severin, E.J.; Doleman, B.J.; Beaver, S.A.; Grubbs, R.H.; Lewis, N.S. Array-Based Vapor Sensing Using Chemically Sensitive, Carbon Black—Polymer Resistors. *Chem. Mater.* **1996**, *4756*, 2298–2312. [[CrossRef](#)]
11. Briglin, S.M.; Lewis, N.S. Characterization of the Temporal Response Profile of Carbon Black—Polymer Composite Detectors to Volatile Organic Vapors. *J. Phys. Chem. B.* **2003**, 11031–11042. [[CrossRef](#)]
12. Chang, C.P.; Yuan, C.L. The fabrication of a MWNTs—Polymer composite chemoresistive sensor array to discriminate between chemical toxic agents. *J. Mater. Sci.* **2009**, 5485–5493. [[CrossRef](#)]
13. Bavastrello, V.; Stura, E.; Carrara, S.; Erokhin, V.; Nicolini, C. Poly (2,5-dimethylaniline)–MWNTs nanocomposite: A new material for conductometric acid vapours sensor. *Sens. Actuators B Chem.* **2004**, *98*, 247–253. [[CrossRef](#)]
14. Hierlemann, A.; Gutierrez-osuna, R. Higher-Order Chemical Sensing. *Chem. Rev.* **2008**, *108*, 563–613. [[CrossRef](#)]
15. Qureshi, A.; Kang, W.P.; Davidson, J.L.; Gurbuz, Y. Diamond & Related Materials Review on carbon-derived, solid-state, micro and nano sensors for electrochemical sensing applications. *Diam. Relat. Mater.* **2009**, *18*, 1401–1420. [[CrossRef](#)]
16. Huang, X.; Qi, X.; Boeya, F.; Zhang, H. Graphene-based composites. *Chem. Soc. Rev.* **2012**, *41*, 525–944. [[CrossRef](#)]
17. Zheng, D.; Vashist, S.K.; Dykas, M.M.; Saha, S.; Al-rubeaan, K.; Lam, E.; Luong, J.H.T.; Sheu, F. Graphene versus Multi-Walled Carbon Nanotubes for Electrochemical Glucose Biosensing. *Materials* **2013**, *6*, 1011–1027. [[CrossRef](#)] [[PubMed](#)]
18. Berger, C.; Song, Z.M.; Li, T.B.; Li, X.B.; Ogbazghi, A.Y.; Feng, R.; Dai, Z.N.; Marchenkov, A.N.; Conrad, E.H.; First, P.N.; et al. Ultrathin Epitaxial Graphite: 2D Electron Gas Properties and a Route toward. *J. Phys. Chem. B* **2004**, 19912–19916. [[CrossRef](#)]
19. Bunch, J.S.; Verbridge, S.S.; Alden, J.S.; van der Zande, A.M.; Parpia, J.M.; Craighead, H.G.; McEuen, P.L. Impermeable Atomic Membranes from Graphene Sheets. *Nanoletters* **2008**, *8*, 2458–2462. [[CrossRef](#)] [[PubMed](#)]
20. Kuilla, T.; Bhadra, S.; Yao, D.; Kim, N.H.; Bose, S.; Lee, J.H. Progress in Polymer Science Recent advances in graphene based polymer composites. *Prog. Polym. Sci.* **2010**, *35*, 1350–1375. [[CrossRef](#)]
21. Sinha, R.S. (Ed.) *Processing of Polymer-Based Nanocomposites*; Springer International Publishing: Cham, Switzerland, 2018; ISBN 978-3-319-97779-9.
22. Macagnano, A.; Zampetti, E.; Kny, E. (Eds.) *Electrospinning for High Performance Sensors*; Springer International Publishing: Cham, Switzerland, 2015; ISBN 978-3-319-14405-4.
23. Avossa, J.; Zampetti, E.; De Cesare, F.; Bearzotti, A.; Scarascia-Mugnozza, G.; Vitiello, G.; Zussman, E. Thermally Driven Selective Nanocomposite PS-PHB/MGC Nanofibrous Conductive Sensor for Air Pollutant Detection. *Front. Chem.* **2018**, *6*, 1–14. [[CrossRef](#)]
24. Esteves, C.H.A.; Iglesias, B.A.; Li, R.W.C.; Ogawa, T.; Araki, K.; Gruber, J. New composite porphyrin-conductive polymer gas sensors for application in electronic noses. *Sens. Actuators B. Chem.* **2014**, *193*, 136–141. [[CrossRef](#)]
25. Paolesse, R.; Nardis, S.; Monti, D.; Stefanelli, M.; Di Natale, C. Porphyrinoids for Chemical Sensor Applications. *Chem. Rev.* **2017**, 2517–2583. [[CrossRef](#)]
26. Olkhov, A.A.; Karpova, S.G.; Tubayeva, P.M.; Lobanov, A.V.; Kurmosov, A.S.; Mastalygina, E.E.; Iordanskii, A.L. Supramolecular structure of electrospun ultrathin fibers based on poly-(3-hydroxibutirate) with zinc-tetraphenylporphyrin complex. *AIP Conf. Proc.* **2018**, 2051. [[CrossRef](#)]

27. Shao, L.; Hu, B.; Dong, P.; Ji, W.; Qi, C. Electrospinning Fe(III)porphyrin/TiO₂/poly(styrene) mixture: Formation of a novel nanofiber photocatalyst for the photodegradation of methyl orange. *J. Porphyr. Phthalocyanines* **2010**, *14*, 993–999. [CrossRef]
28. Hu, M.; Kang, W.; Zhao, Y.; Shi, J.; Cheng, B. A fluorescent and colorimetric sensor based on a porphyrin doped polystyrene nanoporous fiber membrane for HCl gas detection. *RSC Adv.* **2017**. [CrossRef]
29. Yang, Y.; Wang, H.; Su, K.; Long, Y.; Peng, Z.; Li, N.; Liu, F. A facile and sensitive fluorescent sensor using electrospun nanofibrous film for nitroaromatic explosive detection. *J. Mater. Chem.* **2011**, 11895–11900. [CrossRef]
30. Arai, T.; Tanaka, M.; Kawakami, H. Porphyrin-Containing Electrospun Nano fibers: Positional Control of Porphyrin Molecules in Nano fibers and Their Catalytic Application. *Appl. Mater. Interfaces* **2012**. [CrossRef] [PubMed]
31. Jang, K.; Baek, I.W.; Back, S.Y.; Ahn, H. Electrospinning of porphyrin/polyvinyl alcohol (PVA) nanofibers and their acid vapor sensing capability. *J. Nanosci. Nanotechnol.* **2011**, *11*, 6102–6108. [CrossRef] [PubMed]
32. García-Pérez, C.; Menchaca-Campos, C.; García-Sánchez, M.A.; Pereyra-Laguna, E.; Rodríguez-Pérez, O.; Uruchurtu-Chavarrín, J. Nylon/Porphyrin/Graphene Oxide Fiber Ternary Composite, Synthesis and Characterization. *Open J. Compos. Mater.* **2017**, *7*, 146–165. [CrossRef]
33. Uyar, T.; Besenbacher, F. Electrospinning of uniform polystyrene fibers: The effect of solvent conductivity. *Polymer* **2008**, *49*, 5336–5343. [CrossRef]
34. Bychuk, M.A.; Kil'deeva, N.R.; Kurinova, M.A.; Bogdanov, N.V.; Kalinin, M.V.; Novikov, A.V.; Vikhoreva, G.A. Electrospinning of Biodegradable Polymer Scaffolds. *Fibre Chem.* **2015**, *46*, 345–348. [CrossRef]
35. Fuhrhop, J.H.; Smith, K.M. Laboratory methods. In *Porphyrins and Metalloporphyrins*; Smith, K.M., Ed.; Elsevier Science: Amsterdam, The Netherlands, 1975; pp. 757–869.
36. Garg, K.; Bowlin, G.L. Electrospinning jets and nanofibrous structures. *Biomicrofluidics* **2011**, *5*, 013403. [CrossRef]
37. Zhu, G.; Zhao, L.Y.; Zhu, L.T.; Deng, X.Y.; Chen, W.L. Effect of Experimental Parameters on Nanofiber Diameter from Electrospinning with Wire Electrodes. *IOP Conf. Ser. Mater. Sci. Eng.* **2017**, *230*. [CrossRef]
38. Fong, H.; Chun, I.; Reneker, D.H. Beaded nanofibers formed during electrospinning. *Polymer* **1999**, *40*, 4585–4592. [CrossRef]
39. Lee, J.S.; Choi, K.H.; Ghim, H.D.; Kim, S.S.; Chun, D.H.; Kim, H.Y.; Lyoo, W.S. Role of molecular weight of atactic poly(vinyl alcohol) (PVA) in the structure and properties of PVA nanofabric prepared by electrospinning. *J. Appl. Polym. Sci.* **2004**, *93*, 1638–1646. [CrossRef]
40. Wang, X.; Cao, J.; Hu, Z.; Pan, W.; Liu, Z. Jet shaping nanofibers and the collection of nanofiber mats in electrospinning. *J. Mater. Sci. Technol.* **2006**, *22*, 536–540.
41. Su, D. Advanced electron microscopy characterization of nanomaterials for catalysis. *Green Energy Environ.* **2017**, *2*, 70–83. [CrossRef]
42. Zhong, G.; Wang, K.; Zhang, L.; Li, Z.M.; Fong, H.; Zhu, L. Nanodroplet formation and exclusive homogeneously nucleated crystallization in confined electrospun immiscible polymer blend fibers of polystyrene and poly(ethylene oxide). *Polymer* **2011**, *52*, 5397–5402. [CrossRef]
43. Bognitzki, M.; Czado, W.; Frese, T.; Schaper, A.; Hellwig, M.; Steinhart, M.; Greiner, A.; Wendorff, J.H. Nanostructured fibers via electrospinning. *Adv. Mater.* **2001**, *13*, 70–72. [CrossRef]
44. Kim, S.J.; Song, W.; Kim, S.; Kang, M.-A.; Myung, S.; Lee, S.S.; Lim, J.; An, K.-S. Tunable functionalization of graphene nanosheets for graphene-organic hybrid photodetectors. *Nanotechnology* **2016**, *27*. [CrossRef] [PubMed]
45. Gardner, D.J.; Blumentritt, M.; Kiziltas, A.; Kiziltas, E.E.; Peng, Y.; Yildirim, N. Polymer Nanocomposites from the Surface Energy Perspective. *Rev. Adhes. Adhes.* **2013**, *2*, 175–215. [CrossRef]
46. ChemSpider. Search and Share Chemistry. Available online: <http://www.chemspider.com/Chemical-Structure.10291672.html> (accessed on 16 January 2019).
47. MacDiarmid, A.G.; Jones, W.E., Jr.; Norris, I.D.; Gao, J.; Johnson, A.T., Jr.; Pinto, N.J.; Hone, J.; Han, B.; Ko, F.K.; Okuzaki, H.; et al. Electrostatically-generated nanofibers of electronic polymers. *Synth. Met.* **2001**, *27–30*. [CrossRef]
48. Sheng, P. Fluctuation-induced tunneling conduction in disordered materials. *Phys. Rev. B* **1980**, *21*, 2180–2195. [CrossRef]

49. Syurik, J.; Ageev, O.A.; Cherednichenko, D.I.; Konoplev, B.G.; Alexeev, A. Non-linear conductivity dependence on temperature in graphene-based polymer nanocomposite. *Carbon* **2013**, *63*, 317–323. [CrossRef]
50. Gao, C.; Liu, P.; Ding, Y.; Li, T.; Wang, F.; Chen, J.; Zhang, S.; Li, Z.; Yang, M. Non-contact percolation of unstable graphene networks in poly(styrene-co-acrylonitrile) nanocomposites: Electrical and rheological properties. *Compos. Sci. Technol.* **2018**, *155*, 41–49. [CrossRef]
51. Celzard, A.; McRae, E.; Maréché, J.F.; Furdin, G.; Sundqvist, B. Conduction mechanisms in some graphite–polymer composites: Effects of temperature and hydrostatic pressure. *J. Appl. Phys.* **1998**, *83*, 1410–1419. [CrossRef]
52. Feller, J.F.; Linossier, I.; Grohens, Y. Conductive polymer composites: comparative study of poly(ester)—Short carbon fibres and poly(epoxy)—Short carbon fibres mechanical and electrical properties. *Polym. Adv. Technol.* **2002**, *57*, 64–71. [CrossRef]
53. Pillin, I.; Feller, J.F.; Pimbert, S.; Levesque, G. Conductive poly(ester)/poly(olefin)/carbon black composites: Influence of glass transition temperature and crystallinity of the poly(ester) matrix on the electrical properties. *Plast. Rubbers Compos.* **2002**, *31*, 300–306. [CrossRef]
54. Tonelli, A.E. Phenyl Group Rotation in Polystyrene. *Macromolecules* **1973**, *6*, 682–683. [CrossRef]
55. Cao, Q.; Song, Y.; Tan, Y.; Zheng, Q. Thermal-induced percolation in high-density polyethylene/carbon black composites. *Polymer* **2009**, *50*, 6350–6356. [CrossRef]
56. Li, A.; Zhang, C.; Zhang, Y.-F. Thermal Conductivity of Graphene-Polymer Composites: Mechanisms, Properties, and Applications. *Polymers* **2017**, *9*, 437. [CrossRef]
57. Keun, B.; Aratani, N.; Kuk, J.; Kim, D.; Osuka, A.; Yoo, K. Length and temperature dependence of electrical conduction through dithiolated porphyrin arrays. *Chem. Phys. Lett.* **2005**, *412*, 303–306. [CrossRef]
58. Koutsoukis, A.; Georgakilas, V.; Belessi, V.; Zboril, R. Highly Conductive Water-Based Polymer/Graphene Nanocomposites for Printed Electronics. *Chem. Eur. J.* **2017**, 8268–8274. [CrossRef]
59. Kalantar-Zadeh, K. *Sensors: An Introductory Course*; Springer Science & Business Media: New York, NY, USA, 2013; ISBN 978-1-4614-5052-8.
60. Haslam, R.T.; Hershey, R.I.; Kean, R.H. Effect of gas velocity and temperature on rate of absorption. *Ind. Eng. Chem.* **1924**, *16*, 1224–1230. [CrossRef]
61. Ramesh, N.; Duda, J.L. Diffusion in polymers below the glass transition temperature: Comparison of two approaches based on free volume concepts. *Korean J. Chem. Eng.* **2000**, *17*, 310–317. [CrossRef]
62. Technical Bulletin: Choosing an Adsorption System for VOC: Carbon, Zeolite, or Polymers? Available online: <https://www3.epa.gov/ttn/catc/dir1/fadsorb.pdf> (accessed on 16 January 2019).
63. Salthammer, T.; Uhde, E. (Eds.) *Organic Indoor Air Pollutants: Occurrence, Measurement, Evaluation*, 2nd ed.; WILEY-VCH: Weinheim, Germany, 2009; ISBN 978-3-527-31267-2.
64. Toluene. Available online: <https://www.epa.gov/sites/production/files/2016-09/documents/toluene.pdf> (accessed on 5 February 2019).
65. TOXNET. Toxicology Data Network. Available online: <https://toxnet.nlm.nih.gov/cgi-bin/sis/search2/r?dbs+hsdb:@term+@DOCNO+40> (accessed on 5 February 2019).
66. Ndiaye, A.; Bonnet, P.; Pauly, A.; Dubois, M.; Brunet, J.; Varenne, C.; Guerin, K.; Lauron, B. Noncovalent Functionalization of Single-Wall Carbon Nanotubes for the Elaboration of Gas Sensor Dedicated to BTX Type Gases: The Case of Toluene. *J. Phys. Chem. C* **2013**, *117*, 20217–20228. [CrossRef]
67. Nardis, S.; Pomarico, G.; Tortora, L.; Capuano, R.; D’Amico, A.; Di Natale, C.; Paolesse, R. Sensing mechanisms of supramolecular porphyrin aggregates: a teamwork task for the detection of gaseous analytes. *J. Mater. Chem.* **2011**, *21*, 18638. [CrossRef]



Article

Nanostructured Hydrogels by Blend Electrospinning of Polycaprolactone/Gelatin Nanofibers

Lode Daelemans ^{1,†}, Iline Steyaert ^{1,2,†}, Ella Schoolaert ¹, Camille Goudenhoofft ¹,
Hubert Rahier ² and Karen De Clerck ^{1,*}

¹ Department of Materials, Textiles and Chemical Engineering (MaTCh), Ghent University, Technologiepark 907, 9052 Ghent, Belgium; lode.daelemans@ugent.be (L.D.); iline.steyaert@ugent.be (I.S.); ella.schoolaert@ugent.be (E.S.); camille.goudenhoofft@univ-ubs.fr (C.G.)

² Research Unit of Physical Chemistry and Polymer Science, Department of Materials and Chemistry, Vrije Universiteit Brussel, Pleinlaan 2, 1050 Brussels, Belgium; hrahier@vub.ac.be

* Correspondence: karen.declerck@ugent.be; Tel.: +32-9-2645-740

† These authors contributed equally to this work.

Received: 25 June 2018; Accepted: 17 July 2018; Published: 20 July 2018



Abstract: Nanofibrous membranes based on polycaprolactone (PCL) have a large potential for use in biomedical applications but are limited by the hydrophobicity of PCL. Blend electrospinning of PCL with other biomedical suited materials, such as gelatin (Gt) allows for the design of better and new materials. This study investigates the possibility of blend electrospinning PCL/Gt nanofibrous membranes which can be used to design a range of novel materials better suited for biomedical applications. The electrospinnability and stability of PCL/Gt blend nanofibers from a non-toxic acid solvent system are investigated. The solvent system developed in this work allows good electrospinnable emulsions for the whole PCL/Gt composition range. Uniform bead-free nanofibers can easily be produced, and the resulting fiber diameter can be tuned by altering the total polymer concentration. Addition of small amounts of water stabilizes the electrospinning emulsions, allowing the electrospinning of large and homogeneous nanofibrous structures over a prolonged period. The resulting blend nanofibrous membranes are analyzed for their composition, morphology, and homogeneity. Cold-gelling experiments on these novel membranes show the possibility of obtaining water-stable PCL/Gt nanofibrous membranes, as well as nanostructured hydrogels reinforced with nanofibers. Both material classes provide a high potential for designing new material applications.

Keywords: biomaterial; biomedical; nanofibers; scaffolds; reinforced; hybrid material; thermal analysis; nanofibrous membranes

1. Introduction

Electrospun nanofiber membranes have gained a lot of attention the past few years. Their striking resemblance to the morphology of the extracellular matrix (ECM) made them especially interesting for biomedical applications. Nanofibrous membranes can, unlike structures with porosity on a larger scale, provide an environment closely mimicking the natural ECM by providing appropriate cell binding sites. Cell behavior and functionality can be controlled by man-made nanofibrous scaffolds, which are therefore increasingly being used in tissue engineering and wound-healing applications [1,2]. Solvent electrospinning provides a relatively simple way to produce nanofibers from polymer solutions and is therefore currently the most commonly applied processing technique. To fully exploit the potential of electrospun nanofibrous materials, further research toward the use of less toxic, more economical solvents and a stable electrospinning process suitable for upscaling, is essential.

Polycaprolactone (PCL) is commonly used in biomedical products, ranging from sutures or staples for wound closure to contraceptive devices. This is mainly due to its tunable degradation profile, in combination with low cost, easy production and availability of medical-grade material [3,4]. It is thus not surprising that PCL nanofibers for biomedical applications have also been developed [5–10]. The practical application of PCL nanofibers in the biomedical field, however, is severely limited due to the hydrophobic properties adversely affecting cell affinity. Although the nanofiber morphology closely resembles the ECM, its complexity in terms of composition, biological functionality and biophysical properties makes it difficult to reproduce using single polymer systems. Blending synthetic and natural polymers offers the opportunity to tune physical properties and bioactivity while minimizing the disadvantages of both polymer components, thus more closely resembling the native ECM [2,11–13]. Compared to the use of copolymers or modified nanofibers, blending offers an alternative approach that is simple and economical [14].

A wide variety of natural polymers are available for biomedical applications, including several polypeptides and polysaccharides. They provide the desired biological properties in a blend and are biodegradable. Gelatin (Gt) is a commercial polypeptide widely available in medical-grade material and very suitable for biomimetic applications since it displays many integrin binding sites for cell adhesion and differentiation [15–19]. Although it is possible to produce pure Gt nanofibers [20], blending with PCL can give rise to superior mechanical properties [21–23], increasing its application potential.

Our previous work showed that Gt nanofibers are cold-water-soluble due to their high surface-to-volume ratio which promotes water penetration and dissolution. They can be used as an instant cold gel. This presents opportunities for PCL/Gt blended nanofibrous membranes to design new hybrid materials for biomedical applications. In this article, we develop a non-toxic and economical solvent system for the production of PCL/Gt blend nanofibers by electrospinning. An acetic acid (AA)/formic acid (FA) solvent system is selected based on our previous work in which pure PCL and pure Gt nanofibers were produced [5,20]. Several PCL/Gt blend nanofibrous membranes with varying compositions are electrospun and their morphology is characterized. Cold-gelling experiments are performed on nanofibrous membranes with varying PCL/Gt ratio to study its effect on the gel formation of the Gt component and the resulting structure of these novel materials.

2. Materials and Methods

2.1. Materials

Polycaprolactone (average M_n of $80 \text{ kg}\cdot\text{mol}^{-1}$) was purchased from Sigma-Aldrich (Overijse, Belgium). Commercial gelatin isolated from pigskin by the acidic process (type A pharma-grade, 300 Bloom) was kindly supplied by Rousselot, Ghent, Belgium. Both polymers were used as-received for the electrospinning process. AA (99.8 vol%) and FA (98.0 vol%) were supplied by Sigma-Aldrich (Overijse, Belgium).

Efforts in optimization also included testing of a lower molecular weight PCL (average M_w $14 \text{ kg}\cdot\text{mol}^{-1}$) purchased from Sigma-Aldrich (Overijse, Belgium) and a gelatin isolated from bovine bones by the alkaline process (type B pharma-grade, 260 Bloom) kindly supplied by Rousselot, Ghent, Belgium.

2.2. Electrospinning

The electrospinning process allows for easy production of nanofibers using polymer solutions, and is more thoroughly described for PCL and gelatin in our previous papers [5,20]. Blend nanofibers are obtained when the solution used for electrospinning contains two (or more) polymer components.

The PCL/Gt electrospinning solutions were obtained by simultaneous dissolution of PCL and gelatin, allowing for variations in solvent ratio, total polymer concentration and polymer ratio. The electrospinning solutions were characterized prior to use by their viscosity and conductivity. Viscosity was measured using a Brookfield viscometer LVDV-II (standard deviation was on average

8%, Brookfield, Middleboro, MA, USA) and conductivity was determined by a CDM210 conductivity meter of Radiometer Analytical (standard deviation was on average 11%, Düsseldorf, Germany).

All electrospinning trials for process optimization were performed using a mono-nozzle setup, leading to a scalable electrospinning process. Nanofibrous membranes for subsequent analysis were electrospun using a multinozzle or rotating drum setup at low speed [24,25], already providing upscaled samples. The latter samples were electrospun using the AA/FA solvent system (solvent ratio as specified in the text), a polymer concentration of 13 wt% (PCL/Gt ratio as specified in the text), a flow rate of 1 mL·h⁻¹, a tip-to-collector distance of 12.5 cm and the applied voltage adapted for stable electrospinning.

The electrospun samples were examined by scanning electron microscopy (FEI Quanta 200 F, Thermo Fisher Scientific, Eindhoven, The Netherlands) at an accelerating voltage of 20 kV. Sample preparation was done using a sputter coater (Emitech SC7620, coating with Au, Rotterdam, The Netherlands). The nanofiber diameters were measured using ImageJ version 1.48, <https://imagej.net>. The average fiber diameters and their standard deviations are based on 50 measurements per sample.

2.3. Water Treatment of PCL/Gt Blends

Water treatment of PCL/Gt blend nanofibrous membranes was done by washing the samples in a large quantity of demineralized water at 35 °C (maximal temperature without affecting PCL nanofibrous structure) for 30 s. Four repetitions were done before further drying at ambient temperature for over 24 h.

2.4. Materials Characterization

Solution cast films (prepared by solution casting in Teflon evaporation dishes of the electrospinning solution) and nanofibrous membranes were characterized using a Fourier Transform Infrared (FTIR, Thermo Fisher Scientific, Eindhoven, The Netherlands) spectrometer with Attenuated Total Reflectance (ATR) accessory (diamond crystal) from Thermo Scientific. The spectra were recorded in the range 4000–400 cm⁻¹ with a resolution of 4 cm⁻¹. 32 scans were averaged for each spectrum. The films were prepared by sampling the electrospinning solution and solution casting onto Teflon evaporation dishes. All nanofibrous membranes were measured as-spun. Additionally, PCL/Gt nanofibrous membranes were also measured after (partial) removal of gelatin by water treatment as detailed above.

Differential scanning calorimetry (DSC) measurements were performed using a TA Instruments (Asse, Belgium) Q2000 equipped with a refrigerated cooling system and using nitrogen as purge gas (50 mL·min⁻¹). The instrument was calibrated using Tzero technology, including a temperature calibration with indium. DSC measurements were performed on samples of 3.00 ± 0.30 mg conditioned at 65% RH for 24 h, enclosed in hermetic Tzero aluminum crucibles and at a heating rate of 2.5 K·min⁻¹. The standard deviation of the melting enthalpy of PCL nanofibers was 5%.

Dynamic Mechanical Analysis (DMA) measurements were done using a TA Instruments Q800 (Asse, Belgium), equipped with liquid nitrogen cooling (LNCS) and film tension clamps. Calibration was done according to a manufacture-defined procedure. Temperature calibration was performed by means of the melting transition of gallium. Films and nanofibrous membranes were measured in film tension mode, using a Poisson's ratio of 0.44, a frequency of 1 Hz, a strain of 0.5%, a static force of 0.01 N and a heating rate of 2.5 K·min⁻¹. The measurements were performed on as-spun nanofibrous membranes at room humidity (40 ± 10% RH). The samples were not heated above 30 °C to avoid melting of the PCL component.

3. Results and Discussion

3.1. Electrospinning of PCL/Gt Blend Nanofibers Using AA/FA

Our previous investigation of the pure components illustrated that both PCL and gelatin are electrospinnable when dissolved in AA/FA, and this for several concentrations and solvent ratios [5,20].

There is a significant overlap of solution and processing parameters for the stable electrospinning of the pure polymers. Based hereon, a total polymer concentration of 13 wt% and a 70/30 AA/FA solvent system were chosen as a starting point for the blend electrospinning (tip-to-collector distance (TCD)) of 12.5 mm, flow rate of 1 mL·h⁻¹. This solvent choice minimizes the amount of FA, which minimizes degradation of PCL [5], while guaranteeing electrospinning of fine bead-free PCL and gelatin nanofibers.

As illustrated in Figure 1, the full range of PCL/Gt blend ratios is well electrospinnable using the chosen parameters. Indeed, uniform bead-free PCL/Gt nanofibers could be produced in a stable manner for all compositions. Although the conductivity of the electrospinning solution increases significantly, and the viscosity markedly drops with increasing gelatin content (Figure S1), no remarkable differences in nanofiber diameter were observed. Variations in total polymer concentration with a fixed polymer ratio, on the other hand, do affect fiber diameter. Electrospinning of a 50/50 PCL/Gt blend solution results in a stable process and bead-free nanofibers for polymer concentrations between 9 wt% and 17 wt%. Within this electrospinnable window, the nanofiber diameter could be tuned between 140 nm and 550 nm respectively (Figure 2). Blend electrospinning of PCL/Gt using the AA/FA solvent system is thus highly flexible, with both the PCL/Gt ratio and the fiber diameter adjustable to the end application.

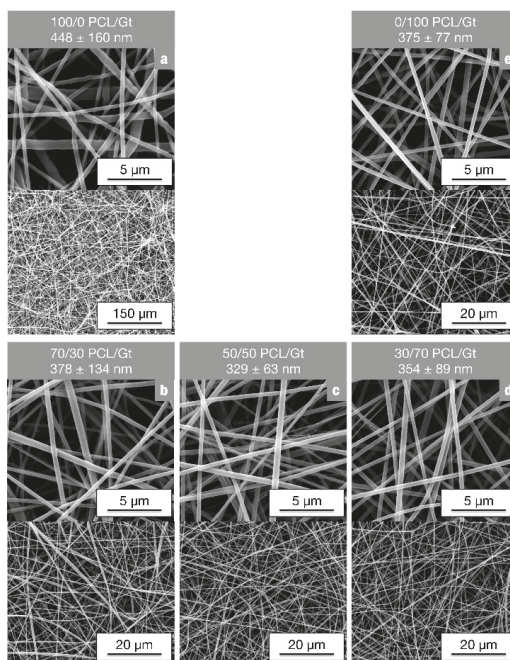


Figure 1. Scanning electron microscopy (SEM) images of PCL/Gt blend nanofibers electrospun using a total polymer concentration of 13 wt% and 70/30 AA/FA (TCD of 12.5 cm, flow rate of 1 mL·h⁻¹ and voltage adjusted in the range of 15–20 kV for stable electrospinning): (a) 100/0 PCL/Gt, (b) 70/30 PCL/Gt, (c) 50/50 PCL/Gt, (d) 30/70 PCL/Gt and (e) 0/100 PCL/Gt. All PCL/Gt blend ratios were well electrospinnable.

Although this clearly did not impede electrospinnability, all the PCL/Gt blend solutions were opaque due to a phase separation resulting in emulsions. The homogeneous emulsions gradually evolved toward two completely separated clear phases over the course of a few hours after complete

dissolution. Within this time frame, however, neither process stability nor fiber morphology were affected. Additionally, continued stirring of the emulsions makes stable electrospinning possible for much longer dwell times (no visible phase separation after 48 h).

PCL degrades significantly in the AA/FA solvent system with prolonged dwell times in solution [5]. Therefore, the polymer blend degradation was investigated for longer dwell times in solution through viscosity measurements (Figure S2). Although the reduction in solution viscosity is not as large as for pure PCL (about 40% after 48 h in 70/30 AA/FA), 50/50 PCL/Gt blends are also characterized by a decrease in viscosity with increasing dwell time in the acid solution (about 20% after 48 h in 70/30 AA/FA). This is probably mainly due to PCL degradation [20], resulting in slightly smaller fiber diameters (276 ± 67 nm after 3 h in solution vs. 233 ± 47 nm after 48 h in solution). Despite the small change in fiber morphology, process stability was not affected by PCL degradation. Using a continuously stirred PCL/Gt emulsion in 70/30 AA/FA, uniform bead-free nanofibrous membranes can thus be produced over the course of 48 h, with only a slight influence on fiber diameter.

As the electrospinning remains stable for a prolonged time, PCL/Gt blend electrospinning using the AA/FA solvent system was readily scalable to produce large nanofibrous membranes. Homogeneous nanofibrous membranes with a nominal size of 300×300 mm² were produced on a multinozzle setup. Their uniformity was validated by using SEM and FTIR analysis at several points throughout the membrane. No significant differences in fiber morphology or diameter were observed. Similarly, for all PCL/Gt blend ratios, FTIR spectra were identical within a single membrane, even though they were electrospun using emulsions. Pure PCL and pure gelatin are characterized by a few non-overlapping peaks in their FTIR spectra (Figure S3 and Table S1) [22,26,27]. Therefore, a qualitative indication of the PCL/Gt composition of the nanofibrous membranes is given by the ration of the carbonyl stretching peak of PCL and the amide I peak of gelatin. The 70/30 AA/FA solvent system thus allows for stable, reproducible, and scalable production of PCL/Gt blend nanofibers with high flexibility in fiber composition and diameter.

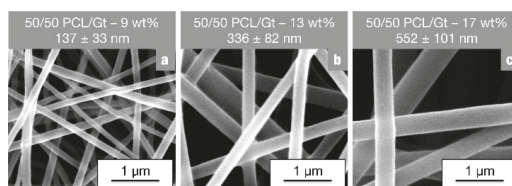


Figure 2. SEM images of 50/50 PCL/Gt blend nanofibers electrospun using 70/30 AA/FA (TCD of 12.5 cm, FR of $1 \text{ mL} \cdot \text{h}^{-1}$ and E adjusted for stable electrospinning) with a total polymer concentration of (a) 9 wt%, (b) 13 wt% and (c) 17 wt%. Varying the total polymer concentration significantly affects fiber diameters.

3.2. Stabilizing the Electrospinning Emulsions by Tuning the Solvent System

Water could be added to the electrospinning solutions up to 5 vol% without affecting solubility of the polymers. It stabilizes the solutions and hinders the phase separation of the PCL/Gt blends into two completely separated phase (the gelatin-rich phase settles at the bottom of the container without continued stirring). This makes electrospinning of bead-free PCL/Gt blend nanofibers possible for low gelatin concentrations without continued stirring (Figure 3b). Moreover, using a 70/25/5 AA/FA/water solvent system, the settling phenomenon can be prevented for gelatin concentrations up to 20 wt% of the total polymer mass. A similar effect has been reported by Feng et al., who illustrated that addition of a small amount of AA to a trifluoroethanol solution increases PCL-gelatin miscibility [22].

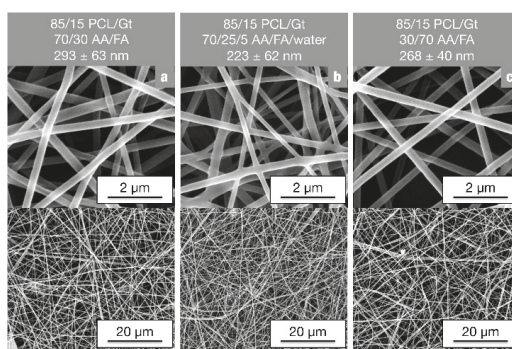


Figure 3. SEM images of 85/15 PCL/Gt nanofibers produced using a polymer concentration of 13 wt% but with differing solvent systems: (a) An emulsion unstable in time; (b) An emulsion stable in time, and; (c) A clear solution stable in time.

Alternatively, the effect of a changing the AA/FA solvent ratio was investigated. With an increasing FA concentration, miscibility is slightly improved. Although the gelatin-rich phase still settles on the bottom of the container when stirring is stopped, the PCL-rich upper phase contains more gelatin with decreasing AA/FA ratio of the solution. This is clearly illustrated by FTIR analysis of solution cast films of the upper and lower phase of an emulsion kept at rest (Figure 4). The gelatin peaks of the PCL-rich upper phase are much more pronounced when dissolved in 30/70 AA/FA ($A_{\text{PCL}}/A_{\text{Gt}} = 1.5$) than in 70/30 AA/FA ($A_{\text{PCL}}/A_{\text{Gt}} = 21.3$) (Figure 4 red curves, b vs. a), pointing to a higher gelatin concentration. Due to this higher miscibility in the PCL-rich phase, clear solutions stable in time were obtained for gelatin concentrations up to 30 wt% of the total polymer mass when using the 30/70 AA/FA solvent system. These clear and stable solutions were well electrospinnable, giving rise to bead-free nanofibers with reproducible diameters (Figure 3c). FTIR analysis of the obtained nanofibrous membranes, however, showed no differences in composition compared to the membranes electrospun using emulsions in 70/30 AA/FA (Figure S4). Consequently, the increased miscibility in 30/70 AA/FA does not affect nanofiber composition on the mm-scale.

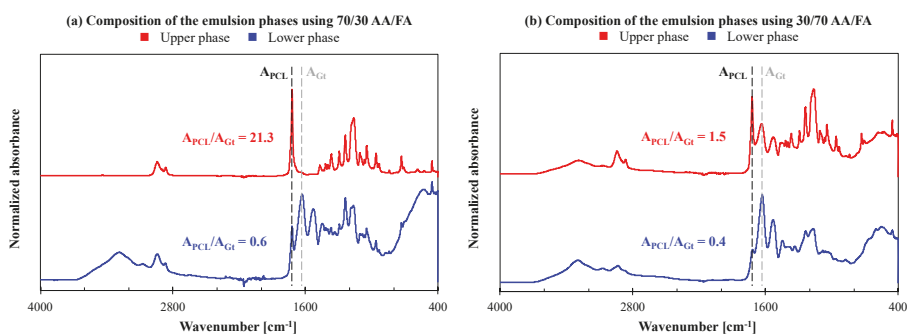


Figure 4. Normalized Attenuated Total Reflectance-Fourier-transform infrared spectroscopy (ATR-FTIR) spectra of films obtained by solution casting the upper (red) or lower (blue) phase, representing the continuous and dispersed phase respectively, of a PCL/Gt emulsion in (a) 70/30 AA/FA or (b) 30/70 AA/FA left at rest.

3.3. Interactions between the PCL and Gt Components by Thermal Analysis

The interactions and miscibility of polymer components in a blend often affect the thermal properties of the blend compared to their pure counterparts. Indeed, in a polymer blend containing a crystallizable component, a decrease in melting temperature and/or crystallinity is often observed; interaction between chains and chain segments of the blend components can cause a decrease in lamellar thickness of the crystals and/or a decrease in the amount of crystallizable material [28–31]. Additional to changes in melting behavior, also the glass transition is possibly affected by blending [28,32], with completely miscible polymer blends showing only one intermediate T_g . Therefore, the PCL/Gt blend nanofibers were analyzed using DSC and DMA and compared to the melting behavior and glass transition to pure PCL nanofibers.

While studying PCL/Gt blend nanofibers using DSC, care has to be taken when analyzing the PCL melting endotherm, since dissociation of gelatin triple helices occurs within the same temperature range [20]. However, the heat effect of this triple helix dissociation is far less than the melting enthalpy measured for pure PCL nanofibers, namely about $4 \text{ J}\cdot\text{g}^{-1}$ and about $70 \text{ J}\cdot\text{g}^{-1}$ respectively. The endothermic transition can thus mainly be attributed to the PCL component. As expected, DSC analysis of PCL/Gt blend nanofibers shows a clear decrease in overall melting enthalpy (Figure 5a). This decrease is in line with the decreasing PCL concentration. Indeed, recalculation of the overall melting enthalpy as a function of PCL mass results in values of about $70 \text{ J}\cdot\text{g}^{-1}$ for all samples (Table 1). The value for 15/85 PCL/Gt nanofibers is slightly higher, probably due to a more significant overlapping heat effect of the triple helix dissociation within the gelatin component and a larger error. Overall, however, the PCL melting enthalpy does not seem to be significantly decreased due to blending. Additionally, the melting trace showed a peak value (T_p) of $55 \pm 1 \text{ }^\circ\text{C}$ for all samples. These results indicate that blending of PCL with gelatin does not significantly affect the melting behavior of the PCL component and interaction between the components is thus low. This also confirms that the analyzed nanofibers contain the expected amount of PCL and gelatin, pointing to a homogeneous blend composition throughout the membranes. Similar results were obtained for all investigated solvent systems (70/30 AA/FA, 30/70 AA/FA and 70/25/5 AA/FA/water). Nanofiber composition, uniformity and PCL-gelatin interactions are thus not affected when electrospinning a clear solution compared to an emulsion. DMA analysis on 85/15 PCL/Gt blend nanofibers illustrated that the glass transition of PCL is hardly affected compared to pure PCL (Figure 5b). This again points to weak interactions and low miscibility between PCL and gelatin.

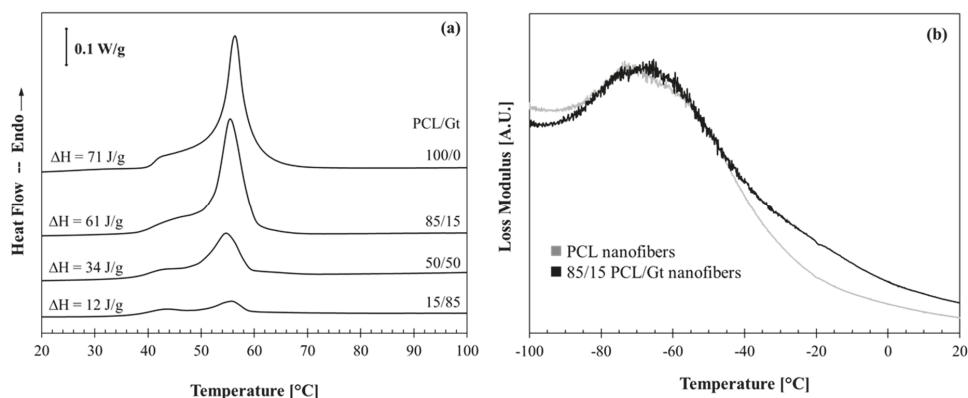


Figure 5. The effect of blending with gelatin, using a 70/30 AA/FA solvent system, on (a) the melting behavior and (b) the glass transition of PCL-based nanofibers measured by DSC at $2.5 \text{ K}\cdot\text{min}^{-1}$ and by DMA respectively.

Table 1. Melting enthalpy measured using DSC (Figure 5a), as a function of total polymer mass and recalculated as a function of PCL mass.

Nanofibrous Membranes	ΔH_m (Joules per Gram Fiber)	ΔH_m (Joules per Gram PCL)
PCL	71	71
85/15 PCL/Gt	61	72
50/50 PCL/Gt	29	68
15/85 PCL/Gt	12	80

3.4. Cold-Water Solubility of the Gelatin Component

As discussed in our previous paper, gelatin nanofibers are cold-water-soluble and dissolve to form a hydrogel in water at room temperature when they are not cross-linked [20]. Blending with PCL could affect this property. The 85/15 PCL/Gt nanofibers do not show significant changes in nanofiber morphology when submerged in cold water, suggesting the gelatin component to be not dissolved. With increasing gelatin concentration, however, a fiber-reinforced hydrogel is obtained, where gelatin partly gels but a nanofibrous network mainly consisting of PCL remains. Although water stability through cross-linking can easily be obtained [33], nanofiber-reinforced gelatin hydrogels could prove to be a promising biomedical material [34–36], combining a soft and elastic consistency while allowing for cell support on a nanofibrous membrane with increased porosity. To characterize the nanofibrous reinforcing structure and gain insight into the phase morphology of PCL/Gt nanofibers, the water-soluble gelatin fraction was removed using water of 35 °C.

All nanofibrous membranes having a PCL concentration of $\geq 50\%$ still showed structural integrity after water treatment. It was, therefore, possible to characterize them using SEM and FTIR (Figure 6 and Table 2). Additionally, the mass loss of the membranes was determined. Since the water treatment procedure does not affect pure PCL nanofibers (Figure 6a,e), this mass reduction can be attributed to a decrease in gelatin content, resulting in a new PCL/Gt ratio.

SEM analysis, the measured mass loss and FTIR analysis all clearly indicate that the rinsing procedure only has a minor influence on 85/15 PCL/Gt nanofibers. Indeed, fiber morphology before and after water treatment is comparable (Figure 6b,f), and the FTIR spectra were identical, resulting in similar A_{PCL}/A_{Gt} ratios (Table 2). A similar result was obtained for 85/15 PCL/Gt nanofibers electrospun using 30/70 AA/FA (clear solutions). The phase separation in the electrospinning solution thus only has a minor effect on the final PCL/Gt fiber morphology. Although PCL-gelatin interaction within the nanofibers is low according to our thermal analysis, the gelatin component no longer dissolves in water. This indicates that the gelatin-rich phase is finely dispersed throughout the nanofibers, so that the hydrophobicity of PCL prevents gelatin dissolution.

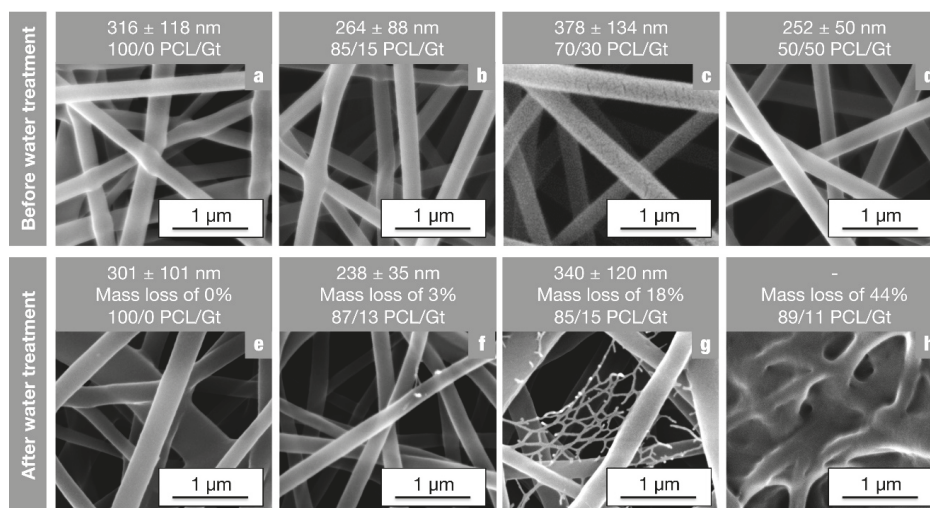


Figure 6. SEM images of PCL/Gt blend nanofibers (13 wt%, 70/30 AA/FA) with different PCL/Gt ratios (a–d) before and (e–h) after water treatment, i.e., rinsing with demineralized water at 35 °C. Mass loss is calculated by weighing the dried weight. Based on this mass loss of gelatin, a new PCL/Gt ratio was calculated for the rinsed samples.

Table 2. Composition of the nanofibrous membranes before and after water treatment, analyzed using the ratio of the carbonyl stretching peak of PCL and the amide I peak of gelatin measured using FTIR. After water treatment, the composition is comparable and reflecting a gelatin concentration of about 15 wt%.

Nanofibrous Membranes	A_{PCL}/A_{Gt} before Water Treatment	A_{PCL}/A_{Gt} after Water Treatment
85/15 PCL/Gt	4.9	5
70/30 PCL/Gt	2.3	4.7
50/50 PCL/Gt	0.9	3.1 *

* A slightly higher gelatin concentration is measured, probably due to the gelatin film covering the membrane, as demonstrated in Figure 6h.

With increasing gelatin content, there is a significant amount of gelatin dissolved by rinsing in demineralized water at 35 °C, as evidenced by the mass loss and the decreasing amide I peak of gelatin in the FTIR spectra (Figure 6 and Table 2 respectively). The influence on the fiber diameter; however, is only small, especially for 70/30 PCL/Gt nanofibers, and no porosity of individual nanofibers is observed (Figure 6g). Additionally, the new PCL/Gt ratio after extraction is about 85/15. It is, therefore, hypothesized that a 70/30 PCL/Gt nanofibrous membrane is built up by a mixture of PCL-rich and gelatin-rich nanofibers. The PCL-rich nanofibers within the membrane contain about 15 wt% of gelatin and are not affected by water treatment, similar to 85/15 PCL/Gt nanofibers. The gelatin-rich nanofibers are dissolved, possibly leaving some PCL residue upon rinsing (Figure 6g). Although there are clearly still intact nanofibers present in the 50/50 PCL/Gt nanofibrous membranes after water treatment, a gelatin film is observed in SEM analysis (Figure 6h). This indicates that the gelatin polypeptide chains are sufficiently immobilized by entanglements with the PCL component to prevent removal by dissolution. Moreover, the gelatin phase must be present more toward the shell of the nanofibers, causing film formation and a slightly higher A_{PCL}/A_{Gt} ratio in FTIR (Table 2).

These results indicate that PCL/Gt blend nanofibrous membranes have a high potential for advanced biomedical material design. On one hand, water-stable PCL/Gt blend nanofibrous

membranes can be produced for gelatin concentrations up to 15 wt%. On the other hand, for higher amounts of gelatin, cold-gelling when in contact with water is possible, giving rise to a nanostructured hydrogel that is physically reinforced by PCL nanofibers. The nanofibers in these nanostructured reinforced hydrogels consist of PCL-rich nanofibers that still contain a significant amount of gelatin (about 10 to 15 wt%).

4. Conclusions

In conclusion, the AA/FA-based solvent system allows for stable, reproducible, and scalable PCL/Gt blend electrospinning with high flexibility, this while the toxicity of the solvent system is significantly reduced compared to traditionally utilized solvents. Indeed, dissolution of PCL/Gt blends in 70/30 AA/FA yields well electrospinnable emulsions for the whole PCL/Gt composition range. Although these emulsions are subject to settling of the gelatin-rich phase, uniform bead-free nanofibers can easily be produced within a time frame of a few hours or by continued stirring of the electrospinning solution. Additionally, the resulting fiber diameter can be tuned by altering the total polymer concentration. Using 30/70 AA/FA, stable and clear electrospinning solutions are obtained for gelatin concentrations up to 30 wt% due to increased miscibility. Further augmentation of gelatin concentration results in phase separation with the formation of an unstable emulsion. For all PCL/Gt ratios, process stability is best, and toxicity is minimized using 70/30 AA/FA. For gelatin concentrations up to 20 wt%, substitution of 5 vol% acid with water stabilizes the emulsion for over 48 h, making electrospinning possible without continued stirring or compromising the lower toxicity of the solvent system.

The resulting PCL/Gt nanofibrous membranes are water-stable up to gelatin concentrations of 15 wt%, irrespective of the possible phase separation in the electrospinning solution used for production (emulsion vs. clear miscible solution). It is hypothesized that membranes containing a higher amount of gelatin are built up of a mixture of nanofibers mainly consisting of PCL (~85/15 PCL/Gt) and nanofibers mainly consisting of cold-water-soluble and cold-gelling gelatin. The PCL-gelatin interactions within the nanofibers were low, as blending did not seem to affect the glass transition or melting of the PCL component. If the original nanofibrous membrane contains a high amount of gelatin (>15 wt%), cold-gelling when in contact with water is possible, giving rise to a nanofiber-reinforced physical gelatin hydrogel. This novel combination of material properties could prove to be a promising material for biomedical applications.

Supplementary Materials: The following are available online at <http://www.mdpi.com/2079-4991/8/7/551/s1>. Figure S1. Viscosity and conductivity measurements of PCL/Gt blend electrospinning solutions, using the 70/30 AA/FA solvent system (a) as a function of the PCL/Gt ratio and (b) as a function of the total polymer concentration. Figure S2. Viscosity measurements of the electrospinning solutions (PCL and/or Gt dissolved in 70/30 AA/FA) with increasing dwell time show that PCL degrades substantially whereas the Gt component remains quite stable. Figure S3. ATR-FTIR spectra of pure PCL and pure Gt, showing their characteristic peaks. Figure S4. Normalized ATR-FTIR spectra of 85/15 PCL/Gt blend nanofibers electrospun using an emulsion (dissolution in 70/30 AA/FA) or a clear solution (dissolution in 30/70 AA/FA). Table S1. Characteristic peaks of a PCL pellet and Gt powder in ATR-FTIR, as indicated in Figure S3.

Author Contributions: Conceptualization, L.D., I.S., H.R. and K.D.C.; Data Curation, L.D. and I.S.; Funding acquisition, K.D.C.; Investigation, L.D., I.S., E.S. and C.G.; Methodology, L.D. and I.S.; Project administration, K.D.C.; Resources, H.R. and K.D.C.; Supervision, H.R. and K.D.C.; Visualization, L.D. and I.S.; Writing—original draft, I.S.; Writing—review and editing, L.D., H.R. and K.D.C.

Funding: This research was funded by the Agency for Innovation by Science and Technology of Flanders (IWT) grant number 111158 and 141344.

Acknowledgments: The authors thank Rousselot for providing the free gelatin samples.

Conflicts of Interest: The authors declare no conflict of interest.

References

1. Lim, E.-H.; Sardinha, J.P.; Myers, S. Nanotechnology Biomimetic Cartilage Regenerative Scaffolds. *Arch. Plast. Surg.* **2014**, *41*, 231–240. [[CrossRef](#)] [[PubMed](#)]
2. Kai, D.; Jin, G.; Prabhakaran, M.P.; Ramakrishna, S. Electrospun synthetic and natural nanofibers for regenerative medicine and stem cells. *Biotechnol. J.* **2013**, *8*, 59–72. [[CrossRef](#)] [[PubMed](#)]
3. Ng, K.W.; Achuth, H.N.; Moochhala, S.; Lim, T.C.; Huttmacher, D.W. In vivo evaluation of an ultra-thin polycaprolactone film as a wound dressing. *J. Biomater. Sci. Polym. Ed.* **2007**, *18*, 925–938. [[CrossRef](#)] [[PubMed](#)]
4. Bölgen, N.; Menceloğlu, Y.Z.; Acatay, K.; Vargel, I.; Pişkin, E. In vitro and in vivo degradation of non-woven materials made of poly(epsilon-caprolactone) nanofibers prepared by electrospinning under different conditions. *J. Biomater. Sci. Polym. Ed.* **2005**, *16*, 1537–1555. [[CrossRef](#)] [[PubMed](#)]
5. Van der Schueren, L.; De Schoenmaker, B.; Kalaoglu, Ö.I.; De Clerck, K. An alternative solvent system for the steady state electrospinning of polycaprolactone. *Eur. Polym. J.* **2011**, *47*, 1256–1263. [[CrossRef](#)]
6. Herrero-Herrero, M.; Gómez-Tejedor, J.A.; Vallés-Lluch, A. PLA/PCL electrospun membranes of tailored fibres diameter as drug delivery systems. *Eur. Polym. J.* **2018**, *99*, 445–455. [[CrossRef](#)]
7. Alves da Silva, M.L.; Martins, A.; Costa-Pinto, A.R.; Costa, P.; Faria, S.; Gomes, M.; Reis, R.L.; Neves, N.M. Cartilage tissue engineering using electrospun PCL Nanofiber Meshes and MSCs. *Biomacromolecules* **2010**, *11*, 3228–3236. [[CrossRef](#)] [[PubMed](#)]
8. Ren, K.; Wang, Y.; Sun, T.; Yue, W.; Zhang, H. Electrospun PCL/gelatin composite nanofiber structures for effective guided bone regeneration membranes. *Mater. Sci. Eng. C* **2017**, *78*, 324–332. [[CrossRef](#)] [[PubMed](#)]
9. Venugopal, J.; Zhang, Y.Z.; Ramakrishna, S. Fabrication of modified and functionalized polycaprolactone nanofibre scaffolds for vascular tissue engineering. *Nanotechnology* **2005**, *16*, 2138–2142. [[CrossRef](#)] [[PubMed](#)]
10. Stafiej, P.; Küng, F.; Thieme, D.; Czugala, M.; Kruse, F.E.; Schubert, D.W.; Fuchsluger, T.A. Adhesion and metabolic activity of human corneal cells on PCL based nanofiber matrices. *Mater. Sci. Eng. C* **2017**, *71*, 764–770. [[CrossRef](#)] [[PubMed](#)]
11. Bhattarai, N.; Li, Z.; Gunn, J.; Leung, M.; Cooper, A.; Edmondson, D.; Veisoh, O.; Chen, M.H.; Zhang, Y.; Ellenbogen, R.G.; et al. Natural-synthetic polyblend nanofibers for biomedical applications. *Adv. Mater.* **2009**, *21*, 2792–2797. [[CrossRef](#)]
12. Beachley, V.; Wen, X. Polymer nanofibrous structures: Fabrication, biofunctionalization, and cell interactions. *Prog. Polym. Sci.* **2010**, *35*, 868–892. [[CrossRef](#)] [[PubMed](#)]
13. Cipitria, A.; Skelton, A.; Dargaville, T.R.; Dalton, P.D.; Huttmacher, D.W. Design, fabrication and characterization of PCL electrospun scaffolds—A review. *J. Mater. Chem.* **2011**, *21*, 9419. [[CrossRef](#)]
14. Gunn, J.; Zhang, M. Polyblend nanofibers for biomedical applications: Perspectives and challenges. *Trends Biotechnol.* **2010**, *28*, 189–197. [[CrossRef](#)] [[PubMed](#)]
15. Schiffman, J.D.; Schauer, C.L. A review: Electrospinning of biopolymer nanofibers and their applications. *Polym. Rev.* **2008**, *48*, 317–352. [[CrossRef](#)]
16. Metcalfe, A.D.; Ferguson, M.W.J. Tissue engineering of replacement skin: The crossroads of biomaterials, wound healing, embryonic development, stem cells and regeneration. *J. R. Soc. Interface* **2007**, *4*, 413–437. [[CrossRef](#)] [[PubMed](#)]
17. Zhang, Y.Z.; Venugopal, J.; Huang, Z.M.; Lim, C.T.; Ramakrishna, S. Crosslinking of the electrospun gelatin nanofibers. *Polymer* **2006**, *47*, 2911–2917. [[CrossRef](#)]
18. Wu, S.-C.; Chang, W.-H.; Dong, G.-C.; Chen, K.-Y.; Chen, Y.-S.; Yao, C.-H. Cell adhesion and proliferation enhancement by gelatin nanofiber scaffolds. *J. Bioact. Compat. Polym.* **2011**, *26*, 565–577. [[CrossRef](#)]
19. Panzavolta, S.; Gioffrè, M.; Focarete, M.L.; Gualandi, C.; Foroni, L.; Bigi, A. Electrospun gelatin nanofibers: Optimization of genipin cross-linking to preserve fiber morphology after exposure to water. *Acta Biomater.* **2011**, *7*, 1702–1709. [[CrossRef](#)] [[PubMed](#)]
20. Steyaert, I.; Rahier, H.; Van Vlierberghe, S.; Olijve, J.; De Clerck, K. Gelatin nanofibers: Analysis of triple helix dissociation temperature and cold-water-solubility. *Food Hydrocoll.* **2016**, *57*, 200–208. [[CrossRef](#)]
21. Zhang, Y.; Ouyang, H.; Chwee, T.L.; Ramakrishna, S.; Huang, Z.M. Electrospinning of gelatin fibers and gelatin/PCL composite fibrous scaffolds. *J. Biomed. Mater. Res. B* **2005**, *72*, 156–165. [[CrossRef](#)] [[PubMed](#)]
22. Feng, B.; Tu, H.; Yuan, H.; Peng, H.; Zhang, Y. Acetic-acid-mediated miscibility toward electrospinning homogeneous composite nanofibers of GT/PCL. *Biomacromolecules* **2012**, *13*, 3917–3925. [[CrossRef](#)] [[PubMed](#)]

23. Prabhakaran, M.P.; Venugopal, J.R.; Chyan, T.T.; Hai, L.B.; Chan, C.K.; Lim, A.Y.; Ramakrishna, S. Electrospun biocomposite nanofibrous scaffolds for neural tissue engineering. *Tissue Eng. A* **2008**, *14*, 1787–1797. [[CrossRef](#)] [[PubMed](#)]
24. Daelemans, L.; van der Heijden, S.; De Baere, I.; Rahier, H.; Van Paepegem, W.; De Clerck, K. Nanofibre bridging as a toughening mechanism in carbon/epoxy composite laminates interleaved with electrospun polyamide nanofibrous veils. *Compos. Sci. Technol.* **2015**, *117*, 244–256. [[CrossRef](#)]
25. Daelemans, L.; van der Heijden, S.; De Baere, I.; Rahier, H.; Van Paepegem, W.; De Clerck, K. Using aligned nanofibres for identifying the toughening micromechanisms in nanofibre interleaved laminates. *Compos. Sci. Technol.* **2016**, *124*, 17–26. [[CrossRef](#)]
26. Zha, Z.; Teng, W.; Markle, V.; Dai, Z.; Wu, X. Fabrication of gelatin nanofibrous scaffolds using ethanol/phosphate buffer saline as a benign solvent. *Biopolymers* **2012**, *97*, 1026–1036. [[CrossRef](#)] [[PubMed](#)]
27. Ghasemi-Mobarakeh, L.; Prabhakaran, M.P.; Morshed, M.; Nasr-Esfahani, M.H.; Ramakrishna, S. Electrospun poly(ϵ -caprolactone)/gelatin nanofibrous scaffolds for nerve tissue engineering. *Biomaterials* **2008**, *29*, 4532–4539. [[CrossRef](#)] [[PubMed](#)]
28. Mathot, V.B.F. *Calorimetry and Thermal Analysis of Polymers*; Carl Hanser Verlag: München, Germany, 1994.
29. Senda, T.; He, Y.; Inoue, Y. Biodegradable blends of poly(ϵ -caprolactone) with alpha-chitin and chitosan: Specific interactions, thermal properties and crystallization behavior. *Polym. Int.* **2002**, *51*, 33–39. [[CrossRef](#)]
30. Mano, F.; Alves, M.; Azevedo, J.V. Development of new poly(ϵ -caprolactone)/chitosan films. *Polym. Int.* **2013**, *62*, 1425–1432. [[CrossRef](#)]
31. Sarasam, A.; Madihally, S.V. Characterization of chitosan-polycaprolactone blends for tissue engineering applications. *Biomaterials* **2005**, *26*, 5500–5508. [[CrossRef](#)] [[PubMed](#)]
32. Young, R.J.; Lovell, P.A. *Introduction to Polymers*, 3rd ed.; CRC Press: Boca Raton, FL, USA, 2011.
33. Pereira, I.H.L.; Ayres, E.; Averous, L.; Schlatter, G.; Hebraud, A.; De Paula, A.C.C.; Viana, P.H.L.; Goes, A.M.; Oréfice, R.L. Differentiation of human adipose-derived stem cells seeded on mineralized electrospun co-axial poly(ϵ -caprolactone) (PCL)/gelatin nanofibers. *J. Mater. Sci. Mater. Med.* **2014**, *25*, 1137–1148. [[CrossRef](#)] [[PubMed](#)]
34. Tonsomboon, K.; Oyen, M.L. Composite electrospun gelatin fiber-alginate gel scaffolds for mechanically robust tissue engineered cornea. *J. Mech. Behav. Biomed. Mater.* **2013**, *21*, 185–194. [[CrossRef](#)] [[PubMed](#)]
35. Jaiswal, M.; Gupta, A.; Dinda, A.K.; Koul, V. An investigation study of gelatin release from semi-interpenetrating polymeric network hydrogel patch for excision wound healing on Wistar rat model. *J. Appl. Polym. Sci.* **2015**, *132*, 25. [[CrossRef](#)]
36. Shi, J.; Wang, L.; Zhang, F.; Li, H.; Lei, L.; Liu, L.; Chen, Y. Incorporating protein gradient into electrospun nanofibers as scaffolds for tissue engineering. *ACS Appl. Mater. Interfaces* **2010**, *2*, 1025–1030. [[CrossRef](#)] [[PubMed](#)]



© 2018 by the authors. Licensee MDPI, Basel, Switzerland. This article is an open access article distributed under the terms and conditions of the Creative Commons Attribution (CC BY) license (<http://creativecommons.org/licenses/by/4.0/>).



Article

Fabrication of Sericin/Agrose Gel Loaded Lysozyme and Its Potential in Wound Dressing Application

Meirong Yang¹, Yejing Wang^{1,2,*}, Gang Tao¹, Rui Cai², Peng Wang², Liying Liu¹, Lisha Ai¹, Hua Zuo³, Ping Zhao^{1,4}, Ahmad Umar⁵, Chuanbin Mao^{6,7} and Huawei He^{1,4,*}

¹ State Key Laboratory of Silkworm Genome Biology, Southwest University, Beibei, Chongqing 400715, China; yangmeirong@email.swu.edu.cn (M.Y.); taogang@email.swu.edu.cn (G.T.); 13341345@email.swu.edu.cn (L.L.); als123@email.swu.edu.cn (L.A.); zhaop@swu.edu.cn (P.Z.)

² College of Biotechnology, Southwest University, Beibei, Chongqing 400715, China; cairui0330@email.swu.edu.cn (R.C.); modelsums@email.swu.edu.cn (P.W.)

³ College of Pharmaceutical Sciences, Southwest University, Beibei, Chongqing 400715, China; zuohua@swu.edu.cn

⁴ Chongqing Engineering and Technology Research Center for Novel Silk Materials, Southwest University, Beibei, Chongqing 400715, China

⁵ Department of Chemistry, College of Science and Arts and Promising Centre for Sensors and Electronics Devices (PCSED), Najran University, P.O. Box 1988, Najran 11001, Saudi Arabia; umahmad@nu.edu.sa

⁶ Department of Chemistry & Biochemistry, Stephenson Life Science Research Center, University of Oklahoma, 101 Stephenson Parkway, Norman, OK 73019, USA; cbmao@ou.edu

⁷ School of Materials Science and Engineering, Zhejiang University, Hangzhou 310027, China

* Correspondence: yjwang@swu.edu.cn (Y.W.); hehuawei@swu.edu.cn (H.H.); Tel.: +86-23-6825-1575 (H.H.)

Received: 6 March 2018; Accepted: 4 April 2018; Published: 13 April 2018



Abstract: Sericin is a biomaterial resource for its significant biodegradability, biocompatibility, hydrophilicity, and reactivity. Designing a material with superabsorbent, antiseptic, and non-cytotoxic wound dressing properties is advantageous to reduce wound infection and promote wound healing. Herein, we propose an environment-friendly strategy to obtain an interpenetrating polymer network gel through blending sericin and agarose and freeze-drying. The physicochemical characterizations of the sericin/agarose gel including morphology, porosity, swelling behavior, crystallinity, secondary structure, and thermal property were well characterized. Subsequently, the lysozyme loaded sericin/agarose composite gel was successfully prepared by the solution impregnation method. To evaluate the potential of the lysozyme loaded sericin/agarose gel in wound dressing application, we analyzed the lysozyme loading and release, antimicrobial activity, and cytocompatibility of the resulting gel. The results showed the lysozyme loaded composite gel had high porosity, excellent water absorption property, and good antimicrobial activities against *Escherichia coli* and *Staphylococcus aureus*. Also, the lysozyme loaded gel showed excellent cytocompatibility on NIH3T3 and HEK293 cells. So, the lysozyme loaded sericin/agarose gel is a potential alternative biomaterial for wound dressing.

Keywords: silk sericin; agarose; lysozyme; composite gel; wound dressing

1. Introduction

Non-healing skin wounds exposed to bacterial infections are biologically characterized by lengthening inflammation, interfering re-epithelialization, disturbing collagen production, and finally delaying wound healing [1]. In wound care, wound dressing is an important biomedical material used to protect the wound from infection and facilitate wound healing [2]. Accompanied by the growing number of chronic diseases, the wound dressing market is evolving rapidly in the present healthcare

system worldwide [3]. The ideal wound dressing should absorb wound exudate in a manner, allow gas exchange and maintain necessary moisture at wound interface without cytotoxicity and allergenic response [4]. Besides, it can promote wound healing by creating a suitable microenvironment to prevent bacterial infection and promote cell adhesion and proper proliferation [5]. Among all wound dressing materials, hydrogel is an attractive alternative in traditional therapeutic approaches for its multifunctional abilities such as hydrophilicity, swelling, drug delivery, and in situ gelling capacity [6].

Sericin (SS) is one of the major protein components of silk, which is discarded as a waste during the degumming process in the textile industry [7]. Sericin is a natural protein, exhibiting immense potential in the field of biomaterial owing to its biodegradability, easy availability, and hydrophilicity [8]. Sericin has numerous biological activities such as anti-oxidation, anti-bacterium, and anti-coagulation, promoting cell growth and differentiation [9]. However, sericin is physically fragile and highly soluble due to its amorphous nature [10], which is unsuitable for biomedical applications. Hence, in order to obtain desired material with improved properties for regenerative medicine application, sericin is mostly designed to copolymerize, crosslink, or blend with other polymers as it has polar side chains with diverse functional groups, such as amine, hydroxyl, and carboxyl groups [11–15]. Agarose (AR) is a transparent, neutrally charged, and thermo-reversible natural polysaccharide [16]. Agarose is used extensively in vitro cartilage tissue engineering as it provides a superior foundation for chondrogenesis and higher glycosaminoglycan deposition to produce constructs with functional properties approaching those of native articular cartilage [17,18]. Additionally, agarose gel is considered as a biological scaffold material for the central nervous system repair and regeneration due to its excellent mechanical properties which can well match the growth and control of nerve axis, the porous structure which is conducive to nutrient delivery, and the implant which does not cause adverse reactions [19]. However, agarose shows low cell adhesiveness and cell proliferation activity in vivo [20]. Therefore, blending agarose with other polymers such as chitosan and gelatin to overcome the valid drawbacks has escalated in recent years [21,22]. Consequently, the present study brought together the innate advantages of sericin and agarose to fabricate a blended hydrogel for prospective application in a wound dressing.

Nevertheless, the hydrogel is limited as a wound dressing material because it may paradoxically provide a preferred environment for infectious bacteria. To prevent bacterial infection on both skin wound and dressing material, antibiotics such as penicillin and methicillin have been widely used. However, the widespread and indiscriminate use of antibiotics now constitutes a major health concern worldwide due to the emergence of numerous resistant pathogens [23]. Therefore, tremendous attention has been paid to the discovery and development of alternative novel antibiotics, particularly with new modes of action to overcome the resistance. Lysozyme is a natural antibacterial agent that has been isolated from the cells and secretions of virtually all the living organisms [24]. Lysozyme plays the role of the anti-microbial agent through catalyzing the hydrolysis of β -1,4 glycosidic bonds between N-acetylmuramic acid and N-acetylglucosamine in peptidoglycans of the bacterial cell wall [25]. It is commercially available at low cost, and classified as GRAS grade by the Food and Drug Administration (FDA, US) and as a food additive by the European Union (E 1105) [26]. Lysozyme has been extensively applied as antibacterial agents in wound dressing and protein separation [27]. Accordingly, the development of lysozyme-based antimicrobial material is significantly important toward an environmentally benign antimicrobial field.

We herein developed an improved lysozyme (LZM) loaded sericin/agarose (SS/AR) gel (SS/AR/LZM). Scanning Electronic Microscopy (SEM), Attenuated Total Reflection Fourier Transform Infrared Spectroscopy (ATR-FTIR), X-ray Diffraction (XRD), Thermogravimetric Analysis (TGA), and swelling behavior test were performed to characterize the physicochemical properties of SS/AR gel. We successfully fabricated lysozyme loaded SS/AR composite biomaterials by solution impregnation method. We investigated the lysozyme loading and release, the antimicrobial activity of SS/AR/LZM gel against typical Gram negative/positive bacteria *Escherichia coli* (*E. coli*) and *Staphylococcus aureus* (*S. aureus*). In addition, the cytotoxicity of the lysozyme loaded SS/AR gel was evaluated on NIH3T3

and HEK293 cells. The results suggested that the SS/AR/LZM gel with antimicrobial activity and cytocompatibility has a great potential in wound dressing application.

2. Materials and Methods

2.1. Materials

Bombyx mori cocoons were provided by the State Key Laboratory of Silkworm Genome Biology, Southwest University (China, 400716). Lysozyme (20,000 U/mg) was obtained from Sangon Biotech Co. Ltd. (Shanghai, China). Agarose G-10 was purchased from Biowest (Nuaille, France). Cell counting kit-8 (CCK-8) was from Beyotime (Beijing, China). LIVE/DEAD cell viability kit was from Thermo Fisher Scientific (Waltham, MA, USA). NIH3T3 (mouse embryonic fibroblast) and HEK293 (human embryonic kidney) cell lines were obtained from China Infrastructure of Cell Line Resources. Chemicals for cell culture such as Dulbecco's modified Eagle's medium (DMEM), Fetal Bovine Serum (FBS), Trypsin-EDTA and Penicillin/Streptomycin were from Gibco BRL (Gaithersburg, MD, USA). Ultrapure water was the product of Milli-Q Plus system from Millipore (Billerica, MA, USA). All other chemicals utilized were of analytical grade.

2.2. Fabrication of SS/AR Gel

Sericin was extracted from *Bombyx mori* cocoons as previous reports [28,29]. Briefly, silkworm cocoons were cut into pieces and autoclaved at 121 °C for 30 min to obtain sericin solution. Subsequently, sericin solution was freeze-drying to become sericin powder, and then dissolved in hot water. Sericin and agarose solution (2%, *w/v*) were mixed gently, and allowed to gel after casting into 24-well cell culture plates. These stable hydrogels were then frozen at −80 °C for 12 h followed by lyophilization for 24 h to become gels. According to the volume ratios of sericin and agarose solution, the corresponding SS/AR gels were termed as S100A0, S75A25, S50A50, S25A75, and S0A100, respectively.

2.3. Characterization of SS/AR Gel

SEM observation was performed on JSM-5610LV (Tokyo, Japan) with working voltage of 25 kV to examine the surface morphologies of the gel. The porosities of SS/AR gels were calculated according to the liquid displacement method [30]. Briefly, SS/AR gel was immersed into water (V_1) in a graduated cylinder, the total volume including water and SS/AR gel was recorded as V_2 . The SS/AR gel was then removed from the cylinder and the residual water volume was recorded as V_3 . The porosity (p) of SS/AR gel was calculated using the following equation:

$$p = (V_1 - V_3)/(V_2 - V_3) \times 100\%. \quad (1)$$

ATR-FTIR spectra of sericin and SS/AR gel were determined in the wavenumber range of 650–4000 cm^{-1} at a resolution of 4 cm^{-1} on a Nicolet iz10 Infrared spectrophotometer from Thermo Fisher Scientific (Waltham, MA, USA). XRD of sericin and SS/AR gel were carried out by X'Pert powder X-ray diffraction system (PANalytical, Almelo, OV, Netherland) within a 2θ range of 10°–70°. The thermal behaviors of sericin and SS/AR gel were analyzed by a thermogravimetric analyzer TGA-Q50 (TA instruments, New Castle, DE, USA) under a nitrogen flow of 20 mL/min [31]. The specimens were heated from room temperature to 600 °C, at a heating rate of 10 °C/min.

2.4. Swelling Behavior

The swelling ability of the SS/AR gel was analyzed using a conventional gravimetric method [32]. Briefly, a pre-weighed dry gel (W_d) was immersed into water at 37 °C for 30 min to achieve equilibrium. The swollen weight of gel was recorded as W_s at specific time intervals. The experiment was repeated

for three times under the same conditions. Swelling ratios (S) were determined as the following equation:

$$S = (W_s - W_d) / W_d \times 100\% \quad (2)$$

2.5. Preparation of SS/AR/LZM Gel

To prepare the lysozyme loaded SS/AR gel, S50A50 was cut into a circular piece with a diameter of 1.5 cm and then immersed into lysozyme solution (20–75 mg/mL) for 16 h. Subsequently, the lysozyme loaded SS/AR gel was removed from lysozyme solution and freeze-dried. According to the lysozyme concentration, the resulting SS/AR/LZM gels were termed as S50A50L20, S50A50L50 and S50A50L75, respectively.

2.6. The Loading and Release of Lysozyme

Lysozyme has a specific absorption peak at 280 nm [33], which could be used to measure the loaded and released lysozyme concentration. Ultraviolet visible spectrophotometer was employed to analyze the loading and release of lysozyme. The loaded lysozyme content was determined by the difference of lysozyme concentration before and after the treatment. The circular SS/AR/LZM gel with a diameter of 1.5 cm was dispensed into a centrifuge tube containing 4 mL of 0.01 M PBS (pH 7.4) buffer at 37 °C. At special time points, an aliquot (1 mL) PBS buffer was collected to measure the absorbance at 280 nm to determine the released lysozyme contents. Then the gel was transferred into 4 mL fresh PBS solution for the next measurement. The cumulative release rate was determined according to the ratio of the released and loaded lysozyme. Various lysozyme concentrations (0.1–0.6 mg/mL) were prepared for the calibration curve. All experiments were performed in triplicate.

2.7. In Vitro Antibacterial Assay

The antibacterial activity was evaluated according to the previous procedures with a slight modification [34,35]. SS/AR and SS/AR/LZM gels were cut pieces with 1 mm in thick and 1.5 cm in diameter, subsequently sterilized with UV radiation for 30 min. *E. coli* and *S. aureus* were grown in Luria–Bertani (LB) media at 37 °C with continuous shaking until the optical density at 600 nm (OD₆₀₀) reached about 1.5. Bacteria (500 µL) were harvested by centrifugation at 1000 rpm for 5 min followed by washing with 0.01 M phosphate buffer saline (PBS, pH 7.4). Subsequently, bacteria were re-suspended and diluted with PBS buffer. Next, 50 µL of the diluted bacterial suspension was cultured at 37 °C for 2 h in the presence of SS/AR gel or SS/AR/LZM gel. Aliquots (1 µL) of the mixture were diluted (1:10,000) in PBS, and then manually spread on LB agar plates. After 16 h incubation at 37 °C, the units of colony formation in each agar plate were counted to check the antibacterial ability of the gels. Each independent experiment was performed in triplicate.

2.8. Cytocompatibility Assay

NIH3T3 and HEK293 cells were cultured in high glucose DMEM supplemented with 10% FBS and 1% penicillin/streptomycin in a humidified atmosphere of 95% and 5% CO₂ at 37 °C. To check the cell viability, NIH3T3 and HEK293 cells (100 µL) were loaded at the density of 1×10^4 cells/well in 96-well plates and incubated 12 h at 37 °C. SS/AR or SS/AR/LZM gel was sterilized by ultraviolet radiation overnight and then added to the cell plates. Non-treated cells were used as a control.

After treated with the gels for 12 h, 24 h and 36 h, CCK-8 assay was used to assess cell viability according to the manufacturer's instructions. CCK-8 solution (10 µL) was added into each well and then incubated at 37 °C for 1.5 h. The optical density (OD) of each well was measured at 450 nm on a microplate reader TECAN (Mannedorf, Switzerland). The cell viability is defined as the percentage of OD value of the treated and control wells. For each experiment, at least three samples were evaluated. The morphologies of NIH3T3 and HEK293 cells after incubation for 24 h in the absence and presence of SS/AR or SS/AR/LZM gel were observed on a fluorescence microscope EVOS FL Auto Cell Imaging System (Life, Bothell, WA, USA).

Additionally, LIVE/DEAD staining assay was carried out to further assess the effects of the gels on the cells viability. NIH3T3 and HEK293 cells were cultured and incubated at 37 °C as described above. The cells after treated with SS/AR or SS/AR/LZM gel for 24 h were incubated with staining solution at 37 °C for 15 min. Then the images were collected on EVOS FL Auto Cell Imaging System. For each sample, the experiment was done in triplicate.

3. Results and Discussion

3.1. Preparation of SS/AR/LZM Gel

In this study, we prepared the SS/AR/LZM gel with good antibacterial activity and cytocompatibility, as illustrated in Figure 1. Sericin and agarose solution were mixed and then freeze-dried to become a porous gel. Thereafter, lysozyme, a natural antimicrobial agent, was loaded into the SS/AR gel. As sericin is negatively charged, agarose is neutral, whereas lysozyme is positively charged, thus the adsorption of lysozyme into the SS/AR gel may be attributed to the electrostatic interactions between the opposite charges of sericin and lysozyme [36]. Also, the physical adsorption caused by free diffusion could promote the adsorption of lysozyme. In addition, lysozyme has carboxyl group, amino groups and four disulfide bonds [37], and sericin has hydroxyl, carboxyl, and amino groups [38]. The special hydrophilic/hydrophobic interactions between lysozyme and sericin are also able to enhance the adsorption of lysozyme. The resulting SS/AR/LZM gel with interconnected porous structures, high swelling ability, good antibacterial activity and cytocompatibility may be a prospective alternative for wound dressing.

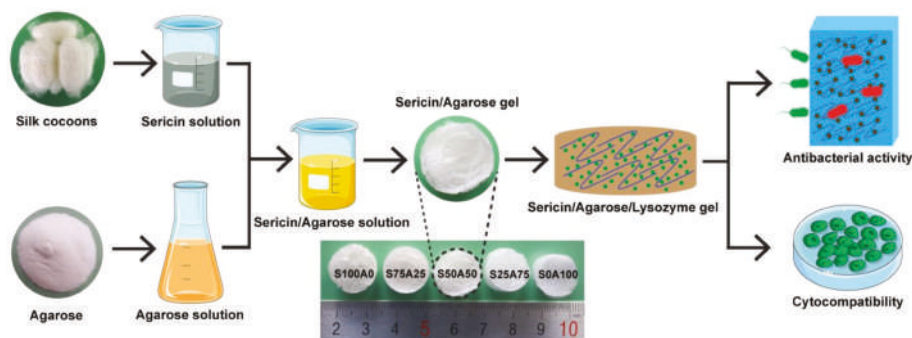


Figure 1. Schematic illustration of the fabrication of sericin (SS)/agarose (AR)/lysozyme (LZM) gel.

3.2. Morphology of SS/AR Gel

Porous materials provide space for cell growth and proliferation, and the microenvironment for the retention and release of bioactive molecules [39]. Furthermore, the porous structure affects the supply of nutrients and oxygen, and the removal of wastes [40], which is of utmost importance to wound dressing. In this study, the prepared gels had macro-porous “open-cell” structures (Figure 2A–D). The porosity of S75A25, S50A50, S25A75, and S0A100 gels were 53.17%, 49.54%, 46.17% and 59.75%, respectively (Figure 2E). Compared to other gels, S50A50 and S25A75 gels had significantly bigger pore sizes. This may be the fact that S50A50 and S25A75 gels could adsorb more water. After lyophilization, the space water occupied resulted in the formation of pores. Consequently, the pore size and porosity of gels were dependent on the ratio of sericin and agarose solution.

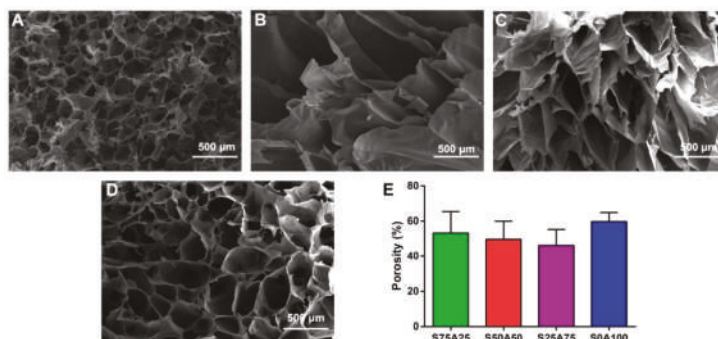


Figure 2. The porous microstructures of S75A25 (A), S50A50 (B), S25A75 (C), and S0A100 (D) gels. The porosity of gels with different ratios of sericin and agarose (E).

3.3. Characterization of SS/AR Gel

ATR-FTIR was employed to analyze the chemical interactions between sericin and agarose as ATR technique can probe to only a shallow depth and thus emphasize any surface coatings [41]. Sericin has a typical spectrum with distinctive peaks at $1600\text{--}1700\text{ cm}^{-1}$ (amide I, C=O stretching vibration), $1480\text{--}1575\text{ cm}^{-1}$ (amide II, N-H bending vibration), and $1229\text{--}1301\text{ cm}^{-1}$ (amide III) [42]. As shown in Figure 3A, sericin gel had characteristic peaks at 1621 cm^{-1} , 1521 cm^{-1} , and 1241 cm^{-1} , corresponding to amide I, amide II, and amide III, respectively. Pure agarose exhibited its characteristic peaks at 1068 cm^{-1} (C-O, axial deformation), 930 cm^{-1} (3, 6-anhydro-galactose), and 891 cm^{-1} (C-H, angular deformation of β anomeric carbon), the result was consistent with the previous study [43]. In the blended gels, the characteristic peaks of both agarose and sericin were recorded, which confirmed the presence of both components. Some slight shifts in amide I and amide II peaks, and the differences in the intensity of peaks were observed in case of the composite gels, which indicated that the backbone structures of sericin and agarose did not change. Lysozyme has characteristic peaks at 3295 cm^{-1} (NAH stretching of the free amino groups), and 2961 cm^{-1} (CAH stretching) as well as amide I ($1600\text{--}1700\text{ cm}^{-1}$), amide II ($1500\text{--}1600\text{ cm}^{-1}$) and amide III ($1230\text{--}1320\text{ cm}^{-1}$) [44]. Few peaks were found to overlap with the peaks of sericin.

The crystalline structure of the composite was analyzed by XRD. Silk protein has main diffraction peaks of Silk I ($2\theta = 12.2^\circ$ and 28.2°), and Silk II ($2\theta = 18.9^\circ$ and 20.7°) [45]. Similar XRD patterns of sericin with peaks at $2\theta = 19.2^\circ$ and 21.15° have been reported [46–49]. Sericin and SS/AR gel exhibited obvious diffraction peaks at 19.08° and 19.56° , respectively (Figure 3B), which indicated the existence of sericin in the SS/AR gel. The difference of 2θ between sericin and SS/AR gel reflect the conversion of the random coil to β -sheet structure for the presence of the intermolecular hydrogen bond in sericin [50].

The thermal stability of sericin and SS/AR gel were examined by TGA. Sericin and SS/AR gel underwent three stages of thermal degradation including dehydration, depolymerization, and decomposition (Figure 3C). The first stage was from room temperature to around 110°C , where the mass loss revealed the removal of adsorbed water molecules in sericin and SS/AR gel. The second major decomposition was attributed to the degradation of sericin and agarose occurred in the temperature range of $120\text{--}410^\circ\text{C}$. At this stage, the mass loss of SS/AR gel was faster than that of sericin, indicating that sericin could improve the thermal stability of the composite gels and delay the thermal degradation process. At the last stage, the mass loss occurred from 420°C to 600°C , which was associated with the breakdown of sericin and agarose.

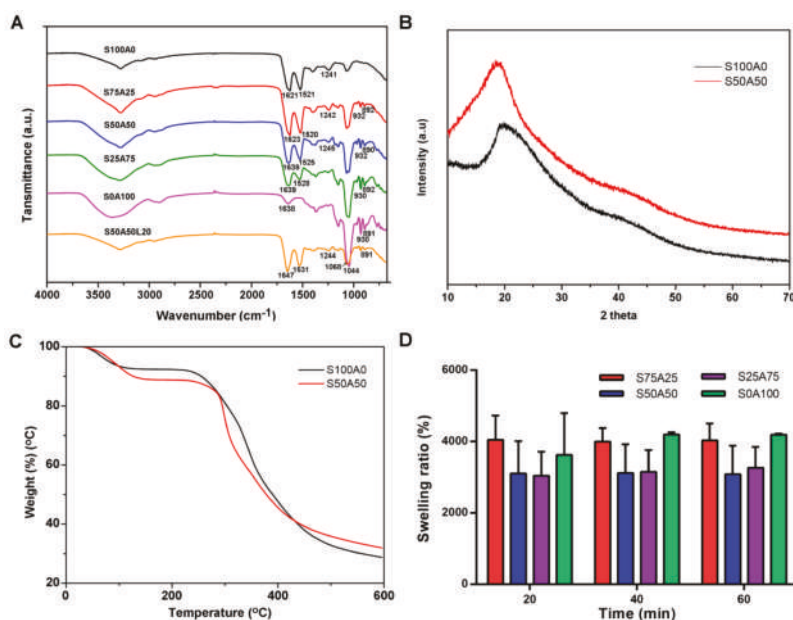


Figure 3. Characterizations of SS/AR gels. (A) Attenuated Total Reflection Fourier Transform Infrared Spectroscopy (ATR-FTIR); (B) X-Ray Diffraction (XRD); (C) Thermogravimetric Analysis (TGA); and (D) swelling ratio.

3.4. Swelling Behavior

Swelling ratio is a vital property to illustrate the uptake of liquids in wound dressing. The swelling ratio of various SS/AR gels were shown in Figure 3D. The results showed that all samples exhibited good swelling behavior. After 60 min, S75A25 and S0A100 gels had the swelling ratios of 3628–4196%, whereas S50A50 and S25A75 had the swelling ratios of 3040–3262%. The swelling ratios of S75A25 and S0A100 gels were higher than those of S50A50 and S25A75 as they had smaller pore size and higher porosities. The swelling of the gels had two stages, including the growing period and equilibrium period. In the initial 20 min, the swelling ratios of all samples increased quickly, indicating the excellent hydrophilicity of the composite gels. Thereafter, all gels quickly reached the swelling equilibrium.

The SS/AR gels with various ratios had a honeycomb structure, high porosity as well as excellent swelling capacity. In this study, we purposed to develop an alternative wound dressing through bringing together the innate advantages of sericin and agarose. High content of sericin will reduce the mechanical property of the gel, and high content of agarose may affect the cell adhesion and proliferation. Hence, we suggested the SS/AR gel with a ratio of 50:50 (S50A50) had moderate mechanical property and cytocompatibility, which may be suitable for wound dressing. The S50A50 gel was chosen for the further experiments.

3.5. Lysozyme Release

To avoid frequent replacement of the dressing and reduce the risk of overexposing wound to bacteria, a wound dressing should have a controllable drug release ability [51,52]. The loaded lysozyme contents of S50A50L20 and S50A50L50 gels were 24.94 mg and 50.78 mg, respectively (Figure 4A). And the loading efficiency of lysozyme was 62% and 51% for S50A50L20 and S50A50L50 gels, respectively (Figure 4B). Increasing lysozyme solution concentration could increase the loaded lysozyme contents, however, reduce its loading efficiency. To assess lysozyme release, we analyzed the

correlation between lysozyme concentration and UV absorption by the standard curve. The results showed that UV absorption was tightly correlated with lysozyme concentration (Figure 4C). Obviously, lysozyme could be released from both S50A50L20 and S50A50L50 gels. Lysozyme release could be divided into burst stage and steady stage (Figure 4D). During the initial burst phase, the release rate was relatively high. This effect is associated with the diffusion of water molecules and desorption of lysozyme close to the surface of the gel [53]. At the steady phase, lysozyme was gradually released from SS/AR/LZM gels up to 60 h. The cumulative release of S50A50L20 and S50A50L50 gels reached 74% and 86% at 3 h, respectively. After 60 h, the cumulative release reached 98% and 99%, indicating lysozyme was almost entirely released from the composite gels. The results suggested that the SS/AR/LZM gel had a sustainable lysozyme releasing ability, which is required for a wound dressing.

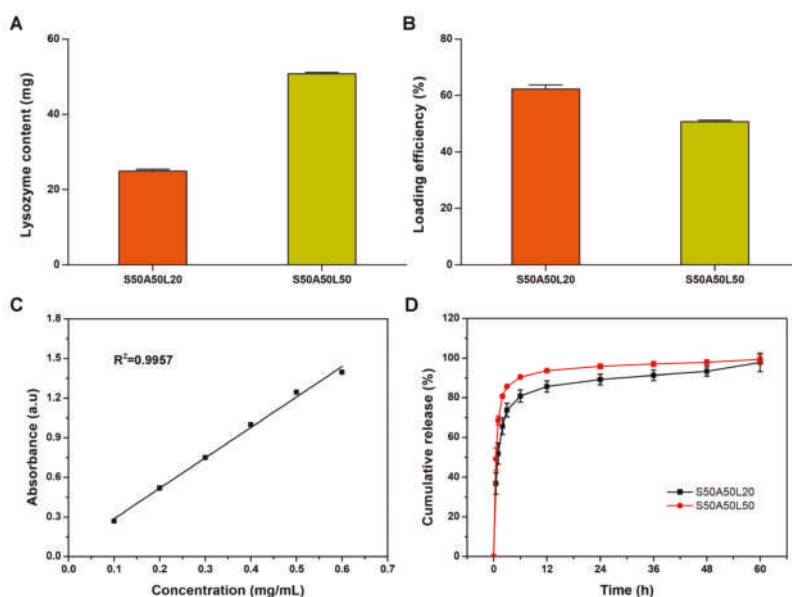


Figure 4. The loading and release of lysozyme. (A) Lysozyme contents loaded on SS/AR gel; (B) loading efficiency; (C) standard curves of UV intensity and lysozyme concentration; and (D) the cumulative release of lysozyme.

3.6. Antibacterial Activity

The antibacterial activity of the composite gels toward *E. coli* and *S. aureus* were shown in Figure 5A. Compared to the control, the total colonies number in the presence of SS/AR/LZM gels significantly decreased, indicating the SS/AR/LZM gel had good antibacterial activity. The S50A50L20 and S50A50L50 gels exhibited the bacteria reduction rates of 76%/87% and 84%/95% toward *E. coli*, *S. aureus*, respectively. The S50A50L75 gel completely inhibited the growth of the bacteria both for *E. coli* and *S. aureus*, suggesting increasing lysozyme solution concentration can improve the bactericidal ability of the composite gel as it increased the loaded and released lysozyme contents.

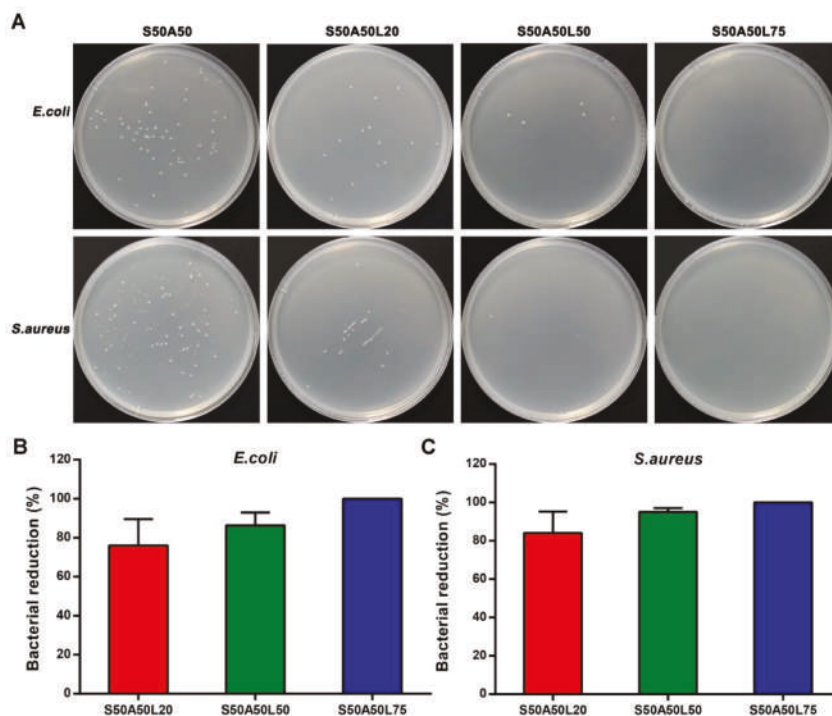


Figure 5. Antibacterial activities of SS/AR/LZM gels against *E. coli* and *S. aureus*. (A) Total bacterial colonies counting; (B, C) Bacterial colonies reduction rate.

Lysozyme is a natural antibacterial agent. Its antibacterial activity is mild compared with inorganic and organic antibacterial agents. To improve the antibacterial effect of lysozyme, some strategies such as physical and chemical modifications or synergistic action with other substances have been developed in recent years [26,54–56]. In this study, the SS/AR/LZM gels for antibacterial test had a dimension of 1 mm in thickness and 1.5 cm in diameter. The size and thickness determined the low loading content of lysozyme. In addition, the bacterial suspension volume affected the release efficiency of lysozyme from the gels. Therefore, SS/AR/LZM gels exhibited expected antibacterial effect; however, the loading content and the release efficiency of lysozyme determined its antibacterial activity.

Various antimicrobial materials have been developed for wound dressing application, such as metals/metal oxides [57], antibiotics [58], and peptides [2]. These materials are associated with a big concern about adverse effects on ecosystems. For instance, silver nanoparticle, one of the most classical and important materials, exert an adverse effect on environmental safety during its preparation and application. Also, the widespread and indiscriminate use of antibiotics response to the emergence of numerous resistant pathogens. The cost of the synthetic antibacterial peptide is very high. Here, the developed SS/AR/LZM material has good cytocompatibility and without toxic side effects and drug resistance. The main advantage of the lysozyme-based material is significantly safe to human and environment, which has exciting and expected potentials in biomedical materials such as wound dressing.

3.7. Cytocompatibility Assay

To evaluate the cytocompatibility of SS/AR and SS/AR/LZM gels, we tested the effects of SS/AR and SS/AR/LZM gels on the viability of NIH3T3 and HEK293 cells. In the CCK-8 test, a soluble

formazan dye with the maximum absorbance at 450 nm produced as metabolically active cells react with a tetrazolium salt in the CCK-8 reagent. And, the higher optical density (OD) value indicates better cell viability and more live cells [59]. As shown in Figure 6A, B, after 12 h, there were no significant differences in the cells viabilities among SS/AR, SS/AR/LZM gels and the control. After 24 h, the cells viabilities for SS/AR, SS/AR/LZM, and control groups increased quickly. After 36 h, the cells in all groups exhibited significantly higher viabilities than those at 24 h. The results suggested the SS/AR/LZM gel had good cytocompatibility on NIH3T3 and HEK293 cells. This may be due to the fact that active sericin promotes cell growth for its cytoprotective and mitogenic abilities [9]. Furthermore, the morphologies of NIH3T3 and HEK293 cells were observed on an optical microscope after 24 h in the absence and presence of SS/AR and SS/AR/LZM gels. The results showed that morphologies of the cells were nearly identical to that of the control (Figure 6C), indicating SS/AR and SS/AR/LZM gels were not toxic on NIH3T3 and HEK293 cells.

After staining with the LIVE/DEAD fluorescent reagent, the alive cells were stained green while the apoptotic cells were stained red. The result showed most of the cells were green and only a few of cells were red (Figure 7), indicating that the SS/AR and SS/AR/LZM gels had good cytocompatibility on NIH3T3 and HEK293 cells. The fluorescence images of the LIVE/DEAD staining assay were in accordance with the results of CCK-8 assay.

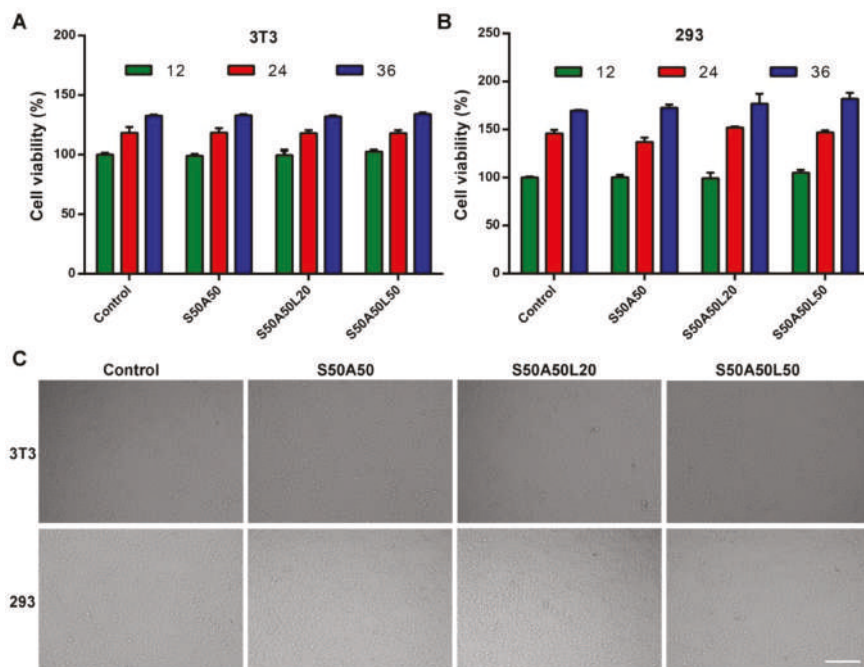


Figure 6. CCK-8 assay of the SS/AR/LZM gels. Cells viability of NIH3T3 (A) and HEK293 (B) in the presence of SS/AR gel or SS/AR/LZM gel, respectively. Microscopic analysis of NIH3T3 and HEK293 cells; ((C), scale bar, 200 μ m).

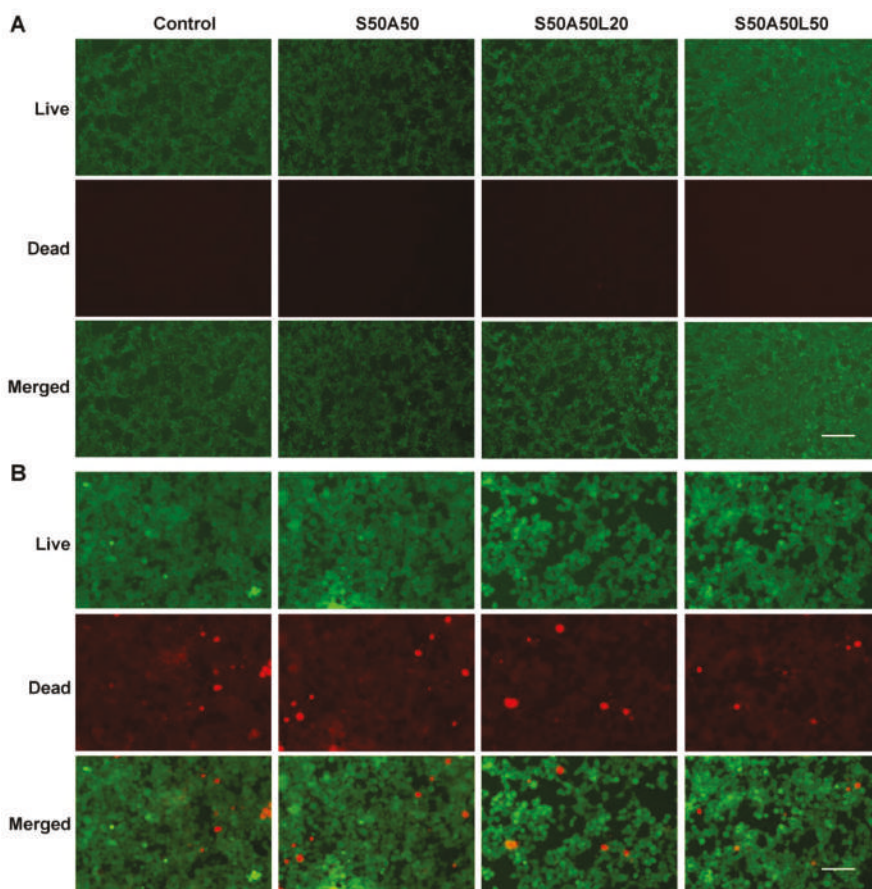


Figure 7. The LIVE/DEAD staining assay. NIH3T3 ((A), scale bar, 200 μm) and HEK293 ((B), scale bar, 100 μm) cells.

4. Conclusions

In summary, the SS/AR composite gel was successfully prepared by blending and freeze-drying. The SS/AR gel had highly porous and inter-connected structure, and good swelling behavior. The lysozyme loaded SS/AR gel had a sustainable lysozyme releasing ability and good antimicrobial activities against *E. coli* and *S. aureus* as well as excellent cytocompatibility on NIH3T3 and HEK293 cells. The SS/AR/LZM gel is expected to develop as an alternative for wound dressing.

Acknowledgments: This work was supported by the National Natural Science Foundation of China (31572465, 51673168), the State Key Program of National Natural Science of China (31530071), Chongqing Research Program of Basic Research and Frontier Technology (cstc2015jcyjja00040, cstc2015jcyjbx0035), the Fundamental Research Funds for the Central Universities (XDJK2018B010, XDJK2018C063), the Graduate Research and Innovation Project of Chongqing (CYS17076, CYS17081, CYB17069), Open Project Program of Chongqing Engineering and Technology Research Center for Novel Silk Materials (silkgczx2016003), and the National Key Research and Development Program of China (2016YFA0100900).

Author Contributions: Meirong Yang, Yejing Wang and Huawei He conceived and designed the experiments; Meirong Yang, Peng Wang, Liying Liu, and Lisha Ai performed the experiments; Meirong Yang and Gang Tao analyzed the data; Gang Tao, Rui Cai, and Hua Zuo contributed reagents/materials/analysis tools; Meirong Yang,

Huawei He, Yejing Wang, Ping Zhao wrote the paper; Meirong Yang, Huawei He, Umar Ahmad and Chuanbin Mao revised the paper.

Conflicts of Interest: The authors declare no conflict of interest.

References

1. Edwards, R.; Harding, K.G. Bacteria and wound healing. *Curr. Opin. Infect. Dis.* **2004**, *17*, 91–96. [[CrossRef](#)] [[PubMed](#)]
2. Song, D.W.; Kim, S.H.; Kim, H.H.; Lee, K.H.; Ki, C.S.; Park, Y.H. Multi-biofunction of antimicrobial peptide-immobilized silk fibroin nanofiber membrane: Implications for wound healing. *Acta Biomater.* **2016**, *39*, 146–155. [[CrossRef](#)] [[PubMed](#)]
3. Sheikh, E.S.; Sheikh, E.S.; Fetterolf, D.E. Use of dehydrated human amniotic membrane allografts to promote healing in patients with refractory non healing wounds. *Int. Wound J.* **2014**, *11*, 711–717. [[CrossRef](#)] [[PubMed](#)]
4. Boateng, J.; Catanzano, O. Advanced therapeutic dressings for effective wound healing. *J. Pharm. Sci.* **2015**, *104*, 3653–3680. [[CrossRef](#)] [[PubMed](#)]
5. Stumpf, T.R.; Pertile, R.A.; Rambo, C.R.; Porto, L.M. Enriched glucose and dextrin mannitol-based media modulates fibroblast behavior on bacterial cellulose membranes. *Mater. Sci. Eng. C* **2013**, *33*, 4739–4745. [[CrossRef](#)] [[PubMed](#)]
6. Xie, Z.; Aphale, N.V.; Kadapure, T.D.; Wadajkar, A.S.; Orr, S.; Gyawali, D.; Qian, G.; Nguyen, K.T.; Yang, J. Design of antimicrobial peptides conjugated biodegradable citric acid derived hydrogels for wound healing. *J. Biomed. Mater. Res. A* **2015**, *103*, 3907–3918. [[CrossRef](#)] [[PubMed](#)]
7. Zhang, Y.-Q. Applications of natural silk protein sericin in biomaterials. *Biotechnol. Adv.* **2002**, *20*, 91–100. [[CrossRef](#)]
8. Kundu, S.C.; Dash, B.C.; Dash, R.; Kaplan, D.L. Natural protective glue protein, sericin bioengineered by silkworms: Potential for biomedical and biotechnological applications. *Prog. Polym. Sci.* **2008**, *33*, 998–1012. [[CrossRef](#)]
9. Lamboni, L.; Gauthier, M.; Yang, G.; Wang, Q. Silk sericin: A versatile material for tissue engineering and drug delivery. *Biotechnol. Adv.* **2015**, *33*, 1855–1867. [[CrossRef](#)] [[PubMed](#)]
10. Wang, Z.; Zhang, Y.; Zhang, J.; Huang, L.; Liu, J.; Li, Y.; Zhang, G.; Kundu, S.C.; Wang, L. Exploring natural silk protein sericin for regenerative medicine: An injectable, photoluminescent, cell-adhesive 3D hydrogel. *Sci. Rep.* **2014**, *4*, 7064. [[CrossRef](#)] [[PubMed](#)]
11. Kundu, B.; Kundu, S.C. Silk sericin/polyacrylamide in situ forming hydrogels for dermal reconstruction. *Biomaterials* **2012**, *33*, 7456–7467. [[CrossRef](#)] [[PubMed](#)]
12. Cho, K.Y.; Moon, J.Y.; Lee, Y.W.; Lee, K.G.; Yeo, J.H.; Kweon, H.Y.; Kim, K.H.; Cho, C.S. Preparation of self-assembled silk sericin nanoparticles. *Int. J. Biol. Macromol.* **2003**, *32*, 36–42. [[CrossRef](#)]
13. Nayak, S.; Talukdar, S.; Kundu, S.C. Potential of 2D crosslinked sericin membranes with improved biostability for skin tissue engineering. *Cell Tissue Res.* **2012**, *347*, 783–794. [[CrossRef](#)] [[PubMed](#)]
14. Aramwit, P.; Siritientong, T.; Kanokpanont, S.; Srichana, T. Formulation and characterization of silk sericin-PVA scaffold crosslinked with genipin. *Int. J. Biol. Macromol.* **2010**, *47*, 668–675. [[CrossRef](#)] [[PubMed](#)]
15. He, H.; Cai, R.; Wang, Y.; Tao, G.; Guo, P.; Zuo, H.; Chen, L.; Liu, X.; Zhao, P.; Xia, Q. Preparation and characterization of silk sericin/PVA blend film with silver nanoparticles for potential antimicrobial application. *Int. J. Biol. Macromol.* **2017**, *104*, 457–464. [[CrossRef](#)] [[PubMed](#)]
16. Bellamkonda, R.; Ranieri, J.P.; Bouche, N.; Aebischer, P. Hydrogel-based three-dimensional matrix for neural cells. *J. Biomed. Mater. Res.* **1995**, *29*, 663–671. [[CrossRef](#)] [[PubMed](#)]
17. Yodmuang, S.; McNamara, S.L.; Nover, A.B.; Mandal, B.B.; Agarwal, M.; Kelly, T.A.; Chao, P.H.; Hung, C.; Kaplan, D.L.; Vunjak-Novakovic, G. Silk microfiber-reinforced silk hydrogel composites for functional cartilage tissue repair. *Acta Biomater.* **2015**, *11*, 27–36. [[CrossRef](#)] [[PubMed](#)]
18. Lima, E.G.; Bian, L.; Ng, K.W.; Mauck, R.L.; Byers, B.A.; Tuan, R.S.; Ateshian, G.A.; Hung, C.T. The beneficial effect of delayed compressive loading on tissue-engineered cartilage constructs cultured with TGF- β 3. *Osteoarthr. Cartil.* **2007**, *15*, 1025–1033. [[CrossRef](#)] [[PubMed](#)]
19. Stokols, S.; Tuszyński, M.H. Freeze-dried agarose scaffolds with uniaxial channels stimulate and guide linear axonal growth following spinal cord injury. *Biomaterials* **2006**, *27*, 443–451. [[CrossRef](#)] [[PubMed](#)]

20. Gruber, H.E.; Fisher, E.C., Jr.; Desai, B.; Stasky, A.A.; Hoelscher, G.; Hanley, E.N., Jr. Human intervertebral disc cells from the annulus: Three-dimensional culture in agarose or alginate and responsiveness to TGF- β 1. *Exp. Cell Res.* **1997**, *235*, 13–21. [[CrossRef](#)] [[PubMed](#)]
21. Doulabi, A.; Mequanint, K.; Mohammadi, H. Blends and nanocomposite biomaterials for articular cartilage tissue engineering. *Materials* **2014**, *7*, 5327–5355. [[CrossRef](#)] [[PubMed](#)]
22. Bhat, S.; Tripathi, A.; Kumar, A. Supermacroporous chitosan-agarose-gelatin cryogels: In vitro characterization and in vivo assessment for cartilage tissue engineering. *J. R. Soc. Interfaces* **2011**, *8*, 540–554. [[CrossRef](#)] [[PubMed](#)]
23. Nikaido, H. Multidrug resistance in bacteria. *Annu. Rev. Biochem.* **2009**, *78*, 119–146. [[CrossRef](#)] [[PubMed](#)]
24. Benkerroum, N. Antimicrobial activity of lysozyme with special relevance to milk. *Afr. J. Biotechnol.* **2008**, *7*, 4856–4867.
25. Hamdani, A.M.; Wani, I.A.; Bhat, N.A.; Siddiqi, R.A. Effect of guar gum conjugation on functional, antioxidant and antimicrobial activity of egg white lysozyme. *Food Chem.* **2018**, *240*, 1201–1209. [[CrossRef](#)] [[PubMed](#)]
26. Gu, J.; Su, Y.; Liu, P.; Li, P.; Yang, P. An environmentally benign antimicrobial coating based on a protein supramolecular assembly. *ACS Appl. Mater. Interfaces* **2017**, *9*, 198–210. [[CrossRef](#)] [[PubMed](#)]
27. Zhao, J.; Wang, X.; Kuang, Y.; Zhang, Y.; Shi, X.; Liu, X.; Deng, H. Multilayer composite beads constructed via layer-by-layer self-assembly for lysozyme controlled release. *RSC Adv.* **2014**, *4*, 24369–24376. [[CrossRef](#)]
28. Yang, M.; Wang, Y.; Cai, R.; Tao, G.; Chang, H.; Ding, C.; Zuo, H.; Shen, H.; Zhao, P.; He, H. Preparation and characterization of silk sericin/glycerol films coated with silver nanoparticles for antibacterial application. *Sci. Adv. Mater.* **2018**, *10*, 1–8. [[CrossRef](#)]
29. He, H.; Tao, G.; Wang, Y.; Cai, R.; Guo, P.; Chen, L.; Zuo, H.; Zhao, P.; Xia, Q. In situ green synthesis and characterization of sericin-silver nanoparticle composite with effective antibacterial activity and good biocompatibility. *Mater. Sci. Eng. C* **2017**, *80*, 509–516. [[CrossRef](#)] [[PubMed](#)]
30. Nazarov, R.; Jin, H.J.; Kaplan, D.L. Porous 3-D scaffolds from regenerated silk fibroin. *Biomacromolecules* **2004**, *5*, 718–726. [[CrossRef](#)] [[PubMed](#)]
31. Tao, G.; Cai, R.; Wang, Y.; Song, K.; Guo, P.; Zhao, P.; Zuo, H.; He, H. Biosynthesis and characterization of agnps-silk/PVA film for potential packaging application. *Materials* **2017**, *10*, 667. [[CrossRef](#)] [[PubMed](#)]
32. Cai, R.; Tao, G.; He, H.; Guo, P.; Yang, M.; Ding, C.; Zuo, H.; Wang, L.; Zhao, P.; Wang, Y. In situ synthesis of silver nanoparticles on the polyelectrolyte-coated sericin/pva film for enhanced antibacterial application. *Materials* **2017**, *10*, 967. [[CrossRef](#)] [[PubMed](#)]
33. Jiang, S.; Qin, Y.; Yang, J.; Li, M.; Xiong, L.; Sun, Q. Enhanced antibacterial activity of lysozyme immobilized on chitin nanowhiskers. *Food Chem.* **2017**, *221*, 1507–1513. [[CrossRef](#)] [[PubMed](#)]
34. Chen, C.; Pan, F.; Zhang, S.; Hu, J.; Cao, M.; Wang, J.; Xu, H.; Zhao, X.; Lu, J.R. Antibacterial activities of short designer peptides: A link between propensity for nanostructuring and capacity for membrane destabilization. *Biomacromolecules* **2010**, *11*, 402–411. [[CrossRef](#)] [[PubMed](#)]
35. Wu, Y.-B.; Yu, S.-H.; Mi, F.-L.; Wu, C.-W.; Shyu, S.-S.; Peng, C.-K.; Chao, A.-C. Preparation and characterization on mechanical and antibacterial properties of chitsoan/cellulose blends. *Carbohydr. Polym.* **2004**, *57*, 435–440. [[CrossRef](#)]
36. Zhou, B.; Li, Y.; Deng, H.; Hu, Y.; Li, B. Antibacterial multilayer films fabricated by layer-by-layer immobilizing lysozyme and gold nanoparticles on nanofibers. *Colloids Surf. B* **2014**, *116*, 432–438. [[CrossRef](#)] [[PubMed](#)]
37. Zhou, T.; Huang, Y.; Li, W.; Cai, Z.; Luo, F.; Yang, C.J.; Chen, X. Facile synthesis of red-emitting lysozyme-stabilized ag nanoclusters. *Nanoscale* **2012**, *4*, 5312–5315. [[CrossRef](#)] [[PubMed](#)]
38. Chuang, C.-C.; Prasannan, A.; Huang, B.-R.; Hong, P.-D.; Chiang, M.-Y. Simple synthesis of eco-friendly multifunctional silk-sericin capped zinc oxide nanorods and their potential for fabrication of hydrogen sensors and UV photodetectors. *ACS Sustain. Chem. Eng.* **2017**, *5*, 4002–4010. [[CrossRef](#)]
39. Al-Abboodi, A.; Fu, J.; Doran, P.M.; Tan, T.T.Y.; Chan, P.P.Y. Injectable 3D hydrogel scaffold with tailorable porosity post-implantation. *Adv. Healthc. Mater.* **2014**, *3*, 725–736. [[CrossRef](#)] [[PubMed](#)]
40. Annabi, N.; Nichol, J.W.; Zhong, X.; Ji, C.; Koshy, S.; Khademhosseini, A.; Dehghani, F. Controlling the porosity and microarchitecture of hydrogels for tissue engineering. *Tissue Eng. Part B* **2010**, *16*, 371–383. [[CrossRef](#)] [[PubMed](#)]

41. Zhang, X.; Wyeth, P. Using FTIR spectroscopy to detect sericin on historic silk. *Sci. China Chem.* **2010**, *53*, 626–631. [CrossRef]
42. Verma, V.K.; Subbiah, S. Prospects of silk sericin as an adsorbent for removal of ibuprofen from aqueous solution. *Ind. Eng. Chem. Res.* **2017**, *56*, 10142–10154. [CrossRef]
43. Singh, Y.P.; Bhardwaj, N.; Mandal, B.B. Potential of agarose/silk fibroin blended hydrogel for in vitro cartilage tissue engineering. *ACS Appl. Mater. Interfaces* **2016**, *8*, 21236–21249. [CrossRef] [PubMed]
44. Wu, T.; Huang, J.; Jiang, Y.; Hu, Y.; Ye, X.; Liu, D.; Chen, J. Formation of hydrogels based on chitosan/alginate for the delivery of lysozyme and their antibacterial activity. *Food Chem.* **2018**, *240*, 361–369. [CrossRef] [PubMed]
45. Gupta, D.; Agrawal, A.; Rangi, A. Extraction and characterization of silk sericin. *Indian J. Fibre Text.* **2014**, *39*, 364–372.
46. Tao, G.; Liu, L.; Wang, Y.; Chang, H.; Zhao, P.; Zuo, H.; He, H. Characterization of silver nanoparticle in situ synthesis on porous sericin gel for antibacterial application. *J. Nanomater.* **2016**, *2016*, 1–8. [CrossRef]
47. Tao, G.; Wang, Y.; Liu, L.; Chang, H.; Zhao, P.; He, H. Preparation and characterization of silver nanoparticles composited on polyelectrolyte film coated sericin gel for enhanced antibacterial application. *Sci. Adv. Mater.* **2016**, *8*, 1547–1552. [CrossRef]
48. Cai, R.; Tao, G.; He, H.; Song, K.; Zuo, H.; Jiang, W.; Wang, Y. One-step synthesis of silver nanoparticles on polydopamine-coated sericin/polyvinyl alcohol composite films for potential antimicrobial applications. *Molecules* **2017**, *22*, 721. [CrossRef] [PubMed]
49. Cao, T.T.; Zhang, Y.Q. Processing and characterization of silk sericin from bombyx mori and its application in biomaterials and biomedicines. *Mater. Sci. Eng. C* **2016**, *61*, 940–952. [CrossRef] [PubMed]
50. Silva, V.R.; Hamerski, F.; Weschenfelder, T.A.; Ribani, M.; Gimenes, M.L.; Scheer, A.P. Equilibrium, kinetic, and thermodynamic studies on the biosorption of bordeaux s dye by sericin powder derived from cocoons of the silkworm bombyx mori. *Desalin. Water Treat.* **2015**, *57*, 5119–5129. [CrossRef]
51. Shemesh, M.; Zilberman, M. Structure-property effects of novel bioresorbable hybrid structures with controlled release of analgesic drugs for wound healing applications. *Acta Biomater.* **2014**, *10*, 1380–1391. [CrossRef] [PubMed]
52. Atar-Froyman, L.; Sharon, A.; Weiss, E.I.; Hourri-Haddad, Y.; Kesler-Shvero, D.; Domb, A.J.; Pilo, R.; Beyth, N. Anti-biofilm properties of wound dressing incorporating nonrelease polycationic antimicrobials. *Biomaterials* **2015**, *46*, 141–148. [CrossRef] [PubMed]
53. Liu, Y.; Sun, Y.; Xu, Y.; Feng, H.; Fu, S.; Tang, J.; Liu, W.; Sun, D.; Jiang, H.; Xu, S. Preparation and evaluation of lysozyme-loaded nanoparticles coated with poly-gamma-glutamic acid and chitosan. *Int. J. Biol. Macromol.* **2013**, *59*, 201–207. [CrossRef] [PubMed]
54. Ibrahim, H.R.; Higashiguchi, S.; Juneja, L.R.; Kim, M.; Yamamoto, T. A structural phase of heat-denatured lysozyme with novel antimicrobial action. *J. Agric. Food Chem.* **1996**, *44*, 1416–1423. [CrossRef]
55. Bernkop-Schnürch, A.; Krist, S.; Vehabovic, M.; Valenta, C. Synthesis and evaluation of lysozyme derivatives exhibiting an enhanced antimicrobial action. *Eur. J. Pharm. Sci.* **1998**, *6*, 301–306. [CrossRef]
56. Wu, T.; Wu, C.; Fu, S.; Wang, L.; Yuan, C.; Chen, S.; Hu, Y. Integration of lysozyme into chitosan nanoparticles for improving antibacterial activity. *Carbohydr. Polym.* **2017**, *155*, 192–200. [CrossRef] [PubMed]
57. Yu, K.; Lu, F.; Li, Q.; Chen, H.; Lu, B.; Liu, J.; Li, Z.; Dai, F.; Wu, D.; Lan, G. In situ assembly of ag nanoparticles (agnps) on porous silkworm cocoon-based wound film: Enhanced antimicrobial and wound healing activity. *Sci. Rep.* **2017**, *7*, 2107. [CrossRef] [PubMed]
58. Kamoun, E.A.; Kenawy, E.-R.S.; Tamer, T.M.; El-Meligy, M.A.; Mohy Eldin, M.S. Poly (vinyl alcohol)-alginate physically crosslinked hydrogel membranes for wound dressing applications: Characterization and bio-evaluation. *Arab. J. Chem.* **2015**, *8*, 38–47. [CrossRef]
59. Yao, Y.; Liu, H.; Ding, X.; Jing, X.; Gong, X.; Zhou, G.; Fan, Y. Preparation and characterization of silk fibroin/poly(L-lactide-co-ε-caprolactone) nanofibrous membranes for tissue engineering applications. *J. Bioact. Compat. Polym.* **2015**, *30*, 633–648. [CrossRef]



Article

Effect of Laminating Pressure on Polymeric Multilayer Nanofibrous Membranes for Liquid Filtration

Fatma Yalcinkaya ^{1,2,*} and Jakub Hruza ^{1,2}

¹ Department of Nanotechnology and Informatics, Institute of Nanomaterials, Advanced Technologies and Innovation, Technical University of Liberec, Studentska 1402/2, 46117 Liberec, Czech Republic; jakub.hruza@tul.cz

² Institute for New Technologies and Applied Informatics, Faculty of Mechatronics, Studentska 1402/2, 46117 Liberec, Czech Republic

* Correspondence: yeneretex@hotmail.com; Tel.: +420-485-353-389

Received: 8 February 2018; Accepted: 23 April 2018; Published: 24 April 2018



Abstract: In the new century, electrospun nanofibrous webs are widely employed in various applications due to their specific surface area and porous structure with narrow pore size. The mechanical properties have a major influence on the applications of nanofiber webs. Lamination technology is an important method for improving the mechanical strength of nanofiber webs. In this study, the influence of laminating pressure on the properties of polyacrylonitrile (PAN) and polyvinylidene fluoride (PVDF) nanofibers/laminate was investigated. Heat-press lamination was carried out at three different pressures, and the surface morphologies of the multilayer nanofibrous membranes were observed under an optical microscope. In addition, air permeability, water filtration, and contact angle experiments were performed to examine the effect of laminating pressure on the breathability, water permeability and surface wettability of multilayer nanofibrous membranes. A bursting strength test was developed and applied to measure the maximum bursting pressure of the nanofibers from the laminated surface. A water filtration test was performed using a cross-flow unit. Based on the results of the tests, the optimum laminating pressure was determined for both PAN and PVDF multilayer nanofibrous membranes to prepare suitable microfilters for liquid filtration.

Keywords: nanofiber; lamination; water filtration

1. Introduction

Electrospun polymeric nanofiber web has gained increasing importance in the production of engineered surfaces with sub-micron to nano-scale fibers. The widely employed areas of electrospun nanofibers are tissue engineering [1,2], wound healing [3], drug delivery systems [4], composites [5], solar cells [6], protective clothing [7], lithium-ion batteries [8,9], sensors [10–12], gas sensors and separators [13,14], and air and water filtration [15–19], owing to their high surface-area-to-volume ratio, highly porous structure and extremely narrow pore size. The main factor influencing the application of nanofibers is their mechanical properties. An electrospun nanofiber has very poor mechanical strength due to low contact and adhesion between the fibers.

Several methods have been developed to provide suitable mechanical strength to electrospun nanofibers. One of the most common methods is to blend several polymers, the advantage of which is that it is easy and low-cost. However, it is necessary to use polymers which can dissolve in the same solvent system, of which there are only a few [20,21]. In another method, lamination was achieved using an epoxy composite. In this method, an electrospun layer was laid on the epoxy/curing agent in a mold and then the curing process was performed for a period of 16 h [22].

Nanofiber reinforced nanomaterials such as carbon nanotubes and graphene represent another route for improving the mechanical strength of nanofibers. However, this method is costly and in some cases has a low efficiency [23,24]. Charles et al. [25] used a dip coating method to improve the mechanical strength of nanofibers. They described the mechanical properties of a composite system comprising hydroxyapatite (HA)-coated poly (L-lactic acid) (PLLA) fibers in a poly (ϵ -caprolactone) (PCL) matrix. A biomimetic method was used to coat the fibers with HA, and a dip-coating procedure served for the application of PCL to the coated fibers. The composite was formed into a bar using compression molding at low temperatures. The disadvantage of this method is that it is a time- and chemical-consuming procedure. Xu et al. [26] developed a self-reinforcing method to enhance the strength of polycarbonate (PC) membranes. In this method, the PC nanofibers were immersed into a solvent (30%) and non-solvent (70%) mixture, which resulted in enhancement in the strength (128%) owing to the fusion of junction points. The entire porous structure on the PC nanofibers was destroyed, which greatly impaired the application of the membranes. The thermal lamination method is one of the most reliable, repeatable, time-saving, environmentally friendly and cost-effective methods used to adhere two surfaces. In this method, an adhesive polymer or web is usually applied between two surfaces. Using heat and pressure, the surfaces adhere to each other. There is a large amount of research related to improving the strength of nanofibers; however, the number of reports is still limited compared to those dealing with lamination technology. Jiricek [27,28] and Yalcinkaya et al. [29,30] used a bi-component polyethylene (PE)/polypropylene (PP) spunbond as a supporting layer for nanofiber layers. A fusing machine was used for the lamination process. A nanofiber layer was adhered on the outer surface of the bi-component due to the low melting point of PE. The resultant multilayer nanofibrous membranes were used for micro and nanofilters. The supporting material and the density of the nanofibers have an influence on the water and air permeability of the multilayer materials. Yoon et al. [7] laminated nanofibers with various densities of polyurethane (PUR) fiber onto different textile surfaces using an adhesive web. The results showed that the various multilayer nanofibrous membrane structure designs had a considerable influence on the degrees of breathability and waterproofness of the textile surfaces. In our previous work [31], it was observed that both the supporting material and the density of the nanofiber web have an influence on the water permeability of the multilayer nanofibrous membranes. The lower area weight with open structure supporting materials has higher water flux and permeability. Kanafchian et al. [32] used a heat-press technique to laminate the polyacrylonitrile (PAN) nanofiber on a polypropylene spunbond at various laminating temperatures. It was observed that, when the applied temperature is lower than the melting point of polypropylene spunbond, the nanofiber web remains unchanged. Moreover, the increase in temperature increased the adhesion between nanofiber while decreasing the air permeability.

Although the system and parameters of the electrospinning process have been well analyzed, there is still a lack of information about a proper lamination technique for nanofiber webs. So far, mainly the effect of temperature on the lamination of electrospun nanofiber webs has been investigated using heat-press methods [32–34]. Yao et al. [33] studied the effect of the heat-press temperature, pressure, and duration on the morphological and mechanical characteristics of an electrospun membrane for membrane distillation. The results showed that the temperature and duration of the heat-press play more important roles than the pressure in the heat-press treatment. However, the pressure varied between 0.7 and 9.8 kPa at 150 °C during a 2-h period, which is time- and energy-consuming and therefore a more comprehensive parametric study is required. The aim of this study is to consider the influence of laminating pressure on the properties of multilayer nanofibrous membranes. Polyvinylidene (PVDF) and polyacrylonitrile (PAN) are the most commonly used nanofiber layers owing to their chemical and thermal stability. Herein, both polymers were electrospun using a semi-industrial scale nanofiber production method. The nanofiber layers were laminated onto a nonwoven surface to improve their mechanical strength via the heat-press method, which is easy to scale and is an energy-saving method at various applied pressures. Other conditions, such as temperature and the duration of lamination, were kept stable. The effect of the laminating pressure

on the nanofiber web has not yet been well reported. To investigate the effect of the pressure on the nanofiber/laminate process, surface morphology under an optical microscope, the minimum bursting pressure, air permeability, water permeability and contact angle tests were applied. Our objective was to optimize the lamination technology and produce multilayer nanofibrous membranes for suitable application in liquid filtration. Another novelty of this paper is that nanofiber layers were produced by using the industrial equipment, and that the layers strongly adhered on the supporting layer without any damage using various lamination pressures to improve their application in liquid filtration.

2. Materials and Methods

2.1. Preparation of Nanofibre Webs

13 wt. % PVDF (Solef 1015, Bruxelles, Belgium) was prepared in *N,N*-dimethylacetamide (DMAC) and 8 wt. % PAN (150 kDa H-polymer, Elmarco, Liberec, Czech Republic) was prepared in *N,N*-dimethylformamide. The solvents were purchased from Penta s.r.o. (Prague, Czech Republic). The solutions were stirred overnight using a magnetic stirrer. Nanofiber webs were prepared using the semi-industrial Nanospider electrospinning device (Elmarco, Liberec, Czech Republic) as shown in Figure 1.

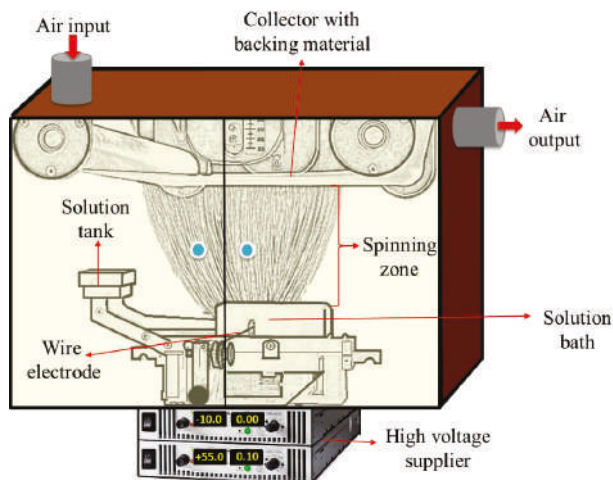


Figure 1. Schematic diagram of an electrospinning unit.

The solution is placed in a solution tank, which is a closed system and connected to a solution bath. The wire electrode passes along a metal orifice in the middle of the solution bath. The solution bath is moved back and forward to feed the surface of the wire electrode. The solution bath feeds the polymer solution on a moving stainless steel wire. The speed of the bath is 240 mm/s. A high voltage supplier is connected to a positively charged wire electrode (55 kV). A second wire electrode, which is connected to a negatively charged voltage supplier (−15 kV), is placed on the top of the spinning unit. A conveyor backing material is placed between the two electrodes. The spinning takes place between the two electrodes. The nanofiber web is collected on baking paper moving in front of the collector electrode. The distance between the electrodes is 188 mm. The distance between the second electrode and the supporting backing material is 2 mm. The speed of the backing material for PAN and PVDF is 15 mm/min and 20 mm/min, respectively. The amount of solution on the wire is controlled with the speed of the solution bath, the diameter of the wire (0.2 mm) and the diameter of the metal orifice (0.6 mm) in the middle of the solution bath. No solution dipping was observed. An air

conditioning unit is used to control the humidity and temperature of the spinning in a closed chamber. The temperature and humidity of the input air are set to 23 °C and 20% by the air-conditioning system. The volumes of air input and output are 100 and 115 m³/h, respectively. The area weight of the PVDF and PAN nanofibers was set at 3 g/m².

2.2. Lamination of Nanofibre Webs

The prepared nanofiber webs were cut into A4 size (210 × 297 mm²). As a supporting layer, 120 g/m² of polyethylene terephthalate spunbond nonwoven and 12 g/m² of adhesive web were used (the supplier information is not given). Heat-press equipment (Pracovni Stroj, Teplice, Czech Republic) was used for the lamination process (Figure 2). In this equipment there are two metallic hot plates (upper and lower) used under pressure. The nanofibers, a copolyamide adhesive web and a polyethylene terephthalate spunbond supporting layer were placed between the two hot plates. Two silicon layers were used to block direct contact between the multilayer nanofibrous membranes and the hot plates. The heat was applied (130 °C) for a duration of 3 min. Pressures of 50, 75 and 100 kN were applied between the upper and lower plates. For each pressure, PVDF and PAN nanofiber webs were used. The resultant multilayer nanofibrous membranes were termed PAN50, PAN75, PAN100, PVDF50, PVDF75, and PVDF100 according to the pressure value.

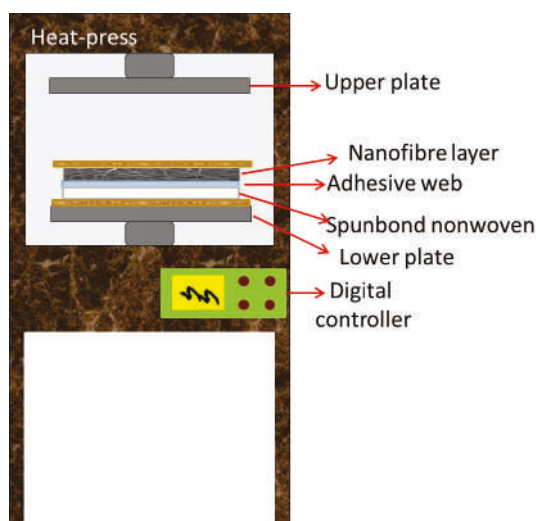


Figure 2. Schematic design of the heat-press equipment and replacement of the multilayer nanofibrous membranes.

2.3. Characterization of the Multilayer Nanofibrous Membranes

The surface morphology of the electrospun fibers and laminated multilayer nanofibrous membranes was observed using a scanning electron microscope (SEM, Vega 3SB, Brno, Czech Republic). From each sample, at least 50 fibers were measured. The fiber diameter was analyzed using the Image-J program (free online program). The Origin-Lab program was used to evaluate the diameter distribution. The surface contact angle of the samples was measured using a Krüss Drop Shape Analyzer DS4 (Krüss GmbH, Hamburg, Germany), at five different points, using distilled water (surface tension 72.0 mN m⁻¹) and ethylene glycol (surface tension 47.3 mN m⁻¹) on the clean and dry samples at room temperature. The air permeability of the multilayer nanofibrous membranes was tested using an SDL

ATLAS Air Permeability Tester (@200 Pa and 20 cm², Rock Hill, SC, USA). At least three measurements were taken for each sample.

The maximum, average and minimum pore sizes were determined by a bubble point measurement device, which was developed in our laboratory. The bubble point test allowed the size of the pores of the porous material to be measured. The pore flow means a set of continuous hole channels connecting the opposite sides of the porous material (see Figure 3). At least three measurements were taken.

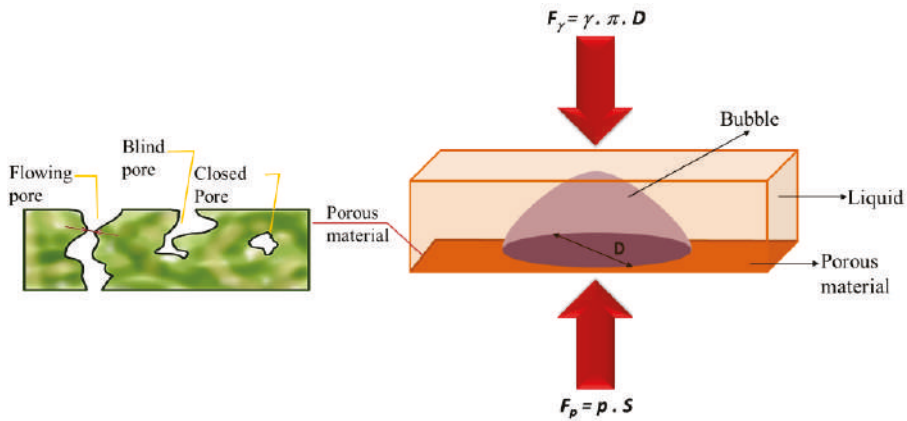


Figure 3. Schematic diagram of pore flow and forces acting on a pore.

The main part of the method was to control the pressure needed to pass a liquid through the tested porous material and for wetting the sample. This is because the wetting force (and hence the opposite force required to extrude the liquid) depends on the pore circumference. The principle for calculating the pore size is shown in Figure 3 and Equations (1) and (2).

$$F_{\gamma} = \gamma \pi D \tag{1}$$

$$F_p = p S \tag{2}$$

where F_{γ} is the force given by surface tension γ of the liquid around the perimeter of πD . The force F_p is given by external pressure p displacing the liquid from the pores and acting on the surface of pore S .

It is possible to calculate the magnitude of the force given by the surface tension and the force given by the pore pressurizing fluid. By increasing the air pressure and measuring its flow through the sample, the size of the average and minimum pores can also be determined. In this case, it is necessary to compare the pressure curve of the wet sample with the pressure curve of the dry sample (see Figure 4). The dry sample pressure curve required to determine the mean and minimum pores is also applicable for determining the air permeability coefficient (K) of the sample calculated according to the relation (Equation (3)):

$$K = Q / (\Delta p A) \tag{3}$$

where Q is the air flow rate (m²/s), Δp is the pressure drop of the sample, and A is the area of air flow (m²).

When the pressure increases in the dry sample, the flow rate also increases. Conversely, in the wet sample, at the beginning, there is no flow because all the pores are filled with the liquid. At a certain pressure, the gas empties the largest pore, which determines the minimum pore size, and gas begins to flow through the wet sample. The intersection between the calculated half-dry and the wet sample gives the mean flow pore size. When all the pores are emptied, an intersection between the wet and dry curve will be observed. This means the relation between the applied pressure and the detected

flow becomes linear and the intersection of the wet and dry curve represents the detected minimum pore size.

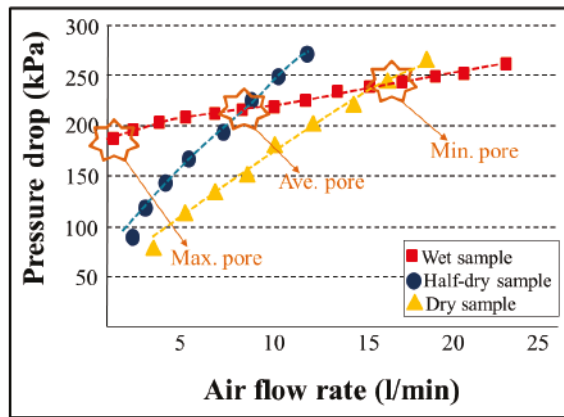


Figure 4. Example of a pressure drop determination to calculate the pore size.

The bursting strength of the multilayer nanofibrous membrane was tested, and the maximum delamination pressure was recorded. The testing device was developed in our laboratory as shown in Figure 5. In this test, the samples were placed between two rings, and the nanofiber side of the samples was placed on the upper side. The sample size was 47 mm in diameter. Pressurized water was sent to the membrane, and the hydrostatic pressure was measured using a pressure controller, which was placed in front of the membrane and connected to a computer. The hydrostatic pressure was increased gradually, and as soon as the nanofiber layer burst, the pressure value on the screen decreased sharply. The maximum pressure value was recorded as the bursting strength of the membrane. The testing samples are shown in Figure 5. After bursting, the nanofiber layer delaminated from the surface of the multilayer membrane. At least three measurements were taken for each membrane.

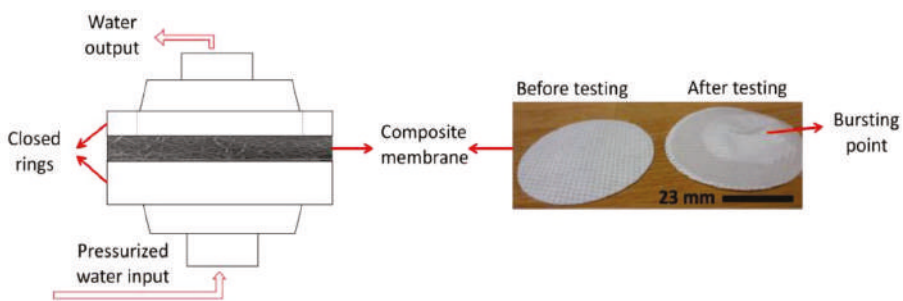


Figure 5. Bursting strength testing unit.

A lab-scale cross-flow filtration unit was developed as shown in Figure 6. Tap water was used as the feed solution. The maximum amount of feed solution was 1500 mL. The flux (F) and the permeability (k) of the membranes were calculated according to Equations (4) and (5) [31,35]:

$$F = \frac{1}{A} \frac{dV}{dt} \tag{4}$$

$$k = \frac{F}{p} \quad (5)$$

where A is the effective membrane area (m^2), V is the total volume of the permeate (L), p is the transmembrane pressure (bar), and t is the filtration time.

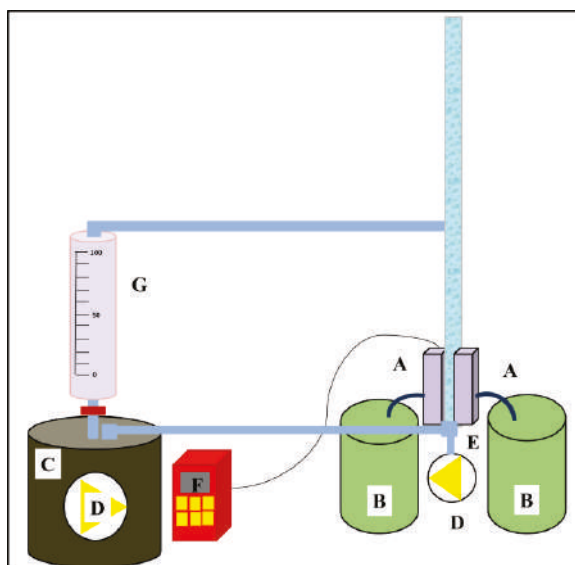


Figure 6. A cross-flow unit: (A) membrane cells; (B) permeate; (C) feed; (D) pump; (E) surface bubble cleaning; (F) pressure controller; (G) feed flow speed controller.

3. Results and Discussion

3.1. Characterization of Nanofibre Webs and Laminated Multilayer Nanofibrous Membranes

To characterize the nanofiber webs into the format of multilayer nanofibrous membranes, various aspects of their material properties were carefully considered. These properties include the fiber diameter, diameter distribution, mean pore size, wetting property, air permeability, and bursting strength.

The surface morphology of the nanofiber webs before and after lamination was imaged using a scanning electron microscope as shown in Figure 7. The average fiber diameter of the PAN and PVDF nanofibers before lamination was determined to be 171 nm and 221 nm, respectively. The diameter of the PVDF nanofibers was greater than that of the PAN nanofibers. The main reason was the difference in viscosity. In previous work [36], it was determined that a 14 wt. % PVDF solution has a viscosity of 969 mPa.s, while 8 wt. % PAN has 191 mPa.s. Based on the viscosity results, one can expect that a polymeric solution with a lower viscosity will have a lower fiber diameter. After the lamination process, neither the PVDF nor the PAN nanofiber diameters significantly changed at a pressure of 50 kN (Figure 8). However, significant changes were observed at laminating pressures of 75 kN and 100 kN. When the highest laminating pressure was applied (i.e., 100 kN), the diameter of the PAN and PVDF nanofibers increased by 14% and 25%, respectively. The fibers were flattened under heat and pressure, and the fiber diameter increased gradually. The highest fiber diameter changes were observed in the case of the PVDF nanofiber layer due to its lower glass transition and melting temperature compared to PAN [37,38].

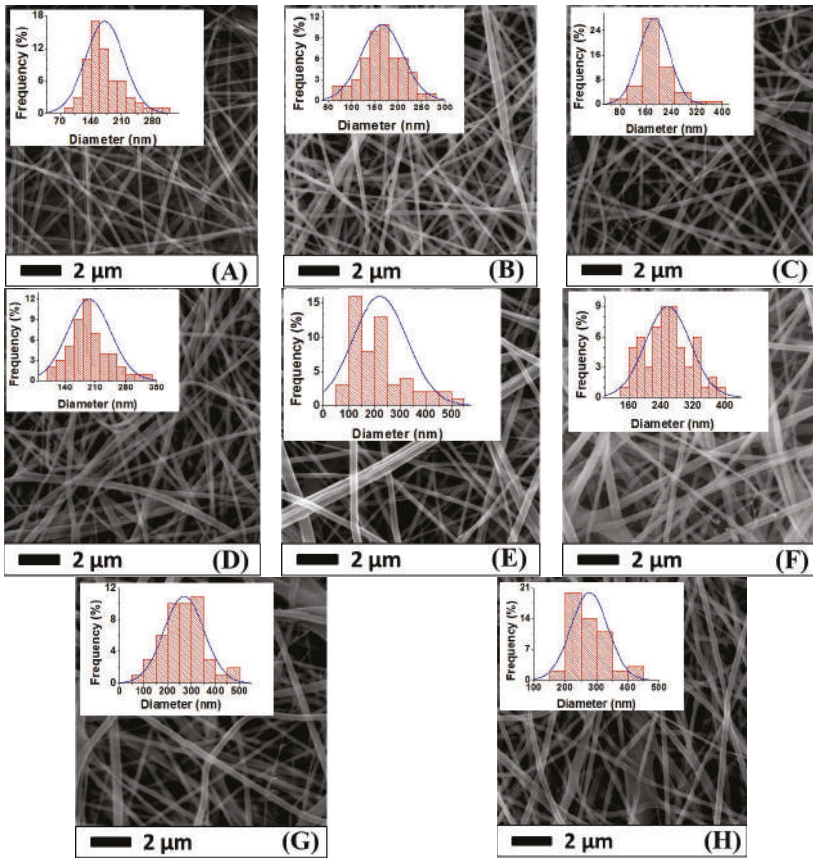


Figure 7. SEM images and fiber diameter distribution of (A) PAN nanofiber web before lamination; (B) PAN50; (C) PAN75; (D) PAN100; (E) PVDF nanofiber web before lamination; (F) PVDF50; (G) PVDF75; and (H) PVDF100.

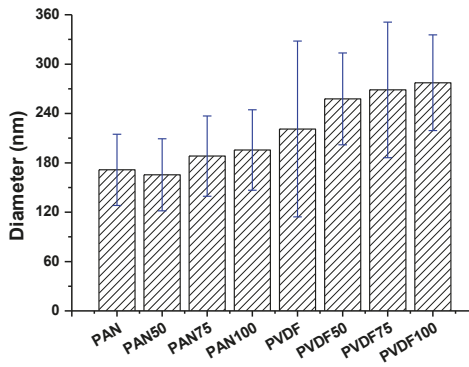


Figure 8. Fiber diameter of various multilayer nanofibrous membranes under different laminating pressures.

It was verified that there is a strong correlation between the electrospun fiber diameters and the polymer concentration, which has been well documented in the literature [39–41]. From the SEM images, the PAN and PVDF multilayer nanofibrous membranes exhibited bead-free surface morphology.

The average pore size of the membranes is given in Figure 9. Electrospun materials readily deform at low pressures. Since the tensile strength of PVDF and PAN nanofibers before lamination is quite low to withstand air pressure, their pore size was not measured.

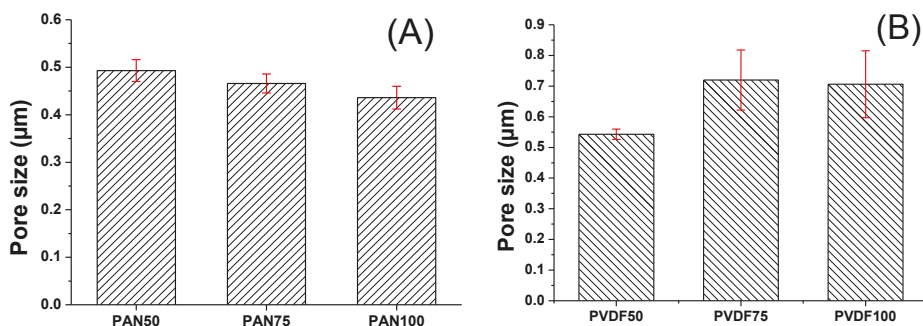


Figure 9. The relationship between the mean pore size and the laminating pressure of (A) PAN and (B) PVDF multilayer nanofibrous membranes.

In general, there is a correlation between the fiber diameter and the average pore size of the nanofibers. Reducing the fiber diameter increases the surface area and compact web structure, which results in a small pore size [42]. Bagherzadeh et al. [43] demonstrated a theoretical analysis to predict the pore size of electrospun nanofibers. According to their theory, at a given web porosity, increasing the fiber diameter and thickness of the web reduces the dimensions of the pores. This theory was validated experimentally, and the results were compared with the existing theory to predict the pore size distribution of nanofiber mats. Their results showed that the pore size significantly increased with an increase in fiber diameter, web porosity and density of the layers. In this work, the correlation between the diameter of the PVDF nanofibers and the mean pore size was compatible with the literature, while PAN showed an opposite correlation. The laminating pressure effect must be taken into consideration. The nanofiber layer did not change; only the fibers flattened after lamination due to the pressure. It was expected that a higher pressure would cause a lower pore size since the fibers flattened and melting adhesive filled more of the pores and covered the surface of the nanofibers as shown in Figure 10. The PAN multilayer nanofibrous membranes fulfilled this expectation while the PVDF did not. Figure 9B shows that the average pore size and the standard deviation of the pore size measurements increased with pressure, which could be due to possible damage of the PVDF nanofibers under high pressure. Gockeln et al. [44] investigated the influence of laminating pressures on the microstructure and electrochemical performance of the lithium-ion battery electrodes. The results indicated that all the laminated samples showed highly porous and homogeneous networks, while the pore size slightly decreased with an increase in laminating pressure. At higher pressures, the intrinsic electrical conductivity was improved due to more compression.

The water and ethylene glycol wettability of the PAN and PVDF multilayer nanofibrous membranes were examined by a contact angle measurement as shown in Figure 11. The surface energy and surface roughness are the dominant factors for the wettability. As can be seen from Figure 11, an increase in laminating pressure decreased the water and ethylene glycol contact angle of both PAN and PVDF multilayer nanofibrous membranes. Hence, ethylene glycol has a lower surface energy compared to water, with the differences in contact angle value being 20° for PAN and 30° for PVDF. Similar behavior was observed in the literature [45,46]. It is well known that when the surface

energy is lowered, and surface roughness is raised, the hydrophobicity is enhanced [47–49]. With the help of heat, the higher laminating pressure on the surface may cause changes to the surface shape and make the surface flatter, which results in an increase in the surface wettability (Figure 11). The PVDF membranes showed hydrophobic characteristics at the lowest laminating pressure (i.e., 50 kN), while at higher laminating pressures they showed hydrophilic properties. By setting the lamination process parameters, one can prepare hydrophilic PVDF multilayer nanofibrous membranes without any surface modification.

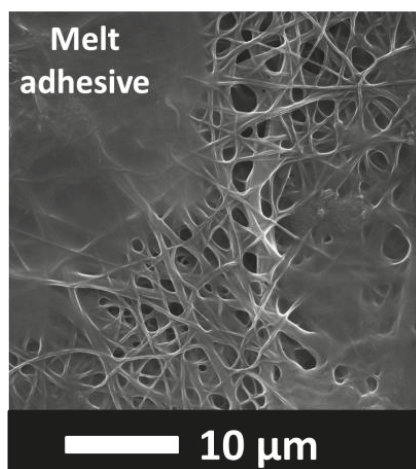


Figure 10. An illustration of adhesive melting over the surface of a nanofiber web, forming a non-porous film.

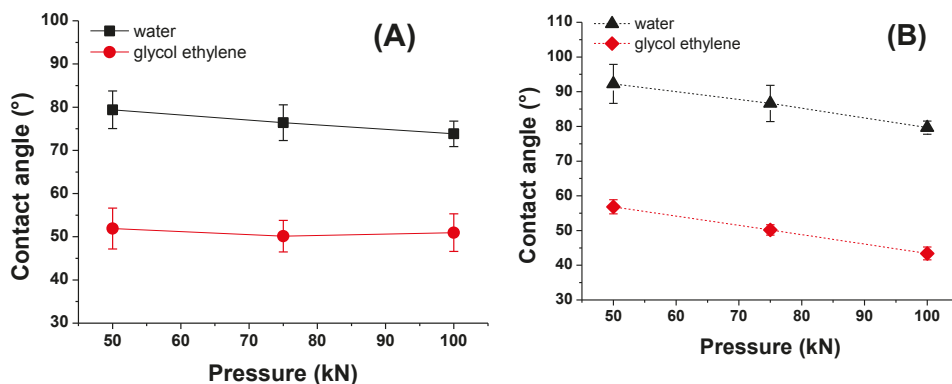


Figure 11. Contact angle vs. laminating pressure of (A) PAN; (B) PVDF multilayer nanofibrous membranes.

The morphology of the nanofiber webs, including their pore size, shape, size distribution and porosity, has a significant influence on the air permeability of the multilayer membrane. To investigate the effect of laminating pressure on the air permeability of the multilayer nanofibrous membranes, the samples were placed on a circular sample holder, and the air flow rates through the samples were measured (Figure 12A). Like the air flows, the areas of the sample and pressure drop remained constant

during the measurement. Due to the weakness of neat nanofiber layers, the air permeability test was not performed. In a previous study [31], the tensile strength of the nanofiber layers was found to be between 3 and 4.33 (N/25 mm), which is extremely low to withstand any external force.

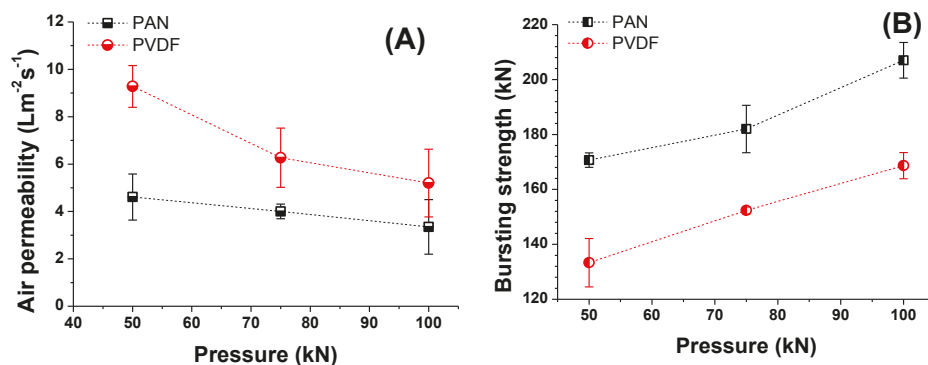


Figure 12. Influence of laminating pressure on (A) air permeability; and (B) bursting strength of multilayer nanofibrous membranes.

Abuzade et al. [50] studied the effects of the process parameters (e.g., concentration of solution, applied voltage) on the porosity and air permeability of an electrospun nanoweb. The results showed that the nanofiber diameter and size distribution are dominant parameters in controlling the pore sizes formed by the nanofiber intersections and air permeability of the electrospun web. Figure 12A showed that increasing the laminating pressure lowered the air permeability of the multilayer membranes. Compression of the melting adhesive, filling the pores of the nanofiber and nonwoven web, covered the surface of the thin nanofiber layer and created a non-porous film (Figure 10). As a result, the breathability of the membranes was decreased. Similarly, Kanafchian et al. [32] claimed that during the lamination, the melt adhesive penetrates through the nanofiber/fabric structure, which leads to filling of the pores of the nanofibers and a decrease in air permeability. The PAN multilayer nanofibrous membrane has a lower air permeability than PVDF, mainly due to the lower fiber diameter of the PAN nanofibers compared to the PVDF nanofibers. Rajak et al. [51] prepared PAN nanofiber webs from various concentrations. The results indicated that changes in concentration affect the fiber diameter. At a higher concentration and fiber diameter, the air permeability has a higher value.

A bursting test was performed to determine the mechanical strength of the laminated layers, and the results are shown in Figure 12B. The test method has been developed in our laboratory. The maximum delamination point of the multilayer nanofibrous membranes was measured using hydrostatic pressure. The results showed that PAN nanofibers have a better adhesion to the supporting layer and a better bursting strength compared to PVDF. The adhesion between the layers is related to the material surface chemistry and its influence on adhesion, together with the properties of adhesive materials and interactions at the adhesive-substrate surface interface. Materials that can wet each other tend to have a better adhesion, and the wettability of the material is related to its surface energy. For instance, low surface energy materials such as poly(tetrafluoroethylene), ceramics, and silicon, are resistant to wetting and adhesive bonding [52]. Lee et al. [53] found that the surface energy of PAN is around 44 mJ/m², while this value was calculated as 54.1 mJ/m² by Pritykin et al. [54]. On the other hand, PVDF has a very low surface energy value of around 26 mJ/m² [55]. Due to the lower surface energy of PVDF compared to PAN, the adhesion between the layers is weaker, which results in low lamination strength. The results show that laminating pressure plays an important role in the bursting strength. By increasing the laminating pressure under heat, the melted adhesive fills the pores of the nanofibers and nonwovens and penetrates through the layers. A better mechanical strength is

achieved due to the entanglement of the adhesive web and the layers. The results showed that the bursting strength of a material can be improved by adjusting the lamination conditions.

3.2. Evaluation of Liquid Filtration by Cross-Flow Filtration

Taking their practical applications into consideration, laminated multilayer nanofibrous membranes were used to further investigate their water permeability performance due to their hydrophilic, porous, small pore size and predominant mechanical properties for liquid filtration. A cross-flow filtration unit was prepared in our laboratory. Using Equation (5), the water permeability of the PAN and PVDF multilayer nanofibrous membranes was calculated (Figures 13 and 14).

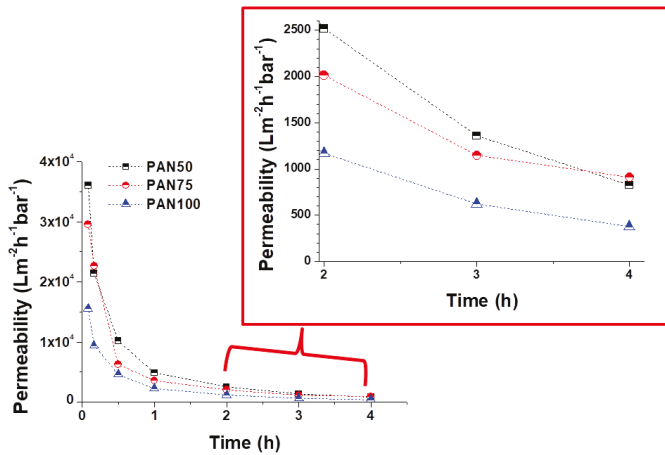


Figure 13. Permeability of PAN multilayer nanofibrous membranes at various laminating pressures over time.

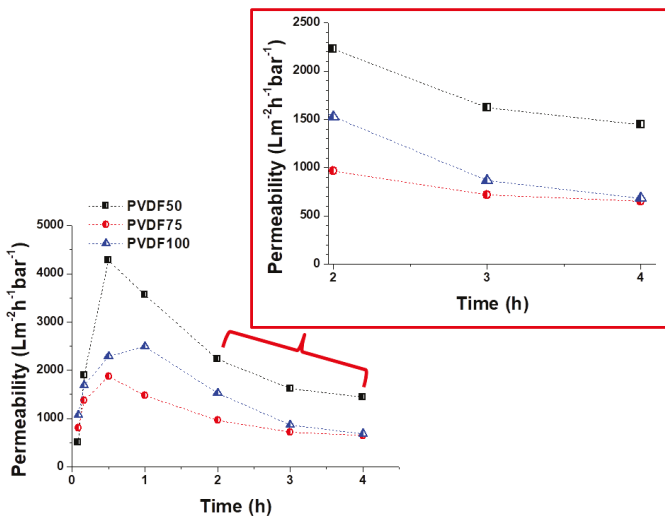


Figure 14. Permeability of PVDF multilayer nanofibrous membranes at various laminating pressures over time.

A decrease in permeability was observed for both the PAN and PVDF multilayer nanofibrous membranes depending on the operation time as shown in Figures 13 and 14. There are a few possible reasons for the decrease in permeability during liquid filtration. The first reason is concentration polarization, which is a consequence of the selectivity of the membrane. When the liquid passes through the membrane, the solute is retained by the membrane surface with a relatively high concentration. Moreover, the hydrophilicity of the membrane decreases over time during filtration due to membrane fouling and concentration polarization. Since tap water is not pure, dissolved molecules, suspended solids, and organics may be contained in the water, which can cause a decrease in the water flux due to fouling. The second reason is that close to the membrane surface, the effective transmembrane pressure (TMP) driving force reduces due to an osmotic pressure difference between the filtrate and the feed solution. TPM is generally observed in the case of ultra-filtration (UF) membranes. Another reason may be related to the compression/collapse of membrane pores, thereby causing a reduction in water permeability. The operating conditions (feed pressure, temperature, pH, flow rate, etc.) are also effective factors in membrane permeability. In general, the flux decline is caused by a decreased driving force and/or an increased resistance of the membrane, raw water characteristics, and particulate matter levels [56–58].

At the beginning, all the PAN membranes had the highest permeability (Figure 13). After a 4-h filtration test, the flux declined to 824, 909, and 375 $\text{Lm}^{-2}\text{h}^{-1}\text{bar}^{-1}$ in the case of PAN50, PAN75, and PAN100, respectively. The results indicated that laminating pressure has a huge impact on the water permeability of the multilayer membranes. The laminating pressure and the permeability of the membranes showed a non-linear relationship in the case of the PAN membranes. PAN50 and PAN75 multilayer nanofibrous membranes showed the best water permeability. On the other hand, all the PVDF membranes showed very low initial permeability at the beginning due to the hydrophobic nature of the PVDF nanofibers, and the melted adhesive web partially occupied the membrane pores, increasing the hydraulic resistance to filtration (Figure 14). The results of 4 h of filtration of PVDF membranes showed that the highest permeability ($1444 \text{ Lm}^{-2}\text{h}^{-1}\text{bar}^{-1}$) was only achieved at the lowest laminating pressure (50 kN). PVDF75 and PVDF100 had almost the same permeability value (650 and $681 \text{ Lm}^{-2}\text{h}^{-1}\text{bar}^{-1}$, respectively) after the 4-h filtration test. Li et al. [59] reported a simple strategy to improve the waterproof/breathable performance and mechanical properties of electrospun PVDF fibrous membranes using a thermo-pressing system. It was found that the effect of temperature and pressure on PVDF has a synergistic effect on the fiber morphology and crystal structure. By properly adjusting the temperature and pressure, robust mechanical properties and excellent waterproof/breathable performance of PVDF membranes were achieved.

In terms of water permeability, PAN75 has the best results from the PAN membranes. PVDF50 showed the best permeability results after the 4-h filtration test from all the PAN and PVDF membranes. The results showed that after proper lamination multilayer nanofibrous membranes are suitable for future application in liquid filtration.

4. Conclusions

There is a huge demand for the filtration application of nanofiber layers due to their specific surface, low pore size and high porosity. In this study, the effect of laminating pressure on PAN and PVDF multilayer nanofibrous membranes was investigated to prepare suitable microfilters for liquid filtration. The surface morphology, average pore size, air permeability, water permeability, bursting strength, and the contact angle of the membranes were compared. Different performance levels were achieved by varying the laminating pressure of the multilayer nanofibrous membranes. The pressure effect had a considerable influence on air permeability, average pore size, contact angle, bursting strength, and water permeability. The surface morphology results showed that the fiber diameter slightly increased with an increase in laminating pressure, while the water and ethylene glycol contact angles decreased. The main effect of laminating pressure was observed on the average pore size, air permeability, bursting strength and water permeability of the membranes. PVDF50 showed the

best water filtration of all the membranes. However, the bursting strength of PVDF50 is the lowest, which may cause possible damage and delamination of the layers under pressure over time. PAN nanofibers have a better adhesion to the surface of the multilayer. PAN75 was selected as the best candidate for liquid filtration due to its high water permeability and mechanical strength. PVDF multilayer nanofibrous membranes showed better air permeability than PAN, which may be better for the possible application of air filtration. These findings imply that to achieve the best permeable membrane results, the lamination process should be carefully optimized.

Author Contributions: Fatma Yalcinkaya conceived and designed the experiments; Fatma Yalcinkaya performed the experiments; Fatma Yalcinkaya analyzed the data; Jakub Hruza contributed reagents/materials/analysis tools and preparation of tools; Fatma Yalcinkaya wrote the paper.

Acknowledgments: This work was supported by project LO1201 obtained through the financial support of the Ministry of Education, Youth and Sports in the framework of the targeted support of the “National Program for Sustainability I” and the OPR&DI project CZ.1.05/2.1.00/19.0386.

Conflicts of Interest: The authors declare that there is no conflict of interest.

References

- Gao, J.; Zhu, J.; Luo, J.; Xiong, J. Investigation of microporous composite scaffolds fabricated by embedding sacrificial polyethylene glycol microspheres in nanofibrous membrane. *Compos. Part A Appl. Sci. Manuf.* **2016**, *91*, 20–29. [[CrossRef](#)]
- Tang, Y.; Chen, L.; Zhao, K.; Wu, Z.; Wang, Y.; Tan, Q. Fabrication of PLGA/HA (core)-collagen/amoxicillin (shell) nanofiber membranes through coaxial electrospinning for guided tissue regeneration. *Compos. Sci. Technol.* **2016**, *125*, 100–107. [[CrossRef](#)]
- Zhang, W.; Ronca, S.; Mele, E. Electrospun nanofibres containing antimicrobial plant extracts. *Nanomaterials* **2017**, *7*, 42. [[CrossRef](#)] [[PubMed](#)]
- Sill, T.J.; von Recum, H.A. Electrospinning: Applications in drug delivery and tissue engineering. *Biomaterials* **2008**, *29*, 1989–2006. [[CrossRef](#)] [[PubMed](#)]
- Tan, L.; Gan, L.; Hu, J.; Zhu, Y.; Han, J. Functional shape memory composite nanofibers with graphene oxide filler. *Compos. Part A Appl. Sci. Manuf.* **2015**, *76*, 115–123. [[CrossRef](#)]
- Zhao, X.G.; Jin, E.M.; Park, J.Y.; Gu, H.B. Hybrid polymer electrolyte composite with SiO₂ nanofiber filler for solid-state dye-sensitized solar cells. *Compos. Sci. Technol.* **2014**, *103*, 100–105. [[CrossRef](#)]
- Yoon, B.; Lee, S. Designing waterproof breathable materials based on electrospun nanofibers and assessing the performance characteristics. *Fibers Polym.* **2011**, *12*, 57–64. [[CrossRef](#)]
- Fehse, M.; Cavaliere, S.; Lippens, P.E.; Savych, I.; Iadecola, A.; Monconduit, L.; Jones, D.J.; Rozière, J.; Fischer, F.; Tessier, C.; et al. Nb-doped TiO₂ nanofibers for lithium ion batteries. *J. Phys. Chem. C* **2013**, *117*, 13827–13835. [[CrossRef](#)]
- Aydın, H.; Çelik, S.Ü.; Bozkurt, A. Electrolyte loaded hexagonal boron nitride/polyacrylonitrile nanofibers for lithium ion battery application. *Solid State Ionics* **2017**, *309*, 71–76. [[CrossRef](#)]
- Wang, X.; Drew, C.; Lee, S.H.; Senecal, K.J.; Kumar, J.; Samuelson, L.A. Electrospun nanofibrous membranes for highly sensitive optical sensors. *Nano Lett.* **2002**, *2*, 1273–1275. [[CrossRef](#)]
- Liu, P.; Wu, S.; Zhang, Y.; Zhang, H.; Qin, X. A fast response ammonia sensor based on coaxial PPy–PAN nanofiber yarn. *Nanomaterials* **2016**, *6*, 121. [[CrossRef](#)] [[PubMed](#)]
- Macagnano, A.; Perri, V.; Zampetti, E.; Bearzotti, A.; De Cesare, F.; Sprovieri, F.; Pirrone, N. A smart nanofibrous material for adsorbing and detecting elemental mercury in air. *Atmos. Chem. Phys.* **2017**, *17*, 6883–6893. [[CrossRef](#)]
- Zhang, X.F.; Feng, Y.; Huang, C.; Pan, Y.; Yao, J. Temperature-induced formation of cellulose nanofiber film with remarkably high gas separation performance. *Cellulose* **2017**, *24*, 5649–5656. [[CrossRef](#)]
- Zampetti, E.; Pantalei, S.; Bearzotti, A.; Bongiorno, C.; De Cesare, F.; Spinella, C.; Macagnano, A. TiO₂ nanofibrous chemoresistors coated with PEDOT and PANi blends for high performance gas sensors. In *Procedia Engineering*; Elsevier: Amsterdam, The Netherlands, 2012; Volume 47, pp. 937–940.
- Ge, J.; Choi, N. Fabrication of functional polyurethane/rare earth nanocomposite membranes by electrospinning and its VOCs absorption capacity from air. *Nanomaterials* **2017**, *7*, 60. [[CrossRef](#)] [[PubMed](#)]

16. Desai, K.; Kit, K.; Li, J.; Michael Davidson, P.; Zivanovic, S.; Meyer, H. Nanofibrous chitosan non-wovens for filtration applications. *Polymer* **2009**, *50*, 3661–3669. [[CrossRef](#)]
17. Liao, Y.; Tian, M.; Wang, R. A high-performance and robust membrane with switchable super-wettability for oil/water separation under ultralow pressure. *J. Memb. Sci.* **2017**, *543*, 123–132. [[CrossRef](#)]
18. Li, Z.; Kang, W.; Zhao, H.; Hu, M.; Wei, N.; Qiu, J.; Cheng, B. A novel polyvinylidene fluoride tree-like nanofiber membrane for microfiltration. *Nanomaterials* **2016**, *6*, 152. [[CrossRef](#)] [[PubMed](#)]
19. Sood, R.; Cavaliere, S.; Jones, D.J.; Rozière, J. Electrospun nanofibre composite polymer electrolyte fuel cell and electrolysis membranes. *Nano Energy* **2016**, *26*, 729–745. [[CrossRef](#)]
20. Yalcinkaya, F. Preparation of various nanofiber layers using wire electrospinning system. *Arab. J. Chem.* **2016**. [[CrossRef](#)]
21. Ding, Y.; Zhang, P.; Long, Z.; Jiang, Y.; Xu, F.; Di, W. The ionic conductivity and mechanical property of electrospun P(VdF-HFP)/PMMA membranes for lithium ion batteries. *J. Memb. Sci.* **2009**, *329*, 56–59. [[CrossRef](#)]
22. Jahanbaani, A.R.; Behzad, T.; Borhani, S.; Darvanjooghi, M.H.K. Electrospinning of cellulose nanofibers mat for laminated epoxy composite production. *Fibers Polym.* **2016**, *17*, 1438–1448. [[CrossRef](#)]
23. Charles, L.E.; Kramer, E.R.; Shaw, M.T.; Olson, J.R.; Wei, M. Self-reinforced composites of hydroxyapatite-coated PLLA fibers: Fabrication and mechanical characterization. *J. Mech. Behav. Biomed. Mater.* **2012**, *17*, 269–277. [[CrossRef](#)] [[PubMed](#)]
24. Iqbal, Q.; Bernstein, P.; Zhu, Y.; Rahamim, J.; Cebe, P.; Staii, C. Quantitative analysis of mechanical and electrostatic properties of poly(lactic) acid fibers and poly(lactic) acid-carbon nanotube composites using atomic force microscopy. *Nanotechnology* **2015**, *26*, 105702. [[CrossRef](#)] [[PubMed](#)]
25. Charles, L.F.; Shaw, M.T.; Olson, J.R.; Wei, M. Fabrication and mechanical properties of PLLA/PCL/HA composites via a biomimetic, dip coating, and hot compression procedure. *J. Mater. Sci. Mater. Med.* **2010**, *21*, 1845–1854. [[CrossRef](#)] [[PubMed](#)]
26. Xu, Y.; Zhang, X.; Wang, X.; Wang, X.; Li, X.; Shen, C.; Li, Q. Simultaneous enhancements in the strength, modulus and toughness of electrospun polymeric membranes. *RSC Adv.* **2017**, *7*. [[CrossRef](#)]
27. Jiříček, T.; Komárek, M.; Chaloupek, J.; Lederer, T. Maximising flux in direct contact membrane distillation using nanofibre membranes. *Desalin. Water Treat.* **2017**, *73*, 249–255. [[CrossRef](#)]
28. Jiříček, T.; Komárek, M.; Chaloupek, J.; Lederer, T. Flux enhancement in membrane distillation using nanofiber membranes. *J. Nanomater.* **2016**, *2016*, 1–7. [[CrossRef](#)]
29. Yalcinkaya, B.; Yalcinkaya, F.; Chaloupek, J. Thin film nanofibrous composite membrane for dead-end seawater desalination. *J. Nanomater.* **2016**, *2016*, 1–12. [[CrossRef](#)]
30. Yalcinkaya, B.; Yalcinkaya, F.; Chaloupek, J. Optimisation of thin film composite nanofiltration membranes based on laminated nanofibrous and nonwoven supporting material. *Desalin. Water Treat.* **2017**, *59*, 19–30. [[CrossRef](#)]
31. Yalcinkaya, F.; Yalcinkaya, B.; Hruza, J.; Hrabak, P. Effect of nanofibrous membrane structures on the treatment of wastewater microfiltration. *Sci. Adv. Mater.* **2016**, *9*, 747–757. [[CrossRef](#)]
32. Kanafchian, M.; Valizadeh, M.; Haghi, A.K. A study on the effects of laminating temperature on the polymeric nanofiber web. *Korean J. Chem. Eng.* **2011**, *28*, 445–448. [[CrossRef](#)]
33. Yao, M.; Woo, Y.C.; Tijing, L.D.; Shim, W.-G.; Choi, J.-S.; Kim, S.-H.; Shon, H.K. Effect of heat-press conditions on electrospun membranes for desalination by direct contact membrane distillation. *Desalination* **2016**, *378*, 80–91. [[CrossRef](#)]
34. Mohammadian, M.; Haghi, A.K. Study on the production of a new generation of electrospun nanofiber webs. *Bulg. Chem. Commun.* **2014**, *46*, 530–534.
35. Yalcinkaya, F.; Siekierka, A.; Bryjak, M. Preparation of fouling-resistant nanofibrous composite membranes for separation of oily wastewater. *Polymers* **2017**, *9*, 679. [[CrossRef](#)]
36. Yalcinkaya, F.; Yalcinkaya, B.; Pazourek, A.; Mullerova, J.; Stuchlik, M.; Maryska, J. Surface modification of electrospun PVDF/PAN nanofibrous layers by low vacuum plasma treatment. *Int. J. Polym. Sci.* **2016**, *2016*, 1–9. [[CrossRef](#)]
37. Gopalan, A.I.; Santhosh, P.; Manesh, K.M.; Nho, J.H.; Kim, S.H.; Hwang, C.G.; Lee, K.P. Development of electrospun PVdF-PAN membrane-based polymer electrolytes for lithium batteries. *J. Memb. Sci.* **2008**, *325*, 683–690. [[CrossRef](#)]

38. Liu, T.-Y.; Lin, W.-C.; Huang, L.-Y.; Chen, S.-Y.; Yang, M.-C. Surface characteristics and hemocompatibility of PAN/PVDF blend membranes. *Polym. Adv. Technol.* **2005**, *16*, 413–419. [[CrossRef](#)]
39. Hammami, M.A.; Krifa, M.; Harzallah, O. Centrifugal force spinning of PA6 nanofibers—Processability and morphology of solution-spun fibers. *J. Text. Inst.* **2014**, *105*, 637–647. [[CrossRef](#)]
40. Essalhi, M.; Khayet, M. Self-sustained webs of polyvinylidene fluoride electrospun nano-fibers: Effects of polymer concentration and desalination by direct contact membrane distillation. *J. Memb. Sci.* **2014**, *454*, 133–143. [[CrossRef](#)]
41. Beachley, V.; Wen, X. Effect of electrospinning parameters on the nanofiber diameter and length. *Mater. Sci. Eng. C Mater. Biol. Appl.* **2009**, *29*, 663–668. [[CrossRef](#)] [[PubMed](#)]
42. Lowery, J.L.; Datta, N.; Rutledge, G.C. Effect of fiber diameter, pore size and seeding method on growth of human dermal fibroblasts in electrospun poly(ϵ -caprolactone) fibrous mats. *Biomaterials* **2010**, *31*, 491–504. [[CrossRef](#)] [[PubMed](#)]
43. Bagherzadeh, R.; Najar, S.S.; Latifi, M.; Tehran, M.A.; Kong, L. A theoretical analysis and prediction of pore size and pore size distribution in electrospun multilayer nanofibrous materials. *J. Biomed. Mater. Res. Part A* **2013**, *101*, 2107–2117. [[CrossRef](#)] [[PubMed](#)]
44. Gockeln, M.; Pokhrel, S.; Meierhofer, F.; Glenneberg, J.; Schowalter, M.; Rosenauer, A.; Fritsching, U.; Busse, M.; Mädler, L.; Kun, R. Fabrication and performance of Li₄Ti₅O₁₂/C Li-ion battery electrodes using combined double flame spray pyrolysis and pressure-based lamination technique. *J. Power Sources* **2018**, *374*, 97–106. [[CrossRef](#)]
45. Stiubianu, G.; Nicolescu, A.; Nistor, A.; Cazacu, M.; Varganici, C.; Simionescu, B.C. Chemical modification of cellulose acetate by allylation and crosslinking with siloxane derivatives. *Polym. Int.* **2012**, *61*, 1115–1126. [[CrossRef](#)]
46. Law, K.-Y.; Zhao, H. Wetting on rough surfaces. In *Surface Wetting*; Springer International Publishing: Cham, Switzerland, 2016; pp. 55–98.
47. Youngblood, J.P.; McCarthy, T.J. Ultrahydrophobic polymer surfaces prepared by simultaneous ablation of polypropylene and sputtering of poly(tetrafluoroethylene) using radio frequency plasma. *Am. Chem. Soc. Polym. Prepr. Div. Polym. Chem.* **1999**, *40*, 563–564. [[CrossRef](#)]
48. Chen, W.; Fadeev, A.Y.; Hsieh, M.C.; Öner, D.; Youngblood, J.; McCarthy, T.J. Ultrahydrophobic and ultralyophobic surfaces: Some comments and examples. *Langmuir* **1999**, *15*, 3395–3399. [[CrossRef](#)]
49. Wenzel, R.N. Surface roughness and contact angle. *J. Phys. Colloid Chem.* **1949**, *53*, 1466–1467. [[CrossRef](#)]
50. Abuzade, R.A.; Zadhoush, A.; Gharehaghaji, A.A. Air permeability of electrospun polyacrylonitrile nanoweb. *J. Appl. Polym. Sci.* **2012**, *126*, 232–243. [[CrossRef](#)]
51. Rajak, A. Synthesis of electrospun nanofibers membrane and its optimization for aerosol filter application. *KnE Eng.* **2016**, *1*. [[CrossRef](#)]
52. Von Fraunhofer, J.A. Adhesion and cohesion. *Int. J. Dent.* **2012**, *2012*, 1–8. [[CrossRef](#)] [[PubMed](#)]
53. Lee, L.-H. Relationships between surface wettability and glass temperatures of high polymers. *J. Appl. Polym. Sci.* **1968**, *12*, 719–730. [[CrossRef](#)]
54. Pritykin, L.M. Calculation of the surface energy of homo- and copolymers from the cohesion parameters and refractometric characteristics of the respective monomers. *J. Colloid Interface Sci.* **1986**, *112*, 539–543. [[CrossRef](#)]
55. Chen, N.; Hong, L. Surface phase morphology and composition of the casting films of PVDF-PVP blend. *Polymer* **2001**, *43*, 1429–1436. [[CrossRef](#)]
56. Kim, K.-M.; Woo, S.; Lee, J.; Park, H.; Park, J.; Min, B. Improved permeate flux of PVDF ultrafiltration membrane containing PVDF-g-PHEA synthesized via ATRP. *Appl. Sci.* **2015**, *5*, 1992–2008. [[CrossRef](#)]
57. Van den Berg, G.B.; Smolders, C.A. Flux decline in ultrafiltration processes. *Desalination* **1990**, *77*, 101–133. [[CrossRef](#)]
58. Meier-Haack, J.; Booker, N.A.; Carroll, T. A permeability-controlled microfiltration membrane for reduced fouling in drinking water treatment. *Water Res.* **2003**, *37*, 585–588. [[CrossRef](#)]
59. Li, X.; Lin, J.; Bian, F.; Zeng, Y. Improving waterproof/breathable performance of electrospun poly(vinylidene fluoride) fibrous membranes by thermo-Pressing. *J. Polym. Sci. Part B Polym. Phys.* **2017**, *56*, 1–10. [[CrossRef](#)]





Article

Porous Aluminum Oxide and Magnesium Oxide Films Using Organic Hydrogels as Structure Matrices

Zimei Chen ^{1,2}, Dirk Kuckling ^{1,*} and Michael Tiemann ^{2,*}

¹ Department of Chemistry—Organic and Macromolecular Chemistry, Paderborn University, 33098 Paderborn, Germany; zimei.chen@uni-paderborn.de

² Department of Chemistry—Inorganic Functional Materials, Paderborn University, 33098 Paderborn, Germany

* Correspondence: dirk.kuckling@uni-paderborn.de (D.K.); michael.tiemann@uni-paderborn.de (M.T.); Tel.: +49-525-160-2171 (D.K.); +49-525-160-2154 (M.T.)

Received: 25 February 2018; Accepted: 21 March 2018; Published: 22 March 2018



Abstract: We describe the synthesis of mesoporous Al₂O₃ and MgO layers on silicon wafer substrates by using poly(dimethylacrylamide) hydrogels as porogenic matrices. Hydrogel films are prepared by spreading the polymer through spin-coating, followed by photo-cross-linking and anchoring to the substrate surface. The metal oxides are obtained by swelling the hydrogels in the respective metal nitrate solutions and subsequent thermal conversion. Combustion of the hydrogel results in mesoporous metal oxide layers with thicknesses in the μm range and high specific surface areas up to 558 m²·g⁻¹. Materials are characterized by SEM, FIB ablation, EDX, and Kr physisorption porosimetry.

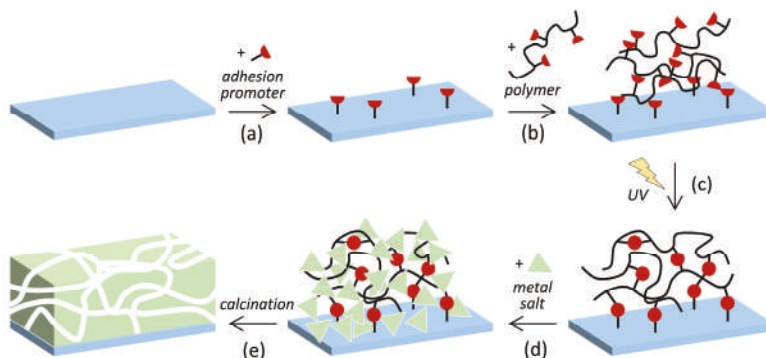
Keywords: mesoporous; Al₂O₃; MgO; poly(dimethylacrylamide); hydrogel; thin film; spin coating; SEM; FIB; Kr physisorption

1. Introduction

The synthesis of metal oxides with uniform mesopores is often achieved by utilization of porogenic structure directors or matrices. For example, micellar aggregates of amphiphilic species—such as surfactants or block co-polymers—are frequently utilized as porogens. They form spontaneously by self-organization and serve as pore fillers or even as structure-directing species during the formation of the inorganic phase by a sol–gel-based synthesis (‘soft templating’) [1,2]. This synthesis method is applicable to a limited variety of inorganic products, such as silica and some other oxidic materials, including aluminum oxide (Al₂O₃) [3–5]. For uniform, continuous layers (‘solid films’) of mesoporous metal oxides at a substrate surface the soft-templating approach is usually the method of choice, because the spontaneous self-aggregation into micellar units can take place inside a liquid film that contains both the amphiphilic species and the inorganic precursor compounds. For this purpose, the micellization is induced by evaporation of the solvent (evaporation-induced self-assembly, EISA) [6,7]. It needs to be stressed, though, that several metal oxides cannot be obtained in this way as their formation may go along with phase-separation and segregation from the amphiphilic species. As an alternative, the concept of using solid, porous structure matrices (‘hard templates’) has been shown to be a more versatile option [8,9]. This method, often called ‘nanocasting’, comprises the synthesis of the desired products within the pores of a silica or carbon matrix, followed by selective removal of the matrix; the product is obtained as a ‘replica’ of the pore system in the matrix. Nanocasting can be used for the fabrication of a multitude of metal oxides, including Al₂O₃ [10–12], as well as those that have so far not been obtained by soft templating, e.g., magnesium oxide (MgO) [12–15]. However, the nanocasting concept still has its limitations when it comes to the synthesis of porous films, since the removal of the structure matrix may cause detachment of the replica film from the substrate.

We have recently described the synthesis of mesoporous metal oxides by using poly(dimethylacrylamide) hydrogels as matrices [16,17]. Hydrogels are three-dimensional structures composed of hydrophilic polymer chains, which can absorb and hold large quantities of water in the spaces between the chains [18]. They can be fabricated via physical or chemical cross-linking [19] and have been used as matrices for porous inorganic materials [16,17,20–22]. Their utilization as porogenic matrices may be regarded as halfway between ‘soft’ and ‘hard templating’. The hydrogel forms a continuous network that can take up the inorganic precursor species (such as a metal salt) with no risk of phase-separation, similar to a hard structure matrix. At the same time, the swollen hydrogel is a highly flexible phase; the (cross-linked) polymer strands are more or less loosely arranged and displaceable, like a soft matrix. In fact, the porogenic impact may even occur when the water-soluble polymer strands are not even cross-linked, but only sterically entangled [23]. We have rationalized that thick bundles of polymer chains (rather than single, individual chains) in poly(dimethylacrylamide) hydrogels form the porogenic entities [16]. The products obtained so far were powders with somewhat uniform mesopores and high specific surface areas.

Here we report on utilizing the same kind of porogenic hydrogels for mesoporous layers (solid films) of aluminum oxide (Al_2O_3) and magnesium oxide (MgO) at the surface of silicon wafer substrates. Photo-cross-linked poly(dimethylacrylamide) hydrogels are attached to the substrate by chemical bonding and serve as matrices for the metal oxides (Scheme 1). Porous Al_2O_3 and MgO with a high surface-to-volume ratio play an important role in separation [24,25] and heterogeneous catalysis [26–29]. Especially for the latter application immobilized layers of the catalyst (MgO) or support (Al_2O_3) materials with large pores are considered advantageous to facilitate easy access of the reactants by diffusion.



Scheme 1. Preparation of porous metal oxide (Al_2O_3 , MgO) layers: (a) anchoring of the adhesion promoter on the Si wafer substrate; (b) spreading of the polymer by spin coating; (c) hydrogel formation and immobilization on the substrate by photo-induced cross-linking; (d) swelling in metal salt solution ($\text{Al}(\text{NO}_3)_3$, $\text{Mg}(\text{NO}_3)_2$); (e) formation of the porous metal oxide and combustion of the hydrogel by calcination.

2. Materials and Methods

Materials: Acryloyl chloride (Alfa Aesar, Karlsruhe, Germany, 96%), allylamine (Sigma-Aldrich, Taufkirchen, Germany, 98%), aluminum nitrate nonahydrate (Sigma-Aldrich, $\geq 98.0\%$), ammonia solution (Stockmeier, Bielefeld, Germany, 25%), bicyclohexyl (Acros, Geel, Belgium, 99%), chloroform (Stockmeier), chlorodimethylsilane (Alfa Aesar, 97%), 1,2-diaminoethane (Acros, $>99\%$), 2,3-dimethylmaleic anhydride (Acros, 97%), di-*tert*-butyl dicarbonate (Boc_2O , Acros, 97%), ethanol, absolute (Sigma-Aldrich), hydrochloric acid, conc. (Stockmeier, 37%), hydrogen peroxide (Stockmeier, 35%), magnesium nitrate hexahydrate (Sigma-Aldrich, $\geq 97\%$), magnesium sulfate (Grüssing, Filsum, Germany, 99%),

platinum(0)-1,3-divinyl-1,1,3,3-tetramethyldisiloxane complex solution in xylene (Sigma-Aldrich, Pt ~2%), 4''-silicon-wafer (Plano, Wetzlar, Germany), sulfuric acid, conc. (Stockmeier, ≥98%), thioxanthone (Sigma-Aldrich, 98%), and triethylamine (TEA, Grüssing, 99%) were used as received. Acetone (Stockmeier), diethyl ether (Hanke+Seidel, Steinfurt, Germany), ethyl acetate (Stockmeier), *n*-hexane (Stockmeier), methanol (Stockmeier), *n*-pentane (Stockmeier), silica gel (VWR), sodium bicarbonate (Stockmeier), and sodium chloride (Stockmeier) were of technical grade and used as received. 1,4-Dioxane (Carl Roth, Karlsruhe Germany, ≥99.5%), *N,N*-Dimethylacrylamide (DMAAm, TCI, Eschborn, Germany, 99%), tetrahydrofuran (THF, BASF, Ludwigshafen, Germany), and toluene (Grüssing, 99.5%) were distilled under low pressure. α,α' -Azobisisobutyronitrile (AIBN, Fluka, Seelze, Germany, >98%) was recrystallized from methanol. Cyclohexanone (Sigma-Aldrich, ≥99.0%) was distilled. Dichloromethane (Stockmeier) was dried over CaCl₂ and distilled.

Characterization: ¹H and ¹³C NMR spectra were recorded on a Bruker AV 500 spectrometer at 500 MHz and 125 MHz, respectively. Reference solvent signals at 7.26 and 2.56 ppm were used for spectra in CDCl₃ (99.8 atom % Deuterium) and DMSO-d₆ (O=S(CD₃)₂, 99.9%), respectively. Gel permeation chromatography (GPC) was performed in chloroform for PDMAAm at 30 °C and at a flow rate of 0.75 mL·min⁻¹ on a Jasco 880-PU Liquid Chromatograph connected to a Shodex RI-101 Detector. The instrument was equipped with four consecutive columns (PSS-SDV columns filled with 5 μm gel particles with a defined porosity of 10⁶ Å, 10⁵ Å, 10³ Å and 10² Å, respectively) and were calibrated by poly(methyl methacrylate) standards. Krypton (Kr) physisorption analysis was performed at 77 K on a Quantachrome Autosorb 6B instrument. The masses of the films were determined by weighing the wafer substrates before and after film synthesis. Several samples of identical films (7 × 7 mm substrate dimensions) were combined for each sorption measurement to provide sufficient overall film masses (1–200 mg). Samples were degassed at 120 °C for 12 h prior to measurement. The specific surface areas were assessed by multi-point BET analysis [30] in the range 0.1 ≤ *p/p*₀ ≤ 0.3. Scanning electron microscopy (SEM) and energy-dispersive X-ray (EDX) spectroscopy were performed on a Zeiss NEON[®] 40 microscope connected with an UltraDry detector from Thermo Fisher Scientific (Waltham, MA, USA).

Cross-Linker Synthesis: 2-(Dimethyl maleimido)-*N*-ethyl-acrylamide (DMIAAm) was synthesized through a four-step reaction as described in the literature [31] and can be found in detail in the Supplementary Materials.

Polymer Synthesis: Poly(DMAAm-*co*-DMIAAm) was synthesized with DMAAm monomer and DMIAAm cross-linker by free radical polymerization initiated with AIBN in an analogous fashion as described in the literature [31]. DMAAm (95 mol %) and DMIAAm (5 mol %) and about 0.002 mol % AIBN relative to the total amount of monomer were dissolved in 1,4-dioxane and purged with argon for 20 min. The total monomer concentration was 1 mol·L⁻¹. The polymerization was carried out at 70 °C for 7 h under argon atmosphere. Afterwards, the polymer was precipitated in diethyl ether and re-precipitated from tetrahydrofuran into diethyl ether for purification. Finally, the polymer was dried in high vacuum and characterized by NMR spectroscopy and GPC. ¹H NMR (500 MHz, CDCl₃): δ (ppm) = 1.51–1.83 (m, CH₂), 1, 94 (s, CH₃), 2.3–2.75 (m, CH), 2.77–3.19 (m, N-CH₂, NH-CH₂, N-CH₃), 3.6 (b, NH). Yield: 88%, *M*_n: 39,000 g·mol⁻¹, DMIAAm composition: 5 mol % (Feed)/4.8 mol % (NMR), PD: 5.1.

Synthesis and Immobilization of the Adhesion Promoter: 1-[3-(Chloro-dimethyl-silanyl)-propyl]-3,4-dimethyl-maleimide was synthesized as described in the literature [32] (see Supplementary Materials). A Si wafer (7 mm × 7 mm) was activated with a mixture (7:3 vol.) of concentrated sulfuric acid (H₂SO₄) and 30% hydrogen peroxide (H₂O₂) solution at 90 °C for 1 h. After repeated rinsing with water and ethanol and drying in argon stream the adhesion promoter was absorbed from 1 vol % solution in bicyclohexyl for 24 h. Finally the wafer was rinsed with chloroform and abs. ethanol and dried in an argon flow.

Preparation of Hydrogel Films: Solutions of the polymer in cyclohexanone (2 mL) with 2 wt % thioxanthone as a sensitizer were spin-coated on a pre-treated Si wafer, using variable spin velocities

and polymer concentrations (see Results and Discussion section); polymer solutions were first spread at 250 rpm for 25 s, followed by 60 s of spinning at the final velocity. The polymer layer on the wafer was irradiated with UV light for one minute by using a 200 W mercury short arc lamp with an intensity of $266 \text{ mW}\cdot\text{cm}^{-2}$.

Preparation of Porous Al_2O_3 and MgO layers: For the preparation of Al_2O_3 , the hydrogel film was re-swelled in saturated aqueous aluminum nitrate solution ($1.9 \text{ mol}\cdot\text{L}^{-1}$) overnight and then treated with the vapor of an aqueous ammonia solution (12.5 wt %) for 3 h at 60°C to convert $\text{Al}(\text{NO}_3)_3$ to $\text{Al}(\text{OH})_3/\text{AlO}(\text{OH})$, followed by drying overnight at 60°C . The material was calcined in a tube furnace for 4 h at 500°C with a heating rate of $1^\circ\text{C}\cdot\text{min}^{-1}$ to combust the polymer and to form a porous Al_2O_3 film on the Si wafer. For the preparation of MgO the hydrogel film was re-swelled in saturated aqueous magnesium nitrate solution ($4.9 \text{ mol}\cdot\text{L}^{-1}$) overnight and then dried at 120°C . The material was calcined in a tube furnace for 2 h at 300°C and 2 h at 500°C with a heating rate of $1^\circ\text{C}\cdot\text{min}^{-1}$ to combust the polymer and to form a porous MgO film on the Si wafer.

In an alternative approach, the above-described preparation of the hydrogel film was modified by dissolving the polymer in methanol (instead of cyclohexanone) and by adding aluminum nitrate or magnesium nitrate to this solution before (instead of after) spin-coating (2500 rpm final spin velocity) and subsequent photo-cross-linking. Otherwise, the same synthesis protocol was used.

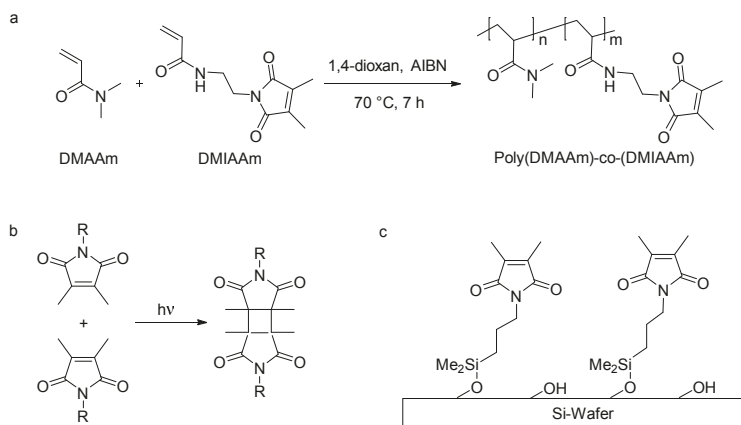
3. Results and Discussion

Photo-cross-linked hydrogel films were used as structure matrices for the preparation of porous alumina (Al_2O_3) and magnesia (MgO) layers. The polymer for the hydrogels was synthesized by free radical polymerization of *N,N*-dimethylacrylamide (DMAAm) and 2-(dimethyl maleimido)-*N*-ethyl-acrylamide (DMIAAm) (Scheme 2a). The synthesized polymers have a molecular weight (M_n) of ca. $39,000 \text{ g}\cdot\text{mol}^{-1}$. DMIAAm served as a photo-cross-linker to form a three-dimensional polymer network (Scheme 2b) by a reaction mechanism that can be primarily described as a [2+2] cycloaddition; however, other mechanisms are also possible [32]. According to NMR data the DMIAA fraction in the polymers is 4.8 mol %, slightly less than the feed composition (5 mol %), which is in accordance with previous findings [33]. To covalently attach the hydrogel to a silicon wafer substrate, 1-[3-(chloro-dimethyl-silylanyl)-propyl]-3,4-dimethyl-maleimide was used as an adhesion promoter. The promoter was applied to the wafer prior to coating with the polymer. For this purpose, the wafer surface was chemically activated by oxidative treatment with piranha solution ($\text{H}_2\text{SO}_4/\text{H}_2\text{O}_2$). The promoter bonds to the surface via its reactive chloro-silane function (Scheme 2c); the maleimide function can react with the polymer during photo-induced cross-linking.

Porous Al_2O_3 or MgO layers were created by pre-fabricating hydrogel films on the substrate and then adding the inorganic precursor species in a second step (Scheme 1). The polymer was spin-coated on the pretreated Si wafer by using cyclohexanone as a solvent. The polymer concentration and spin velocity were varied in order to obtain variable film thicknesses. Photo-cross-linking of the polymer film was then achieved by UV irradiation as described in the Experimental Section. The cross-linked network forms a thin hydrogel film at the Si wafer surface. Figure 1 shows example scanning electron microscopic (SEM) images of dry films exhibiting high degrees of homogeneity. (further examples are shown in Figure S1 in the Supplementary Materials). The film thicknesses were analyzed by focused ion beam (FIB) ablation. Figure 1d shows a rectangular hole cut out of the film. The image was taken from a tilted angle (ca. 45° to the film surface), showing both the section through the film and the underlying substrate. This way, the average thickness of the film can be measured; depending on polymer concentration and spin velocity it ranges from $0.187 \mu\text{m}$ to $0.851 \mu\text{m}$ (Table 1).

The hydrogel film was then impregnated with $\text{Al}(\text{NO}_3)_3$ or $\text{Mg}(\text{NO}_3)_2$ by swelling in a saturated aqueous solution of the respective salt. The Al salt was transformed to $\text{Al}(\text{OH})_3/\text{AlO}(\text{OH})$ by exposure to ammonia vapor and subsequently calcined to create Al_2O_3 ; this procedure is frequently applied for the structure-directed synthesis of Al_2O_3 [10,11]. The Mg salt was directly transformed to MgO by calcination. In both cases, the calcination procedure leads to the thermal combustion of the hydrogel

matrix, leaving behind metal oxide layers that remain attached to the Si wafer substrates (presumably by Si-O-Al bonds in case of Al₂O₃ and by ionic interaction with the charged oxidized Si surface in case of MgO, respectively). Identification of the metal oxide phases by XRD was not feasible due to the very low thickness of the layers (see below), but previous studies [16,17,23] have shown that the applied synthesis conditions lead to formation of γ -Al₂O₃ (with low crystallinity) and MgO, respectively.



Scheme 2. (a) Synthesis of the polymer serving as the precursor for the hydrogel films; (b) photo-cross-linking of the polymer; (c) schematic [19] of the adhesion promoter attachment to the Si wafer surface.

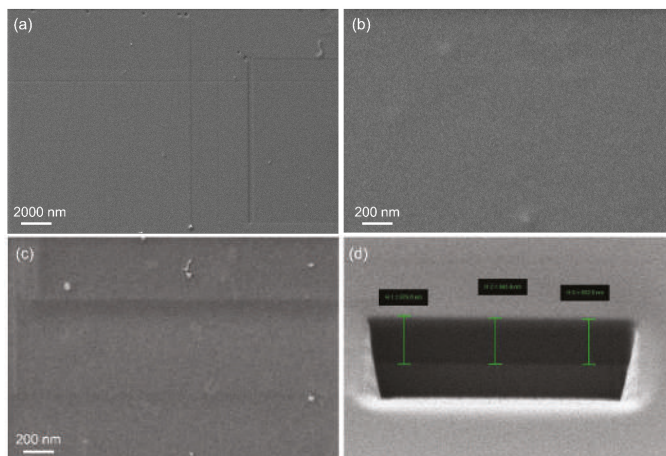


Figure 1. SEM images of dry hydrogel films prepared by spin-coating with variable polymer concentration and spin velocity (average film thicknesses: (a) 0.187 μm ; (b) 0.588 μm ; (c,d) 0.851 μm ; see Table 1). Image (d) shows an example of the FIB ablation analysis of a film (average thickness: 0.851 μm ; green bars: 0.8796, 0.8439, 0.8320 μm).

Table 1. Characteristics of dry hydrogel films obtained by spin-coating of the polymer and subsequent photo-cross-linking.

Spin Velocity (rpm)	Polymer Conc. (wt %)	Film Thickness (μm)
2500	5	0.187
2500	7.5	0.306
2500	10	0.588
1000	5	0.607
1000	7.5	0.801
1000	10	0.851

Figure 2 shows SEM images with FIB analysis of two examples of porous Al_2O_3 and MgO layers. (further examples are shown in Figure S2 in the Supplementary Materials) EXD analysis confirms the approximate stoichiometry of $\text{Al}/\text{O} = 1.5$ and $\text{Mg}/\text{O} = 1$, respectively (Table S1 in the Supplementary Materials). The Al_2O_3 layer (Figure 2a,b) exhibits a fairly smooth and homogeneous texture and an average thickness of $1.77 \mu\text{m}$, three times the thickness of the non-swollen (dry) hydrogel film that was used as the matrix ($0.588 \mu\text{m}$). This difference reflects the swelling of the hydrogel and also indicates a certain degree of porosity in the Al_2O_3 layer, as will be substantiated below.

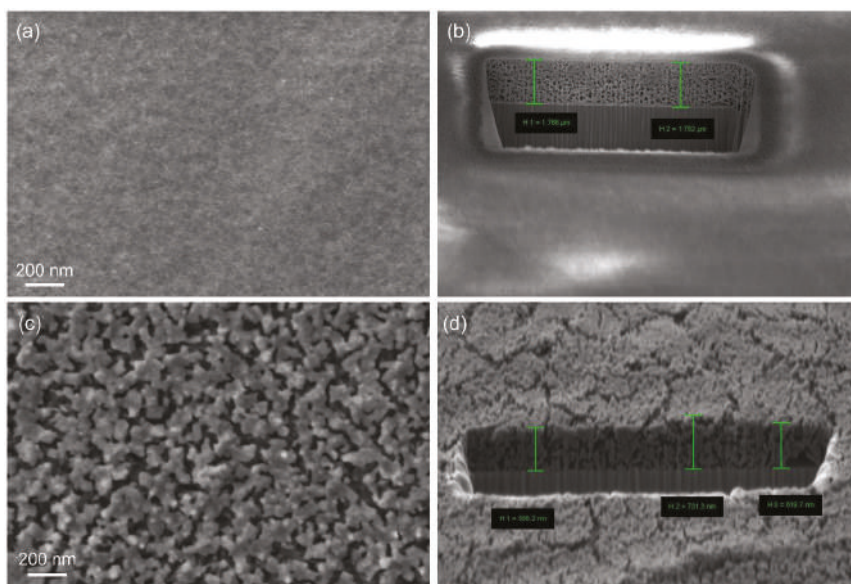


Figure 2. SEM images and FIB ablation analysis of two example layers of Al_2O_3 ((a,b); average thickness: $1.77 \mu\text{m}$, prepared with a hydrogel film of $0.588 \mu\text{m}$ thickness; green bars: 1.766 and $1.782 \mu\text{m}$) and MgO ((c,d); average thickness: $0.646 \mu\text{m}$, prepared with a hydrogel film of $0.851 \mu\text{m}$ thickness; green bars: 0.5862 , 0.7313 , $0.6197 \mu\text{m}$).

Assessment of the pore size distribution by nitrogen (N_2) or argon (Ar) physisorption analysis was not possible due to the low overall amount of material (as frequently encountered for thin layers of porous material), but krypton (Kr) physisorption allowed a five-point BET analysis, as shown in Figure 3a. The isotherm showing the adsorbed amount of Kr is shown in Figure S3 in the Supplementary Materials. The specific surface area of the Al_2O_3 layer is $370 \text{ m}^2 \cdot \text{g}^{-1}$, corresponding to $0.259 \text{ m}^2 \cdot \text{cm}^{-2}$ if normalized to the covered area of the substrate. The latter value incorporates the

respective film thickness, while the former value is independent of the film dimensions. This large surface area confirms that the Al_2O_3 layer is indeed porous. As mentioned in the Introduction section, we have recently reported on the synthesis of $\gamma\text{-Al}_2\text{O}_3$ materials synthesized by the same procedure (using the same type of hydrogels), but in form of powders rather than as thin layers [16,17,23]. The powder samples exhibited similar BET surface areas ($250\text{--}370\text{ m}^2\cdot\text{g}^{-1}$) with narrow pore size distributions around ca. 4 nm and mesopore volumes in the range of $0.4\text{--}0.5\text{ cm}^3\cdot\text{g}^{-1}$. Hence, it is fair to assume similar mesopores for the Al_2O_3 layer presented here. The origin of these mesopores is the porogenic impact of bundles of polymer strands in the hydrogel; the combustion of the hydrogel creates disordered, tubular mesopores, as previously described [16]. The MgO layer (Figure 2c,d), on the other hand, is significantly less homogeneous than the Al_2O_3 layer; it exhibits a rough surface with raptures and an almost granular texture. Its average thickness is $0.646\text{ }\mu\text{m}$, which is actually less than the thickness if the respective non-swollen (dry) hydrogel film ($0.851\text{ }\mu\text{m}$). This indicates a lower degree of porosity which is confirmed by a low BET surface area of $112\text{ m}^2\cdot\text{g}^{-1}$ ($0.025\text{ m}^2\cdot\text{cm}^{-2}$; Figure 3b). Obviously, the polymer network does not have a strong porogenic impact in this case. This may be due to the fact that the hydrogel matrix starts to decompose before a sufficiently stable network of MgO has formed.

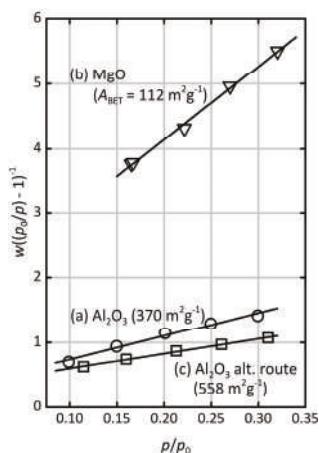


Figure 3. BET plots of Kr physisorption data of porous metal oxide layers: (a) Al_2O_3 layer ($1.77\text{ }\mu\text{m}$ thickness); (b) MgO ($0.646\text{ }\mu\text{m}$); (c) Al_2O_3 (prepared by pre-mixing the polymer).

In an alternative synthesis approach, we simplified the process by dissolving the metal salts and the precursor polymer in methanol before applying them to the silicon wafer by spin-coating and subsequent photo-cross-linking of the polymer. Hence, no drying of the hydrogel films and subsequent re-swelling in metal salt solutions is necessary which facilitates the overall procedure. The rest of the synthesis was carried out in the same way as before. Two example SEM images of the resulting Al_2O_3 and MgO layers are shown in Figure 4. Further examples are listed in Table S2 and shown in Figure S4 in the Supplementary Materials. The Al_2O_3 layer (Figure 4a) exhibits an average thickness of $0.364\text{ }\mu\text{m}$ and shows a fairly homogeneous texture, although not as smooth as in case of the synthesis procedure described above (i.e., by re-swelling the pre-fabricated hydrogel films with metal salt solutions). However, it exhibits a higher BET surface area of $558\text{ m}^2\cdot\text{g}^{-1}$. Figure 3c; the surface area per substrate area, $0.080\text{ m}^2\cdot\text{cm}^{-2}$, is lower as a consequence of a lower layer thickness. The MgO layer (Figure 4b) is even less homogeneous; it appears seriously granular and rough, with a similar BET surface area as for the material prepared by the first route ($112\text{ m}^2\cdot\text{g}^{-1}$). In summary, the alternative synthesis approach, despite being simpler and easier to carry out, cannot be regarded

as equally successful as the first route in terms of the homogeneity and smoothness of the resulting metal oxide layers.

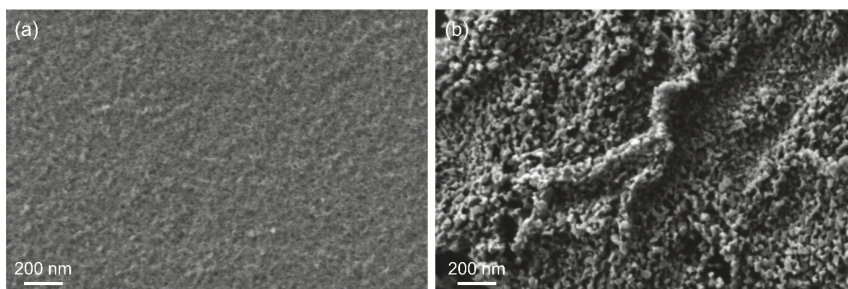


Figure 4. SEM images of two example layers of (a) Al_2O_3 and (b) MgO prepared by pre-mixing the polymer ((a): 200 mg; (b): 150 mg) with the metal salts ((a): 600 mg $\text{Al}(\text{NO}_3)_3 \cdot 9\text{H}_2\text{O}$; (b): 450 mg $\text{Mg}(\text{NO}_3)_2 \cdot 6\text{H}_2\text{O}$) prior to spin-coating and subsequent photo-cross-linking and calcination.

4. Conclusions

In summary, we have shown that the concept of using poly(dimethylacrylamide) hydrogels as porogenic matrices for the synthesis of mesoporous metal oxides can be applied to the preparation of porous layers on silicon substrates by anchoring the hydrogel to the substrate via chemical bonding. Homogeneous mesoporous layers of Al_2O_3 with high specific surface areas (up to $558 \text{ m}^2 \cdot \text{g}^{-1}$) are obtained. The MgO layers display lower homogeneity and porosity.

Supplementary Materials: The following are available online at <http://www.mdpi.com/2079-4991/8/4/186/s1>, Figure S1: SEM images of dry hydrogel films, Figure S2: SEM images of Al_2O_3 and MgO layers, Figure S3: Kr physisorption isotherms, Figure S4: SEM images of Al_2O_3 and MgO layers prepared by pre-mixing, Table S1: EDX analysis, Table S2: Amounts of polymer and metal salts for pre-mixing synthesis.

Acknowledgments: We thank Marc Hartmann for help with the Kr physisorption measurements and Manuel Traut for help with SEM/FIB.

Author Contributions: Z.C., M.T., and D.K. conceived and designed the experiments; Z.C. performed the experiments; Z.C., M.T., and D.K. wrote the paper.

Conflicts of Interest: The authors declare no conflict of interest.

References

1. Gu, D.; Schüth, F. Synthesis of non-siliceous mesoporous oxides. *Chem. Soc. Rev.* **2014**, *43*, 313–344. [[CrossRef](#)] [[PubMed](#)]
2. Smarsly, B.; Antonietti, M. Block copolymer assemblies as templates for the generation of mesoporous inorganic materials and crystalline films. *Eur. J. Inorg. Chem.* **2006**, *6*, 1111–1119. [[CrossRef](#)]
3. Bagshaw, S.A.; Pinnavaia, T.J. Mesoporous alumina molecular sieves. *Angew. Chem. Int. Ed.* **1996**, *35*, 1102–1105. [[CrossRef](#)]
4. Čejka, J. Organized mesoporous alumina: Synthesis, structure and potential in catalysis. *Appl. Catal. A* **2003**, *254*, 327–338. [[CrossRef](#)]
5. Morris, S.M.; Fulvio, P.F.; Jaroniec, M. Ordered mesoporous alumina-supported metal oxides. *J. Am. Chem. Soc.* **2008**, *130*, 15210–15216. [[CrossRef](#)] [[PubMed](#)]
6. Brinker, C.J.; Lu, Y.; Sellinger, A.; Fan, H. Evaporation-Induced Self-Assembly: Nanostructures Made Easy. *Adv. Mater.* **1999**, *11*, 579–585. [[CrossRef](#)]
7. Grosso, D.; Cagnol, F.; Soler-Illia, G.J.A.A.; Crepaldi, E.L.; Amenitsch, H.; Brunet-Bruneau, A.; Bourgeois, A.; Sanchez, C. Fundamentals of mesostructuring through evaporation-induced self-assembly. *Adv. Funct. Mater.* **2004**, *4*, 309–322. [[CrossRef](#)]

8. Tiemann, M. Repeated templating. *Chem. Mater.* **2007**, *20*, 961–971. [[CrossRef](#)]
9. Ren, Y.; Ma, Z.; Bruce, P.G. Ordered mesoporous metal oxides: Synthesis and applications. *Chem. Soc. Rev.* **2012**, *41*, 4909–4927. [[CrossRef](#)] [[PubMed](#)]
10. Liu, Q.; Wang, A.; Wang, X.; Zhang, T. Ordered crystalline alumina molecular sieves synthesized via a nanocasting route. *Chem. Mater.* **2006**, *18*, 5153–5155. [[CrossRef](#)]
11. Haffer, S.; Weinberger, C.; Tiemann, M. Mesoporous Al₂O₃ by nanocasting: Relationship between crystallinity and mesoscopic order. *Eur. J. Inorg. Chem.* **2012**, 3283–3288. [[CrossRef](#)]
12. Weinberger, C.; Roggenbuck, J.; Hanss, J.; Tiemann, M. Synthesis of Mesoporous Metal Oxides by Structure Replication: Thermal Analysis of Metal Nitrates in Porous Carbon Matrices. *Nanomaterials* **2015**, *5*, 1431–1441. [[CrossRef](#)] [[PubMed](#)]
13. Roggenbuck, J.; Tiemann, M. Ordered mesoporous magnesium oxide with high thermal stability synthesized by exotemplating using CMK-3 carbon. *J. Am. Chem. Soc.* **2005**, *127*, 1096–1097. [[CrossRef](#)] [[PubMed](#)]
14. Roggenbuck, J.; Koch, G.; Tiemann, M. Synthesis of mesoporous magnesium oxide by CMK-3 carbon structure replication. *Chem. Mater.* **2006**, *18*, 4151–4156. [[CrossRef](#)]
15. Roggenbuck, J.; Waitz, T.; Tiemann, M. Synthesis of Mesoporous Metal Oxides by Structure Replication: Strategies of Impregnating Porous Matrices with Metal Salts. *Microporous Mesoporous Mater.* **2008**, *113*, 575–582. [[CrossRef](#)]
16. Birnbaum, W.; Weinberger, C.; Schill, V.; Haffer, S.; Tiemann, M.; Kuckling, D. Synthesis of mesoporous alumina through photo cross-linked poly(dimethylacrylamide) hydrogels. *Colloid Polym. Sci.* **2014**, *292*, 3055–3060. [[CrossRef](#)]
17. Weinberger, C.; Chen, Z.; Birnbaum, W.; Kuckling, D.; Tiemann, M. Photo-cross-linked polydimethylacrylamide hydrogels as porogens for mesoporous alumina. *Eur. J. Inorg. Chem.* **2017**, *2017*, 1026–1031. [[CrossRef](#)]
18. Döring, A.; Birnbaum, W.; Kuckling, D. Responsive hydrogels—Structurally and dimensionally optimized smart frameworks for applications in catalysis, micro-system technology and material science. *Chem. Soc. Rev.* **2013**, *40*, 7391–7420. [[CrossRef](#)] [[PubMed](#)]
19. Kuckling, D.; Hoffmann, J.; Plötner, M.; Ferse, D.; Kretschmer, K.; Adler, H.-J.P.; Arndt, K.-F.; Reichelt, R. Photo cross-linkable poly(*N*-isopropylacrylamide) copolymers III: Micro-fabricated temperature responsive hydrogels. *Polymer* **2003**, *44*, 4455–4462. [[CrossRef](#)]
20. Kurumada, K.; Nakamura, T.; Suzuki, A.; Umeda, N.; Kishimoto, N.; Hiro, M. Nanoscopic replication of cross-linked hydrogel in high-porosity nanoporous silica. *J. Non-Cryst. Solids* **2007**, *353*, 4839–4844. [[CrossRef](#)]
21. Cui, X.; Tang, S.; Zhou, H. Mesoporous alumina materials synthesized in different gel templates. *Mater. Lett.* **2013**, *98*, 116–119. [[CrossRef](#)]
22. Jiang, R.; Zhu, H.-Y.; Chen, H.-H.; Yao, J.; Fu, Y.-Q.; Zhang, Z.-Y.; Xu, Y.-M. Effect of calcination temperature on physical parameters and photocatalytic activity of mesoporous titania spheres using chitosan/poly(vinyl alcohol) hydrogel beads as a template. *Appl. Surf. Sci.* **2014**, *319*, 189–196. [[CrossRef](#)]
23. Chen, Z.; Weinberger, C.; Tiemann, M.; Kuckling, D. Organic Polymers as Porogenic Structure Matrices for Mesoporous Alumina and Magnesia. *Processes* **2017**, *5*, 70. [[CrossRef](#)]
24. Li, L.; Wen, X.; Fu, X.; Wang, F.; Zhao, N.; Xiao, F.; Wie, W.; Sun, Y. MgO/Al₂O₃ Sorbent for CO₂ Capture. *Energy Fuels* **2010**, *24*, 5773–5780. [[CrossRef](#)]
25. Wie, J.; Ren, Y.; Luo, W.; Sun, Z.; Cheng, X.; Li, Y.; Deng, Y.; Elzatahry, A.A.; Al-Dahyan, D.; Zhao, D. Ordered mesoporous alumina with ultra-large pores as an efficient absorbent for selective bioenrichment. *Chem. Mater.* **2017**, *29*, 2211–2217.
26. Martín-Aranda, R.; Čejka, J. Recent Advances in Catalysis Over Mesoporous Molecular Sieves. *Top. Catal.* **2010**, *53*, 141–153. [[CrossRef](#)]
27. Choudary, B.M.; Mulukutla, R.S.; Klubunde, K.J. Benzoylation of aromatic compounds with different crystallites of MgO. *J. Am. Chem. Soc.* **2003**, *125*, 2020–2021. [[CrossRef](#)] [[PubMed](#)]
28. Trueba, M.; Trasatti, S.P. γ -Alumina as a support for catalysts: A review of fundamental aspects. *Eur. J. Inorg. Chem.* **2005**, *17*, 3393–3403. [[CrossRef](#)]
29. Yu, X.; Yu, J.; Cheng, B.; Jaroniec, M. Synthesis of Hierarchical Flower-like AlOOH and TiO₂/AlOOH Superstructures and their Enhanced Photocatalytic Properties. *J. Phys. Chem. C* **2009**, *113*, 17527–17535. [[CrossRef](#)]

30. Brunauer, S.; Emmett, P.H.; Teller, E. Adsorption of gases in multimolecular layers. *J. Am. Chem. Soc.* **1938**, *60*, 309–319. [[CrossRef](#)]
31. Vo, C.D.; Kuckling, D.; Adler, H.-J.; Schönhoff, M. Preparation of thermosensitive nanogels by photo-cross-linking. *Colloid Polym. Sci.* **2002**, *280*, 400–409. [[CrossRef](#)]
32. Yu, X.; Corten, C.; Görner, H.; Wolff, T.; Kuckling, D. Photodimers of *N*-alkyl-3,4-dimethylmaleimides-product ratios and reaction mechanism. *J. Photochem. Photobiol. A* **2008**, *198*, 34–44. [[CrossRef](#)]
33. Kuckling, D.; Adler, H.-J.; Ling, L.; Habicher, W.D.; Arndt, K.-F. Temperature sensitive polymers based on 2-(dimethylmaleinimido)-*N*-ethyl-acrylamide: Copolymers with *N*-isopropylacrylamide. *Polym. Bull.* **2000**, *44*, 269–276. [[CrossRef](#)]



© 2018 by the authors. Licensee MDPI, Basel, Switzerland. This article is an open access article distributed under the terms and conditions of the Creative Commons Attribution (CC BY) license (<http://creativecommons.org/licenses/by/4.0/>).



Article

Comparison of Surface-Bound and Free-Standing Variations of HKUST-1 MOFs: Effect of Activation and Ammonia Exposure on Morphology, Crystallinity, and Composition

Brandon H. Bowser [†], Landon J. Brower [†], Monica L. Ohnsorg, Lauren K. Gentry, Christopher K. Beaudoin and Mary E. Anderson ^{*}

Department of Chemistry, Hope College, 35 E. 12th Street, Holland, MI 49422, USA; bbbowser@gmail.com (B.H.B.); landon.brower@hope.edu (L.J.B.); monica.ohnsorg@gmail.com (M.L.O.); lauren.gentry@memphistr.org (L.K.G.); chrbeaudoin@gmail.com (C.K.B.)

^{*} Correspondence: meanderson@hope.edu; Tel.: +1-616-395-7425

[†] These authors contributed equally to this work.

Received: 28 June 2018; Accepted: 21 August 2018; Published: 23 August 2018



Abstract: Metal-organic frameworks (MOFs) are extremely porous, crystalline materials with high surface area for potential use in gas storage, sequestration, and separations. Toward incorporation into structures for these applications, this study compares three variations of surface-bound and free-standing HKUST-1 MOF structures: surface-anchored MOF (surMOF) thin film, drop-cast film, and bulk powder. Herein, effects of HKUST-1 ammonia interaction and framework activation, which is removal of guest molecules via heat, are investigated. Impact on morphology and crystal structure as a function of surface confinement and size variance are examined. Scanning probe microscopy, scanning electron microscopy, powder X-ray diffraction, Fourier-transform infrared spectroscopy, and energy dispersive X-ray spectroscopy monitor changes in morphology and crystal structure, track ammonia uptake, and examine elemental composition. After fabrication, ammonia uptake is observed for all MOF variations, but reveals dramatic morphological and crystal structure changes. However, activation of the framework was found to stabilize morphology. For activated surMOF films, findings demonstrate consistent morphology throughout uptake, removal, and recycling of ammonia over multiple exposures. To understand morphological effects, additional ammonia exposure experiments with controlled post-synthetic solvent adsorbates were conducted utilizing a HKUST-1 standard powder. These findings are foundational for determining the capabilities and limitation of MOF films and powders.

Keywords: metal-organic framework; microscopy; thin films; powders

1. Introduction

Highly porous crystalline materials known as metal-organic frameworks (MOFs) have been the focus of much attention over recent years due to their promising potential for a wide range of applications, including gas storage, separation, catalysis, and sensing [1–3]. Careful selection of the inorganic nodes and organic linkers that compose the chemical structure of the material can lead to a variety of highly tunable pore sizes and chemical functionality [4]. Varying synthetic conditions, such as processing solvent [5], temperature [6], concentration [7], etc., also allows one to tailor MOF properties. This careful control makes it possible to embed MOF materials within an array of hierarchical architectures and composites [8]. Once synthesized, MOF crystallinity and morphology are typically evaluated to determine quality. However, when testing the materials in the presence of

different gases, it is rare to find studies that monitor possible morphological changes, even though changes in crystal structure are often investigated [9]. This lack of structural understanding needs to be addressed for a variety of MOF systems and host-guest interactions if they are to become a viable option for integration into more complex designs. This study herein characterizes the morphological impact of one such interaction for the HKUST-1 MOF, providing previously neglected insights into how the MOF may perform in modern applications.

The most widely studied MOF is HKUST-1, also known as Cu_3BTC_2 or MOF-199, which was first discovered by Chui et al. [10] and uses copper(II) ions and benzene-1,3,5-tricarboxylate (BTC) as the inorganic and organic building blocks, respectively. One of the reasons HKUST-1 has garnered so much attention is because of its ability to capture and store a wide variety of gases, including carbon monoxide, carbon dioxide, nitric oxide, nitrogen, hydrogen, and sulfur dioxide [11–13]. Furthermore, HKUST-1 has been shown to be a suitable candidate for the sequestration of harmful gases like hydrogen sulfide, arsine, and ammonia [14,15]. One of the key features of HKUST-1 is that it allows for the adsorption of these different gases in the copper paddlewheel unit, depicted in Figure 1. In this paddlewheel unit, Cu^{2+} ions are connected to form Cu^{2+} dimers through a weak bond and are bridged by four carboxylate units. The as-synthesized framework typically contains solvent molecules weakly bound to the axial coordination sites of the Cu^{2+} ions. These solvent molecules can be removed through a simple activation procedure (i.e., heating under vacuum), thus enabling the Cu^{2+} ions to act as Lewis acidic sites for the binding of molecules possessing basic character, such as ammonia. Herein, this research explores the effect of residual solvent molecules on the adsorption of ammonia in HKUST-1, highlighting for the first time how the presence of solvent (or lack thereof) affects morphology.

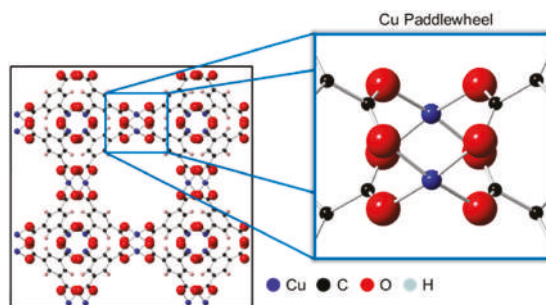


Figure 1. Unit cell (left) of the HKUST-1 metal-organic framework system ((100) crystal face) [10]. HKUST-1 is composed of four benzene-1,3,5-tricarboxylate organic ligands coordinated to Cu^{2+} dimer. Highlighted is the copper paddlewheel structure (right) characteristic of the HKUST-1 system. Each Cu^{2+} dimer completes its octahedral coordination sphere with two axial positions (vacant here) opposite of the Cu-Cu vector.

The synthesis of HKUST-1 can be varied so as to achieve a wide range of geometries, morphologies, and composites, allowing the MOF to be tailored toward specific applications [16]. For example, HKUST-1 can be tethered to a substrate as a surface-anchored MOF (surMOF) or a drop-cast thin film; and it can be synthesized to be a free-standing material (bulk powder). However, most studies for HKUST-1 only characterize and analyze one of its possible variations, typically its powder form. This is especially true in the investigation of the HKUST-1 interaction with ammonia gas. There have been studies that compare pure HKUST-1 powder to composite materials that contain it, but there is a deficiency of ammonia studies that directly compare different MOF variations [17].

The research herein compares the behavior of surface-bound and free-standing HKUST-1 materials. A study by Nijem et al. [18] suggested that aspects of the HKUST-1 interaction with ammonia may vary depending on whether the MOF is confined to a substrate. Also, the effect of size on MOF behavior is studied; the three MOF variations investigated herein all had the same chemical composition but

were on different size scales. The aim of the study is to investigate how these different variations respond to ammonia in order to gain insights into the effects of size and substrate confinement on morphology, composition, and crystallinity. This is important because films of different size regimes are required depending on the application [19,20]. For example, films prepared on the nanometer scale may be useful as dielectric layers in transistors [21], whereas gas filtration technologies might require micron-sized films or larger [22]. For the creation of successful MOF-based devices it should not be assumed that material properties and reactivity will remain consistent across size regimes; therefore, more comprehensive studies such as the one conducted herein are needed in order to better understand the scope and broad applicability of various host-guest interactions.

Specifically, this study compares the three different variations of HKUST-1 mentioned above: the surMOF, drop-cast thin film, and bulk powder. Metal-organic frameworks anchored to a surface are able to integrate both the versatility and tunability of MOF systems into hierarchical architectures for potential applications in electronic or sensing devices [23,24]. Bulk powders have shown promise in their capabilities for incorporation into MOF-graphene hybrid materials and real-world gas mask filtrations [15,25]. The bulk powder used in this study was synthesized, yielding large, microscale, free-standing MOF crystals [26]. The surMOF was prepared via a well-established layer-by-layer approach where nanoscale MOF crystallites were deposited in a controlled fashion onto a carboxylic acid-functionalized gold substrate [27,28]. The formation of MOF crystals on the substrate using this method was recently found to occur via a Volmer–Weber growth mechanism, giving rise to a discontinuous surface of nucleating MOF crystallites [29,30]. Lastly, the drop-cast thin film was also formed on a functionalized gold substrate, yielding a uniform film of highly-oriented crystals [26]. This is the first time that a parallel study has investigated these three MOF variations to determine whether or not they exhibit uniform behavior independent of substrate confinement and size variance.

In this study, these three variations were used to probe the interaction of HKUST-1 with ammonia gas. Metal-organic framework interactions with ammonia have been the subject of much attention over recent years because they have been shown to outperform other materials in their ability to adsorb ammonia [14,31,32]. The high-performance capabilities for the HKUST-1 system have been attributed to the copper paddlewheel, a preferential binding site for the chemisorption of Lewis bases such as ammonia [33]. In addition, ammonia is also able to interact with various other parts of the MOF as well, such as the organic linkers [17]. The HKUST-1 is known to react with ammonia in different ways depending on the presence of water, making it a useful test case for examining the effect of activation and gas exposure [34]. The HKUST-1 has been shown to adsorb more ammonia under humid conditions because the ammonia can bind to the Lewis acidic Cu ions and is also able to dissolve into films of water that are contained within the pores [35]. Peterson et al. [36] showed that under dry conditions, ammonia reacted with the open-metal binding sites of the copper paddlewheel to form a copper(II)-diamine species. That same study also showed that under humid conditions, the MOF underwent a more severe degradation owing to the reaction of ammonia with the BTC linkers to form $\text{Cu}(\text{OH})_2$ and $(\text{NH}_4)_3\text{BTC}$ species. After exposure under both wet and dry conditions, the ammonia was removed via heating under vacuum to regenerate the material, which could then successfully re-uptake ammonia upon subsequent exposures. The research herein examines morphology throughout multiple cycles of regeneration and re-exposure for the activated surMOF material, which adds new and practical information about the viability of using surface-constrained MOF nanomaterials.

The interaction of ammonia with HKUST-1 has been modeled by simulations [17,37] and has been monitored via breakthrough studies [14]; IR spectroscopy [38]; X-ray crystallography [39]; nuclear magnetic resonance spectroscopy [36]; X-ray photoelectron, extended X-ray absorption fine structure, X-ray absorption near edge structure, UV–vis, electron paramagnetic resonance spectroscopies [34]; and microcalorimetry [40]. More recent work has shifted focus toward preventing or reducing MOF degradation upon ammonia exposure [41,42] and creating systems in the bulk that could function as filters in real-world applications [15]. Although positive approaches in these areas are underway,

there are still fundamental aspects of the HKUST-1 ammonia interaction that need to be explored. A major shortcoming in those studies is the lack of details about the morphological changes that occur under different conditions. Therefore, for the first time ever, this study presents microscopic images for three HKUST-1 variations that show the morphological transformations upon exposure to ammonia for both the as-synthesized and activated material. This type of knowledge pertaining to changes in morphological structure has thus far been overlooked in the literature, but is essential if HKUST-1 is to be used in combination with another material, such as graphene-MOF composites [43], or integrated into device structures.

In addition, this study examines the effect of residual solvent adsorbates on the HKUST-1 ammonia interaction. For most synthetic routes towards HKUST-1, the solvent used for processing is still bound to the as-synthesized MOF either via chemisorption or physisorption [44]. It is well known that the solvent used for the processing of MOFs has an influence on the properties of the resulting framework [11]. For example, the size and porosity of HKUST-1 was shown to be altered by varying the ratio of solvents used during synthesis [45]. The presence of solvent can also hinder the ability for many MOFs to perform their desired function due to competition and blockage of binding sites [46]. The presence or absence of solvent plays a major factor in how the MOF interacts with ammonia, as evidenced by the effect of water on the reaction discussed prior. Research described herein will further explain the impact that solvent has on MOF degradation by exploring how different crystallographic and morphological changes occur depending on whether solvent molecules are within pores prior to ammonia exposure. Solvent is easily removed from HKUST-1 via activation by heat at reduced pressures, resulting in a visual color change of turquoise (as-synthesized) to dark blue (activated MOF) [10,11]. Multiple studies have confirmed that this activation process does not disrupt crystallinity [47], but potential effects on substrate morphology are not reported. Research described herein examines the morphological stability upon activation of the HKUST-1 surMOF.

Three variations of the HKUST-1 system and its interaction with ammonia gas were interrogated for both substrate-bound and free-standing materials. Ammonia gas exposure was investigated for as-synthesized and activated samples to explore the effect of residual solvent molecules. Further studies were done to gain insights into ammonia removal and re-exposure to the surMOF material. Additionally, ammonia exposure experiments, utilizing a purchased standard of HKUST-1 powder (Basolite[®] C 300), were completed to explore the effect of additional processing solvents bound to the framework. Fourier-transform infrared spectroscopy (FT-IR), scanning electron microscopy (SEM), energy dispersive X-ray spectroscopy (EDS), scanning probe microscopy (SPM), and powder X-ray diffraction (XRD) characterized samples before and after ammonia exposure. These techniques were used to track uptake and release of ammonia, monitor changes in surface morphology, examine elemental composition, and observe effects on overall crystal structure. These fundamental studies of HKUST-1 ammonia gas interactions elucidate which effects are inherent to the MOF system, as opposed to effects that are dependent on substrate confinement or size variance, and are critical for the successful incorporation of HKUST-1 into hierarchical architectures.

2. Materials and Methods

2.1. Materials

Copper (II) acetate monohydrate and copper (II) nitrate hemi(pentahydrate) were purchased from Fisher Scientific (Fair Lawn, NJ, USA). Absolute, anhydrous ethanol (200 proof, ACS/USP Grade) was obtained from Pharmco-Aaper (Shelbyville, KY, USA). Trimesic acid (TMA, H₃BTC) (95%), dimethyl sulfoxide (DMSO) (spectrophotometric grade), and 16-mercaptohexadecanoic acid (MHDA) (90%) were purchased from Aldrich (St. Louis, MO, USA). The DMSO was purged with nitrogen and passed through columns of molecular sieves. Gold substrates composed of silicon wafers with 5 nm Ti adhesion layer and 100 nm Au were purchased from Platypus Technologies (New Orleans, LA, USA). Anhydrous ammonia gas was obtained from Alexander Chemical Company (Kingsbury, IN, USA).

2.2. Sample Preparation

Three variations of MOFs were fabricated: surface-anchored MOFs (surMOF) via layer-by-layer deposition, MOF thin films by drop-cast method, and MOF powder synthesized to produce microcrystals.

2.2.1. surMOF

The surMOFs were fabricated according to literature precedent on a gold substrate functionalized by a self-assembled monolayer (SAM) using alternating, solution-phase deposition [27–29]. The gold substrate was first immersed in a 1 mM ethanol solution of MHDA for 1 h to form the foundational SAM that anchors the framework to the substrate. The substrate was then rinsed with ethanol and dried with nitrogen. Next, the sample was submerged in a 1 mM ethanol solution of copper acetate monohydrate. The substrate was removed after 30 min, rinsed, and dried as before. The sample was then submerged in a 0.1 mM ethanol solution of TMA for 1 h. Again, the substrate was rinsed, dried, and returned to the 1 mM copper acetate monohydrate solution. Four deposition cycles of the copper and TMA solutions yielded a film with an average thickness, roughness, and surface coverage of 10 nm, 20 nm, and 24%, respectively [29]. For all experiments herein, solutions were held at room temperature. After film formation, the substrate was characterized by SPM and IR.

2.2.2. Thin Film

The MOF thin film was prepared according to a modified drop-cast procedure [26]. The starting reagents, 2.8 mmol (0.59 g) TMA and 5.3 mmol (1.2 g) copper (II) nitrate hemi (pentahydrate), were combined in 5 mL of DMSO. This solution underwent sonication and stirring until powders were completely dissolved. A 1 mL portion of the resulting blue solution was then diluted to 5 mL by the addition of DMSO. A gold substrate that had been functionalized with a SAM of MHDA (according to the aforementioned method) was placed on a hotplate. A pipet transferred the diluted solution onto the gold to form a liquid layer that completely covered the substrate. The sample was covered with a glass beaker, the hotplate was ramped up to 100 °C over a 10-min period, and the sample was held at that temperature for an additional 10 min. As the solvent evaporated, a thin blue-green film was formed. Once the solvent was fully evaporated, the substrate was removed from the hotplate and placed onto an aluminum heat sink to cool the film to room temperature for characterization by XRD, SEM, and IR. This procedure yielded surface-confined crystals ranging in size from 1 to 10 microns. A quantitative study of crystal size and homogeneity was not undertaken.

2.2.3. Powder

The MOF bulk powder was prepared according to an optimized procedure [26]. First, 2.8 mmol (0.59 g) TMA and 5.1 mmol (1.2 g) copper (II) nitrate hemi(pentahydrate) were sonicated in 5 mL DMSO solution until completely dissolved. The solution was then heated in a beaker to 100 °C on a hotplate for 2 h, which resulted in the formation of blue-green crystals. After cooling, the precipitate was sonicated in ethanol, dried by vacuum filtration, and washed with additional ethanol solvent. The powder was transferred to a test tube, suspended in dichloromethane, and centrifuged for 6 min at 3300 rpm. This process was repeated three times, after which the resulting blue powder was dried overnight under high vacuum and then stored in a vacuum desiccator to be characterized by XRD, SEM, and IR. This procedure yielded free-standing crystals ranging in size from 10 to 100 microns. A quantitative study of crystal size and homogeneity was not undertaken.

2.3. Ammonia Exposure

Ammonia exposure was investigated for as-synthesized as well as activated samples. The activation process was undertaken by heating the sample under vacuum to evacuate the pores and remove any solvent (residual or coordinated). All samples that were regenerated and re-exposed underwent the same regeneration procedure.

2.3.1. Activation Process

Samples were placed under high vacuum at 180 °C for 2 h. The samples were then cooled under vacuum for 30 min prior to exposure.

2.3.2. Ammonia Exposure

For ammonia exposure, a sample under high vacuum at 25 °C was exposed to 360 torr of ammonia gas for 1 h. Samples exposed as-synthesized were held under high vacuum for 5 min at 25 °C prior to exposure. All samples (with and without prior activation) were exposed without breaking vacuum.

2.3.3. Regeneration and Re-Exposure

To undergo regeneration, samples were held under high vacuum at 180 °C for 1 h. The samples were then cooled under vacuum for 30 min prior to characterization. Prior to re-exposure, samples were left open to the atmosphere for at least 1 h. Each sample that was re-exposed underwent the same exposure method to which it was originally exposed.

2.4. Standard Powder Investigation of Solvent Effects

Basolite® C 300 powder was obtained from Aldrich (St. Louis, MO, USA) and was used as a standard for comparison to the HKUST-1 MOF powders fabricated as described above. The powder underwent ammonia exposures with and without activation in the manner outlined previously. Additional experimental exposures were undertaken to expose the Basolite® C 300 powder to solvents prior to ammonia exposures.

2.4.1. H₂O Exposure

Standard samples underwent H₂O exposure before subsequent ammonia exposure. The powder was exposed for 5 min to high vacuum conditions, and then for 2 h to H₂O vapor that had been heating to 85 °C under vacuum. Next, the sample was exposed for 5 min to high vacuum. The powder was then characterized and subsequent ammonia exposure was undertaken as described in the above section “ammonia exposure”.

2.4.2. DMSO Exposure

Standard samples underwent exposure to DMSO prior to subsequent ammonia exposure. A 100–250 mg portion of powder was suspended in 10–15 mL DMSO. The mixture was stirred for 2 h, after which the powder was dried via vacuum filtration and overnight house vacuum. Once dry, the powder was characterized and exposed to ammonia gas without activation.

2.5. Characterization

All samples underwent characterization by microscopy and infrared spectroscopy. The surMOF samples were characterized by scanning probe microscopy. The drop-cast thin films and the powder samples were characterized by scanning electron microscopy with energy dispersive spectroscopy, as well as by powder X-ray diffraction.

2.5.1. Scanning Probe Microscopy (SPM)

A Dimension Icon Scanning Probe Microscope (Bruker, Santa Barbara, CA, USA) that operated in peak force tapping mode was used to obtain several images (512 × 512 pixels) for each sample, both before and after exposures, at 5 μm × 5 μm and 500 nm × 500 nm. Etched silicon tips, SCANASYST-AIR (Bruker, Santa Barbara, CA, USA), with a spring constant range of 0.2–0.8 N/m and a resonant frequency range of 45–95 kHz were used. Scan parameters were as follows: 1 Hz scan rate, 12 μm z-range, 250–370 mV amplitude set point, and 100–450 mV drive amplitude. Image analysis was carried out by Nanoscope Analysis software (Bruker, Santa Barbara, CA, USA).

2.5.2. Infrared Spectroscopy (IR)

Infrared spectra were collected from 3800–600 cm^{-1} in ATR (Attenuated Total Reflectance) mode and used a Thermo Scientific Nicolet iS50 instrument. The spectra were collected at a resolution of 4 cm^{-1} and used a bare gold substrate as the background for the surMOF studies and ambient air as the background for the powder and thin-film studies.

2.5.3. Scanning Electron Microscopy (SEM) and Energy Dispersive X-ray Spectroscopy (EDS)

The SEM images were collected by a Hitachi TM-3000 tabletop microscope and used an accelerating voltage of 15 kV with the detection of back-scattered electrons. The EDS data were collected at this voltage by this microscope coupled with a Bruker XFlash MIN SVE detector and scan generator for EDS capability.

2.5.4. Powder X-ray Diffraction (XRD)

The XRD patterns were collected by a Rigaku Miniflex X-ray diffractometer and used Cu $K\alpha$ radiation at 30 kV and 15 mA. Data were collected from 10.00° to 79.99° for the powder and 10.00° to 34.00° for the drop-cast thin film (range selected to avoid the intense gold peaks from the underlying substrate). All samples were analyzed at a sampling width of 0.03° and scan speed of 3°/min.

3. Results and Discussion

To investigate how ammonia interacts with the HKUST-1 metal-organic framework, three different variations of the material (surMOF, drop-cast thin film, and powder) were exposed to ammonia; and the effect was monitored via microscopy, IR, and powder XRD. For these MOF variations, both as-synthesized and activated (heated under vacuum to remove species within pores) samples were investigated. The SPM characterization was undertaken to monitor how ammonia interacts with the surMOF deposited by a layer-by-layer protocol onto a gold surface functionalized with a self-assembled monolayer. The SEM characterization was used to monitor both a thin-film framework fabricated via drop-casting onto a functionalized gold surface as well as the synthesized bulk powder of microcrystals. Infrared spectroscopy was utilized in all three cases to track the uptake and release of ammonia. For the thin film and powder, powder XRD patterns were collected to gain further insights into how ammonia affects the overall crystal structure; and EDS was used to examine elemental composition. Beyond monitoring the effect of the initial ammonia exposure, both SPM and IR were used to understand what happens when ammonia is removed and re-introduced to the surMOF material. To further investigate the findings from the aforementioned experiments and explore the effect of different processing solvents, experiments utilizing a purchased standard of HKUST-1 powder (Basolite® C 300) were conducted.

3.1. Morphological Characterization

Integral to understanding how the material is affected by its interaction with ammonia, SPM and SEM characterization reveal the morphological structure of the surMOF, thin film, and powder HKUST-1 variations. Images of these structures before ammonia exposure, after exposure without activation, and after exposure with prior activation are shown in Figure 2. In all three cases, when the framework was exposed to ammonia without activation, the material undergoes a dramatic morphological change. The surface of the surMOF material changed from smaller, evenly distributed crystallites (Figure 2a) to larger bundles of nanowire-like structures (Figure 2b). A similar change of surface morphology was observed in the thin film (Figure 2d,e). The powder material also underwent a complete morphological change from octahedral shaped crystals (Figure 2g) to the nanowire-like structures (Figure 2h).

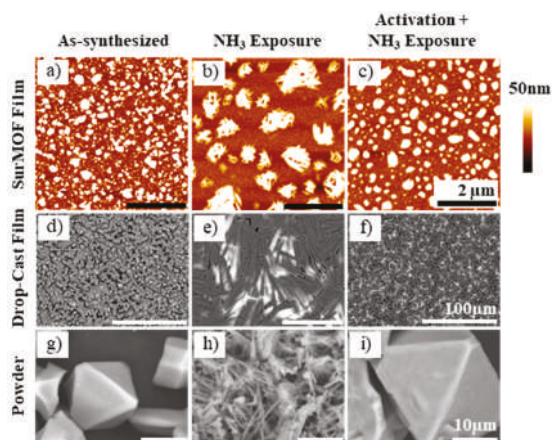


Figure 2. Top: Representative SPM images of HKUST-1 surMOFs (a) before exposure to NH_3 ; (b) after exposure without activation; and (c) after exposure with prior activation. Middle: SEM images of HKUST-1 drop-cast thin film (d) before exposure to NH_3 ; (e) after exposure without activation; and (f) after exposure with prior activation. Note: Due to high conductivity, underlying gold substrate appears bright in SEM images (especially prevalent in (e) and (f)). Bottom: SEM images of HKUST-1 powder (g) before exposure to NH_3 ; (h) after exposure without activation; and (i) after exposure with prior activation. All scale bars in (a–c) are 2 μm , in (d–f) are 100 μm , and in (g–i) are 10 μm .

A minor morphological change was observed when the framework was activated prior to ammonia exposure. The surMOF underwent a slight morphological change where the sharpness of the nanocrystallite features were reduced; and the size of the isolated structures on the surface increased (Figure 2c) relative to the film features before exposure (Figure 2a). The thin film and the powder materials did not undergo significant morphological changes after exposure to ammonia with activation (Figure 2f,i).

These images and observations provide new and important information as to how ammonia affects the morphology of the HKUST-1 crystals dependent on whether or not the material was activated (removing water or residual solvent) before the framework was exposed to the gas. When the sample was not activated, the ammonia-framework interaction resulted in a dramatic morphological change that was not observed when the framework was activated prior to exposure. This result is consistent with the findings of Peterson et al. [36] that the presence of water or residual solvent alters the reaction of the MOF with ammonia. Based on the morphological changes observed and the conclusions by Peterson, it can be hypothesized that the nanowires formed by exposure without prior activation could be $\text{Cu}(\text{OH})_2$ crystallites and that the changes (or lack thereof) observed in the samples exposed with prior activation could be due to the formation of a copper(II)-diamine species. Regardless of the products formed, the images clearly show that different interactions are taking place dependent on whether the sample was activated.

Further, it was confirmed that the heating process involved did not cause a significant morphological change on the surMOF, which is an important observation because MOF materials are often activated prior to being used. This was shown by an experiment in which the as-synthesized sample was characterized following the activation process without subsequent ammonia exposure (shown in Section 3.5).

3.2. Compositional Characterization

Infrared spectra were obtained to investigate the chemical composition of the framework. This characterization technique was utilized to monitor uptake of ammonia and to examine how this

exposure affected the framework. A comparison was conducted for when the sample underwent exposure to ammonia both without and with activation. Spectra of the framework before ammonia exposure, after exposure of an as-synthesized sample, and after exposure of an activated sample are shown in Figure 3 for the surMOF, thin film, and powder variations of the framework. The EDS was obtained for the powder and thin film samples to investigate the chemical identity of compounds captured within the framework, such as the DMSO solvent or the ammonia gas.

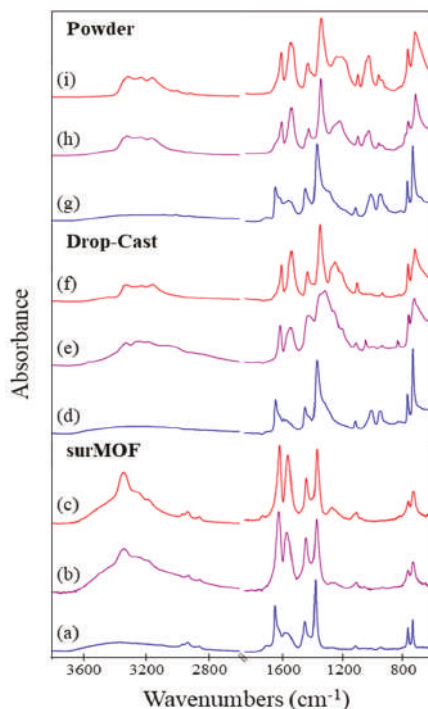


Figure 3. Infrared (IR) spectra of HKUST-1: (a) surMOF before exposure to NH_3 ; (b) surMOF after exposure without activation; (c) surMOF after exposure with prior activation; (d) drop-cast thin film before exposure to NH_3 ; (e) drop-cast thin film after exposure without activation; (f) drop-cast thin film after exposure with prior activation; (g) powder before exposure to NH_3 ; (h) powder after exposure without activation; and (i) powder after exposure with prior activation.

Characteristic IR peaks for HKUST-1 are present in all samples prior to exposure [27,34,38]; and a few small differences between the MOF variations are observed (Figure 3a,d,g). The asymmetric COO^- stretch ($\sim 1650 \text{ cm}^{-1}$) and the C–C aromatic vibration peak, corresponding to the linker molecule ($\sim 1440 \text{ cm}^{-1}$), are present in all spectra. All spectra for the as-synthesized materials also contain a very broad peak at $\sim 3000\text{--}3400 \text{ cm}^{-1}$, indicative of water or deposition solvent within the framework (Figure 3a,d,g). Peaks at 2930 cm^{-1} and 2855 cm^{-1} are only present in the surMOF sample and correspond to the C–H stretch of the underlying self-assembled monolayer on the gold substrate (Figure 3a–c) [48]. Peaks at 950 cm^{-1} and 1000 cm^{-1} are present only in the thin film and powder spectra (Figure 3d,g) and correspond to the DMSO solvent, indicating that it is present within the framework. The DMSO also has broad peaks around $\sim 3000 \text{ cm}^{-1}$, which occur at the same vibrational frequency as water [49]. For both the as-synthesized thin film and powder sample, EDS data confirm the presence of the DMSO deposition solvent, showing a 1:1 ratio of the Cu:S (SI Figures 1 and 4). This suggests that each open axial copper paddlewheel position may be occupied by one DMSO ligand.

All of the data gleaned from the IR spectra indicate that ammonia was present after exposure regardless of prior activation and HKUST-1 variation. Changes occurred in the spectra when the framework was exposed to ammonia (Figure 3b,c,e,f,h,i) consistent with literature observations [34]. A new distinct peak appeared around 3300 cm^{-1} that corresponds to the N-H stretch of ammonia on the framework [50]. This was true regardless of whether the framework was activated prior to exposure, which indicated that the uptake of ammonia into the framework was not dependent on activating the framework. Other changes that occurred upon exposure to ammonia were the shifting of the peak at 1650 cm^{-1} to 1625 cm^{-1} , the increase in intensity of peak at 1560 cm^{-1} , the appearance of two peaks in the $1260\text{--}1210\text{ cm}^{-1}$ range, and the broadening/shifting of the 1370 cm^{-1} and 1450 cm^{-1} peaks. All of these observations are in accord with previous studies investigating the effect of ammonia gas on the HKUST-1 framework [34]. After ammonia exposure for both as-synthesized and activated samples, EDS for the thin film and powder variations confirmed the presence of nitrogen and the removal of sulfur (SI Figures 2, 3, 5 and 6). (Note that the low-energy -ray peak associated with nitrogen in the crowded region with carbon and oxygen did not permit quantitative analysis of the nitrogen composition, but did qualitatively confirm its presence.) The data show that the ammonia gas displaced any solvent molecules present within the as-synthesized framework.

3.3. Crystal Structure Characterization

Powder XRD data were obtained for the thin film and powder systems, but could not be obtained for the surMOF films investigated in this study due to the low density of material bound to the surface. The similarities observed via microscopy and IR analysis for all three variations suggest that crystal structure findings for the thin film and powder likely translate to the surMOF variation.

Powder XRD was important for confirming the HKUST-1 structure for the synthesized thin film and bulk samples, as well as for characterization of the crystal structure after ammonia exposure. Patterns for the material before ammonia exposure, after exposure without activation, and after exposure with prior activation are shown in Figure 4 for the thin film and powder variations of the framework. The peaks corresponding to the thin film and powder material pre-exposure (Figure 4b,e) match well with the reference pattern (Figure 4a), indicating that the HKUST-1 crystal structure was obtained. The MOF deposited as a thin film (Figure 4e) demonstrates a preferred (111) crystal orientation. Noteworthy is that the XRD for the powder has broader peaks in comparison to the film, revealing the highly crystalline nature of the film.

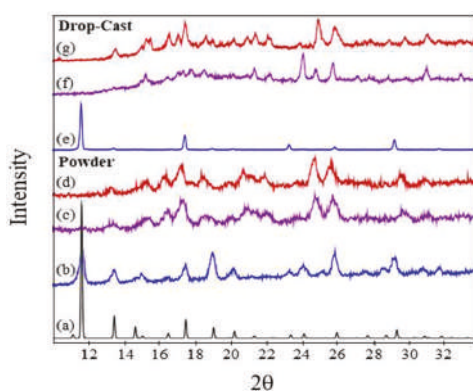


Figure 4. XRD patterns of (a) reference for HKUST-1 powder (ICDD pdf number 00-062-1183); (b) powder before exposure to NH_3 ; (c) powder after exposure without activation; (d) powder after exposure with prior activation; (e) drop-cast thin film before exposure to NH_3 ; (f) drop-cast thin film after exposure without activation; and (g) drop-cast thin film after exposure with prior activation.

Ammonia exposure with and without activation resulted in a change in crystal structure as observed by powder XRD (Figure 4c,d,f,g); and the resulting patterns are in general agreement with previous studies investigating the effect of ammonia on HKUST-1 [10,36,46]. For the HKUST-1 powder, the patterns for both as-synthesized and activated samples after ammonia exposures are consistent with one another (Figure 4c,d). This indicates that the activation step did not prevent the change in the crystal structure, despite what the SEM revealed with the crystal morphology remaining consistent. The same was observed for the as-synthesized and activated HKUST-1 thin films (Figure 4f,g). These observations highlight the importance of monitoring changes in both the morphology and the crystal structure, demonstrating that changes in crystallographic structure does not necessitate significant changes in substrate morphology. When comparing the ammonia exposures for the film and powder, the broadness of the peaks for the ammonia exposures to the film and powder are different, but the locations are consistent, revealing that the same crystal structure transformation is observed. The differences in the patterns are that the powder sample has broad peaks, while the film sample has sharper and therefore more distinguishable peaks. This is consistent with the samples before exposure with broader peaks observed for the synthesized powder (Figure 4b) and sharper peaks observed for the synthesized film (Figure 4e).

3.4. Standard Powder Investigation of Solvent Effects

Experiments with a standard HKUST-1 powder were undertaken in order to investigate a sample with and without residual solvent ligands within the framework. For the synthesized thin film and powder HKUST-1 samples, DMSO was found to be present in the as-synthesized materials and is likely coordinated to the open copper paddlewheel site. For the surMOF HKUST-1 sample, water is within the framework and likely bound at this same site. By conducting the experiments with a standard powder obtained commercially, this study investigated (1) the outcome of ammonia exposures on this standard powder void of residual solvent; (2) the effect of residual water and DMSO on this powder; and (3) the outcome of an ammonia exposure after the water or DMSO solvent were present within the framework.

3.4.1. Standard Powder as Received

The obtained standard powder was found to be consistent with literature precedent for HKUST-1 by SEM [11], IR [34], and XRD [10,36,46] characterization (Figures 5a, 6a and 7b). The SEM analysis of the crystal morphology for the standard powder was consistent with the powder synthesized by the procedure described herein. The EDS data showed no evidence of nitrogen present and minimal (2%–3%) sulfur (SI Figure 7). It is noteworthy that the standard powder matched the peak intensities of the HKUST-1 reference pattern (Figure 7a,b) more so than the synthesized powder shown in Figure 4b.

Exposures of ammonia gas for as-synthesized and activated samples were both successful, as IR confirmed the presence of ammonia (Figure 6b,c); and EDS data qualitatively showed similar uptake of nitrogen for both ammonia exposures (SI Figures 8 and 9). The SEM images reveal no morphological changes after either type of exposure (Figure 5b,c), suggesting that the standard powder was activated as received. (Note that the presence of silicon was observed via EDS (SI Figure 7), and this diatomaceous earth was observed in SEM images, which was likely an active desiccant to help maintain activation.) Despite the lack of morphological changes, the crystal structure observed by XRD did change upon exposure to ammonia (Figure 7b–d). The XRD patterns for the standard powder without and with activation (Figure 7c,d) are consistent with one another as well as with the XRD patterns for the ammonia exposures of the as-synthesized HKUST-1 powder (Figure 4c,d).

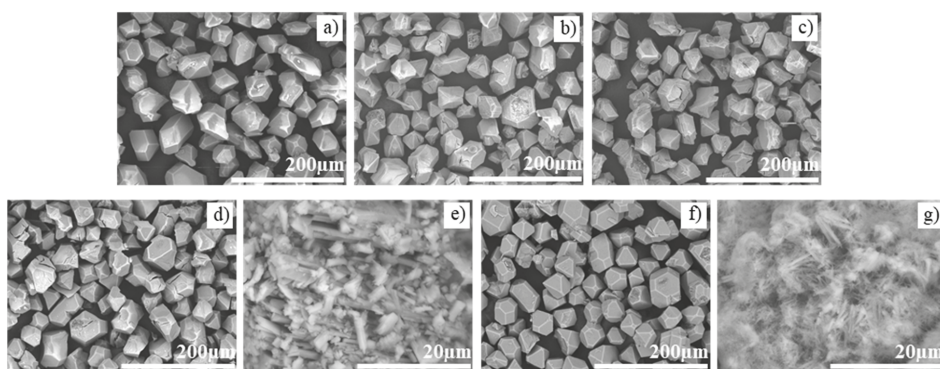


Figure 5. Representative SEM images of HKUST-1 powder (obtained commercially as Basolite® C 300) (a) before gas exposure; (b) after NH₃ exposure without activation; (c) after NH₃ exposure with prior activation; (d) after H₂O vapor exposure; (e) after H₂O vapor and subsequent NH₃ exposure without activation; (f) after DMSO exposure; (g) after DMSO and subsequent NH₃ exposure without activation.

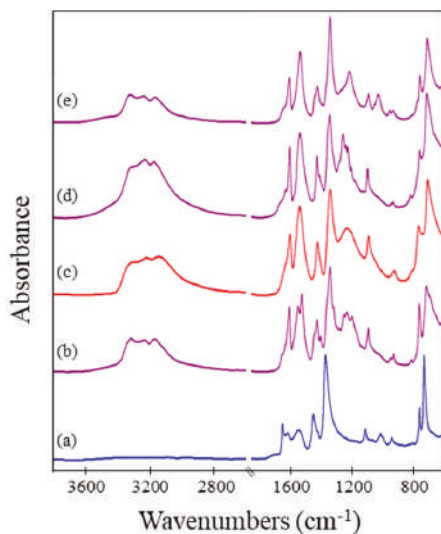


Figure 6. IR spectra of HKUST-1 powder (obtained commercially as Basolite® C 300) (a) before gas exposure; (b) after NH₃ exposure without activation; (c) after NH₃ exposure with prior activation; (d) after H₂O vapor and subsequent NH₃ exposure without activation; (e) after DMSO and subsequent NH₃ exposure without activation.

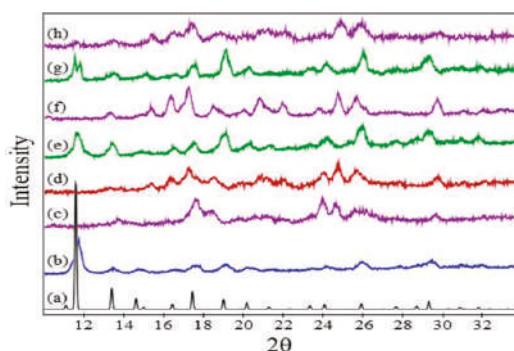


Figure 7. XRD patterns of (a) reference pattern for HKUST-1 powder (ICDD pdf number 00-062-1183); (b) commercially obtained HKUST-1 powder (Basolite® C 300) before gas exposure; (c) after NH_3 exposure without activation; (d) after NH_3 exposure with prior activation; (e) after H_2O vapor exposure; (f) after H_2O vapor and subsequent NH_3 exposure without activation; (g) after DMSO exposure; (h) after DMSO and subsequent NH_3 exposure without activation.

3.4.2. Standard Powder with Water Exposure

After exposing the standard powder to water vapor, the crystal morphology observed via SEM was unchanged (Figure 5d), and the crystal structure was maintained according to XRD (Figure 7e). Noteworthy, the peak intensities observed in the diffraction pattern were more similar to the synthesized powder (Figure 4b) rather than the standard powder as-received (Figure 5b). This is indicative that the water is bound to the framework of the standard powder after water exposure.

For this standard powder exposed to water vapor, an ammonia exposure resulted in a change in crystal morphology observed by SEM (Figure 5e), the uptake of ammonia detected by EDS (SI Figure 10) and IR (Figure 6d), and a change in crystal structure seen by XRD (Figure 7f). The morphology for this sample that had undergone an ammonia exposure after water vapor exposure (Figure 5e) was similar to that of the as-synthesized HKUST-1 powder upon exposure to ammonia (Figure 2h). The XRD data after ammonia exposure for this sample (Figure 7f) was consistent with the exposures on the standard powder (Figure 7c,d) and the synthesized powder (Figure 4c,d).

3.4.3. Standard Powder with DMSO Exposure

After exposing the standard powder to DMSO, the crystal morphology was unchanged as observed via SEM (Figure 5f). The crystal structure was maintained with the same small change in peak intensity (Figure 7g) as observed for the standard powder after water exposure (Figure 7e), which again was similar to that of the synthesized powder (Figure 4b). The IR shows peaks at approximately 950 cm^{-1} and 1000 cm^{-1} which are consistent with DMSO. The EDS shows a 1:1 ratio of Cu:S (SI Figure 8), which correlates with the same ratio found for the synthesized powder. This IR and EDS data suggests 1 DMSO may be coordinated to each axial copper paddlewheel site.

Upon subsequent ammonia exposure, IR and EDS data indicated that ammonia was captured (Figure 6e) (SI Figures 11 and 12). The SEM showed that the crystal morphology changed (Figure 5g) in a manner consistent with what had been observed for all ammonia exposures of as-synthesized samples (Figure 2b,e,h). The resulting XRD pattern (Figure 7h) is consistent with the patterns for other ammonia exposures (Figures 7c,d,f and 4c,d), especially those of the synthesized powder (Figure 4c,d). For the standard powder with water exposure before ammonia exposure, the XRD peaks (Figure 7f) were sharper, correlating with the size of the crystals observed by SEM (Figure 5f) relative to those for both the standard powder exposed to DMSO and the synthesized powder after ammonia exposure (Figures 5g and 2h, respectively).

3.4.4. Discussion of Solvent Effects on Standard Powder

This study shows that the presence of different solvent ligands results in the loss of crystal morphology after ammonia exposure, while the crystal structure is essentially the same independent of the solvent molecules presence. Why does the presence of the ligand result in loss of the crystal morphology? Based on this research, it is hypothesized that this may be that the ligand is bound to the copper paddlewheel, destabilizing the structure. This is specifically supported by the change in the XRD pattern of the standard powder after it is exposed to water and DMSO. The change in peak intensities may be indicative of this destabilization. In addition, if water or solvent is in fact bound to the copper paddlewheel as hypothesized, then this creates a competition for binding when ammonia is introduced [37]. This competition likely changes the way ammonia is able to interact with the various parts of the framework, explaining why the morphology change is different depending on the absence or presence of solvent. By activating the HKUST-1 before ammonia exposure, one is not able to prevent the change in crystal structure but is able to prevent the dramatic change in morphology, which remained unknown until now. This is advantageous because morphological changes destroy film continuity and would affect the packing and interaction of the powder within a composite material or device architecture. Understanding and preventing this degradation is fundamental toward the integration of MOF materials into hierarchical structures for the realization of their potential in applications as thin film sensors or for industrial gas sequestration.

3.5. Characterization of Regeneration and Re-exposure

This research has shown that the presence of residual solvent disrupts the morphology of three HKUST-1 variations upon exposure to ammonia and that this disruption can be prevented by activation prior to initial gas exposure. Will the original morphology be preserved upon the removal of the ammonia from within the framework and, if so, then what about after a second round of gas exposure? Toward future applications, it is necessary for the material to be morphologically stable not just upon initial exposure, but also for the ammonia uptake to be reversible for multiple cycles of exposure, removal, and re-exposure. This investigation was undertaken for the surMOF HKUST-1 variation with SPM and IR. This was done to determine if the ammonia can be removed after exposure and then whether the framework can re-uptake ammonia upon a subsequent exposure.

Scanning probe microscopy images and IR spectra in Figure 5 show that the activated surMOF (Figure 8b) remained morphologically stable after it was exposed to ammonia once (Figure 8c), regenerated by the removal of ammonia (Figure 8d), and exposed to ammonia a second and sixth time (Figure 8e,f). The SPM images reveal a minor loss in the sharpness of the features after the initial exposure, but the morphology did not change again even after multiple rounds of regeneration and re-exposure. The IR data support that the ammonia was removed by the regeneration process and re-incorporated upon re-exposure. The peak in the IR spectra ($\sim 3300\text{ cm}^{-1}$) corresponding to ammonia was no longer present after regeneration (Figure 8d'), and the peak was again observed after the second (Figure 8e') and sixth (Figure 8f') exposures, indicating successful removal and re-addition of ammonia onto the framework. The observation that ammonia can re-bind to the substrate even after the material undergoes a morphological change is consistent with the results of Peterson et al., which showed that ammonia could still interact with the substrate after undergoing its initial changes in structure and composition [36].

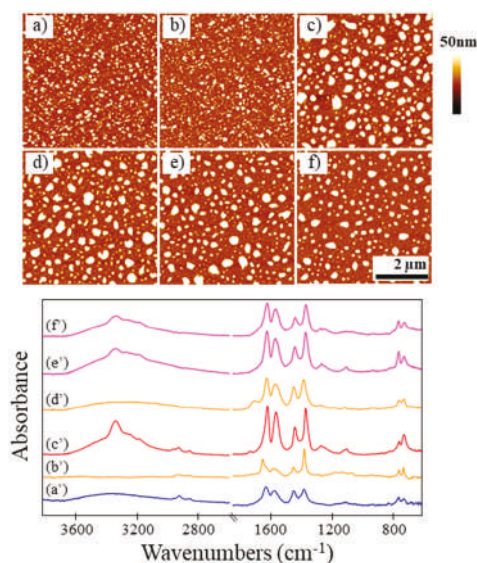


Figure 8. Top: Representative SPM images of HKUST-1 surMOFs (a) before exposure to NH_3 ; (b) after activation; (c) after exposure with prior activation; (d) after regeneration; (e) after second exposure with activation; and (f) after sixth exposure with activation. Bottom: Corresponding IR spectra (a'–f').

4. Conclusions

For the successful incorporation of HKUST-1 into hierarchical architectures, fundamental research is necessary to investigate the effect of heat and gas on the material structure. This study explored how the morphology and crystal structure of the MOF respond to ammonia gas exposure, yielding insights into the effect of different residual solvent molecules within the HKUST-1 framework. In studying three variations of HKUST-1 (surMOF, drop-cast thin film, bulk powder), it was found that all responded similarly, independent of substrate confinement and size variance. While microscopy demonstrated a dramatic change in the morphological structure upon ammonia exposure for the as-synthesized material, activation of the framework by prior heating was demonstrated to rid the framework of solvent molecules and thus mitigates the disruption. An alteration in crystal structure, observed by XRD, was shown to occur in both the drop-cast film and powder, regardless of activation. Additionally, IR supported the successful uptake of ammonia, independent of activation prior to exposure. For activated surMOF films, ammonia uptake was shown to be reversible, permitting removal and recycling upon additional exposures, preserving framework morphology throughout. These findings provide new information about the HKUST-1 ammonia interaction specific to morphological stability and crystal structure change.

Building upon the research herein, additional avenues of study will be explored to expand the versatility and performance capability of HKUST-1 and other MOF systems for gas capture. Morphological stability studies involving exposure with additional gas varieties, such as arsine or hydrogen sulfide, are of interest to further understand the morphological impact induced by the host-guest interaction within both free-standing and surface-anchored HKUST-1 variations. Literature precedent has shown by XRD that HKUST-1 degrades upon arsine exposure without prior activation, whereas hydrogen sulfide is observed to disrupt the framework with or without prior activation [15]. Additional MOF systems, such as MOF-5, MOF-177, and UiO-66, shall be observed to determine morphological stability upon ammonia exposure with and without activation. Prior studies demonstrated that UiO-66 was stable according to XRD upon activated exposure [51],

while both MOF-5 and MOF-177 systems were observed to degrade via XRD [52]. This area of research will yield further understanding regarding the potential capabilities and limitations of MOF materials, continuing toward the goal of incorporating MOF assemblies as smart interfaces for sensing applications or selective gas adsorption devices.

Supplementary Materials: The following are available online at <http://www.mdpi.com/2079-4991/8/9/650/s1>, SI Figures 1–12: Energy Dispersive X-ray Spectroscopy Data.

Author Contributions: Conceptualization, B.H.B., L.J.B., C.K.B. and M.E.A.; Data curation, L.J.B.; Formal analysis, B.H.B. and L.J.B.; Funding acquisition, M.E.A.; Investigation, B.H.B., L.J.B., M.L.O. and L.K.G.; Methodology, M.L.O., L.K.G. and C.K.B.; Project administration, M.E.A.; Resources, M.E.A.; Supervision, M.E.A.; Writing—original draft, B.H.B.; Writing—review & editing, L.J.B. and M.E.A.

Funding: This research was funded by NSF-CHE-158244-RUI, NSF-CHE-1263097-REU, ACS-PRF-54106-UNI5, and NSF-MRI-1126462. Additional funding was provided by the Arnold and Mabel Beckman Foundation Scholars Program (M.L.O.), the Towsley Foundation (M.E.A.), and Hope College.

Acknowledgments: We thank Jennifer Hampton for technical assistance.

Conflicts of Interest: The authors declare no conflict of interest.

References

- Li, B.; Wen, H.-M.; Zhou, W.; Chen, B. Porous Metal–Organic Frameworks for Gas Storage and Separation: What, How, and Why? *J. Phys. Chem. Lett.* **2014**, *5*, 3468–3479. [[CrossRef](#)] [[PubMed](#)]
- Liu, J.; Chen, L.; Cui, H.; Zhang, J.; Zhang, L.; Su, C.-Y. Applications of Metal–Organic Frameworks in Heterogeneous Supramolecular Catalysis. *Chem. Soc. Rev.* **2014**, *43*, 6011–6061. [[CrossRef](#)] [[PubMed](#)]
- Yi, F.-Y.; Chen, D.; Wu, M.-K.; Han, L.; Jiang, H.-L. Chemical Sensors Based on Metal–Organic Frameworks. *Chempluschem* **2016**, *81*, 675–690. [[CrossRef](#)]
- Lu, W.; Wei, Z.; Gu, Z.-Y.; Liu, T.-F.; Park, J.; Park, J.; Tian, J.; Zhang, M.; Zhang, Q.; Gentle, T.; et al. Tuning the Structure and Function of Metal–Organic frameworks via Linker Design. *Chem. Soc. Rev.* **2014**, *43*, 5561–5593. [[CrossRef](#)] [[PubMed](#)]
- Li, P.Z.; Wang, X.J.; Li, Y.; Zhang, Q.; Tan, R.H.D.; Lim, W.Q.; Ganguly, R.; Zhao, Y. Co(II)-Tricarboxylate Metal–Organic Frameworks Constructed from Solvent-Directed Assembly for CO₂ Adsorption. *Microporous Mesoporous Mater.* **2013**, *176*, 194–198. [[CrossRef](#)]
- Jiang, H.; Zhou, J.; Wang, C.; Li, Y.; Chen, Y.; Zhang, M. Effect of Cosolvent and Temperature on the Structures and Properties of Cu-MOF-74 in Low-Temperature NH₃-SCR. *Ind. Eng. Chem. Res.* **2017**, *56*, 3542–3550. [[CrossRef](#)]
- Kim, D.; Song, X.; Yoon, J.H.; Lah, M.S. 3,6-Connected Metal–Organic Frameworks Based on Tricarboxylate as a 3-Connected Organic Node and a Linear Trinuclear Co₃(COO)₆ Secondary Building Unit as a 6-Connected Node. *Cryst. Growth Des.* **2012**, *12*, 4186–4193. [[CrossRef](#)]
- Liu, X.-W.; Sun, T.-J.; Hu, J.-L.; Wang, S.-D. Composites of Metal–Organic Frameworks and Carbon-Based Materials: Preparations, Functionalities and Applications. *J. Mater. Chem. A* **2016**, *4*, 3584–3616. [[CrossRef](#)]
- Mazaj, M.; Kaucic, V.; Logar, N.Z. Chemistry of Metal–Organic Frameworks Monitored by Advanced X-ray Diffraction and Scattering Techniques. *Acta Chim. Slov.* **2016**, *63*, 440–458. [[CrossRef](#)] [[PubMed](#)]
- Chui, S.S.-Y.; Lo, S.M.-F.; Charmant, J.P.H.; Orpen, A.G.; Williams, I.D. A Chemically Functionalizable Nanoporous Material [Cu₃(TMA)₂(H₂O)₃]_n. *Science* **1999**, *283*, 1148–1150. [[CrossRef](#)] [[PubMed](#)]
- Lin, K.-S.; Adhikari, A.K.; Ku, C.-N.; Chiang, C.-L.; Kuo, H. Synthesis and Characterization of Porous HKUST-1 Metal Organic Frameworks for Hydrogen Storage. *Int. J. Hydrogen Energy* **2012**, *37*, 13865–13871. [[CrossRef](#)]
- Bordiga, S.; Regli, L.; Bonino, F.; Groppo, E.; Lamberti, C.; Xiao, B.; Wheatley, P.S.; Morris, R.E.; Zecchina, A. Adsorption Properties of HKUST-1 Toward Hydrogen and Other Small Molecules Monitored by IR. *Phys. Chem. Chem. Phys.* **2007**, *9*, 2676–2685. [[CrossRef](#)] [[PubMed](#)]
- Dathe, H.; Peringer, E.; Roberts, V.; Jentys, A.; Lercher, J.A. Metal Organic Frameworks Based on Cu²⁺ and Benzene-1,3,5-Tricarboxylate as Host for SO₂ Trapping Agents. *Comptes Rendus Chim.* **2005**, *8*, 753–763. [[CrossRef](#)]

14. Britt, D.; Tranchemontagne, D.; Yaghi, O.M. Metal-organic Frameworks with High Capacity and Selectivity for Harmful Gases. *Proc. Natl. Acad. Sci. USA* **2008**, *105*, 11623–11627. [[CrossRef](#)] [[PubMed](#)]
15. Peterson, G.W.; Britt, D.K.; Sun, D.T.; Mahle, J.J.; Browe, M.; Demasky, T.; Smith, S.; Jenkins, A.; Rossin, J.A. Multifunctional Purification and Sensing of Toxic Hydride Gases by CuBTC Metal–Organic Framework. *Ind. Eng. Chem. Res.* **2015**, *54*, 3626–3633. [[CrossRef](#)]
16. Stock, N.; Biswas, S. Synthesis of Metal-Organic Frameworks (MOFs): Routes to Various MOF Topologies, Morphologies, and Composites. *Chem. Rev.* **2012**, *112*, 933–969. [[CrossRef](#)] [[PubMed](#)]
17. Petit, C.; Huang, L.; Jagiello, J.; Kenvin, J.; Gubbins, K.E.; Bandoz, T.J. Toward Understanding Reactive Adsorption of Ammonia on Cu-MOF/Graphite Oxide Nanocomposites. *Langmuir* **2011**, *27*, 13043–13051. [[CrossRef](#)] [[PubMed](#)]
18. Nijem, N.; Fursich, K.; Bluhm, H.; Leone, S.R.; Gilles, M.K. Ammonia Adsorption and Co-Adsorption with Water in HKUST-1: Spectroscopic Evidence for Cooperative Interactions. *J. Phys. Chem. C* **2015**, *119*, 24781–24788. [[CrossRef](#)]
19. Bétard, A.; Fischer, R.A. Metal-Organic Framework Thin Films: From Fundamentals to Applications. *Chem. Rev.* **2012**, *112*, 1055–1083. [[CrossRef](#)] [[PubMed](#)]
20. Shekhah, O.; Liu, J.; Fischer, R.A.; Wöll, C. MOF Thin Films: Existing and Future Applications. *Chem. Soc. Rev.* **2011**, *40*, 1081–1106. [[CrossRef](#)] [[PubMed](#)]
21. Gu, Z.-G.; Chen, S.-C.; Fu, W.-Q.; Zheng, Q.; Zhang, J. Epitaxial Growth of MOF Thin Film for Modifying the Dielectric Layer in Organic Field-Effect Transistors. *ACS Appl. Mater. Interfaces* **2017**, *9*, 7259–7264. [[CrossRef](#)] [[PubMed](#)]
22. Zhao, Z.; Ma, X.; Kasik, A.; Li, Z.; Lin, Y.S. Gas Separation Properties of Metal Organic Framework (MOF-5) Membranes. *Ind. Eng. Chem. Res.* **2013**, *52*, 1102–1108. [[CrossRef](#)]
23. Eslava, S.; Zhang, L.; Esconjauregui, S.; Yang, J.; Vanstreels, K.; Baklanov, M.R.; Saiz, E. Metal-Organic Framework ZIF-8 Films As Low- κ Dielectrics in Microelectronics. *Chem. Mater.* **2013**, *25*, 27–33. [[CrossRef](#)]
24. Kreno, L.E.; Hupp, J.T.; Van Duyne, R.P. Metal-Organic Framework Thin Film for Enhanced Localized Surface Plasmon Resonance Gas Sensing. *Anal. Chem.* **2010**, *82*, 8042–8046. [[CrossRef](#)] [[PubMed](#)]
25. Travlou, N.A.; Singh, K.; Rodríguez-Castellón, E.; Bandoz, T.J. Cu-BTC MOF/Graphene-Based Hybrid Materials as Low Concentration Ammonia Sensors. *J. Mater. Chem. A* **2015**, *3*, 11417–11429. [[CrossRef](#)]
26. Ameloot, R.; Cobechiya, E.; Uji-i, H.; Martens, J.A.; Hofkens, J.; Alaerts, L.; Sels, B.F.; DeVos, D.E. Direct Patterning of Oriented Metal-Organic Framework Crystals via Control Over Crystallization Kinetics in Clear Precursor Solutions. *Adv. Mater.* **2010**, *22*, 2685–2688. [[CrossRef](#)] [[PubMed](#)]
27. Shekhah, O.; Wang, H.; Kowarik, S.; Schreiber, F.; Paulus, M.; Tolan, M.; Sternemann, C.; Evers, F.; Zacher, D.; Fischer, R.A.; et al. Step-By-Step Route for the Synthesis of Metal-Organic Frameworks. *J. Am. Chem. Soc.* **2007**, *129*, 15118–15119. [[CrossRef](#)] [[PubMed](#)]
28. Shekhah, O.; Wang, H.; Zacher, D.; Fischer, R.; Wöll, C. Growth mechanism of metal-organic frameworks: Insights into the nucleation by employing a step-by-step route. *Angew. Chemie Int. Ed.* **2009**, *48*, 5038–5041. [[CrossRef](#)] [[PubMed](#)]
29. Ohnsorg, M.L.; Beaudoin, C.K.; Anderson, M.E. Fundamentals of MOF Thin Film Growth via Liquid-Phase Epitaxy: Investigating the Initiation of Deposition and the Influence of Temperature. *Langmuir* **2015**, *31*, 6114–6121. [[CrossRef](#)] [[PubMed](#)]
30. Summerfield, A.; Cebula, I.; Schröder, M.; Beton, P.H. Nucleation and Early Stages of Layer-by-Layer Growth of Metal Organic Frameworks on Surfaces. *J. Phys. Chem. C* **2015**, *119*, 23544–23551. [[CrossRef](#)] [[PubMed](#)]
31. Kajiwara, T.; Higuchi, M.; Watanabe, D.; Higashimura, H.; Yamada, T.; Kitagawa, H. A Systematic Study on the Stability of Porous Coordination Polymers Against Ammonia. *Chem. A Eur. J.* **2014**, *20*, 15611–15617. [[CrossRef](#)] [[PubMed](#)]
32. Rieth, A.J.; Dinca, M. Controlled Gas Uptake in Metal–Organic Frameworks with Record Ammonia Sorption. *J. Am. Chem. Soc.* **2018**, *140*, 3461–3466. [[CrossRef](#)] [[PubMed](#)]
33. DeCoste, J.B.; Peterson, G.W. Metal–Organic Frameworks for Air Purification of Toxic Chemicals. *Chem. Rev.* **2014**, *114*, 5695–5727. [[CrossRef](#)] [[PubMed](#)]
34. Borfecchia, E.; Maurelli, S.; Gianolio, D.; Groppo, E.; Chiesa, M.; Bonino, F.; Lamberti, C. Insights into Adsorption of NH₃ on HKUST-1 Metal–Organic Framework: A Multitechnique Approach. *J. Phys. Chem. C* **2012**, *116*, 19839–19850. [[CrossRef](#)]

35. Petit, C.; Mendoza, B.; Bandoz, T.J. Reactive Adsorption of Ammonia on Cu-Based MOF/Graphene Composites. *Langmuir* **2010**, *26*, 15302–15309. [[CrossRef](#)] [[PubMed](#)]
36. Peterson, G.W.; Wagner, G.W.; Balboa, A.; Mahle, J.; Sewell, T.; Karwacki, C.J. Ammonia Vapor Removal by $\text{Cu}_3(\text{BTC})_2$ and Its Characterization by MAS NMR. *J. Phys. Chem. C* **2009**, *113*, 13906–13917. [[CrossRef](#)] [[PubMed](#)]
37. Huang, L.; Bandoz, T.; Joshi, K.L.; Van Duin, A.C.T.; Gubbins, K.E. Reactive Adsorption of Ammonia and Ammonia/Water on CuBTC Metal-Organic Framework: A ReaxFF Molecular Dynamics Simulation. *J. Chem. Phys.* **2013**, *138*, 034102. [[CrossRef](#)] [[PubMed](#)]
38. Shekhah, O.; Wang, H.; Strunskus, T.; Cyganik, P.; Zacher, D.; Fischer, R.; Wöll, C. Layer-by-Layer Growth of Oriented Metal Organic Polymers on a Functionalized Organic Surface. *Langmuir* **2007**, *23*, 7440–7442. [[CrossRef](#)] [[PubMed](#)]
39. Bashkova, S.; Bandoz, T.J. Effect of Surface Chemical and Structural Heterogeneity of Copper-Based MOF/Graphite Oxide Composites on the Adsorption of Ammonia. *J. Colloid Interface Sci.* **2014**, *417*, 109–114. [[CrossRef](#)] [[PubMed](#)]
40. Petit, C.; Wrabetz, S.; Bandoz, T.J. Microcalorimetric Insight into the Analysis of the Reactive Adsorption of Ammonia on Cu-MOF and its Composite with Graphite Oxide. *J. Mater. Chem.* **2012**, *22*, 21443–21447. [[CrossRef](#)]
41. DeCoste, J.B.; Denny, M.S.; Peterson, G.W.; Mahle, J.J.; Cohen, S.M. Enhanced Aging Properties of HKUST-1 in Hydrophobic Mixed-Matrix Membranes for Ammonia Adsorption. *Chem. Sci.* **2016**, *7*, 2711–2716. [[CrossRef](#)] [[PubMed](#)]
42. DeCoste, J.B.; Peterson, G.W.; Smith, M.W.; Stone, C.A.; Willis, C.R. Enhanced Stability of Cu-BTC MOF via Perfluorohexane Plasma-Enhanced Chemical Vapor Deposition. *J. Am. Chem. Soc.* **2012**, *134*, 1486–1489. [[CrossRef](#)] [[PubMed](#)]
43. Petit, C.; Bandoz, T.J. Synthesis, Characterization, and Ammonia Adsorption Properties of Mesoporous Metal–Organic Framework (MIL(Fe))–Graphite Oxide Composites: Exploring the Limits of Materials Fabrication. *Adv. Funct. Mater.* **2011**, *21*, 2108–2117. [[CrossRef](#)]
44. Bhunia, M.K.; Hughes, J.T.; Fettinger, J.C.; Navrotsky, A. Thermochemistry of Paddle Wheel MOFs: Cu-HKUST-1 and Zn-HKUST-1. *Langmuir* **2013**, *29*, 8140–8145. [[CrossRef](#)] [[PubMed](#)]
45. Zhang, B.; Zhang, J.; Liu, C.; Sang, X.; Peng, L.; Ma, X.; Wu, T.; Han, B.; Yang, G. Solvent Determines the Formation and Properties of Metal–Organic Frameworks. *RSC Adv.* **2015**, *5*, 37691–37696. [[CrossRef](#)]
46. Schlichte, K.; Kratzke, T.; Kaskel, S. Improved Synthesis, Thermal Stability and Catalytic Properties of the Metal-Organic Framework Compound $\text{Cu}_3(\text{BTC})_2$. *Microporous Mesoporous Mater.* **2004**, *73*, 81–88. [[CrossRef](#)]
47. Prestipino, C.; Regli, L.; Vitillo, J.G.; Bonino, F.; Damin, A.; Lamberti, C.; Zecchina, A.; Solari, P.L.; Kongshaug, K.O.; Bordiga, S. Local Structure of Framework Cu(II) in HKUST-1 Metallorganic Framework: Spectroscopic Characterization upon Activation and Interaction with Adsorbates. *Chem. Mater.* **2006**, *18*, 1337–1346. [[CrossRef](#)]
48. Daniel, T.A.; Uppili, S.; McCarty, G.; Allara, D.L. Effects of Molecular Structure and Interfacial Ligation on the Precision of Cu-Bound a,w-Mercaptoalkanoic Acid “Molecular Ruler” Stacks. *Langmuir* **2007**, *23*, 638–648. [[CrossRef](#)] [[PubMed](#)]
49. NIST Chemistry WebBook Dimethyl Sulfoxide. Available online: <http://webbook.nist.gov/cgi/cbook.cgi?ID=C67685&Type=IR-SPEC&Index=2#Top> (accessed on 28 June 2018).
50. NIST Chemistry WebBook Ammonia. Available online: <http://webbook.nist.gov/cgi/cbook.cgi?ID=C7664417&Type=IR-SPEC&Index=1> (accessed on 28 June 2018).
51. Morris, W.; Doonan, C.J.; Yaghi, O.M. Postsynthetic Modification of a Metal-Organic Framework for Stabilization of a Hemiaminal and Ammonia Uptake. *Inorg. Chem.* **2011**, *50*, 6853–6855. [[CrossRef](#)] [[PubMed](#)]
52. Saha, D.; Deng, S. Ammonia Adsorption and its Effects on Framework Stability of MOF-5 and MOF-177. *J. Colloid Interface Sci.* **2010**, *348*, 615–620. [[CrossRef](#)] [[PubMed](#)]





Article

In-Situ Growth of NiAl-Layered Double Hydroxide on AZ31 Mg Alloy towards Enhanced Corrosion Protection

Xin Ye ¹, Zimin Jiang ², Linxin Li ¹ and Zhi-Hui Xie ^{1,*}

¹ Chemical Synthesis and Pollution Control Key Laboratory of Sichuan Province, China West Normal University, Nanchong 637002, China; xinchem4@163.com (X.Y.); Linxinyj@163.com (L.L.)

² College of Foreign Language Education, China West Normal University, Nanchong 637002, China; jenny8116@126.com

* Correspondence: zhxie@cwnu.edu.cn; Tel./Fax: +86-817-256-8081

Received: 20 May 2018; Accepted: 1 June 2018; Published: 7 June 2018



Abstract: NiAl-layered double hydroxide (NiAl-LDH) coatings grown in-situ on AZ31 Mg alloy were prepared for the first time utilizing a facile hydrothermal method. The surface morphologies, structures, and compositions of the NiAl-LDH coatings were characterized by scanning electron microscopy (SEM), three dimensional (3D) optical profilometer, X-ray diffractometer (XRD), Fourier transform infrared spectrometer (FT-IR), and X-ray photoelectron spectroscopy (XPS). The results show that NiAl-LDH coating could be successfully deposited on Mg alloy substrate using different nickel salts, i.e., carbonate, nitrate, and sulfate salts. Different coatings exhibit different surface morphologies, but all of which exhibit remarkable enhancement in corrosion protection in 3.5 wt % NaCl corrosive electrolyte. When nickel nitrate was employed especially, an extremely large impedance modulus at a low frequency of 0.1 Hz ($|Z|_{f=0.1\text{ Hz}}$), 11.6 M Ω cm², and a significant low corrosion current density (j_{corr}) down to 1.06 nA cm⁻² are achieved, demonstrating NiAl-LDH coating's great potential application in harsh reaction conditions, particularly in a marine environment. The best corrosion inhibition of NiAl-LDH/CT coating deposited by carbonate may partially ascribed to the uniform and vertical orientation of the nanosheets in the coating.

Keywords: Mg alloy; LDH; corrosion; deposition; coating

1. Introduction

Mg alloy has excellent physical and mechanical properties but a high chemical reactivity and susceptibility to corrosion, which hinders its practical application and development in more fields [1]. Efforts by formation of protective coatings on Mg alloy surface to decrease the corrosion rate and extend the serving time have aroused an increasing interest in the area of surface engineering [1,2]. Many traditional coating methods are adopted to protect Mg alloy from corrosion, such as electroless Ni plating [3,4]. However, more and more attendant problems, especially environmental issues, emerge with increasing usage of these techniques, such as the high cost and complexity in dealing with the waste plating bath, and the detrimental effect of Cr to the ecosystem [3]. Thus, it is highly urgent to find state-of-the-art alternative coatings with low pollution emissions but with efficient corrosion inhibition.

Layered double hydroxides (LDHs) have received extensive attention for potential application in supercapacitor [5], catalysis [6], adsorbents [7], and corrosion protection [8] because of their diversity in compositions and structures. The charge of the metal layer in the LDHs is compensated by interlayer anions such as CO₃²⁻. Once CO₃²⁻ anions are intercalated, it cannot be exchanged by most corrosive anions, such as SO₄²⁻ and Cl⁻, due to the high ion-exchange equilibrium constant of CO₃²⁻ anions,

thereby the corrosion of the substrate under the LDHs coating will be delayed. From this point of view, CO_3^{2-} anions intercalated LDHs are an ideal choice for obtaining a LDHs coating with high corrosion inhibition capacity. The most widely reported CO_3^{2-} intercalated LDHs on Mg alloy matrix is MgAl-LDHs coating, which is obtained, in most cases, by in-situ growth technology owing to the simplification of operation and strong adhesion of the coating [9]. Recently, MgFe-LDH and MgCr-LDH films were also obtained on anodized AZ31 Mg alloy by in-situ growth measurement [10]. However, the orders of magnitude of the j_{corr} of these in-situ grown LDH coatings are higher than -8 , mostly range from -5 to -7 (Table 1) [8,11–14]. To break the bottleneck of j_{corr} , it is advisable to prepare carbonate-based LDHs film by attempting more different divalent or trivalent metallic cations. Though most recent research results proved that NiAl-LDH nanoparticles possess good photocatalytic performance [15], in-situ growth of NiAl-LDH film on Mg alloy for corrosion protection has not yet been reported to date.

Table 1. Corrosion inhibition of different layered double hydroxide (LDH) coatings on Mg alloy from most recent published literature.

Substrate	LDH Coatings	Corrosive Medium	E_{corr} V vs. SCE	j_{corr} (A cm^{-2})	Ref.
Mg alloy	MgAl- NO_3^-	Phosphate buffer saline	-1.53	3.63×10^{-7}	[14]
Anodized AZ31 Mg alloy	MgAl- NO_3^-	3.5 wt % NaCl solution	-0.47	9.48×10^{-7}	[8]
Anodized AZ31 Mg alloy	MgAl- VO_3^-	3.5 wt % NaCl solution	-0.40	2.48×10^{-7}	[8]
Anodized AZ31 Mg alloy	MgAl- NO_3^-	3.5 wt % NaCl solution	-1.34	1.18×10^{-7}	[10]
AZ31 Mg alloy	MgAl-5-fluorouracil	Phosphate buffer saline	-1.12	3.34×10^{-5}	[13]
Plasma electrolytic oxidation pretreated AZ31 Mg alloy	MgAl-5-fluorouracil	Phosphate buffer saline	-1.20	3.92×10^{-6}	[13]
AZ31 Mg alloy	MgAl-5-fluorouracil	Phosphate buffer saline	-1.42	3.27×10^{-5}	[16]
Anodized AZ31 Mg alloy	MgFe- NO_3^-	3.5 wt % NaCl solution	-1.44	1.09×10^{-6}	[10]
Anodized AZ31 Mg alloy	MgCr- NO_3^-	3.5 wt % NaCl solution	-1.47	2.16×10^{-6}	[10]
AZ91D Mg alloy	ZnAl- VO_3^-	3.5 wt % NaCl solution	-1.30	2.21×10^{-6}	[17]
AZ91D Mg alloy	ZnAl- Cl^-	3.5 wt % NaCl solution	-1.39	2.52×10^{-6}	[17]
AZ91D Mg alloy	ZnAl- NO_3^-	3.5 wt % NaCl solution	-1.42	1.33×10^{-5}	[17]
AZ31 Mg alloy	MgAl- CO_3^{2-}	3.5 wt % NaCl solution	-0.36	8.40×10^{-7}	[18]
Anodized AZ31	MgAl- CO_3^{2-}	3.5 wt % NaCl solution	-0.29	3.50×10^{-7}	[18]

Herein, we report a facile hydrothermal measurement to in-situ growth of NiAl-LDH nanocomposite on Mg alloy by use of alkaline solutions with three different nickel salts for preparation of a highly enhanced corrosion-resistant coating with an extraordinary low corrosion rate (Figure 1). The NiAl-LDH coating prepared by nickel carbonate exhibits uniformly and vertically aligned nanoarrays with an extremely large impedance modulus at a low frequency of 0.1 Hz ($|Z|_{f=0.1\text{ Hz}}$), $11.6 \text{ M}\Omega \text{ cm}^2$, and a significantly low j_{corr} down to 1.06 nA cm^{-2} in 3.5 wt % NaCl corrosive electrolyte, which outperforms the values of the foregoing achieved LDH coating on Mg alloy (Table 1) [8,10,13,14,16–18]. The NiAl-LDH coatings were characterized, and the enhanced corrosion inhibition mechanism was proposed and discussed.

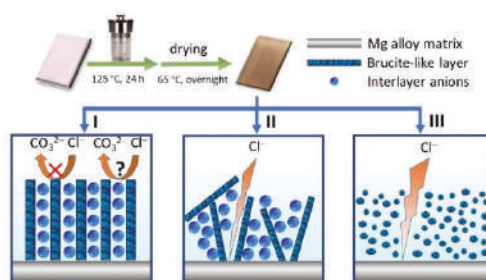


Figure 1. Schematic illustration of various microstructures of NiAl-LDH coatings prepared with different nickel salts. (I) nickel carbonate; (II) nickel nitrate; and (III) nickel sulfate. The interlayer anions are not given in case III.

2. Methods

2.1. Materials and Reagents

The matrix used is AZ31 Mg alloy with a chemical composition in wt %: 2.75 Al, 1.15 Zn, 0.16 Mn, and Mg balance. Primary chemicals include nickel carbonate (AR), nickel nitrate ($\geq 98\%$), nickel sulphate ($\geq 98.5\%$), sodium carbonate ($\geq 99.8\%$), and sodium hydroxide ($\geq 98\%$). Chemicals were acquired from Aladdin Industrial Inc. (Shanghai, China) and Sinopharm Chemical Reagent Co., Ltd. (Shanghai, China), and all chemicals were used without further purification. Ultrapure water used in the experiments was obtained using a water purification system (UPT-II-10T, Ulupure Corporation, Chengdu, China) with a resistivity of $18.2 \text{ M}\Omega \text{ cm}$ at 25°C .

2.2. Preparation of NiAl-LDH Coatings on Mg Alloy

All the NiAl-LDH coatings were grown on Mg alloy substrate by a simple one step hydrothermal method with the same steps and conditions but with three different nickel salts. The obtained coatings by use of nickel carbonate, nickel nitrate, and nickel sulphate are denoted as NiAl-LDH/CT, NiAl-LDH/NT, and NiAl-LDH/ST coatings, respectively. The mole ratio of Ni^{2+} , Al^{3+} , and CO_3^{2-} in the precursor solution is 6:2:1. Take the preparation of NiAl-LDH/CT coating, for example, which is described as follows:

Pre-treatment of substrate: The AZ31 Mg alloy was ground mechanically with SiC waterproof sand paper and degreased in an alkaline solution at 65°C for 10 min [3].

Preparation of precursor solution: 40 mL aluminum nitrate solution ($0.002 \text{ mol Al}(\text{NO}_3)_3 \cdot 9\text{H}_2\text{O}$) was first added to a nickel solution ($\sim 40 \text{ mL}$) containing $0.002 \text{ mol NiCO}_3 \cdot 2\text{Ni}(\text{OH})_2 \cdot 4\text{H}_2\text{O}$. Then, 0.001 mol anhydrous Na_2CO_3 was added, followed by pH adjustment of the solution to about 12 by use of a NaOH solution ($\sim 3.7 \text{ mL}$). Finally, the above solution was diluted to a volume of 100 mL by adding ultrapure water.

Growth of NiAl-LDH film: The solution above was then transferred into a 100 mL Teflon-lined autoclave where a pre-treated Mg alloy has been placed. Then, the autoclave was placed and kept in an oven with a temperature of 125°C for 24 h for in-situ growth of NiAl-LDH films on the matrix.

After that, the samples were taken out of the autoclave, rinsed with water, dried overnight in an oven at 65°C , and designed as NiAl-LDH/CT coating. The amount of nickel salts is 0.006 mol for deposition of NiAl-LDH/NT and NiAl-LDH/ST coatings, which is the sole difference in comparison with preparation of NiAl-LDH/CT coating.

2.3. Characterization and Electrochemical Tests

The surface morphologies and roughness of the different NiAl-LDH coatings were observed by scanning electron microscopy (SEM, Hitachi S-4800, Hitachi High-Technologies

Corporation, Tokyo, Japan), and three dimensional (3D) optical profilometer (Bruker Contour GT-K, Billerica, MA, USA), respectively. The arithmetical mean deviation of the profile (R_a) is used to estimate the roughness. The microstructures of the coatings were identified by X-ray diffractometer (XRD, D8 Advance). Fourier transform infrared spectroscopic acquisition of the specimens were obtained (FT-IR, Nicolet 6700, Thermo Scientific, Waltham, MA, USA) in the range of 4000–500 cm^{-1} . The elemental compositions of the sample surface were recorded by X-ray photoelectron spectroscopy (XPS, 250Xi, Thermo Scientific, Waltham, MA, USA) and energy dispersive X-ray spectroscopy (EDS) equipped in SEM. The water contact angles were measured with a water drop volume of 5 μL , utilizing optical contact angle meter (JC2000D, Shanghai Zhongchen Digital Technology Apparatus Co., Ltd., Shanghai, China) at 298 K. The electrochemical impedance spectroscopy (EIS) and Tafel curves were achieved using a classical three-electrode system with saturated calomel electrode (SCE) as reference electrode, Pt foil as counter electrode, and freshly ground bare Mg alloy and as-prepared NiAl-LDH coatings as working electrode (exposed area: $1 \times 1 \text{ cm}^2$) on an electrochemical workstation (CHI660E, Chenhua, Shanghai, China). The EIS frequencies range from 10^5 –0.1 Hz using an AC perturbation of 10 mV versus the open circuit potential (OCP). The Tafel measurement was performed at a scan rate of 5 mV/s in the potential region of ± 500 mV versus OCP. All the electrochemical tests were carried out in a 3.5 wt % NaCl solution at 298 K.

3. Results and Discussion

The digital photos of bare Mg alloy and three different NiAl-LDH coatings are shown in Figure 2. The substrate shows a shiny surface after polishing and pre-treatment processes, as shown in Figure 2a. After coating, all the samples show a light bronze-like surface in color, suggesting the successfully deposition of NiAl-LDH coating on the Mg alloy (Figure 2b–d). The surface brightness of NiAl-LDH/CT and NiAl-LDH/NT coatings are very close, and both of which are brighter than that of NiAl-LDH/ST coating.

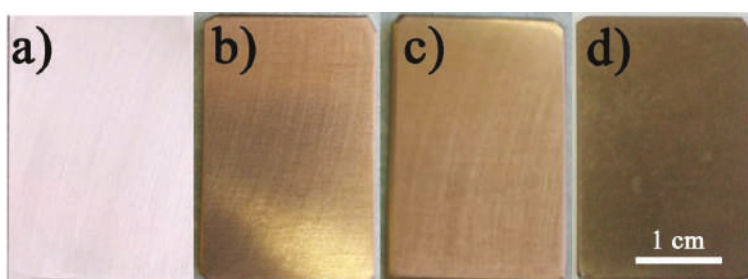


Figure 2. Digital photos of (a) bare Mg alloy; (b) NiAl-LDH/CT; (c) NiAl-LDH/NT; and (d) NiAl-LDH/ST coatings.

Figure 3a shows the XRD patterns of Mg alloy and NiAl-LDH coatings obtained with different nickel salts. For the substrate, three strong peaks at (2θ) 32.20° , 34.40° , and 36.62° , and several relatively weak peaks at 47.83° , 63.06° , and 72.50° , etc. are ascribed to the characteristic diffraction peaks of Mg (PDF 35-0821). These small and weak peaks at 18.59° , 38.02° , 58.64° , and 62.07° are the characteristic peaks of $\text{Mg}(\text{OH})_2$ (PDF 07-0239) [19,20]. The XRD patterns of all coatings are almost identical and two new peaks appear at ca. 11.73° and 23.58° , which correspond to the (003) and (006) planes of NiAl-LDH (PDF 15-0087) [15]. Figure 3b shows that all samples present almost the same absorption peaks in the FT-IR spectra. The relatively strong peak at 3692 cm^{-1} is related to the O–H stretching vibration of Ni–O–H, and the broadening adsorption peaks at 3464 cm^{-1} and 1630 cm^{-1} are associated with the O–H stretching and bending vibrations from interlamellar water molecules [21] owing to formation of hydrogen-bond. The absorption bands located at 1368 and ca. 1070 cm^{-1} correspond

to the asymmetrical and symmetrical stretching vibrations of C-O in CO_3^{2-} , respectively. The weak bands below 800 cm^{-1} are assigned to lattice vibrations of metal-oxygen (M-O) in the brucite-like layers [8]. XPS survey spectrum in Figure 3c shows that the primary elements of substrate are Mg and O, and C 1s peaks is hardly seen. After coating, two new peaks appeared at ca. 856.5 and 74.2 eV which are assigned to Ni 2p and Al 2s, respectively. In addition, significant intensification of C 1s peak at ca. 284 eV is observed. The Ni 2p high-resolution XPS spectra exhibit two major peaks along with two pairs of shake-up satellites (Figure 3d). The major peaks at 873.4 and 855.7 eV relating to Ni $2p_{1/2}$ and Ni $2p_{3/2}$ with a spin-energy separation of 17.7 eV are characteristics of Ni (II) in $\text{Ni}(\text{OH})_2$. The Al 2p spectra showing peaks at ca. 74.4 eV (Figure 3e) are ascribed to Al^{3+} species (Al-O). The C 1s spectrum is deconvoluted into three separate peaks related to different types of carbon bonds including C-C at 284.8 eV owing to adventitious carbon, C-O (286.3 eV) and O-C=O (288.7 eV) from CO_3^{2-} (Figure 3f). These characterizations demonstrate the successful formation of NiAl-LDH crystal phase on the matrix.

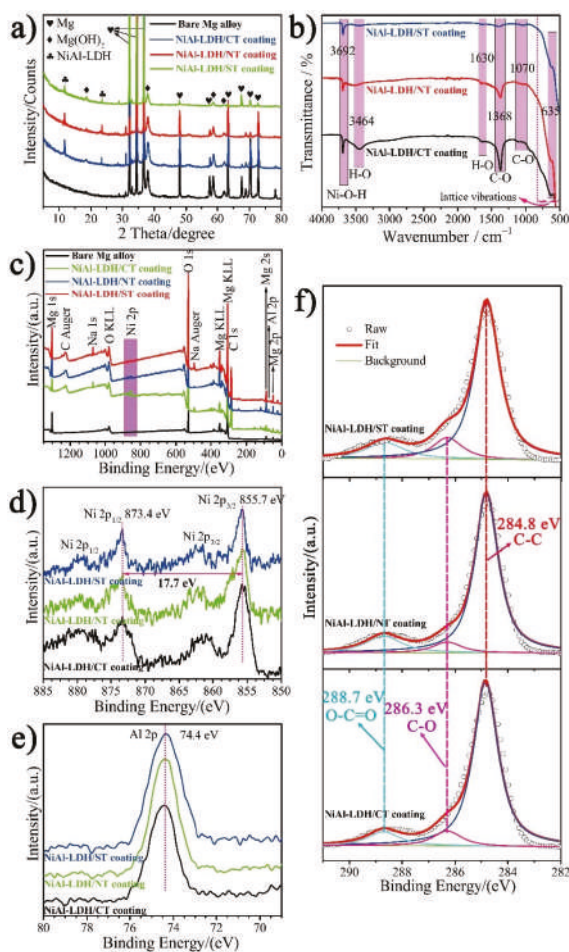


Figure 3. (a) XRD patterns; (b) FT-IR; and (c–f) XPS spectra of different NiAl-LDH coatings.

Figure 4a–c exhibits the matrix surface fully covered with vertically aligned nanoflake arrays for the NiAl-LDH/CT coating, both vertically and horizontally aligned, and randomly-inclined nanoflakes for the NiAl-LDH/NT coating, and nanonodules for the NiAl-LDH/ST coatings. These coatings are composed of Ni, Al, C, and O, and distribute uniformly all over the LDHs coating surfaces (Figure 4d–f). The thickness and side length of the nanoflakes are 63 and 425 nm, respectively, for NiAl-LDH/CT coating. The thickness of the nanoflakes for NiAl-LDH/NT coating is about 34 nm, and the length cannot be determined due to random orientation and irregular shape which result in a much higher R_a , 11.76 μm , than that of NiAl-LDH/CT coating (4.24 μm) (Figure 4g–i). The NiAl-LDH/ST coating exhibits a flat surface packed by uniform nanonodules with a size of ca. 17 nm, producing the lowest R_a , 2.01 μm , among the three types of NiAl-LDH coatings. The different shapes of the deposits result in different water contact angles (Figure 4j–l). The water contact angles of NiAl-LDH/CT and NiAl-LDH/NT coatings are 84.8° and 82.1°, respectively, while the value of NiAl-LDH/ST coating is only 67.9°. The variation in water contact angles led to a slight difference in corrosion inhibition for these coatings.

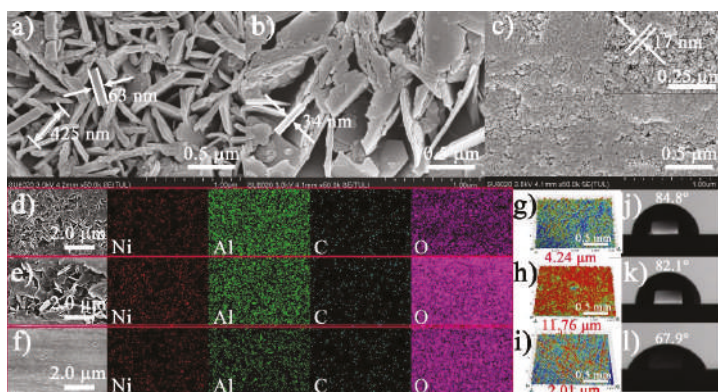


Figure 4. (a–c) SEM; (d–f) SEM-EDS mapping; and (g–i) 3D roughness images of the surface morphologies; and (j–l) water contact angles for (a,d,g,j) NiAl-LDH/CT, (b,e,h,k) NiAl-LDH/NT, and (c,f,i,l) NiAl-LDH/ST coatings.

Electrochemical impedance spectroscopy (EIS) was carried out in 3.5 wt % NaCl corrosive electrolyte to evaluate the corrosion resistance of the three NiAl-LDH coatings [22], which is depicted in Figure 5. EIS results show that Mg alloy has a two-time constant (Figure 5a), i.e., one capacitive loop at high frequency and one inductive loop with ranges from intermediate to low frequency region, which are ascribed to the electric double layer at the electrode/electrolyte interface and relaxation diffusion of corrosion products such as $\text{Mg}(\text{OH})^+_{\text{ads}}$, respectively [20,23]. According to the fitting results by use of an equivalent circuit (EC) model as given in Figure 6a [20], the charge transfer resistance (R_{ct}) of the bare Mg alloy is only 369.20 $\Omega \text{ cm}^2$. After deposition of NiAl-LDH films, totally different Nyquist plots were observed. The fitting results based on an EC model consisting of R_f , R_{ct} , and Z_w (Figure 6b) are listed in Table 2. All the coatings show a very high R_f along with a remarkable increment of R_{ct} , manifesting the significant enhancement of corrosion protection by the coatings. In contrast, NiAl-LDH/CT coating exhibits the highest R_f (6.2 $\text{M}\Omega \text{ cm}^2$) and R_{ct} (3.5 $\text{M}\Omega \text{ cm}^2$), followed by NiAl-LDH/NT coating with medium R_f (3.7 $\text{M}\Omega \text{ cm}^2$) and R_{ct} (1.8 $\text{M}\Omega \text{ cm}^2$), and the NiAl-LDH/ST coating with the lowest R_f (1.4 $\text{M}\Omega \text{ cm}^2$) and R_{ct} (0.72 $\text{M}\Omega \text{ cm}^2$). The impedance modulus at a low frequency, such as $|Z|_{f=0.1 \text{ Hz}}$, which can be obtained directly from the Bode plots without fitting, also represent the corrosion-resistant capability of a coating [20,21]. It can be seen from Table 2 that the NiAl-LDH/CT coating also possesses the highest $|Z|_{f=0.1 \text{ Hz}}$, 11.6 $\text{M}\Omega \text{ cm}^2$,

in comparison with that values of NiAl-LDH/NT (6.7 MΩ cm²) and NiAl-LDH/ST (3.4 MΩ cm²) coatings. The biggest radius of curvature in Figure 5b also confirms the best corrosion resistance of NiAl-LDH/CT coating.

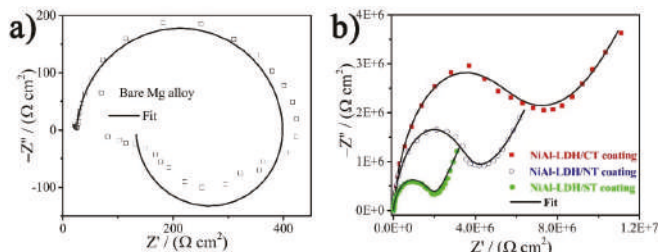


Figure 5. Nyquist plots of (a) bare Mg alloy and (b) different coatings.

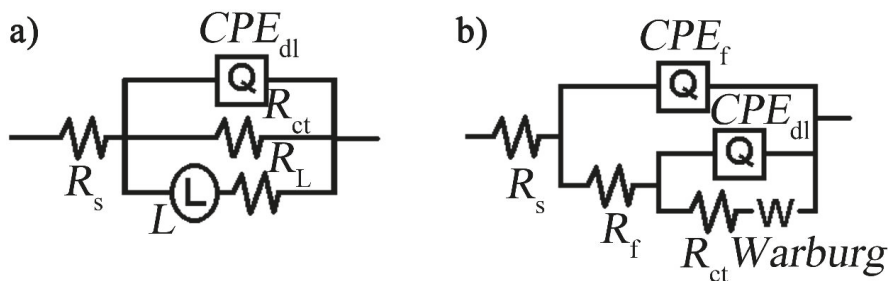


Figure 6. The equivalent circuit models used for fitting the EIS results of the (a) bare Mg alloy and (b) different NiAl-LDH coatings. The equivalent circuit (EC) model of the Mg alloy for fitting is $R_s(Q_{dl}R_{ct}(R_L L))$ where R_s is solution resistance, Q_{dl} is double layer capacitance, R_{ct} is charge transfer resistance, R_L is inductance resistance, and L is inductance. The EC model for coatings is $R_s(Q_f(R_f(Q_{dl}(R_{ct}Z_w))))$ where Q_f and R_f are capacitance and resistance of the coatings, respectively. Z_w is Warburg diffusion resistance.

Table 2. Parameters of EIS for three different NiAl-LDH coatings.

Samples	$Q_{dl}/10^{-9}$ (S s ⁿ cm ⁻²)	R_f (MΩ cm ²)	$Q_{dl}/10^{-9}$ (S s ⁿ cm ⁻²)	R_{ct} (MΩ cm ²)	$W/10^{-7}$ (S s ^{0.5} cm ⁻²)	$ Z _{f=0.1 \text{ Hz}}$ (MΩ cm ²)	$\chi^2/10^{-3}$
NiAl-LDH/CT coating	2.1 ± 0.029	6.2 ± 0.17	62.8 ± 7.6	3.5 ± 0.45	3.5 ± 0.17	11.6	0.31
NiAl-LDH/NT coating	1.5 ± 0.021	3.7 ± 0.14	113.5 ± 9.8	1.8 ± 0.22	3.5 ± 0.35	6.7	0.22
NiAl-LDH/ST coating	0.84 ± 0.087	1.4 ± 0.15	24.5 ± 2.6	0.72 ± 0.076	6.9 ± 0.27	3.4	1.5

A further Tafel test was performed to ascertain the corrosion potential, E_{corr} vs. SCE, and j_{corr} of the samples [24,25], the results of which are shown in Figure 7 and listed in Table 3. The E_{corr} and j_{corr} of a bare Mg alloy are −1450 mV and 3242 nA cm⁻², respectively. After deposition of NiAl-LDH/CT film, the E_{corr} shifts positively by ca. 800 mV to −674 mV, and j_{corr} is decreased by a factor of 3058 in comparison with that value of the matrix. The j_{corr} of NiAl-LDH/NT and NiAl-LDH/ST coatings are 3.24 and 5.75 nA cm⁻², respectively, which are in positive agreement with the variation of $|Z|_{f=0.1 \text{ Hz}}$ because a coating with higher impedance always has lower j_{corr} and better corrosion resistance. However, it is worth noting that a material with a lower j_{corr} does not always possess a higher E_{corr} . For example, the NiAl-LDH/ST coating has the highest j_{corr} but the lowest E_{corr} (Table 3). That is because E_{corr} is a thermodynamic parameter, which stands for the corrosion tendency, while corrosion rate is proportional to the j_{corr} , i.e., there is no direct relationship between E_{corr} and j_{corr} .

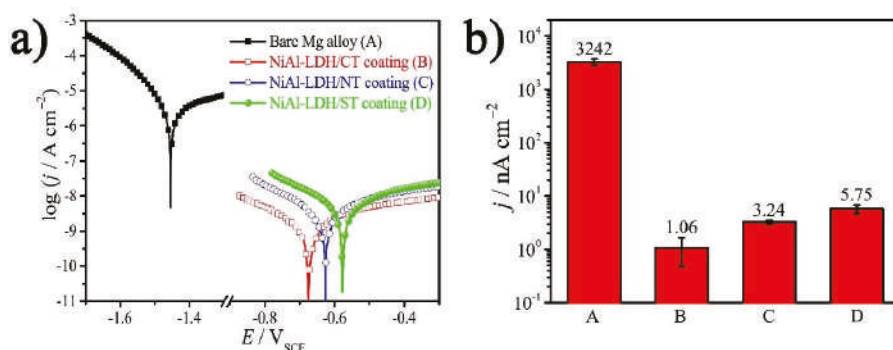


Figure 7. (a) Tafel curves of the bare Mg alloy and different NiAl-LDH coatings in NaCl corrosive medium. (b) The corresponding j_{corr} of substrate and coatings extracted from the Tafel curve.

Table 3. Parameters of Tafel curves for bare Mg alloy and different NiAl-LDH coatings.

Samples	E_{corr} (mV)	j_{corr} (nA cm ⁻²)	β_a (mV dec ⁻¹)	$-\beta_c$ (mV dec ⁻¹)
Bare Mg alloy	-1450 ± 52	3242 ± 425	331	95
NiAl-LDH/CT coating	-674 ± 42	1.06 ± 0.59	190	171
NiAl-LDH/NT coating	-625 ± 96	3.24 ± 0.25	244	184
NiAl-LDH/ST coating	-577 ± 51	5.75 ± 1.03	270	188

The high capacity and slight difference in corrosion resistance of the three different NiAl-LDH coatings are ascribed to the high affinity of LDHs towards CO_3^{2-} in comparison with the corrosive Cl^- , the different orientations of the nanosheets, and the different shapes of the deposition, which is illustrated in Figure 1. The corrosive species cannot be exchanged with the brucite-like layer and have to exchange with the CO_3^{2-} anions to arrive at the substrate surface, but the ion-exchange is not easy due to the high affinity of LDHs to CO_3^{2-} anions, enabling high enhancement in corrosion inhibition in all the as-prepared NiAl-LDH coatings. Due to the vertically-aligned nanosheets in the NiAl-LDH/CT coating, the carbonate anions distribute evenly in the interlayer spaces, which further increase the difficulty of the ion-exchange between CO_3^{2-} anions and corrosive species (Case I in Figure 1). For the NiAl-LDH/NT coating, the basal spacing becomes larger at some locations and CO_3^{2-} anions distribute unevenly in the interlayer spaces owing to irregular orientation of the nanosheets, which increases the probability for corrosive species to arrive at the substrate surface by going through fewer CO_3^{2-} anions, resulting in reduction of corrosion inhibition (Case II in Figure 1). In general, the dense plate-like arrangement of LDHs is favorable for increasing corrosion resistance of the film due to lower exposure of CO_3^{2-} anions for ion-exchange. However, for the NiAl-LDH/ST coating in this work, nanomodules with many obvious voids rather than nanoflakes were formed, as demonstrated by the SEM image in Figure 4c, which decreases the corrosion-resistant capability of the LDHs film. In addition, the smaller water contact angle of NiAl-LDH/ST coating in comparison with that of NiAl-LDH/CT and NiAl-LDH/NT coatings should also be responsible for the decreasing corrosion inhibition of NiAl-LDH/ST coating. It is worth noting that although these explanations above account for the difference in corrosion resistance of the three different coatings, the influences of the different orientation and shapes of the deposition on the corrosion inhibition are not significant because all the j_{corr} of the coatings remain in the level of nA cm^{-2} .

4. Conclusions

A facile hydrothermal strategy was progressed to achieve in-situ NiAl-LDH coatings on Mg alloy to improve the corrosion protection. All the NiAl-LDH coatings obtained by different nickel salts show

remarkable enhancement in corrosion inhibition in NaCl solution compared with Mg alloy substrate, which is attributed to the strongly affinity between charge-compensating CO_3^{2-} and brucite-like layers. The different orientation of the nanosheets and the different shapes of the deposition are mainly responsible for the slight difference in corrosion inhibition performance among the three different coatings. The NiAl-LDH/CT coating deposited by carbonate shows relatively the highest $|Z|_{f=0.1\text{ Hz}}$ and lowest j_{corr} , suggesting its best corrosion inhibition. It is believed that these findings may inspire the design and development of other LDH nanosheet arrays, such as NiCr-LDH arrays, as highly enhanced corrosion protection film for a susceptible lightweight metal matrix.

Author Contributions: The conceptualization of the work was conceived by Z.-H.X. The experiments were mainly carried out by X.Y. Z.J. revised and edited the article. Some electrochemical tests were carried out by L.L. Z.-H.X. supervised all the experiments, discussed the results with all the authors, and reviewed and revised the manuscript.

Funding: This research was funded by the National Natural Science Foundation of China (51501157, 21571148); the Fundamental Research Funds of China West Normal University (17B005); and the Chemical Synthesis and Pollution Control Key Laboratory of Sichuan Province (CSPC2014-4-2).

Conflicts of Interest: The authors declare no conflict of interest.

References

- Xie, Z.-H.; Li, D.; Skeete, Z.; Sharma, A.; Zhong, C.-J. Nanocontainer-Enhanced Self-Healing for Corrosion-Resistant Ni Coating on Mg Alloy. *ACS Appl. Mater. Interfaces* **2017**, *9*, 36247–36260. [[CrossRef](#)] [[PubMed](#)]
- Zhang, J.; Xie, Z.-H.; Chen, H.; Hu, C.; Li, L.; Hu, B.; Song, Z.; Yan, D.; Yu, G. Electroless Deposition and Characterization of a Double-Layered Ni-B/Ni-P Coating on AZ91D Mg Alloy from Eco-Friendly Fluoride-Free Baths. *Surf. Coat. Technol.* **2018**, *342*, 178–189. [[CrossRef](#)]
- Xie, Z.H.; Chen, F.; Xiang, S.; Zhou, J.; Song, Z.; Yu, G. Studies of Several Pickling and Activation Processes for Electroless Ni-P Plating on AZ31 Magnesium Alloy. *J. Electrochem. Soc.* **2015**, *162*, D115–D123. [[CrossRef](#)]
- Rajabalizadeh, Z.; Seifzadeh, D. Application of Electroless Ni-P Coating on Magnesium Alloy via CrO_3/HF Free Titanate Pretreatment. *Appl. Surf. Sci.* **2017**, *422*, 696–709. [[CrossRef](#)]
- Duan, C.; Zhao, J.; Qin, L.; Yang, L.; Zhou, Y. Ternary Ni-Co-Mo Oxy-Hydroxide Nanoflakes Grown on Carbon Cloth for Excellent Supercapacitor Electrodes. *Mater. Lett.* **2017**, *208*, 65–68. [[CrossRef](#)]
- Wang, L.; Wang, Y.; Feng, X.; Ye, X.; Fu, J. Small-Sized Mg-Al LDH Nanosheets Supported on Silica Aerogel with Large Pore Channels: Textural Properties and Basic Catalytic Performance after Activation. *Nanomaterials* **2018**, *8*, 113. [[CrossRef](#)] [[PubMed](#)]
- Ding, Y.; Liu, L.; Fang, Y.; Zhang, X.; Lyu, M.; Wang, S. The Adsorption of Dextranase onto Mg/Fe-Layered Double Hydroxide: Insight into the Immobilization. *Nanomaterials* **2018**, *8*, 173. [[CrossRef](#)] [[PubMed](#)]
- Zhang, G.; Wu, L.; Tang, A.; Zhang, S.; Yuan, B.; Zheng, Z.; Pan, F. A Novel Approach to Fabricate Protective Layered Double Hydroxide Films on the Surface of Anodized Mg-Al alloy. *Adv. Mater. Interfaces* **2017**, *4*, 1700163. [[CrossRef](#)]
- Guo, L.; Wu, W.; Zhou, Y.; Zhang, F.; Zeng, R.; Zeng, J. Layered Double Hydroxide Coatings on Magnesium Alloys: A Review. *J. Mater. Sci. Technol.* **2018**. [[CrossRef](#)]
- Wu, L.; Yang, D.; Zhang, G.; Zhang, Z.; Zhang, S.; Tang, A.; Pan, F. Fabrication and Characterization of Mg-M Layered Double Hydroxide Films on Anodized Magnesium Alloy AZ31. *Appl. Surf. Sci.* **2018**, *431*, 177–186. [[CrossRef](#)]
- Zhang, F.; Liu, Z.-G.; Zeng, R.-C.; Li, S.-Q.; Cui, H.-Z.; Song, L.; Han, E.-H. Corrosion Resistance of Mg-Al-LDH Coating on Magnesium Alloy AZ31. *Surf. Coat. Technol.* **2014**, *258*, 1152–1158. [[CrossRef](#)]
- Yan, L.; Zhou, M.; Zhang, X.; Huang, L.; Chen, W.; Roy, V.A.L.; Zhang, W.; Chen, X. A Novel Type of Aqueous Dispersible Ultrathin-Layered Double Hydroxide Nanosheets for in Vivo Bioimaging and Drug Delivery. *ACS Appl. Mater. Interfaces* **2017**, *9*, 34185–34193. [[CrossRef](#)] [[PubMed](#)]
- Peng, F.; Wang, D.; Tian, Y.; Cao, H.; Qiao, Y.; Liu, X. Sealing the Pores of PEO Coating with Mg-Al Layered Double Hydroxide: Enhanced Corrosion Resistance, Cytocompatibility and Drug Delivery Ability. *Sci. Rep.* **2017**, *7*, 8167. [[CrossRef](#)] [[PubMed](#)]

14. Peng, F.; Li, H.; Wang, D.; Tian, P.; Tian, Y.; Yuan, G.; Xu, D.; Liu, X. Enhanced Corrosion Resistance and Biocompatibility of Magnesium Alloy by Mg-Al-Layered Double Hydroxide. *ACS Appl. Mater. Interfaces* **2016**, *8*, 35033–35044. [[CrossRef](#)] [[PubMed](#)]
15. Ni, J.; Xue, J.; Xie, L.; Shen, J.; He, G.; Chen, H. Construction of Magnetically Separable NiAl LDH/Fe₃O₄-RGO Nanocomposites with Enhanced Photocatalytic Performance under Visible Light. *Phys. Chem. Chem. Phys.* **2018**, *20*, 414–421. [[CrossRef](#)] [[PubMed](#)]
16. Peng, F.; Wang, D.; Cao, H.; Liu, X. Loading 5-Fluorouracil into Calcined Mg/Al Layered Double Hydroxide on AZ31 Via Memory Effect. *Mater. Lett.* **2018**, *213*, 383–386. [[CrossRef](#)]
17. Zhou, M.; Yan, L.; Ling, H.; Diao, Y.; Pang, X.; Wang, Y.; Gao, K. Design and Fabrication of Enhanced Corrosion Resistance Zn-Al Layered Double Hydroxides Films Based Anion-Exchange Mechanism on Magnesium Alloys. *Appl. Surf. Sci.* **2017**, *404*, 246–253. [[CrossRef](#)]
18. Zhang, G.; Wu, L.; Tang, A.; Weng, B.; Atrons, A.; Ma, S.; Liu, L.; Pan, F. Sealing of Anodized Magnesium Alloy AZ31 with MgAl Layered Double Hydroxides Layers. *RSC Adv.* **2018**, *8*, 2248–2259. [[CrossRef](#)]
19. Li, D.; Chen, F.; Xie, Z.-H.; Shan, S.; Zhong, C.-J. Enhancing Structure Integrity and Corrosion Resistance of Mg Alloy by a Two-Step Deposition to Avoid F Ions Etching to Nano-SiO₂ Reinforcement. *J. Alloy. Compd.* **2017**, *705*, 70–78. [[CrossRef](#)]
20. Xie, Z.-H.; Shan, S. Nanocontainers-Enhanced Self-Healing Ni Coating for Corrosion Protection of Mg Alloy. *J. Mater. Sci.* **2018**, *53*, 3744–3755. [[CrossRef](#)]
21. Zeng, R.-C.; Liu, Z.-G.; Zhang, F.; Li, S.-Q.; Cui, H.-Z.; Han, E.-H. Corrosion of Molybdate Intercalated Hydrotalcite Coating on AZ31 Mg Alloy. *J. Mater. Chem. A* **2014**, *2*, 13049–13057. [[CrossRef](#)]
22. Chen, Y.; Zhang, J.; Dai, N.; Qin, P.; Attar, H.; Zhang, L.-C. Corrosion Behaviour of Selective Laser Melted Ti-TiB Biocomposite in Simulated Body Fluid. *Electrochim. Acta* **2017**, *232*, 89–97. [[CrossRef](#)]
23. Gan, R.; Wang, D.; Xie, Z.-H.; He, L. Improving Surface Characteristic and Corrosion Inhibition of Coating on Mg Alloy by Trace Stannous (II) Chloride. *Corros. Sci.* **2017**, *123*, 147–157. [[CrossRef](#)]
24. Dai, N.; Zhang, J.; Chen, Y.; Zhang, L.-C. Heat Treatment Degrading the Corrosion Resistance of Selective Laser Melted Ti-6Al-4V Alloy. *J. Electrochem. Soc.* **2017**, *164*, C428–C434. [[CrossRef](#)]
25. Chen, Y.; Zhang, J.; Gu, X.; Dai, N.; Qin, P.; Zhang, L.-C. Distinction of Corrosion Resistance of Selective Laser Melted Al-12Si Alloy on Different Planes. *J. Alloy. Compd.* **2018**, *747*, 648–658. [[CrossRef](#)]



© 2018 by the authors. Licensee MDPI, Basel, Switzerland. This article is an open access article distributed under the terms and conditions of the Creative Commons Attribution (CC BY) license (<http://creativecommons.org/licenses/by/4.0/>).

MDPI
St. Alban-Anlage 66
4052 Basel
Switzerland
Tel. +41 61 683 77 34
Fax +41 61 302 89 18
www.mdpi.com

Nanomaterials Editorial Office
E-mail: nanomaterials@mdpi.com
www.mdpi.com/journal/nanomaterials



MDPI
St. Alban-Anlage 66
4052 Basel
Switzerland

Tel: +41 61 683 77 34
Fax: +41 61 302 89 18

www.mdpi.com



ISBN 978-3-03928-739-0